

IMPACT OF ELECTRICALLY ASSISTED TURBOCHARGING  
ON THE TRANSIENT RESPONSE OF AN OFF-HIGHWAY  
DIESEL ENGINE

Nicola Terdich

This thesis is submitted for the award of Doctor of Philosophy (PhD)  
Department of Mechanical Engineering,  
Imperial College London

I declare that the work presented in this thesis is my own and relevant citations have been included to acknowledge the work of others.

.....

Nicola Terdich

The copyright of this thesis rests with the author and is made available under a Creative Commons Attribution Non-Commercial No Derivatives licence. Researchers are free to copy, distribute or transmit the thesis on the condition that they attribute it, that they do not use it for commercial purposes and that they do not alter, transform or build upon it. For any reuse or redistribution, researchers must make clear to others the licence terms of this work.

## ABSTRACT

Engine boosting via turbocharging is a method to increase the engine power output with minimal or no increase in engine parasitic, frictional and pumping losses. Turbocharging in conjunction with engine down-sizing and down-speeding allows a reduction of engine fuel consumption, while maintaining a high engine power output. However, turbocharging introduces a lag in engine transient response, caused by the finite amount of time required by the turbocharger to accelerate, which has to be minimized.

Electric turbocharger assistance consists of coupling an electric motor/generator to a standard turbocharger. The scope of the motor/generator is to increase the power available to accelerate the rotor assembly, so that the time to boost is reduced. The motor/generator could also be utilized to brake the turbocharger to control boost and avoid over-speeds, thus replacing the conventional waste-gate. Furthermore, electric assistance allows turbocompounding to be implemented. Turbocompounding improves the engine efficiency by utilizing the turbine and motor/generator to recuperate additional exhaust flow energy.

In this thesis, the electric turbocharger assistance impact on the turbocharger and engine performance is studied. An electrically assisted turbocharger prototype has been developed by industrial partners and it has been tested by the author of this thesis. The performance of the turbocharger turbine and motor/generator has been characterized over the full speed range and the impact of the electric assistance on the turbine flow has been investigated experimentally. It has not been possible to characterize the turbine up to choking conditions, so the data has been extrapolated via a mean-line model. The performance data obtained has been utilized to generate a model of the assisted turbocharger, which has been coupled to a one-dimensional model of a non-highway 7-litre diesel engine. This model has been utilized to study the impact of electric turbocharger assistance on the engine transient performance.

The electrical machine characterization revealed that the switched reluctance motor/generator operates efficiently up to a speed of 135,000 rev/min, making it one of the fastest running switched reluctance machines of this size. The peak machine efficiency is 93% (excluding the turbocharger bearing losses) and the maximum power output measured is 5.3 kW in generating mode and 4.3 kW in motoring mode. The motor/generator rotor aerodynamic drag loss has been calculated via computational fluid dynamics software and has been found to be 63 W at 140,000 rev/min.

Via a novel experimental technique, it has been possible to characterize the turbocharger turbine down to an expansion ratio of 1.00. This experiment revealed that the mass flow rate



drops to zero at an expansion ratio higher than unity and that below this critical pressure ratio the turbine flow is reversed. The characterization of the turbine during speed transients showed that the operating point on the performance map deviates from the quasi-steady line. This indicates that minor unsteady effects occur in the turbine and exhaust manifold flow. A further experiment revealed that the motor/generator torque oscillations have a negligible impact on the turbine performance.

The engine simulations showed that the ideal electric assistance motoring power for this application is in the 5 to 10 kW range. A 5 kW machine reduces the engine speed drop, which occurs when the engine load is suddenly increased, by up to 83%, depending on the initial load and load step size, and reduces the time to recover the original speed by up to 86%. The simulations also revealed that electric assistance is more effective than the turbine variable geometry system in improving the engine transient response, but the variable geometry system is useful to optimize boost for engine specific fuel consumption over different engine loading conditions.

## ACKNOWLEDGEMENTS

I would like to thank my supervisor, Professor Ricardo Martinez-Botas, for being an exceptionally good supervisor and mentor. I would also like to express my gratitude to the *Technology Strategy Board*, *Caterpillar* and *BorgWarner* for funding the *VERITAS* research project and sponsoring my PhD. I am particularly grateful to the people in *Caterpillar* for giving me full responsibility on tasks of fundamental importance for the success of the *VERITAS* project and for having supported me throughout the project. I am also thankful to the group in *Loughborough University* for the exchange of information during the project and to *Fleadh* for setting-up the motor/generator control system.

My thanks also go to Apostolos Pesiridis, Colin Copeland and Dave Howey, who were the post doctorate researchers of *Imperial College* that worked on the *VERITAS* project, for assisting me in the initial phases of the test-rig design and laboratory set-up. A special thank you to Peter Newton for all the helpful discussions we had when he was a student and for continuing the *VERITAS* project work, as a post doctorate researcher, after I started writing this thesis. I am very grateful to all my office mates, especially Alessandro Romagnoli, Mingyang Yang and Srithar Rajoo for being my mentors. Alessandro has also been, and is, a great friend. An enormous thank you to Aaron Costall for being a great project leader when he was at *Caterpillar* and for all the support he gave me after he joined *Imperial College London*.

The completion of this project would have not been possible without the help of the *Imperial College* staff. I am very thankful to the late Guljar Singh for manufacturing many of the test-rig components and for teaching me how to make the components I have manufactured myself, to Asanka Munasinghe and Leroy Grey for helping out with the wiring of the laboratory, to Harminder Flora and Niall McGlashan for assisting me with the design of the test-rig, and to Chrissy Stevens for processing the orders of the test-rig components.

Finally, I am extremely thankful to my family for supporting me throughout the PhD. This has been one of the toughest periods of my life and their support has been of vital importance in helping me to finish the project.

*Questa tesi è dedicata ai miei genitori e ai miei nonni. Senza il loro esempio e i loro insegnamenti non sarei mai potuto arrivare fin qui.*

# CONTENTS

Abstract .....	4
Acknowledgements .....	6
Contents.....	8
List of Figures.....	12
List of Tables.....	18
Nomenclature.....	19
1. Introduction .....	21
1.1 Turbocharging.....	21
1.1.1 General Principles.....	21
1.1.2 Turbocharger Matching .....	23
1.1.3 Diesel Engine Transient Response .....	24
1.2 Electrically Assisted Turbochargers.....	26
1.3 Research Motivation and Background .....	27
1.4 The Electrically Assisted Turbocharger Prototype .....	29
1.5 Research Objectives .....	29
1.6 Thesis Outline .....	30
2. Literature Review .....	32
2.1 Engine Down-Sizing and Down-Speeding.....	32
2.2 Turbocharged Engine Transient Behaviour.....	33
2.3 Electrically Assisted Turbochargers.....	38
2.3.1 Transient Response Improvement.....	40
2.3.2 Turbocompounding.....	46
2.3.3 Structural Design and Electrical Machine Considerations.....	48
2.4 Switched Reluctance Motor/Generator .....	52
2.5 Alternative Electrical Turbocharging and Turbocompounding Systems .....	54
2.6 Areas to Be Investigated.....	54
2.7 Chapter Summary .....	55

3. Characterization of Motor/Generator .....	57
3.1 Measurement of Electromagnetic and Frictional Losses .....	57
3.1.1 Electrically Assisted Turbocharger Details .....	57
3.1.2 Losses Occurring in an Electrically Assisted Turbocharger .....	59
3.1.3 Motor/Generator Characterization Objectives.....	60
3.1.4 Approach to Meet the Objectives of the Motor/Generator Characterization .....	61
3.1.5 Motor/Generator Characterization Methodology.....	62
3.1.6 Motor/Generator Characterization Test-Rig Layout .....	65
3.1.7 Torque Measurement.....	67
3.1.8 Other Measurements Required to Characterize Motor/Generator .....	77
3.1.9 Data-logger .....	80
3.1.10 Data-log and Control Software .....	81
3.1.11 Motor/Generator Characterization Procedure.....	82
3.1.12 Emergency Test-Rig Shutdown.....	84
3.1.13 Motor/Generator Characterization Results and Discussion .....	85
3.2 Computational Estimation of Motor/Generator Rotor Drag.....	96
3.2.1 Motor/Generator Rotor Drag Estimation Methodology.....	96
3.2.2 Motor/Generator Rotor Drag Estimation Results and Discussion.....	98
3.3 Chapter Summary .....	102
4. Steady State Characterization of Turbine.....	104
4.1 Experimental Turbine Characterization.....	104
4.1.1 Turbocharger Turbine Description .....	104
4.1.2 Turbine Characterization Objectives.....	104
4.1.3 Approach to Meet the Objectives of the Turbine Characterization.....	106
4.1.4 Non-Dimensional Parameters .....	106
4.1.5 Velocity Triangles .....	110
4.1.6 Turbine Characterization Methodology .....	110
4.1.7 Vanes Settings .....	112
4.1.8 Turbine Characterization Test-Rig Layout.....	112

4.1.9 Turbine Characterization Measurements.....	112
4.1.10 Turbine Characterization Procedure.....	117
4.1.11 Turbine Characterization Results and Discussion .....	118
4.2 Turbine Maps Extrapolation.....	137
4.2.1 Turbine Mean-Line Model.....	137
4.2.2 Further Data Interpolation and Extrapolation .....	142
4.2.3 Turbine Maps Extrapolation Results and Discussion .....	144
4.3 Chapter Summary .....	147
5. Motor/Generator Driven Turbine Unsteady Effects .....	149
5.1 Transient Turbine Testing.....	149
5.1.1 Transient Turbine Testing Test-Rig Layout.....	150
5.1.2 Turbine Transient Cycle.....	153
5.1.3 Turbine Transient Testing Procedure.....	155
5.1.4 Turbine Transient Data Filtering .....	156
5.1.5 Turbine and Air Pipe Equivalent Volume and Assistance Torque.....	157
5.1.6 Turbine Transient Testing Results and Discussion .....	159
5.2 Motor/Generator Oscillating Torque Impact on Turbine Flow .....	165
5.2.1 Impact of Oscillating Torque Investigation Description.....	166
5.2.2 Impact of Oscillating Torque Investigation Test-Rig .....	167
5.2.3 Impact of Oscillating Torque Investigation Experimental Procedure .....	168
5.2.4 Impact of Oscillating Torque Investigation Results and Discussion.....	169
5.3 Chapter Summary .....	174
6. Steady and Unsteady Impact of Turbocharger Assist on Diesel Engine .....	176
6.1 Turbocharged Diesel Engine Model Description .....	176
6.1.1 Engine and Turbocharger Details .....	176
6.1.2 Dynasty Environment .....	177
6.1.3 Custom Components Models.....	177
6.1.4 Dynasty Built-In Component Models.....	179
6.2 Turbocharged Diesel Engine Model Validation .....	182

6.2.1 Combustion Chamber Validation .....	182
6.2.2 Complete Turbocharged Engine Validation.....	185
6.2.3 Transient Turbocharger Behaviour Validation.....	187
6.3 Optimization of Turbine Vanes Opening for Steady State Operation.....	189
6.3.1 Boost Optimization Technique Description.....	189
6.3.2 $\lambda$ -Parameter.....	190
6.3.3 Boost Optimization Results and Discussion .....	191
6.4 Motor/Generator Power Impact on Engine Transient Response .....	194
6.4.1 Motor/Generator Power Impact Investigation Description .....	194
6.4.2 Motor/Generator Power Impact Investigation Results and Discussion .....	195
6.5 Electric Assistance and Variable Geometry Turbine Interaction .....	207
6.5.1 Electric Assistance and VGT Interaction Investigation Description .....	208
6.5.2 Electric Assistance and VGT Interaction Investigation Results and Discussion.....	209
6.6 Chapter Summary .....	219
6.7 Further Work.....	221
7. Conclusions .....	222
7.1 Research Objectives .....	222
7.2 Research Achievements.....	222
7.3 Recommendations for Assisted Turbocharger Prototype Improvements .....	225
7.4 Suggestions for Further Work.....	226
References .....	228
Appendix A – Turbine Performance Data in Reverse Flow Conditions .....	233
Appendix B – Complete Results Set of the Study on the Motor/Generator Oscillating Torque Impact on Turbine.....	234
Speed Parameter 2633 rev/min/ $\sqrt{K}$ .....	234
Speed Parameter 3292 rev/min/ $\sqrt{K}$ .....	235
Speed Parameter 3950 rev/min/ $\sqrt{K}$ .....	236
Speed Parameter 4608 rev/min/ $\sqrt{K}$ .....	237

## LIST OF FIGURES

Figure 1.1 – Representation of a turbocharged diesel engine .....	22
Figure 1.2 – Typical turbocharger compressor performance map.....	23
Figure 1.3 – Typical work cycle of an off-highway diesel engine installed on an excavator.....	25
Figure 1.4 – Representation of an electrically assisted turbocharging system .....	26
Figure 2.1 – Effect of engine speed on friction mean effective pressure, showing the impact of different engine components (Kovach, Tsakiris and Wong, 1982) .....	33
Figure 2.2 – Typical transient response of a turbocharged diesel engine (Watson and Janota, 1982) .....	34
Figure 2.3 – Transient response of a turbocharged diesel engine with two different fuel limits (Benajes et al., 2002).....	35
Figure 2.4 – Effects of different over-fuelling margins on diesel engine transient behaviour (Watson and Janota, 1982).....	36
Figure 2.5 – Effects of different exhaust manifold volumes on diesel engine transient behaviour (Watson and Janota, 1982).....	36
Figure 2.6 – Effects of diesel engine valve overlap on engine transient behaviour (Watson and Janota, 1982) .....	37
Figure 2.7 – Diesel engine transient performance improvement by the application of a variable geometry turbine (Filipi, Wang and Assanis, 2001) .....	38
Figure 2.8 – Picture of the electrically assisted turbocharger prototype built by Ibaraki et al. (2006).....	<b>Errore. Il segnalibro non è definito.</b>
Figure 2.9 – Results obtained by Panting et al. (2001), showing compressor speed, compressor pressure ratio and engine power during vehicle acceleration.....	40
Figure 2.10 – Results obtained by Kutrašnik et al. (2003), showing turbocharger speed, boost pressure, engine power and equivalence ratio during vehicle acceleration .....	42
Figure 2.11 – Results obtained by Kutrašnik et al. (2005), showing engine speed, engine power and boost pressure during an increase in engine load at nominally constant engine speed.....	43
Figure 2.12 – Results obtained by Balis et al. (2003) and Ibaraki et al. (2006), showing that electrical boosting can significantly increase the low speed engine torque.....	44
Figure 2.13 – Transient response results obtained by Millo et al. (2006), showing turbocharger speed, boost pressure, fuel mass injected during each stroke and compressor state during a transient event.....	45
Figure 2.14 – Compressor exit pressure and turbocharger speed during an engine transient (Ibaraki et al., 2006) .....	45



Figure 2.15 – Results obtained by Hopmann and Algrain (2003) on the steady state effects of turbocompounding, showing the effect of turbocompounding power on fuel consumption for a single operation point.....	46
Figure 2.16 – Cross section of two different ETA devices. The machine on the left is the one designed by Hopmann and Algrain (2003), which includes EM stator water cooling and roller bearings. The right figure shows the <i>ELEGT</i> device (Ryder, Sutter and Jaeger, 2006).....	48
Figure 2.17 – Stress analysis of the motor/generator rotor designed by Hopmann and Algrain (2003) at 20% over speed and of the <i>ELEGT</i> rotor at 130,000 <i>rev/min</i> (Ryder, Sutter and Jaeger, 2006) .....	49
Figure 2.18 – Heat transfer analysis of the device designed by Balis et al. (2003).....	50
Figure 2.19 – Rotor-dynamics of the <i>ELEGT</i> turbocharger (Ryder, Sutter and Jaeger, 2006).....	50
Figure 2.20 – Electrical charge flow through the power electronics and windings of a single phase of a switched reluctance motor/generator .....	52
Figure 3.1 – Representation of the electrically assisted turbocharger prototype under study....	57
Figure 3.2 – Asymmetric inverter power electronics arrangement as designed by subcontractor .....	58
Figure 3.3 – Section view of the modified electrically assisted turbocharger prototype .....	63
Figure 3.4 – Free body diagrams showing the forces and moments acting on the turbocharger rotor and bearing housing during testing.....	64
Figure 3.5 – Representation of the motor/generator test-rig showing the principal components and how they are arranged .....	65
Figure 3.6 – Assembly drawing of the initial version of the modified turbocharger .....	69
Figure 3.7 – Cross sectional drawing of the initial version of the gimbal bearings and retaining system assembly.....	69
Figure 3.8 – Air leakage path shown on the cross sectional drawing of the initial version of the gimbal bearings and retaining system assembly .....	71
Figure 3.9 – Displacement results of the structural finite element analysis of the load-cell attachment arm.....	71
Figure 3.10 – Assembly drawing of the Data Set 1 version of the modified turbocharger .....	72
Figure 3.11 – Cross sectional drawing of the Data Set 1 version of the gimbal bearings and retaining system assembly .....	73
Figure 3.12 – Displacement results of the structural finite element analysis of the NBR o-ring which blocks the flow through the gimbal bearings.....	74
Figure 3.13 – Assembly and cross sectional drawing of the cooling oil inlet hose attachment system .....	75
Figure 3.14 – Assembly drawing of the Data Set 2 version of the modified turbocharger .....	76

Figure 3.15 – Cross sectional drawing of the Data Set 2 version of the gimbal bearings and retaining system assembly .....	76
Figure 3.16 – Motor/generator testing procedure flowchart .....	83
Figure 3.17 – Data Set 1 motor/generator efficiency plotted against shaft power output. Frictional losses included (turbocharger bearing load and motor/generator rotor drag) .....	86
Figure 3.18 – Data Set 2 motor/generator efficiency plotted against shaft power output. Frictional losses included (turbocharger bearing load and motor/generator rotor drag) .....	86
Figure 3.19 – Comparison of Data Set 1 and Data Set 2 motor/generator efficiency at 80,000 rev/min. Frictional losses included (turbocharger bearing load and motor/generator rotor drag).....	87
Figure 3.20 – Data Set 1 motor/generator efficiency plotted against shaft power output. Frictional losses not included (turbocharger bearing load and motor/generator rotor drag) ...	88
Figure 3.21 – Data Set 2 motor/generator efficiency plotted against shaft power output. Frictional losses not included (turbocharger bearing load and motor/generator rotor drag) ...	88
Figure 3.22 – Comparison of Data Set 1 and Data Set 2 motor/generator efficiency at 80,000 rev/min. Frictional losses not included (turbocharger bearing load and motor/generator rotor drag).....	90
Figure 3.23 – Boundary conditions of the computational fluid dynamics model of the motor/generator air gap .....	97
Figure 3.24 – Results of the computational fluid dynamics analysis, showing the motor/generator rotor drag loss as a function of rotational speed .....	98
Figure 3.25 – Rotor drag loss and electromagnetic losses proportions for Data Set 2 .....	99
Figure 3.26 – Data Set 1 motor/generator efficiency plotted against shaft power output. Bearing losses not included.....	101
Figure 3.27 – Data Set 2 motor/generator efficiency plotted against shaft power output. Bearing losses not included.....	101
Figure 4.1 – 3D drawing of the turbine tested.....	104
Figure 4.2 – Typical turbine mass flow parameter and efficiency maps .....	105
Figure 4.3 – Expected turbine mass flow rate results .....	109
Figure 4.4 – Typical velocity triangles for a radial turbine .....	110
Figure 4.5 – Free body diagrams of the modified turbocharger rotor and bearing housing showing the moments and forces that occur during testing .....	111
Figure 4.6 – Representation of the turbine test-rig showing the principal components and how they are arranged .....	113
Figure 4.7 – Location of the inlet and outlet pressure tapplings and thermocouples relative to the turbine housing for the steady state turbine test.....	114

Figure 4.8 – McCrometer V-Cone schematic .....	115
Figure 4.9 – Steady state turbine testing procedure flowchart.....	117
Figure 4.10 – Collected turbine mass flow data. Showing only one speed-line of the 60% VGT opening.....	119
Figure 4.11 – Collected turbine total to static efficiency data. Showing only one speed-line of the 60% VGT opening.....	119
Figure 4.12 – Collected turbine mass flow data in reverse flow conditions. Showing only one speed-line of the 60% VGT opening .....	122
Figure 4.13 – Collected turbine total to total efficiency data in reverse flow conditions. Showing only one speed-line of the 60% VGT opening.....	122
Figure 4.14 – Turbine rotor outlet velocity triangle in reverse mass flow conditions .....	123
Figure 4.15 – Collected turbine mass flow data. Showing only the speed-lines of the 60% VGT opening.....	124
Figure 4.16 – Collected turbine total to static efficiency data. Showing only the speed-lines of the 60% VGT opening.....	125
Figure 4.17 – Collected turbine mass flow data in reverse flow conditions. Showing only the speed-lines of the 60% VGT opening .....	125
Figure 4.18 – Collected turbine mass flow data. Showing the full data set .....	127
Figure 4.19 – Collected turbine total to static efficiency data. Showing the full data set .....	128
Figure 4.20 – Collected turbine mass flow data in reverse flow conditions. Showing the full data set.....	128
Figure 4.21 – Gas compressibility impact on turbine performance .....	132
Figure 4.22 – Sketch of the turbine cross section which shows the location of the mean-line model nodes.....	137
Figure 4.23 – Structure of the turbine mean-line model.....	138
Figure 4.24 – Turbine zero-mass-flow pressure ratio interpolation over rotational speed .....	143
Figure 4.25 – Mass flow parameter results of the turbine mean-line model.....	144
Figure 4.26 – Total to static efficiency results of the turbine mean-line model .....	144
Figure 4.27 – Turbine mass flow parameter extrapolation results.....	146
Figure 4.28 – Turbine total to static efficiency extrapolation results.....	147
Figure 5.1 – Graph showing the relative importance and frequency content of the different sources of flow unsteadiness in an automotive turbocharger turbine (Copeland et al., 2012)..	149
Figure 5.2 – Drawing of the test-rig modified for transient turbine testing.....	151

Figure 5.3 – Location of the hot-wire anemometer, pressure sensors and thermocouples relative to the turbine housing for the turbine transient test .....	152
Figure 5.4 – Circuitry of the constant temperature anemometer (Dantec Dynamics A/S, 2013) .....	153
Figure 5.5 – Typical VGT turbocharger speed trace during an engine load increase transient..	154
Figure 5.6 – Motor/generator torque demand for Cycle A (motoring) and Cycle B (generating) .....	155
Figure 5.7 – Transient turbine testing procedure flowchart.....	156
Figure 5.8 – Schematic of the turbine transient testing test-rig .....	157
Figure 5.9 – Turbine rotational speed traces obtained from the transient test .....	160
Figure 5.10 – Mass flow parameter traces during the turbine speed transients obtained from the transient test .....	161
Figure 5.11 – Total to static efficiency traces during the turbine speed transients obtained from the transient test.....	161
Figure 5.12 – schematic showing how the miniature pressure sensors are mounted .....	168
Figure 5.13 – Motor/generator oscillating torque impact on turbine flow testing procedure flowchart.....	168
Figure 5.14 – Frequency spectrum of the inlet pressure signal.....	170
Figure 5.15 – Frequency spectrum of the outlet pressure signal .....	171
Figure 6.1 – Representation of the turbocharged diesel engine modelled.....	176
Figure 6.2 – Experiment and simulation in-cylinder pressure traces for seven different engine loading conditions.....	183
Figure 6.3 – Validation of the electrically assisted turbocharger in transient conditions .....	188
Figure 6.4 – Plot of the difference between compressor outlet pressure and turbine inlet pressure as a function of compressor outlet pressure for different $\lambda$ -parameter values .....	190
Figure 6.5 – Engine brake specific fuel consumption, pumping mean effective pressure and $\lambda$ -parameter as a function of inlet manifold pressure.....	192
Figure 6.6 – Intake and exhaust valve mass flow rate as a function of engine crank angle for two different intake manifold pressures .....	193
Figure 6.7 – Engine speed and engine torque time traces for a step change in load from 100 Nm to 399 Nm (WCA) .....	196
Figure 6.8 – Engine speed and engine torque time traces for a step change in load from 534 Nm to 817 Nm (WCB) .....	197

Figure 6.9 – Percentage improvement of speed drop and recovery time as a function of assistance power .....	198
Figure 6.10 – Turbocharger speed, intake manifold pressure and exhaust manifold pressure time traces for a step change in load from 100 Nm to 399 Nm (WCA).....	199
Figure 6.11 – Turbocharger speed, intake manifold pressure and exhaust manifold pressure time traces for a step change in load from 534 Nm to 817 Nm (WCB).....	200
Figure 6.12 – Compressor outlet pressure minus turbine inlet pressure and turbocharger torque balance time traces for a step change in load from 100 Nm to 399 Nm (WCA) .....	202
Figure 6.13 – Compressor outlet pressure minus turbine inlet pressure and turbocharger torque balance time traces for a step change in load from 534 Nm to 817 Nm (WCB) .....	203
Figure 6.14 – Compressor and turbine operating traces, plotted on their respective performance maps, for a step change in load from 100 Nm to 399 Nm (WCA).....	204
Figure 6.15 – Compressor and turbine operating traces, plotted on their respective performance maps, for a step change in load from 534 Nm to 817 Nm (WCB).....	205
Figure 6.16 – Engine speed, engine torque and compressor outlet pressure time traces for a step change in load from 100 Nm to 399 Nm (WCA) .....	210
Figure 6.17 – Engine speed, engine torque and compressor outlet pressure time traces for a step change in load from 534 Nm to 817 Nm (WCB) .....	211
Figure 6.18 – Turbine inlet pressure, inlet temperature and power time traces for a step change in load from 100 Nm to 399 Nm (WCA).....	212
Figure 6.19 – Turbine inlet pressure, inlet temperature and power time traces for a step change in load from 534 Nm to 817 Nm (WCB).....	213
Figure 6.20 – Engine cycle average pumping mean effective pressure and efficiency time traces for a step change in load from 100 Nm to 399 Nm (WCA).....	215
Figure 6.21 – Engine cycle average pumping mean effective pressure and efficiency time traces for a step change in load from 534 Nm to 817 Nm (WCB).....	216
Figure 6.22 – Compressor operating traces plotted on the device performance map. ....	218

## LIST OF TABLES

Table 2.1 – Results obtained by Hopmann and Algrain (2003) on the steady state effects of turbocompounding.....	47
Table 2.2 – Engine fuel consumption improvements over five different driving cycles obtained via mild turbocompounding (Millo et al., 2006).....	47
Table 3.1 – Motor/generator and power electronics data .....	59
Table 3.2 – Oil cart specifications .....	66
Table 3.3 – Data-logger connection details.....	81
Table 3.4 – Automatic system shutdown conditions.....	84
Table 3.5 – List of the motor/generator efficiency maps presented in this chapter .....	85
Table 3.6 – Results of the motor/generator CFD model elements size sensitivity study.....	97
Table 4.1 – Predicted peak efficiency velocity ratio (left part), predicted incidence angle at peak efficiency velocity ratio (central part), and predicted exit kinetic energy as a fraction of isentropic work at peak efficiency velocity ratio (right part).....	130
Table 4.2 – Calibrated turbine mean-line model empirical coefficients.....	145
Table 5.1 – Turbine transient data filter parameters .....	156
Table 5.2 – Transient turbine testing results uncertainty.....	165
Table 5.3 – Rotational speed and loading conditions tested during the motor/generator torque oscillations impact investigation .....	166
Table 5.4 – Turbulent kinetic energy at pipe centre for different turbine loading conditions ...	171
Table 5.5 – Frequencies of electrical machine force and torque oscillations.....	173
Table 6.1 – Engine specifications .....	177
Table 6.2 – Numerical results of the combustion chamber validation.....	184
Table 6.3 – Numerical results of the complete engine system validation.....	186
Table 6.4 – Turbocharger bearing housing validation.....	187
Table 6.5 – Improvements in speed drop and recovery time caused by electric assistance .....	198
Table 6.6 – Turbine and Compressor maximum $\zeta$ number reached during the transients.....	206
Table 6.7 – Summary of the cases simulated .....	208
Table 6.8 – Speed drop and recovery time results .....	209

# NOMENCLATURE

## ABBREVIATIONS

1D	One-dimensional
3D	Three-dimensional
A/R	Area/radius
AC	Alternate current
BMEP	Brake mean effective pressure
BSFC	Brake specific fuel consumption
CAN	Controller area network
CFD	Computational fluid dynamics
DC	Direct current
ECM	Engine control module
EGR	Exhaust gas recirculation
EM	Electrical machine
EMF	Electromotive force
ETA	Electric turbocharger assist
FAR	Fuel to air ratio
FEA	Finite element analysis
FIR	Finite impulse response
FMEP	Friction mean effective pressure
IGBT	Insulated gate bipolar transistor
IMEP	Indicated mean effective pressure
ISG	Integrated starter generator
JANAF	Joint army navy air force
NBR	Nitrile butadiene rubber
PI	Proportional integrative
PID	Proportional integrative derivative
PMEP	Pumping mean effective pressure
RPM	Revolutions per minute
VGT	Variable geometry turbine
WCA	Work cycle A
WCB	Work cycle B

## SYMBOLS

### GREEK

$\alpha$	Absolute flow angle
$\beta$	Relative flow angle
$\gamma$	Specific heats ratio
$\Delta$	Change
$\varepsilon$	Uncertainty, turbine rotor clearance height
$\zeta$	Dimensionless number related to flow unsteadiness
$\eta$	Efficiency

q	Parameter
R	Electrical resistance, gas constant
r	Radius
$\mathcal{R}$	Magnetic reluctance
Re	Reynolds number
S	Tangential momentum loss factor
$S_g$	Gas specific gravity
SP	Speed parameter
t	Time
T	Temperature, time period
U	Blade velocity
u	x component of velocity
V	Electrical voltage, volume
v	Velocity, y component of velocity
VR	Velocity ratio
W	Relative flow velocity, work
x	Independent variable
X	Position
y	Derived variable
Z	Gas compressibility, number of blades

## SUBSCRIPTS

0	Total condition
acc	Acceleration
amb	Ambient
ax	Axial
bal	Balance
cl	Clearance
cold	Cold conditions
comp	Component
comp	Compressor
cyl	Cylinder
dev	Deviation
df	Disk friction
drop	Drop
elect	Electrical
EM	Electrical machine
Flow	flow
fluid	Fluid
frict	Friction
gap	Gap
hot	Hot conditions
in	Inlet
inc	Incidence

$\theta$	Angle	is	Isentropic
$\lambda$	Dimensionless number related to engine pumping losses	jet	Jet
$\mu$	Dynamic viscosity	LC	Load-cell
$\pi$	3.14159	leak	Leakage
$\Pi$	Dimensionless ratio	max	Maximum
$\rho$	Density	meas	Measurement
$\sigma$	Electrical conductivity	min	Minimum
$\tau$	Torque	N	Number
$\omega$	Rotational speed	n	Number
		nozz	Nozzles
		opt	Optimal
		out	Outlet
<i>LATIN</i>		pass	Passage
A	Area	pl	Pressure loss
a	Acceleration	rad	Radial
B	Flow blockage factor, magnetic flux density, total bias	recov	Recovery
b	Bias component	ref	Reference
C	Absolute flow velocity	rev	Reverse flow
$C_d$	Discharge coefficient	rot	Rotor
$c_p$	Constant pressure specific heat	shaft	Shaft
d	Diameter	t	Time
$D_h$	Hydraulic diameter	tip	Tip
f	Frequency, friction factor	ts	Total to static
F	Force	tt	Total to total
h	Height, thickness	turb	Turbine
I	Electrical current, moment of inertia	turbo	Turbocharger
JVP	Jet velocity parameter	turbol	Turbulence
k	Constant	valve	Valve
k	z component of velocity	VGT	Variable geometry turbine system
KE	Kinetic energy	vol	Volume
L	Angular momentum, electrical inductance, loss	wire	Wire
l	Length	x	Independent variable
m	Mass	y	Derived variable
MFP	Mass flow parameter	$\theta$	Tangential
N	Number, revolutions per time unit		
P	Pressure, total precision error	<b>ACCENTS</b>	
PR	Pressure ratio	·	Time derivative
Q	Heat	‘	Deviation from mean
		—	Mean



# 1. INTRODUCTION

The recent rise in fuel price and the increasingly stringent engine emissions regulations are forcing off-highway engine manufacturers to produce significantly down-sized and down-speeded engines. Engine down-sizing and down-speeding aim at reducing engine frictional losses, so that an improvement in engine brake specific fuel consumption is achieved. However, reducing the engine displacement and speed would result in lower power output. It is paramount that engine performance is maintained at a similar level to the non down-sized or down-speeded equivalent engine, in order to meet the expectations of customers, who require powerful engines capable of operating heavy-duty work cycles to maximise the machine's productivity. The output power is increased by engine boosting, which consists of raising the inlet air density so that more fuel can be burned (and thus greater torque developed) for the same air/fuel ratio. Boosting is achieved either via a mechanically driven supercharger, via one or more exhaust gas driven turbochargers or via a combination of both. Turbocharging has the advantage over supercharging of not significantly increasing the engine parasitic losses and, as a consequence, this is the most common boosting technique in the diesel engines manufacturing industry.

## 1.1 TURBOCHARGING

### 1.1.1 GENERAL PRINCIPLES

A turbocharger extracts energy from the engine exhaust gases and employs it to compress fresh air into the engine cylinders. A turbocharger consists of a turbine, which expands the hot exhaust gas and recuperates part of the gas energy; a compressor, which utilizes the energy extracted by the turbine to compress fresh air; and the shaft and bearing system, which mechanically connect the turbine and compressor impellers, so that energy can be transferred from the engine exhaust flow to the intake flow. A typical turbocharging system is represented in **Figure 1.1**.

The turbine is typically of the radial inflow kind. This type of turbine is composed by a volute, a nozzle ring (which is often not present in small turbochargers to reduce costs) and an impeller (often called "wheel"). The exhaust gases enter the turbine radially via the volute, which has the role of distributing the gas flow around the nozzle ring or the impeller, and of accelerating the flow. The nozzle ring is designed to further accelerate the flow and to change the angle at which the flow approaches the wheel (Japikse and Baines, 1994). The scope of the impeller is to turn the flow from the radial to the axial direction and to turn this change of flow momentum into shaft power.

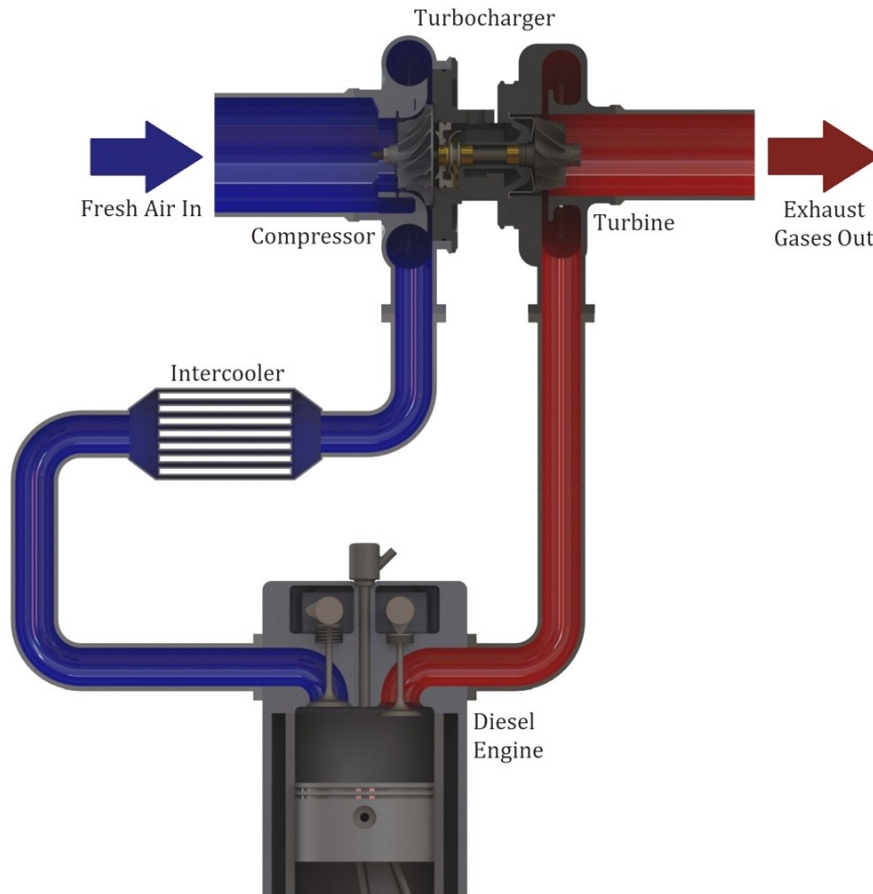


**Figure 1.1 – Representation of a turbocharged diesel engine**

The compressor is typically of the centrifugal kind and is composed of a wheel and a volute. Fresh air enters the compressor axially and is accelerated by the wheel, which is designed to turn the flow from the axial to the radial direction. The volute is designed to decelerate the flow to obtain a rise in static pressure and density.

Charge cooling is often applied in conjunction with turbocharging. Charge cooling, typically referred to as “intercooling” in the automotive industry, consists of introducing a cooler between the compressor and the engine. The scope of this cooler is to reduce the flow temperature, hence increasing the air density. This allows more fuel to be burned thanks to the increased mass of fresh air available in the cylinders, which translates to an increase of engine power output.

A turbocharger does not require power from the engine shaft to increase the intake manifold pressure since it utilizes the energy which is exhausted by the engine. This is a clear advantage over a mechanically driven supercharger, which consumes part of the engine power output to increase the intake manifold pressure. In fact, turbocharged engines can potentially have lower brake specific fuel consumption when compared to supercharged and naturally aspirated engines (Ferguson and Kirkpatrick, 2001). However, turbocharging affects the engine pumping

losses, which are the losses that occur during the cylinder scavenging process. As a consequence, the turbocharger must be carefully matched to the engine to avoid a significant drop in power-train efficiency.

### 1.1.2 TURBOCHARGER MATCHING

The turbocharger matching process aims at selecting the turbocharger which delivers the required engine torque-speed characteristics with the lowest engine brake specific fuel consumption. There are various constraints to this matching process. The most important constraint can be understood by looking at **Figure 1.2**, which shows a typical compressor performance map. The dashed line on the left side of the map represents the surge line, which is the minimum mass flow rate limit below which the compressor surges. When surge occurs, the flow in the compressor wheel becomes unstable and damage to the device can potentially occur. Clearly, the turbocharger must be matched so that the compressor never runs into surge at any engine loading and speed condition. The second constraint is that compressor choke should be avoided since the compressor would not be able to deliver the mass flow rate required to obtain the desired engine torque. Choke occurs at high mass flow rates, i.e. on the right side of the compressor performance map shown in **Figure 1.2**.

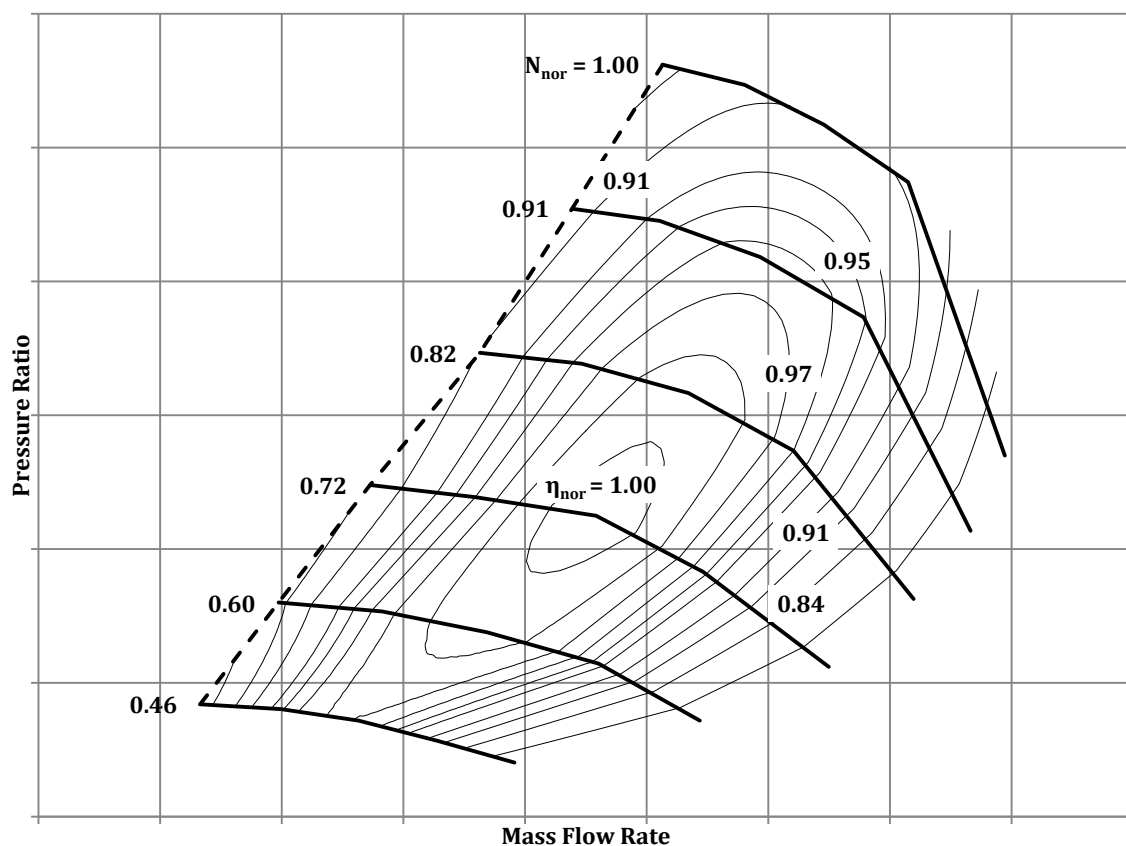


**Figure 1.2** - Typical turbocharger compressor performance map.  $N_{nor}$  stands for normalized rotor speed and  $\eta_{nor}$  stands for normalized isentropic efficiency. The dashed line on the left side of the map represents the surge line

The third constraint is that the maximum turbocharger rotational speed must not be exceeded to avoid damaging the device. However, most turbochargers include a waste-gate system which consists of a turbine bypass activated by the compressor outlet pressure. Because the compressor outlet pressure is a function of rotational speed, when the pressure which corresponds to the maximum turbocharger speed is exceeded, the turbine bypass is opened. This reduces the turbine power and prevents the turbocharger from further accelerating. If the turbine is of the variable geometry type, the waste-gate is not present, and over-speeds are avoided by opening the turbine vanes.

The main target of the matching process is that the turbocharger must be able to deliver the boost necessary to achieve the required engine power output and soot emissions. In a turbocharger which has a nozzle-less fixed geometry turbine, this is mainly achieved by tuning the turbine volute inlet area/radius ( $A/R$ ) ratio. A turbine with a low  $A/R$  ratio restricts the exhaust flow more than a turbine with a high  $A/R$  ratio, resulting in a higher turbine expansion ratio and power. This means that by tuning the turbine  $A/R$  ratio the engine boost is adjusted. In a turbocharger which has a variable geometry turbine (VGT) the nozzles angle can be varied dynamically to adjust the turbine swallowing capacity. This is equivalent to changing the  $A/R$  ratio in a nozzle-less fixed geometry turbine.

Within the constraints of compressor operation and minimum engine output torque outlined above, the compressor is selected so that it operates in the high efficiency region of its performance map, and the turbine inlet  $A/R$  ratio is selected to achieve the boost at which the best engine efficiency occurs. As it will be demonstrated by the results shown in this thesis, this optimum boost depends on the turbine and compressor efficiency, on the combustion process within the cylinders and on the energy available in the exhaust gases. As a consequence, this optimum boost changes depending on the engine loading and speed conditions, and the turbocharger must be matched considering the typical work cycle of the engine. The drawback of optimizing the engine boost for efficiency is that, for most applications, the resulting engine transient response is unsatisfactory. To overcome this issue, the boost pressure is typically set to be higher than the best efficiency boost, with the result that the brake specific fuel consumption increases.

### *1.1.3 DIESEL ENGINE TRANSIENT RESPONSE*

A fast engine transient response is necessary in many off-highway applications. **Figure 1.3** shows a typical work cycle of a diesel engine installed on an excavator. It can be noticed that the load fluctuates rapidly, and the engine must be able to respond quickly to these load changes to avoid stalls or excessive drops in speed. When large changes in load occur, a rise in boost is

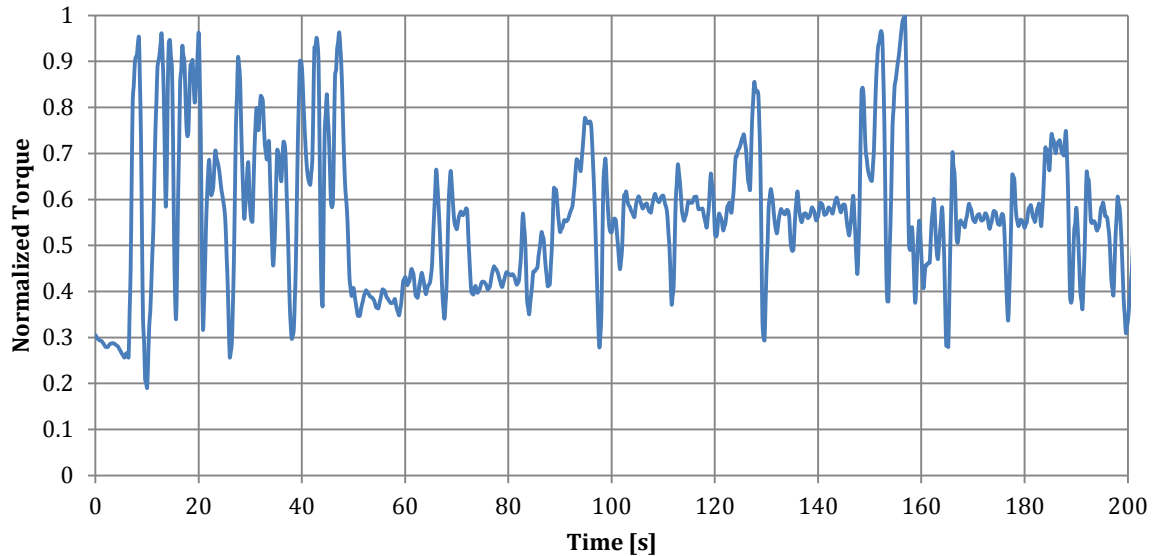


**Figure 1.3 – Typical work cycle of an off-highway diesel engine installed on an excavator**

required so that the engine is able to produce sufficient torque to overcome the increase in load. In a diesel engine, the increase in boost is produced by the larger amount of fuel injected in the cylinders, which increase the exhaust gases temperature, which in turn cause a higher turbine power.

The turbocharger takes a considerable amount of time, up to a few seconds, to reach the rotational speed which generates the boost necessary to produce the increased engine torque. This time lag is known as the turbo-lag and it is the major reason for poor diesel engine transient response. The reason why turbo-lag occurs is the turbocharger inertia combined with the fact that the power available to accelerate the turbocharger (i.e. the power not consumed by the compressor and the bearing load) is relatively small.

To reduce the turbo-lag, the turbocharger is typically matched so that it produces a boost which is higher than the best brake specific fuel consumption boost, by having a smaller turbine inlet A/R ratio. The turbo-lag improvement arises from the fact that the turbocharger speed at the beginning of the transient is higher and that the turbine power during the transient is improved. However, this increase in boost causes the engine pumping losses to increase and, as a result, the engine efficiency drops.

Turbo-lag is accentuated in down-sized and down-speeded engines, which are highly boosted to match the power output of larger and faster engines. This turbo-lag can be improved by increasing the boost over the efficiency optimized boost. However, the increase in pumping losses diminishes the efficiency benefits gained by the reduction of engine friction. Turbo-lag is therefore a major limitation to the amount by which an engine can be down-sized or down-

speeded. A good option to overcome this issue is to implement electric turbocharger assistance, which is capable of improving engine transient response without continuously increasing the pumping losses.

## 1.2 ELECTRICALLY ASSISTED TURBOCHARGERS

One device which is capable of reducing the turbo-lag with minimal increase in engine pumping losses is the electrically assisted turbocharger. This device consists of a standard turbocharger which is mechanically lin

ked to an electrical motor/generator, as shown in **Figure 1.4**. The electrically assisted turbocharger operates like a standard turbocharger. However, when the engine load increases, the motor assists the turbine in accelerating the turbocharger rotor. This means that the time required to reach the desired boost is reduced without increasing the steady state pumping losses.

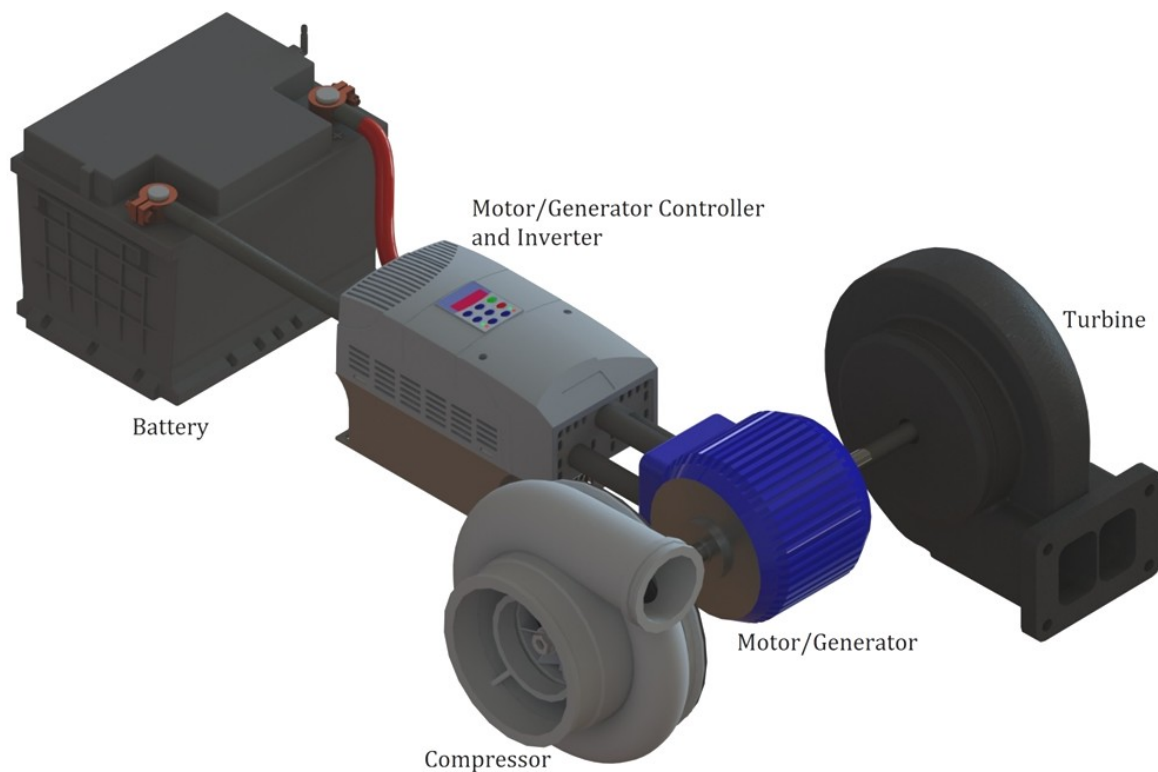


**Figure 1.4 - Representation of an electrically assisted turbocharging system**

Because the motor/generator is capable of increasing the load on the turbine by operating in generating mode, it can be employed to avoid turbocharger over-speeds and, for gasoline engines, to control boost. As a consequence, the waste-gate and the turbine variable geometry systems are not necessary, making the electrically assisted turbocharger more cost effective. Nevertheless, the turbine variable geometry system is not made redundant by electric

assistance because it adds an extra degree of freedom which could be exploited in different ways. The motor/generator can also be utilized to slow down the turbocharger when the engine load drops, so that part of the turbocharger rotor kinetic energy is recuperated. One further advantage of the electrically assisted turbocharger is that it can be implemented to achieve electrical turbocompounding. This allows to reduce the engine brake specific fuel consumption by recuperating part of the exhaust gases energy and returning it to the power-train.

The power absorbed or generated by the motor/generator can be taken from or stored in a battery system. The charge state of this battery system must be controlled so that it stays within specified limits. This battery system could be connected to the turbocharger electrical machine alone, in which case the power absorbed by the electric assistance must be equal to the power generated over the engine work cycle. To maintain the energy balance it is necessary to temporarily operate the electric assistance in generating mode, momentarily increasing the engine pumping losses. Alternatively, the battery system can be connected to the engine via a second motor/generator coupled to the engine shaft, so that an energy transfer could occur between the turbocharger and the engine.

The motor/generator can be coupled to the turbocharger via a number of different methods. If the electrical machine is sufficiently small, it can be packaged within the turbocharger bearing housing. This is a cost effective method because the motor/generator rotor can be directly mounted on the turbocharger shaft, reducing the number of parts required. This method also results in the most compact turbocharger so that it can be packaged on existing engines with minimal modifications.. Alternatively, the electrical machine can be installed outside the bearing housing, and can be connected to the turbocharger rotor via a gearing system or, if positioned on the same axis of the turbocharger, via a coupling device. This results in a more difficult to package turbocharger, but the cooling of the electrical machine is easier.

### 1.3 RESEARCH MOTIVATION AND BACKGROUND

This PhD project is part of a research and development project sponsored by the United Kingdom government *Technology Strategy Board*, whose scope is to stimulate technological innovation to produce United Kingdom economic growth; *Caterpillar*, which is a leading non-highway engine and machinery producer; and *BorgWarner*, which is a major turbocharger and automotive components supplier. This project includes two university partners which are *Imperial College London* and *Loughborough University*.

The scope of this project is to develop an electrically assisted turbocharger prototype and to demonstrate that this turbocharger is capable of improving the transient response of an off-highway, 7-litre diesel engine. The validation of this technology will allow *Caterpillar* to down-

size and down-speed its engines to improve the fuel consumption and CO<sub>2</sub> emissions, while maintaining or improving engine transient performance. This will result in reduced operating costs and increased productivity for the end user of Caterpillar's machines and power systems.

The work which has to be carried out within this project has been divided amongst the partners in the following way:

- **Caterpillar** – The lead partner provides the application and route to market through its off-highway machine products and power systems. In addition to managing the overall direction of the project, *Caterpillar* is responsible for the analysis of the machine duty cycle, specifying the performance requirements, and supporting the demonstration of the engine level benefits which can be attained by assisting the turbocharger. These benefits will be demonstrated both by numerical simulations and by engine testing.
- **BorgWarner** – The main role of *BorgWarner* is to design and manufacture the electrically assisted turbocharger prototype. *BorgWarner* also has to test the prototype to prove that it will survive in an engine environment. The motor/generator and power electronics development was subcontracted.
- **Imperial College London** – The role of *Imperial College* is to study and analyze the physics of the electrically assisted turbocharger, focusing on the air system and turbine. *Imperial College* is also responsible for testing and providing performance data on the motor/generator and turbocharger turbine. Both sets of data are required by *Loughborough University* to set-up the electric assistance controller. The motor/generator data is required by the electrical machine inverter designer to set-up the motor/generator control system.
- **Loughborough University** – The main role of this partner is to develop the electric assistance control algorithm. *Loughborough University* must also carry out the engine testing in its laboratories, in collaboration with *Caterpillar*.

The *Imperial College* group that works on this project is guided by Professor Ricardo Martinez-Botas. The group is formed by one full-time PhD student (the author of this thesis) and two part-time post-doctorate researchers. The role of the author is to study the physics of the electrically assisted turbocharger, and to design and carry out performance tests on the turbocharger prototype. The scientific objectives of the author's work are to analyze the impact of the electric assistance on the turbine aerodynamics and to understand the mechanisms that lead to improved engine transient performance. The role of the post-doctorate researchers is to specify the electrical system required to run the motor/generator, specify the oil cart required to lubricate and cool the turbocharger during testing, specify the laboratory compressed air pipe-



work, and to specify the data-logging system. The post-doctorate researchers have also assisted the author in the initial phases of the motor/generator performance test design and have carried out some computational fluid dynamics simulations to assess the motor/generator windage losses. The electrical machine windage losses have also been investigated independently by the author and in this thesis only the results obtained by the author are published.

#### 1.4 THE ELECTRICALLY ASSISTED TURBOCHARGER PROTOTYPE

The electrically assisted turbocharger prototype designed by *BorgWarner* has the layout shown in **Figure 1.4**, where the motor/generator sits inside the turbocharger bearing housing. The assisted turbocharger is based on the *BV63* turbocharger produced by *BorgWarner*. Only the shaft and the bearing housing differ from the production turbocharger. The compressor is of the centrifugal type and the turbine is of the radial inflow type. The turbine has a variable geometry system which consists of an electrically actuated mechanical system which changes the angle of the stator vanes.

The motor/generator is of the switched reluctance type and has six stator poles and four rotor poles. It is designed to have a nominal power output of 7.5 kW and a maximum rotational speed of 140,000 rev/min. The machine is very compact and the assisted turbocharger inertia is only approximately 10% higher than the inertia of the *BV63* production turbocharger. The motor/generator stator is oil cooled. The turbocharger bearing system is of the hydrodynamic type and it consists of two journal bearings and one thrust bearing.

#### 1.5 RESEARCH OBJECTIVES

The objectives of this research have been determined by reviewing the relevant literature and by the need of fulfilling the sponsoring companies' requirements. The gaps in the literature are mainly related to the impact of electric assistance on turbine performance, the sizing of the motor/generator, the electric assistance interaction with the variable geometry turbine system, the electrical and energy storage system, turbocompounding, and turbocharger assistance control. Additional details on this are given in **Chapter 2**, where the relevant literature is summarized.

The scientific scope of this research is to study the impact of electric assistance on the engine and turbocharger flow and to obtain data on the performance of the electrically assisted turbocharger. Therefore, the objectives of this research are the following:

- Experimentally characterize the performance of the motor/generator employed to assist the turbocharger, in order to understand what are the electric assistance losses.

- Study turbine steady and unsteady aerodynamic performance in regimes with electrical assistance, to understand if the aerodynamic losses are affected by electric assistance.
- Investigate the impact of electric assistance on engine transient response and how it is affected by electrical machine performance.
- Study how the turbocharger assistance system and the turbine variable geometry system can be employed simultaneously to improve engine transient response and reduce pumping losses.

## 1.6 THESIS OUTLINE

**Chapter 1: Introduction** – This chapter sets the thesis into context. A brief description of electrically assisted turbocharging and the motivation behind this research project is provided. The objectives of the research are given in this chapter.

**Chapter 2: Literature Review** – In this chapter the relevant literature is summarized. The chapter is divided into sections which cover diesel engine transient response, electrically assisted turbocharger benefits and design difficulties, and switched reluctance motor/generators. The gaps in the literature are assessed from which the research objectives are drawn.

**Chapter 3: Characterization of Motor/Generator** – This chapter provides a description and the results of the motor/generator performance characterization. This experimental investigation helps to build an understanding of where the different losses occur in an electrically assisted turbocharger and to separate the electromagnetic losses from other forms of loss. A computational fluid dynamic analysis is carried out to quantify the drag on the electrical machine rotor.

**Chapter 4: Steady State Characterization of Turbine** – This chapter describes the steady state turbine characterization work. The turbocharger turbine is characterized at low pressure ratio to understand how it behaves when it is motored by the electrical machine. The data obtained via this test is extrapolated via a mean-line model to cover the turbine performance map areas which could not be characterized experimentally.

**Chapter 5: Motor/Generator Driven Turbine Unsteady Effects** – In this chapter the unsteady effects in the turbine flow caused by the motor/generator are studied. The chapter is divided in two sections. The first section concerns the low frequency unsteady effects caused by the increased turbocharger acceleration. The second section concerns the high frequency unsteady effects generated by the motor/generator torque oscillations.

**Chapter 6: Steady and Unsteady Impact of Turbocharger Assist on Diesel Engine** – This chapter is focused on the impact of electric assistance on engine performance. Three different investigations are carried out. The first study describes the optimization of engine boost for improving engine efficiency. The second investigation focuses on the impact of electric assistance on engine response and on the sizing of the motor/generator. The last study explores how electric assistance and the variable geometry turbine can be actuated simultaneously to further improve engine performance.

**Chapter 7: Conclusions** – In this chapter the key findings of this research are summarized and recommendations on improvements and modifications to the electrically assisted turbocharger prototype are given.

## 2. LITERATURE REVIEW

This chapter summarizes the literature relevant to the topic of electrically assisted turbocharging. The chapter begins with a summary of the benefits achieved via engine down-sizing and down-speeding, which are the main drivers of the electric turbocharger assistance implementation in this project, and continues with an explanation of how turbocharged diesel engines behave during transients. The core of the chapter is a summary of the research carried out on electrically assisted turbochargers, which covers the transient response benefits, turbocompounding, design issues and switched reluctance motor/generators. From this summary, the research areas which still need to be investigated are identified.

### 2.1 ENGINE DOWN-SIZING AND DOWN-SPEEDING

Down-sizing consists of reducing the displacement of an engine by reducing the cylinders number and/or by reducing the displaced volume of each cylinder. The fuel consumption benefits arise from the fact that the engine operates at higher Brake Mean Effective Pressure (BMEP), where the efficiency is higher (Lumley, 1999). An engine with fewer cylinders will have less mechanical losses (Fraser, 2011), (Balis, Middlemass and Shahed, 2003), as there will be fewer bearings, poppet valves and pistons. In addition, the weight of a down-sized engine will be lower than the weight of the original engine, which translates to better vehicle dynamics and lower fuel consumption for on-road applications, as a smaller mass has to be accelerated and decelerated. A smaller engine will also have a lower thermal inertia, so it takes less time to warm-up to ideal working conditions (Fraser, 2011). The downside is that a smaller engine with lower inertia will have a worse transient response in constant speed applications such as electric generators, where a high engine inertia reduces the speed drop caused by the sudden increase in load (Katrašnik, Medica and Trenc, 2005), (Watson and Janota, 1982).

Down-sizing by reducing the number of cylinders leads to greater benefits compared to just reducing the displacement of each cylinder. This is because a smaller number of large bore cylinders will have lower friction than a large number of small bore cylinders (Lumley, 1999). Moreover, as the surface to volume ratio decreases with increasing cylinder size, a large cylinder will also suffer less heat loss (Ferguson and Kirkpatrick, 2001). An advantage of an engine with a high number of cylinders is that, for the same BMEP, piston speed and brake power, it will be lighter than a geometrically similar engine with fewer cylinders (Lumley, 1999).

Down-speeding, similarly to down-sizing, reduces the mechanical losses, as these losses are dependent on engine speed (**Figure 2.1**) (Lumley, 1999). Having an engine with a peak torque

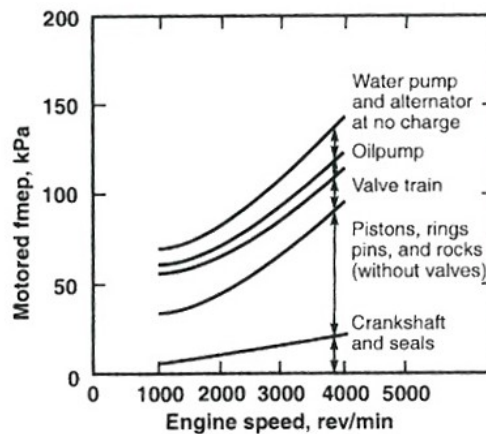


Figure 2.1 - Effect of engine speed on friction mean effective pressure, showing the impact of different engine components (Kovach, Tsakiris and Wong, 1982). Copyrights Society of Automotive Engineers Inc.

at a lower rev/min also means that the exhaust valve opening can be delayed (Lumley, 1999), reducing the exhaust blow-down losses. In addition, a more aggressive camshaft profile is possible (Lumley, 1999), thereby improving the volumetric efficiency and reducing the pumping losses. On the other hand, heat losses will be higher as more time is allowed for heat transfer to occur.

Both down-sizing and down-speeding will cause a performance decrement of the engine unless the maximum engine BMEP is increased. In on-road applications engine performance is very important in terms of sales, as customers have high expectations of vehicle acceleration and drivability both for emotional and practical reasons (Fraser, 2011). In off-road applications engine power is particularly important since it translates directly to ability to do work (productivity) and therefore to a reduction of the impact of fixed costs on final product cost (Gosling, 2007). For all the reasons stated above, it is paramount to maintain a high maximum engine BMEP via boosting or, if the engine already boosted, by increasing the boost pressure.

## 2.2 TURBOCHARGED ENGINE TRANSIENT BEHAVIOUR

It is well known that turbocharged engines have poor transient response unless the turbocharger is matched to minimize this problem. The poor transient response is caused by the finite amount of time required by the turbocharger to accelerate and deliver the required boost. This is the consequence of the high turbocharger inertia relative to the turbine power available to accelerate the turbocharger. This problem becomes more accentuated when the boosting level is very high, which is typical of extremely down-sized engines. This is because the maximum fuel which can be injected at the beginning of the transient is generally lower for a highly boosted small displacement engine than for a larger displacement less boosted engine, assuming negligible boosting at the beginning of the transient for both situations (Watson and Janota, 1982), and therefore the fuel energy available is less for the smaller engine. As it will be

seen later, the transient response depends on the maximum rate at which fuel can be injected during the transient while maintaining the same level of emissions.

When the engine is operating in steady state at low speed and/or load, the exhaust gas energy content is low and so is the boost pressure. In a diesel engine, when the torque demand is increased, the fuel to air ratio is increased and the exhaust gas energy content rises (Benajes et al., 2002). At this point, the turbine power exceeds the compressor power and so the turbocharger accelerates. As the boost increases, the compressor load increases too, but more fuel can be injected and the exhaust energy further increases. Towards the end of the transient, when the desired engine torque is reached, the fuel to air ratio (FAR) is reduced while the boosting pressure is still increasing. As a result, the power consumption of the compressor now matches the power output of the turbine, and the turbocharger stops accelerating. Due to the fact that the compressor power consumption increases as soon as the turbocharger accelerates, the power surplus available to accelerate the turbocharger is always relatively low compared to

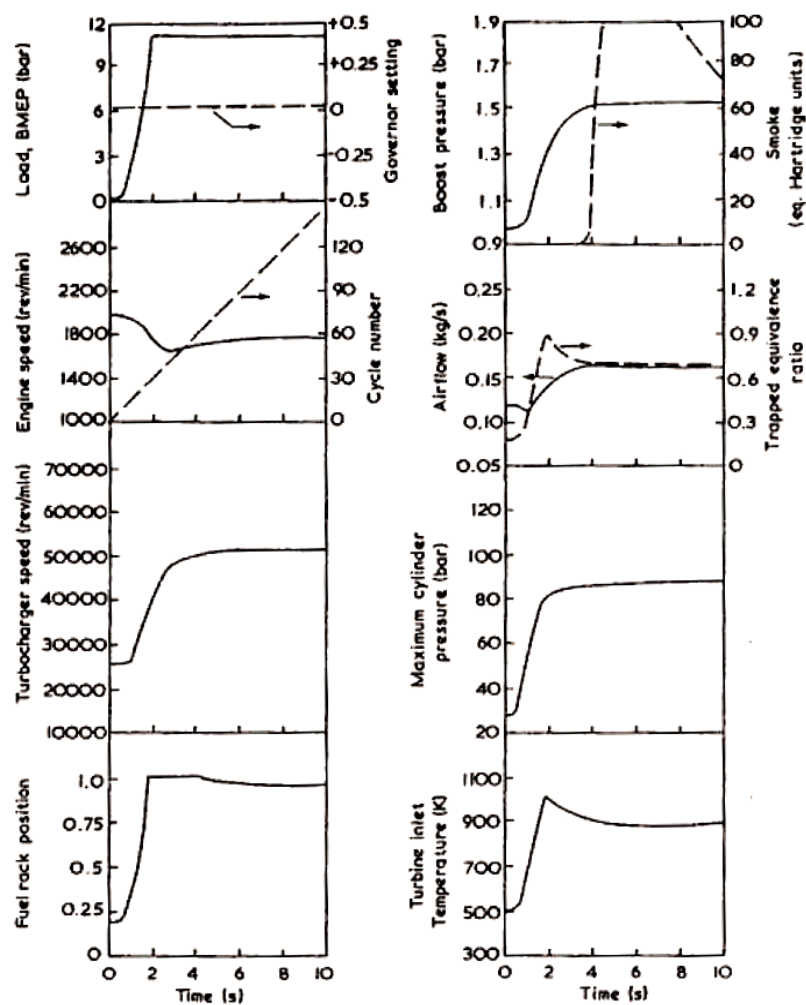
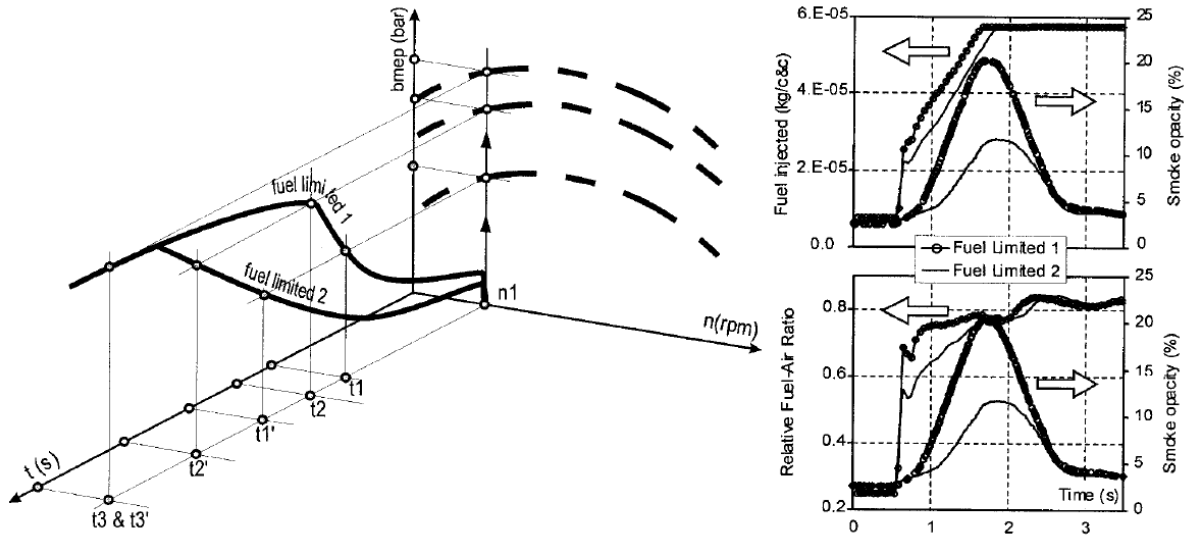


Figure 2.2 - Typical transient response of a turbocharged diesel engine (Watson and Janota, 1982). Note how the increase in boost pressure is driven by the increase in fuelling which causes an increase in exhaust gases temperature. Copyrights Watson and Janota



**Figure 2.3 – Transient response of a turbocharged diesel engine with two different fuel limits (Benajes et al., 2002). Note how the more stringent limit (No. 2) reduces the soot emission but worsen the engine response. Used with permission from SAGE Publications Ltd.**

the total turbine power. Therefore the turbocharger takes a non-negligible amount of time to deliver the required boost. Something similar occurs in a gasoline engine, but instead of increasing the FAR to increase the exhaust gases energy, the throttle valve is opened.

Obviously, the more fuel that is added during the transient, the more energy that is available in the exhaust manifold and the faster is the engine response, as shown in **Figure 2.3**. However, **Figure 2.3** also shows that increasing fuelling raises the soot emission as well and therefore increasing the fuelling is not always possible due to the need to control legislated pollutants emissions. Moreover, an excessive increase in fuelling can sometimes worsen the engine transient response either due to excessive jet penetration (Benajes et al., 2002) or due to equivalence ratio above unity (Watson and Janota, 1982). **Figure 2.4** shows an example where risen fuelling worsens the engine response due to excessive equivalence ratio.

A further cause of turbo-lag is the finite amount of time required to fill the exhaust and inlet manifolds (Watson and Janota, 1982). In order to increase the inlet air density, the compressor must pump air into the intake manifold. The larger the manifold is, the more time it requires to fill and therefore the longer it takes to reach steady state boosting. Similarly, a large exhaust manifold will take longer to fill, resulting in lower specific energy available at the turbine (Watson and Janota, 1982). Twin and double entry turbines, which make maximum use of the pulsating flow, will have a better transient response compared to single entry turbines (Watson and Janota, 1982), as shown in **Figure 2.5**.

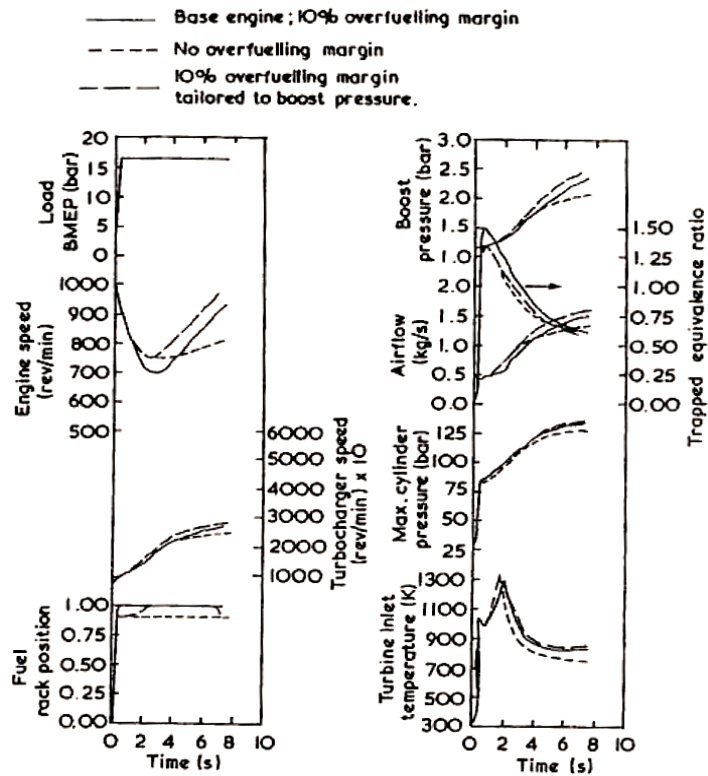


Figure 2.4 - Effects of different over-fuelling margins on diesel engine transient behaviour (Watson and Janota, 1982). Transient response is deteriorated due to excessive fuel injection. Copyrights Watson and Janota

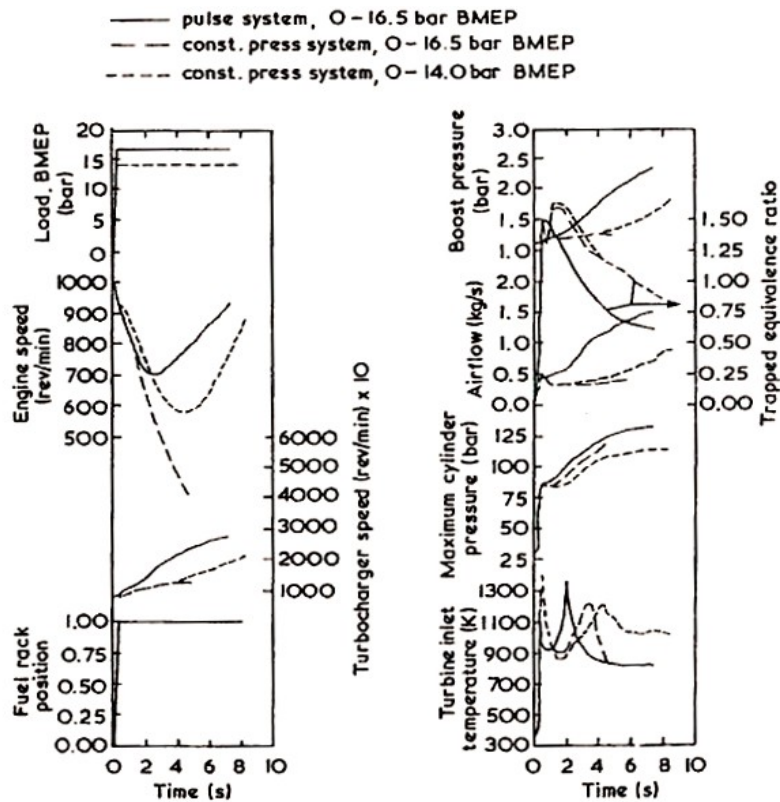


Figure 2.5 - Effects of different exhaust manifold volumes on diesel engine transient behaviour (Watson and Janota, 1982). With the larger exhaust volume (constant pressure system) the load change had to be decreased from 16.5 bar to 14.0 bar BMEP to avoid engine stalling. Copyrights Watson and Janota



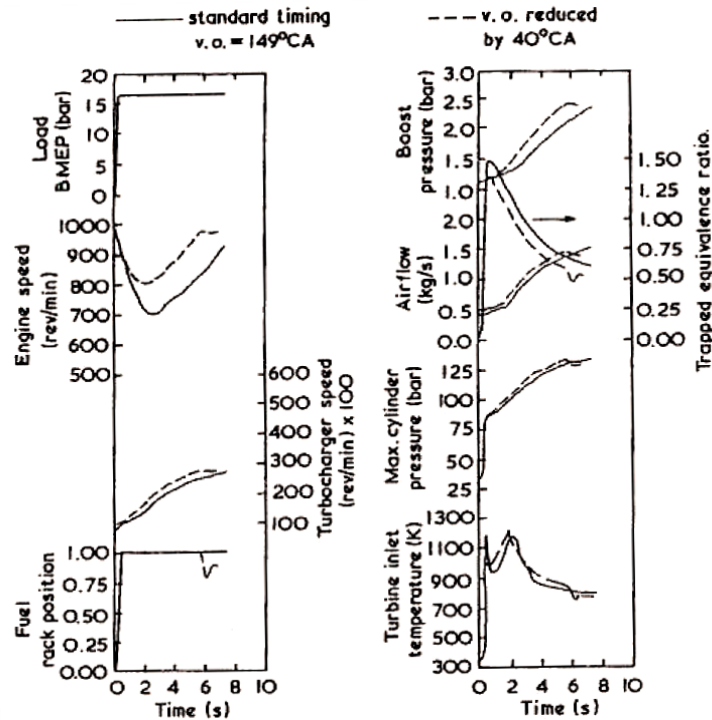


Figure 2.6 – Effects of diesel engine valve overlap on engine transient behaviour (Watson and Janota, 1982). Transient behaviour is significantly improved by reducing the valve overlap. Copyrights Watson and Janota

Thermal inertia will affect transient response too (Benajes et al., 2002). As the exhaust and turbine components warm-up, the temperature gradient between the gases and the exhaust/volute walls reduces, and so does the heat lost by the gases. As a result, the transient state only truly ends when the heat transfer flux has stabilized at a constant value (Benajes et al., 2002).

Valve timing plays an important role in turbocharger response. Some diesel engines have large valve overlap to promote scavenging and exhaust valve cooling (Watson and Janota, 1982). They rely on the fact that high efficiency turbochargers generate a negative pressure gradient from the inlet to the exhaust. In transient response, if the fuel-air ratio is too high, this pressure gradient can be reversed causing some backflow which causes the engine response to deteriorate (Watson and Janota, 1982). This problem can be overcome by reducing the valve overlap period (Watson and Janota, 1982), as shown in **Figure 2.6**.

Transient response is an important consideration when matching the turbocharger to the engine. A turbocharger which is matched for optimum steady state fuel consumption usually has a poor transient response (Panting, Pullen and Martinez-Botas, 2001). For this reason, smaller turbines are often used so that more exhaust energy is available. Nevertheless, if the turbine trim is excessively small, the back pressure would significantly increase the pumping losses, the turbocharger could over-speed and the high boost provided could damage the

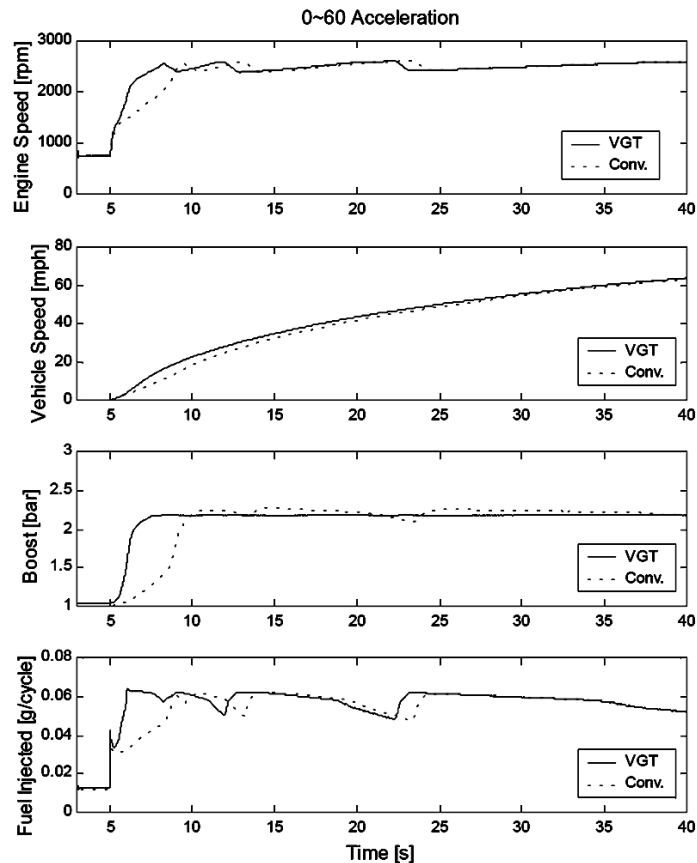
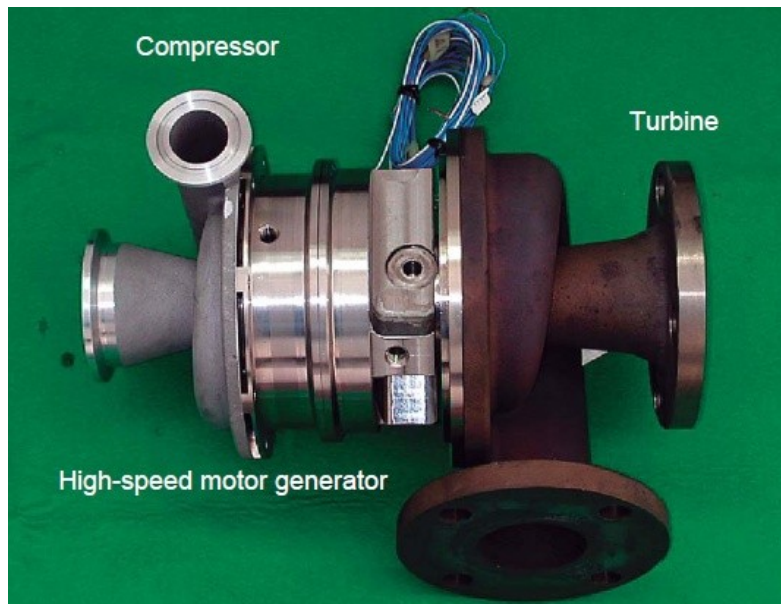


Figure 2.7 - Diesel engine transient performance improvement by the application of a variable geometry turbine (Filipi, Wang and Assanis, 2001). Copyrights Society of Automotive Engineers Inc.

engine. To avoid this, a waste-gate is usually implemented. A typical waste-gate consists of a valve on the exhaust manifold or turbine housing which is opened when the inlet manifold pressure go beyond the maximum value. The valve allows some of the exhaust gases to bypass the turbine, resulting in useful energy being wasted. Alternatively, a Variable Geometry Turbine (VGT) can be implemented to improve engine transient response. The VGT system can effectively change the flow characteristics of the turbine and can be controlled to improve engine performance or emissions (Filipi, Wang and Assanis, 2001). **Figure 2.7** shows how a variable geometry turbine, with a performance oriented control system, can improve the transient response of the engine.

### 2.3 ELECTRICALLY ASSISTED TURBOCHARGERS

Electrically assisted turbochargers are conventional turbochargers assisted by a high speed electric motor/generator (EM). Electrically assisting the turbocharger is a relatively new concept and as of writing no production engine adopts this solution yet. Only a few projects have been extensively described in the literature. The most important of these is the *ELEGT* (ELectric Exhaust Gas Turbocharger) project (Bumby et al., 2004), (Bumby, Spooner and Jagiela, 2006), (Bumby, Spooner and Jagiela, 2006), (Millo et al., 2006), (Ryder, Sutter and Jaeger, 2006),



**Figure 2.8 – Picture of the electrically assisted turbocharger prototype built by Ibaraki et al. (2006). Used with permission from Mitsubishi Heavy Industries Ltd.**

which involved *IVECO*, *Holset Engineering*, *Politecnico di Torino* and *Durham University*. In this project an electrically assisted turbocharger was applied to a medium to heavy-duty diesel engine. *Mitsubishi Heavy Industries* (Ibaraki et al., 2006), (Noguchi et al., 2007) has carried out extensive research on high speed electrically assisted turbochargers applied to automotive engines. At the beginning of last decade, *Honeywell* (Arnold et al., 2005), (Arnold et al., 2005), (Balis, Middlemass and Shahed, 2003) began working on electrically assisted turbochargers for light duty engines. *Caterpillar* (Algrain, 2005), (Hopmann and Algrain, 2003), (Gerke, 2001) published some work on high power electrical turbocharger assistance with the main objective of turbocompounding. Research, mainly computational, has also been carried out at *Imperial College London* (Panting, Pullen and Martinez-Botas, 2001), *University of Ljubljana* (Katrašnik, Medica and Trenc, 2005),(Katrašnik et al., 2003) and *Ford* (Kolmanovsky, Stefanopoulous and Powell, 1999).

A list of possible major benefits obtained from Electric Turbocharger Assistance (ETA) has been given by Panting et al. (2001):

- Compressor and turbine design can be optimized for steady state efficiency
- Turbocompounding to recuperate a greater fraction of the exhaust gases energy
- Boost increase at low engine speeds to preserve efficiency and power
- No need of waste-gate as turbocharger speed can be controlled via ETA

In addition to these advantages, Balis et al. (2003) and Hopmann and Algrain (2003) also state that the ETA device can be used as part of the air management system. All these benefits make

ETA a key enabler to reduce green house gases emissions from transportation (Arnold et al., 2005).

### 2.3.1 TRANSIENT RESPONSE IMPROVEMENT

A number of investigations on engine transient response improvement through electrically assisted turbochargers have been completed in recent years. A range of EM types and sizes have been tested, computationally or/and experimentally, on different applications. An enhancement in response has always been shown. However, the degree of improvement is not always the same.

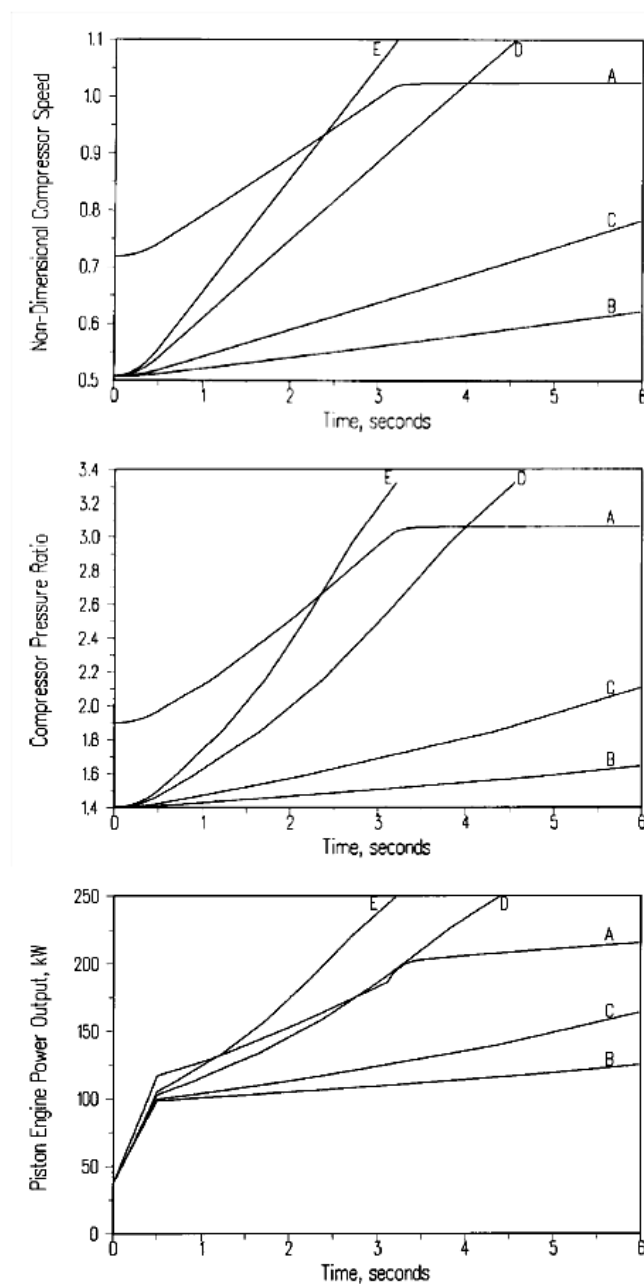


Figure 2.9 – Results obtained by Panting et al. (2001), showing compressor speed, compressor pressure ratio and engine power during vehicle acceleration. Used with permission from SAGE Publications Ltd.

Panting et al. (2001), reported a computational study aimed at improving turbocharger transient response through ETA in order to better match the turbocharger to the engine. The scope of this investigation was to assess if a turbocharger can be matched for optimum steady state performance, while maintaining good transient operation. According to the authors, this combination will improve engine brake specific fuel consumption (BSFC), as high compressor and turbine efficiencies will be beneficial to overall engine efficiency. To investigate this, a simplified 'filling and emptying' model of a typical large truck diesel engine was built and different systems simulated. The datum system (*System A*) consisted of an engine whose parameters have been taken from the literature. This system was subsequently optimised for efficiency and different levels of electric assistance were applied (0 kW for *System B*, 10 kW for *System C*, 50 kW for *System D* and 100 kW for *System E*). In steady state, the efficiency optimized system was 4.4% more efficient than the datum, mainly due to reduced pumping losses. During the transient, as the initial turbocharger speed of the optimized system was lower than the non-optimized one, it was only possible to fully recover (and improve) the time-to-boost with the 100 kW machine. Nevertheless, all assist powers showed an improvement over the optimized system with no ETA, and the same rate of boost increase as the non-optimized system was achieved with a 50 kW EM. A secondary effect of the slower response of the optimized system was that it suffered from over-fuelling, which can negatively impact the emissions.

The results obtained by this study are encouraging, but care must be taken in interpreting them. First of all, there has been no experimental validation of the model. Due to computational constraints the model was greatly simplified: the inlet manifold conditions have been computed from the compressor map and the engine has been modelled as quasi multi-cylinder. Both of these simplifications are likely to affect the transient response of the engine, as the inlet manifold requires time to fill and manifold conditions vary rapidly during the transient, affecting the in-cylinder conditions. Moreover, no data on motor/generator inertia has been provided. The effectiveness of the EM depends on its torque-to-inertia ratio (Katrašnik et al., 2003) and this could heavily impact the transient results.

Despite the fact that the quantification of the benefits might not be accurate, the simulations outcomes indicate that electric assist is effective in improving turbocharger response, as expected. More importantly, this work shows that the system can be optimized for efficiency to achieve a BSFC reduction with minimal or no transient response decrement.

Katrašnik has studied the effects of electrically assisted turbochargers on large turbocharged diesel engines for both on-road (Katrašnik et al., 2003) and off-road (Katrašnik, Medica and Trenc, 2005) applications. In both cases a mean-value model of a 6-cylinder, 6.87-litre,

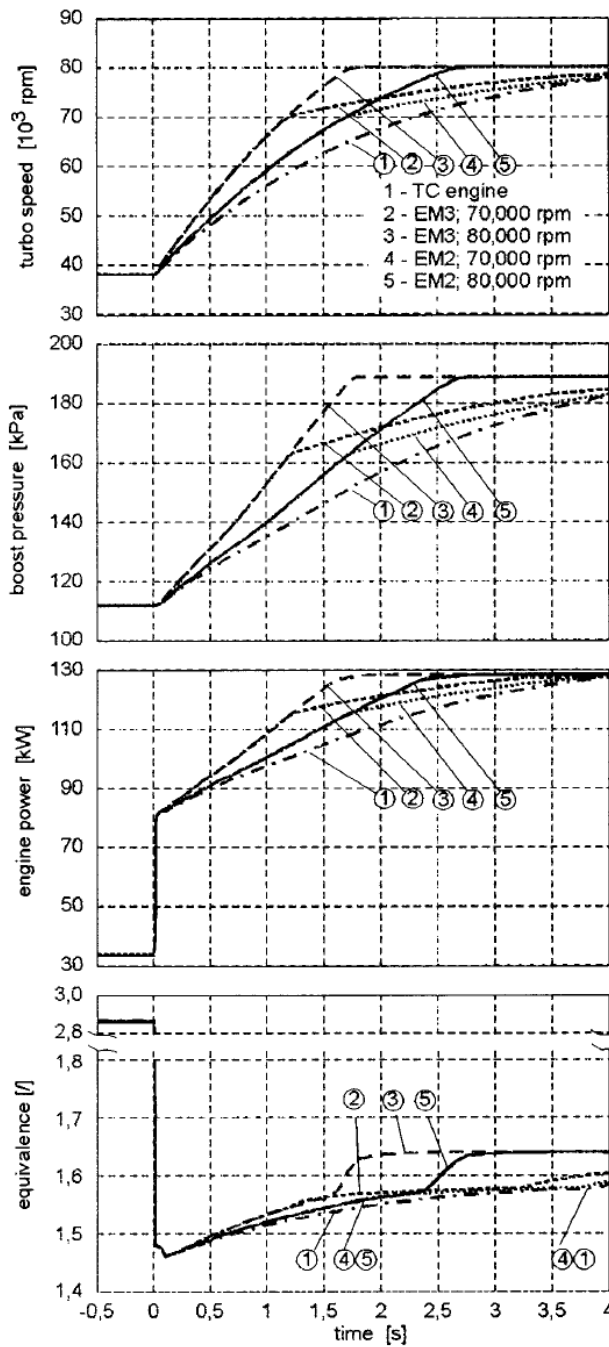


Figure 2.10 – Results obtained by Ktrašnik et al. (2003), showing turbocharger speed, boost pressure, engine power and equivalence ratio during vehicle acceleration. Used with permission from The American Society of Mechanical Engineers

turbocharged and intercooled *MAN D0826 LOH 15* diesel engine was employed. This model was experimentally validated both in steady and transient state. It showed errors of engine power, manifold pressures and turbo speed within 4% in steady state and good torque agreement during transients.

In the first investigation (Ktrašnik et al., 2003), the engine model was applied to a large truck. Two different motor/generators, both of the asynchronous type, were assessed: *EM 2* had a

mass moment of inertia of  $6 \times 10^{-5} \text{ kgm}^2$  with a maximum torque of 0.2 Nm; *EM 3* had the same inertia but a maximum torque of 0.4 Nm. The transient simulation consisted of an increase in power from 25% to 100% at 1500 rev/min. Using electric assistance, the time to reach the desired power changed from 3.9 s to 2.4 s using *EM 2* and to 1.9 s using *EM 3*. Moreover, as it can be seen in the last chart of **Figure 2.10**, the electric assistance improved the equivalence ratio in the latter part of the transient.

In the second investigation (Katrašnik, Medica and Trenc, 2005), the application of the engine was an electric generator. The scope of this study was to minimize alternating current frequency drop with change in demand. The datum system was compared with electrically assisting the turbocharger and using an integrated starter generator (ISG). The turbocharger was assisted with two different motor/generators: *EM 2* (described earlier), and another EM (*EMG*), manufactured by *GfAS mbH*, which had a maximum torque of 0.57 Nm and inertia of

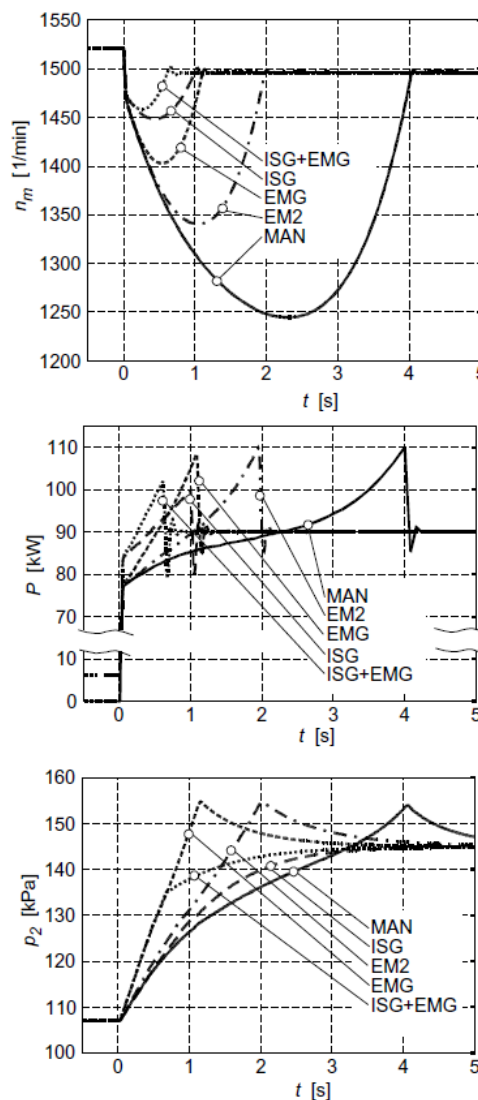


**Figure 2.11** - Results obtained by Katrašnik et al. (2005), showing engine speed, engine power and boost pressure during an increase in engine load at nominally constant engine speed. Used with permission from Elsevier B.V.

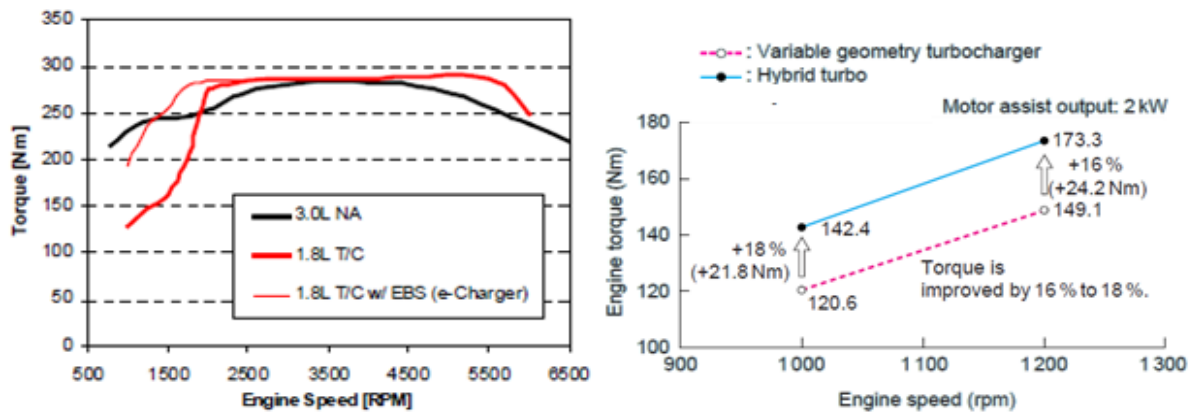


Figure 2.12 – Results obtained by Balis et al. (2003) (left) and Ibaraki et al. (2006) (right), showing that electrical boosting can significantly increase the low speed engine torque. Used with permission from the Office of Scientific and Technical Information (left) and from Mitsubishi Heavy Industries Ltd. (right)

$2.87 \times 10^{-5} \text{ kgm}^2$ . The investigation revealed that the ISG was more effective in minimizing frequency drops than the ETA, but it also consumed more electrical energy. The advantage of directly adding power to the crankshaft was that the torque increase was immediate and therefore the rate of speed drop in the initial phase was lower. The electrically assisted turbocharger had no immediate effect, but the required boost level was achieved faster.

Balis et al. (2003) reported on the development of an electrically assisted turbocharger, developed by *Honeywell*, for medium size automotive diesel engines. The scope was to use electric assistance to recover low speed torque and transient response of down-sized engines. To support the sizing of the components, an engine model, whose characteristics were not given, was generated and validated with experimental data both in steady state and transient, showing good agreement in both conditions. A prototype of an electrical compressor was then built to verify if low engine speed torque could be improved. Using this prototype in series with a turbocharger, the authors experimentally demonstrated that, with significant turbocharging and over-boost at low engine speed, a 40% down-sized engine can have the same torque of the original natural aspirated engine (Figure 2.12). However, no information was given on the power consumed by the EM. It is therefore impossible to assess if there are benefits in fuel consumption by down-sizing and recovering torque with electrical boosting. Prototypes of full electrically assisted turbochargers, with an EM power of 1.4 kW, were subsequently built and tested. The improvement in response reported was significant: to reach 1.5 bar of boost pressure, the non assisted engine required 6 s while the electrically assisted engine required just 1 s.

As part of the *Mitsubishi Heavy Industries* project, Ibaraki et al. (2006) investigated the application of an electrically assisted turbocharger to a 2-litre passenger car diesel engine. Similarly to the study of Balis et al. (2003), the aim of the motor/generator was to assist the



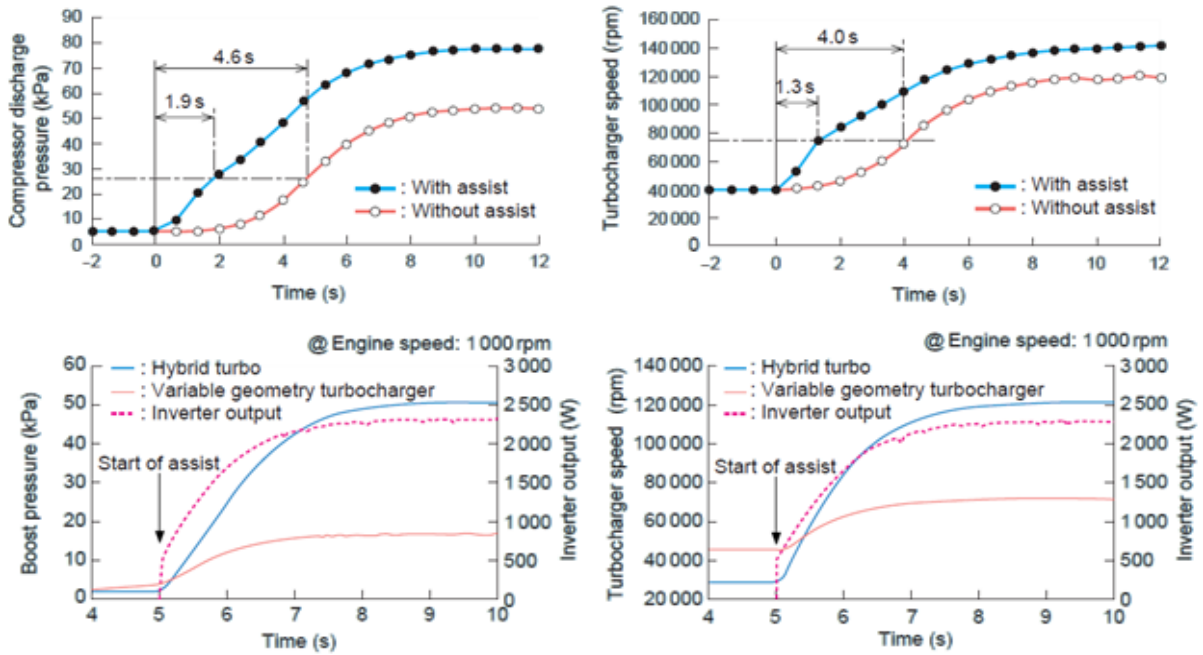


Figure 2.13 – Compressor exit pressure and turbocharger speed during an engine transient (Ibaraki et al., 2006). The top two charts show the comparison with original turbocharger, while the bottom two shows the comparison with the VGT system. Used with permission from Mitsubishi Heavy Industries Ltd.

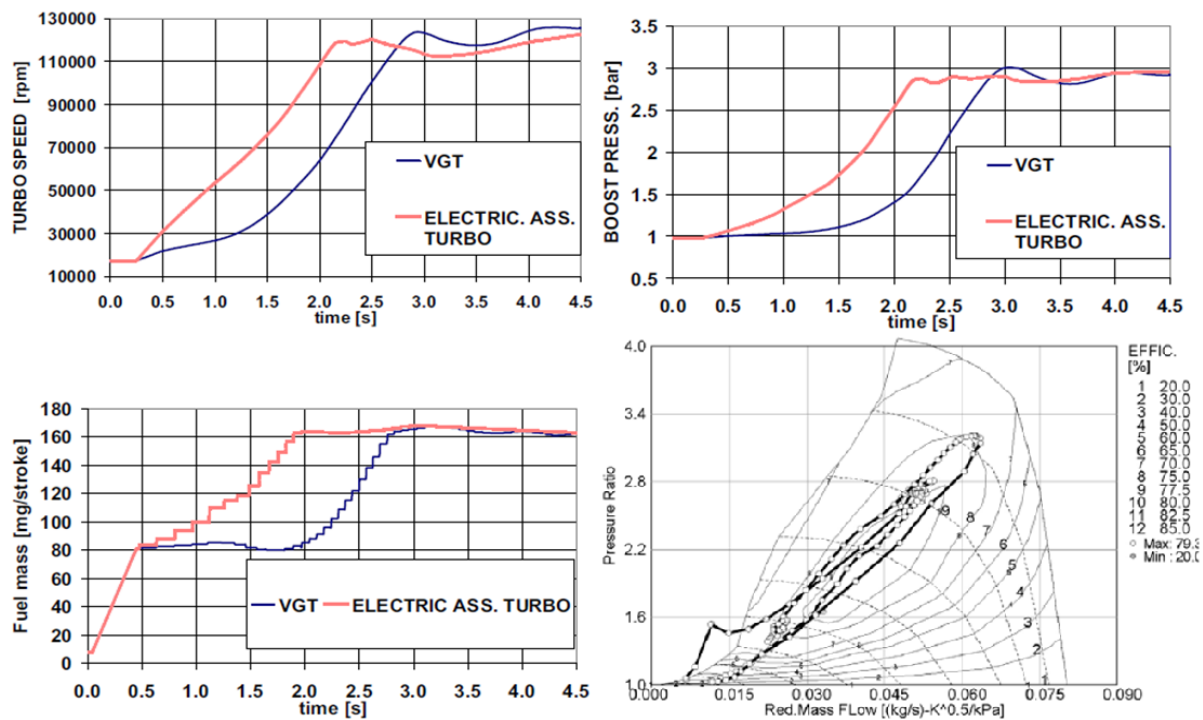


Figure 2.14 – Transient response results obtained by Millo et al. (2006), showing turbocharger speed, boost pressure, fuel mass injected during each stroke and compressor state during a transient event. Copyrights Society of Automotive Engineers Inc.

turbo at low engine load and speed, improving transient response. A prototype with a 2 kW EM was built and tested on an engine. The results showed an improvement in steady state torque between 1,000 to 1,200 rev/min (Figure 2.12). Moreover, the time to boost was significantly reduced compared to an equivalent VGT system (Figure 2.13).

Improvements in engine transient response were also computationally demonstrated, via an experimentally validated *GT-POWER* model, by Millo et al. (2006) during the *ELEGT* project. As it can be seen from **Figure 2.14**, ETA can improve the time to boost by approximately 25% over the original VGT system. Moreover, Millo et al. also state that compressor surge can be caused during acceleration transients as shown in the bottom right chart of **Figure 2.14**. In the bottom left chart of **Figure 2.14** it can be seen that electric assistance allows more fuel to be burned due to a higher boost pressure during the transient. Similar results to these presented in this section were also reported by Bumby et al. (2006) and Kolmanovsky et al. (1999).

### 2.3.2 TURBOCOMPOUNDING

As part of the *Caterpillar* project, Hopmann and Algrain (2003) studied the capabilities of electrically assisted turbochargers in turbocompounding applications. The system consisted of an electrically assisted turbocharger, with no extra power turbine, and an electric motor/generator mechanically connected to the crankshaft. The intent of this system was to feed power from the engine crankshaft to the turbocharger during transients and use excess turbine power in steady state for turbocompounding. The turbocharger was assisted by a motor/generator of the switched reluctance type. The efficiency of this machine in generating mode, combined with the power electronics, was above 92%. The maximum speed was 66,500 rev/min and the maximum power was 40 kW in continuous generating mode and 60 kW in intermittent operation. The efficiency of the crankshaft EM, including power electronics, was above 90% and the maximum power was 40 kW in continuous motoring mode 60 kW in intermittent mode. To improve the system efficiency, the compressor and turbine have been redesigned for the task. The maximum efficiency (total to static) of both has been quoted to be 85%. However, these figures were obtained through simulation and have not been experimentally validated.

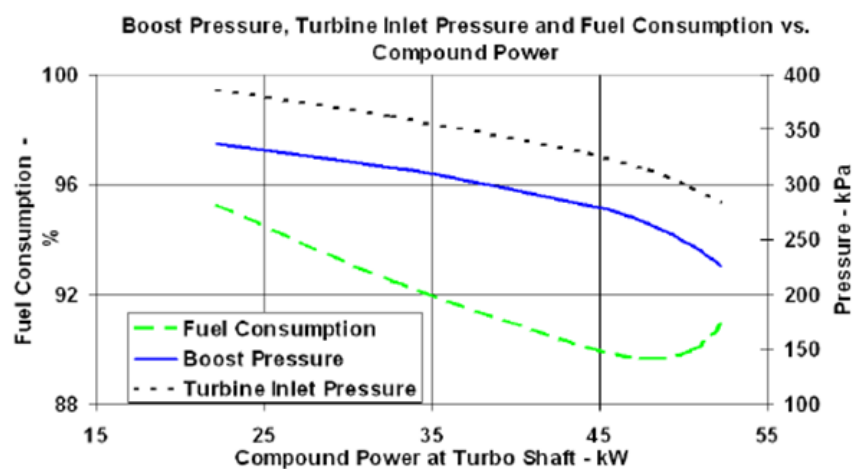


Figure 2.15 – Results obtained by Hopmann and Algrain (2003) on the steady state effects of turbocompounding, showing the effect of turbocompounding power on fuel consumption for a single operation point. Copyrights Society of Automotive Engineers Inc.

The system described above was simulated using 1D simulation software developed by *Caterpillar*. A truck diesel engine model was built using this software and validated using experimental data. The simulation results (**Figure 2.15**) showed that the minimum BSFC at the rated conditions was obtained when 15% of the engine power came from the turbine. The authors argued that a further increase in turbine power would excessively increase the pumping losses, thereby reducing the BSFC improvement. Different engine conditions were tested and, as shown in **Figure 2.15** and **Table 2.1**, the maximum improvement in BSFC was 10% and the average was 5%.

**Table 2.1 – Results obtained by Hopmann and Algrain (2003) on the steady state effects of turbocompounding. Summary of the BSFC benefits obtained by optimizing the turbocompounding power at different engine operating points**

		Engine Speed [rev/min]			
		1200	1500	1800	2100
Load [%]	100	-5.1%	-7.3%	-10.3%	-4.9%
	75	-4.9%	-5.1%	-10.1%	n/a
	50	-3.8%	-4.0%	-5.5%	n/a
	25	n/a	-2.8%	-2.5%	n/a

Millo et al. (2006) carried out an investigation on minimal turbocompounding capabilities of the ETA system developed during the *ELEGT* project. The device was applied to an *IVECO* city bus equipped with an engine which produced 259 kW at 2400 rev/min and 1280 Nm at 1080 rev/min. The EM was of the induction type with a torque of 1 Nm up to 60,000 rev/min and a power of 6.3 kW up to 120,000 rev/min (intermittent). The maximum speed was 130,000 rev/min and the continuous generating power was 7.6 kW. To store the excess electrical energy, super-capacitors were adopted. These super-capacitors could be charged from the engine alternators and could feed excess energy to the vehicle electrical system.

**Table 2.2 – Engine fuel consumption improvements over five different driving cycles obtained via mild turbocompounding. Results shown for high and low efficiency turbines, and for high and low efficiency crankshaft alternator (Millo et al., 2006)**

		High efficiency turbine Alternator efficiency = 55%	High efficiency turbine Alternator efficiency = 75%	Low efficiency turbine Alternator efficiency = 55%
		Driving Cycle	CBD	5.9%
TRL03	6.2%		5.0%	4.2%
TRL08	1.6%		n/a	0.0%
TRL09	4.0%		2.8%	3.0%
HWFET	6.4%		5.3%	5.4%

In this investigation, the scope of electrically assisting was to improve transient response and use excess turbine power in steady state to switch off some of the (low efficiency) alternators. The analysis was carried out via an experimentally validated *GT-POWER* engine model. As this 1D model was computationally expensive, a simplified model was created to simulate long drive cycles. The drive cycles simulated ranged from congested traffic to extra-urban driving. The results acquired show that the maximum BSFC reduction (5%) was obtained during extra-urban driving, as the excess turbine power allowed alternators to be switched off. No BSFC benefit was

obtained in congested traffic, as little electricity could be generated by turbocompounding in such circumstances. The authors also state that the turbine was a VGT type and that the vane setting was kept constant during the simulations. They state that by having a higher efficiency fixed geometry turbine, the BSFC could be further reduced.

Panting et al. (2001), Ibaraki et al. (2006) and Wei et al. (2010) also showed benefits in engine efficiency if turbocompounding is implemented.

### 2.3.3 STRUCTURAL DESIGN AND ELECTRICAL MACHINE CONSIDERATIONS

The designing of a turbocharger with an integrated EM for electrical assistance was described by Hopmann and Algrain (2003) (*Caterpillar*), Balis et al. (2003) (*Honeywell*), Ryder et al. (2006) (*ELEGT*) and Ibaraki et al. (2006) (*Mitsubishi Heavy Industries*). In all these cases, the device was structured with the electrical machine within the turbocharger bearing housing, sitting between the two journal bearings.

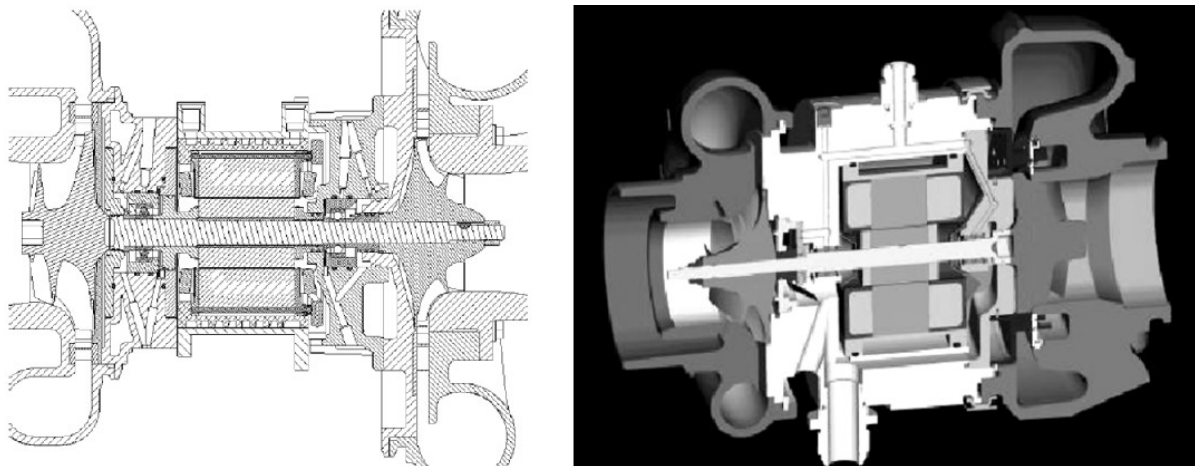


**Figure 2.16 – Cross section of two different ETA devices. The machine on the left is the one designed by Hopmann and Algrain (2003), which includes EM stator water cooling and roller bearings (copyrights Society of Automotive Engineers Inc.). The right figure shows the *ELEGT* device (Ryder, Sutter and Jaeger, 2006) (used with permission from Elsevier B.V.)**

Hopmann and Algrain (2003), Balis et al. (2003) and Ryder et al. (2006) reported that the key design features required for a successful design are:

- Low inertia – It is important to keep the inertia low so that good transient response is achieved with low EM power.
- High speed – The device must be able to rotate at the same speed as the original turbocharger to maintain the mass flow and efficiency characteristics.
- Efficiency – High component efficiency is important to minimize the fuel consumption, especially for turbocompounding applications (Hopmann and Algrain, 2003).
- EM power – High EM power is required for fast transient response (Panting, Pullen and Martinez-Botas, 2001).

- Cooling – A powerful cooling system is required to avoid overheating.
- Packaging – The ETA should be able to fit in a space of similar size of the original turbocharger.

Given the requirements stated above, which imply high speeds and temperatures, it was reported that rotor-dynamic, rotor stress and heat transfer issues were the major concerns (Balis, Middlemass and Shahed, 2003), (Hopmann and Algrain, 2003), (Ryder, Sutter and Jaeger, 2006).

Due to the high speeds involved, a small rotor radius is essential to minimize centrifugal stresses (Hopmann and Algrain, 2003) to obtain a reasonable safety factor and fatigue life (Bumby et al., 2004). Both Hopmann and Algrain (2003) and Ryder et al. (2006) carried out an structural FEA analysis of the EM rotor and reported that the maximum stresses were within the yield limits.

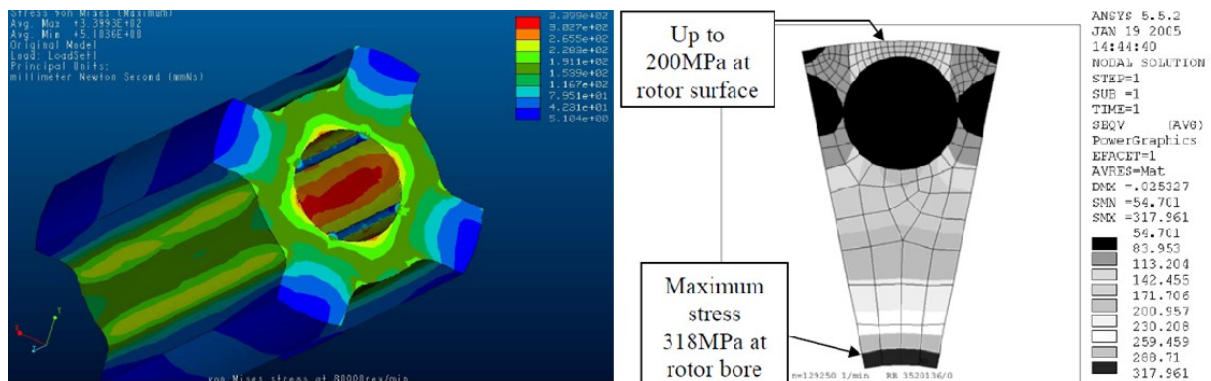


**Figure 2.17 – Stress analysis of the motor/generator rotor designed by Hopmann and Algrain (2003) at 20% over speed (left figure, copyrights Society of Automotive Engineers Inc.) and of the *ELEGT* rotor at 130,000 rev/min (Ryder, Sutter and Jaeger, 2006) (right figure, used with permission from Elsevier B.V.)**

The heat transfer issue is due to the fact that heat is transferred from the exhaust gases to the EM and is also generated within the EM coils during operation. As there is a maximum temperature at which the motor/generator can operate to avoid the melting of the insulation on the windings, the cooling system was essential to keep the EM within this temperature limit.

The maximum temperature an EM can withstand depends on the EM type. Hopmann and Algrain (2003) quoted a maximum stator coil temperature for a switched reluctance machine of 180 °C for continuous operation and 205 °C for intermittent operation. Ryder et al. (2006) quoted 300 °C as maximum shaft temperature for a solid rotor induction machine. To stay within the shaft temperature limit might be a problem during hot shut down, since heat is transferred from the hot turbine wheel after the cooling system is off (Bumby et al., 2004).

Hopmann and Algrain (2003), Balis et al. (2003) and Ryder et al. (2006) carried out thermal FEA analyses on their devices. The design of Balis et al. (2003) suffered from overheating problems, which were solved by redesigning the cooling system. Balis et al. (2003) also generated a transient thermal model which showed that the EM temperatures were satisfactory even when a mountain driving cycle was simulated (**Figure 2.18**).

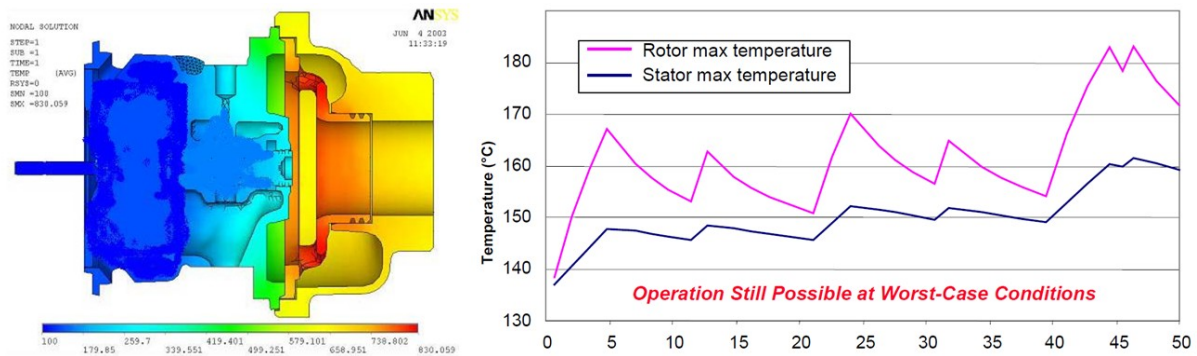


**Figure 2.18 – Heat transfer analysis of the device designed by Balis et al. (2003). The left part shows a steady state FEA analysis. The right part shows a transient heat transfer analysis which shows that maximum temperatures are satisfactory even for the most demanding mountain driving cycle. Used with permission from the Office of Scientific and Technical Information**

Due to the extra shaft mass and length, rotor-dynamic instability was reported in the literature as a risk. Excessive shaft motion during instability must be avoided as the rotating components might collide with the stationary parts, damaging the device. In addition, large amplitude shaft motion affects turbo-machine efficiency by increasing the aerodynamic clearances (Balis, Middlemass and Shahed, 2003) and reduces the EM flux density by increasing the reluctance caused by the EM air gap (Hughes, 2006).

The magnetic attraction between the EM rotor and stator can reduce the stability margin of the shaft (Bumby et al., 2004). When the rotor and stator are perfectly concentric, the attraction forces are balanced. But when eccentricity occurs due to shaft motion, these forces become unbalanced, promoting instability (Bumby et al., 2004).

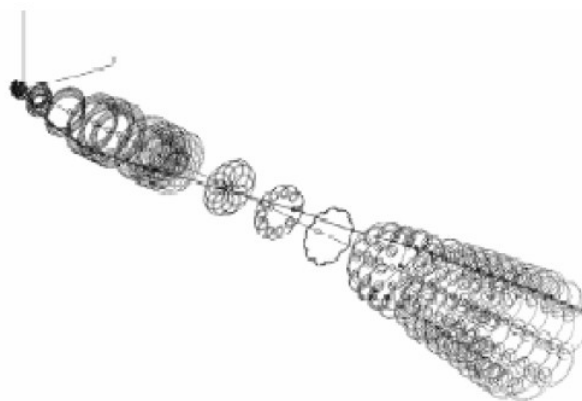


**Figure 2.19 – Rotor-dynamics of the ELEGT turbocharger shaft (Ryder, Sutter and Jaeger, 2006). Used with permission from Elsevier B.V.**

Hopmann and Algrain (2003) designed an ETA device which used roller elements bearings, while Ryder et al. (2006) designed a device where the shaft was supported by journal bearings (**Figure 2.16**). It was reported that roller bearings reduce mechanical losses (Hopmann and Algrain, 2003) and that journal bearings require larger a EM air gap to avoid rotor-stator contact (Bumby, Spooner and Jagiela, 2006). For both machines, the rotor-dynamic characteristics were analyzed and the results were satisfactory in both cases.

Given all the requirements for the full ETA device, the main requirements of the EM are (Bumby et al., 2004), (Hopmann and Algrain, 2003):

- Robust and simple design to withstand high speeds and high temperatures
- High efficiency
- High power density
- Economical to manufacture

There are three main types of EM that could meet the requirements listed above. These are (Bumby et al., 2004), (Hopmann and Algrain, 2003):

- Brushless permanent magnet – Permanent magnet machines have the disadvantage that the excitation cannot be de-energised and therefore they produce high EMF at high speeds (Bumby et al., 2004).
- Cage rotor and solid rotor induction – Induction machines are very robust and have the possibility of sensor-less application (Bumby et al., 2004). Moreover they are very compact and therefore easy to package within the bearing housing (Bumby et al., 2004).
- Switched-reluctance – Switched-reluctance machines have a simple and rugged design, making them suitable for high speeds (Bumby et al., 2004), and have the possibility of being controlled by a sensor-less system (Bumby et al., 2004).

From the literature it is clear that there is no single best EM type, as this might depend on the precise application. Ryder et al. (2006) and Bumby et al. (2004), (2006) (*ELEGT*) selected a solid rotor induction machine and obtained 6 kW of maximum power and a maximum speed of 130,000 rev/min. Hopmann and Algrain (2003) (*Caterpillar*) selected the switched reluctance type and obtained a maximum power of 40 kW (60 kW for intermittent operation) with a maximum speed of 66,500 rev/min. Ibaraki et al. (2006) and Noguchi et al. (2007) (*Mitsubishi Heavy Industries*) designed a 2 kW permanent magnet machine with a maximum speed of 220,000 rev/min.

Ryder et al. (2006), Ibaraki et al. (2006) and Balis et al. (2003) tested prototypes of their respective devices and no major issues were reported.



## 2.4 SWITCHED RELUCTANCE MOTOR/GENERATOR

The type of motor/generator selected by the project partners is the switched reluctance kind. A good description of how switched reluctance EMs function is given by Ahn (2011) and by Hughes (2006). The switched reluctance machine differs from other machines because it generates power via reluctance torque action. When the poles are misaligned and a magnetic flux flows through them, a torque is generated to align the poles so that the reluctance of the magnetic circuit is reduced. An equation which describes the reluctance torque as a function of phase inductance and current is given by Soares and Costa-Branco (2001) (modified for a single phase):

$$\tau = \frac{1}{2} \frac{dL}{d\theta} I^2 \quad (2.1)$$

From this equation it is clear that when the inductance gradient ( $dL/d\theta$ ) is positive, the torque is positive, and when the inductance gradient is negative, the torque is negative. Therefore, if the phase windings are excited when the poles are aligning (increasing inductance) the machine operates in motoring mode. If the phase windings are excited when the rotor pole is moving away from the stator pole, the machine operates in generating mode.

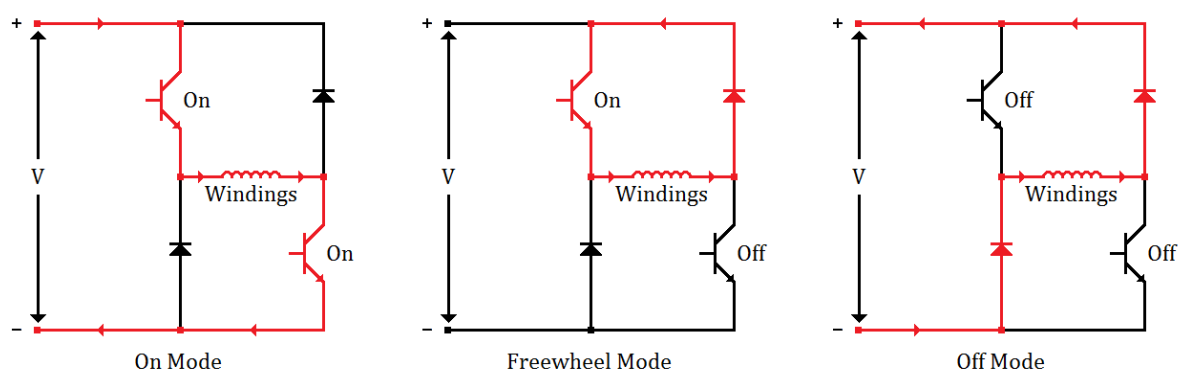


**Figure 2.20 - Electrical charge flow through the power electronics and windings of a single phase of a switched reluctance motor/generator. The small arrows indicate the direction of the electrical current**

Ahn (2011) provides a description of the energy transfer between the electrical power supply and the magnetic field. The most important concept is that not all the energy transferred from the power supply to the magnetic field is converted into mechanical work, and the surplus energy stored in the magnetic field is partly returned to the power supply and partly dissipated as heat. How this is achieved can be understood by looking at how electrical charge flows through the power electronics and phase windings shown in **Figure 2.20**.

In motoring mode the power supply feeds energy to the electrical machine phase by allowing current to flow via the transistors. Some of this energy is converted to mechanical work via **Equation 2.1**, and the rest is stored in the magnetic field. When the transistors are turned off,



the current in the machine windings cannot instantaneously drop to zero due to the non-zero windings inductance, and therefore it flows through the diodes until all the energy stored in the windings drops to zero. The transistor switching is typically controlled so that one is turned off a few degrees before the other. This operation mode of the power electronics is known as free-wheel mode. In this mode the power supply does not provide or receive energy, but part of the energy stored in the windings is converted to mechanical work.

When the machine operates in generating mode, the transistors firing occurs in the same order as in motoring mode, but the sequence starts later so that the phase is excited when the inductance gradient is negative. The power supply still feeds energy to the magnetic field when both transistors are on. However, this energy is not turned to mechanical energy. Instead, the opposite occurs and energy is fed from the machine shaft to the magnetic field. In free-wheel mode, further energy is absorbed from the shaft, but no energy is supplied by the power supply. When both transistors are off, the energy stored in the magnetic field is returned to the power supply. Because energy is transferred from the shaft to the magnetic field, the amount of energy returned to the power supply is larger than the amount of energy fed from the power supply to the magnetic field. As a result, electrical energy is produced.

Not all the energy stored in the magnetic field of the machine is turned into mechanical work or returned to the power supply. Part of this energy is converted into heat due to iron and copper losses (Materu and Krishnan, 1992). Copper losses are caused by the resistance of the windings to the flow of current. Iron losses are caused by eddy currents forming in the machine core and the magnetic hysteresis of the core material.

The application of a switched reluctance motor/generator to assist an automotive turbocharger was extensively analyzed by Calverley (2001). In his PhD thesis he describes the design, construction and testing of a switched reluctance machine with 6 stator poles and 4 rotor poles, capable of running up to 100,000 rev/min. The main findings of his research are that switched reluctance machines are suitable for assisting a turbocharger due to their robustness, low cost, capability of operating at high temperatures and the fact that there are no iron losses when the machine windings are not excited. Calverley also analyzed the rotor aerodynamic drag losses and he concluded that these losses account for approximately 0.5% of the machine rated power. However, these losses are a strong function of the machine air gap, so they can vary significantly depending on the machine design. Another important part of Calverley's work is related to the analysis of iron losses. He concluded that a NNNSSS winding arrangement produces 8% lower iron losses than a NSNSNS arrangement, where N stands for north and S stands for south.

Unfortunately, due to bearings failure caused by overheating, only limited testing was carried out on the device.

## 2.5 ALTERNATIVE ELECTRICAL TURBOCHARGING AND TURBOCOMPOUNDING SYSTEMS

The main alternative to improve transient response is to have an electric supercharger working in parallel (Münz et al., 2001) or in series (Lee, Filipi and Assanis, 2009) with a normal turbocharger. Such a device has been designed by *BorgWarner Turbo Systems* (Münz et al., 2001) and they have shown a clear improvement in transient response. Noguchi et al. (2005) describe an electrical machine specifically designed for this purpose.

Electric turbines have been developed for turbocompounding purposes. Mamat et al. (2011) designed a high efficiency low pressure ratio turbine to work in series with the turbocharger and recuperate a larger portion of the exhaust gases energy. Thompson et al. (2011) studied the effects of a similar device on the transient response of the engine. They showed that the transient response was improved mainly due to a smaller turbocharger turbine. Michon et al. (2007) designed and tested an electric turbine to work with a naturally aspirated engine. Wei et al. (2010) compared electrically assisted turbochargers with a turbine-generator in series and in parallel with a standard turbocharger. Their results show that the highest efficiency is obtained with the power turbine in series. On the other hand, they did not optimize the turbocharger for electrical assistance and it is not clear how this will affect the results.

## 2.6 AREAS TO BE INVESTIGATED

Although the literature covers extensively the function and design of the electrically assisted turbocharger, many areas have still not been investigated. First of all, it is not clear how the electrical machine must be sized to achieve the desired turbo-lag reduction. This is because only a limited range of electrical machine power has been investigated, and these investigations were carried out on engines of different displacement and running speed. As a consequence, the impact of electrical machine power has to be investigated by comparing the improvements generated by different assistance power on the same engine.

The effectiveness in improving engine performance of the electrically assisted turbocharger has been compared with the effectiveness of the turbine variable geometry system by Ibaraki et al. (2006). However, it has not been considered how the two systems can be coupled to obtain further improvements in engine performance, and whether having both systems on the same device can generate better engine transient response than one system alone. Alternatively, one system could be controlled to improve the engine fuel consumption while the other could be controlled to improve the transient response. Because the prototype provided by the project

partners is equipped with both systems, there is a good opportunity to explore this area within this research project.

There is a lack of information also on how the turbocharger flow is impacted by the electric assistance, particularly on the turbine side. Although there is plenty of information and data on how the turbine performs at high pressure ratios, a condition which occurs when the electrical machine operates in generating mode, there is very little information on how the turbine performs at low pressure ratio, a condition which occurs when the turbine is motored by the electrical machine. Consequently, the turbine needs to be characterized at these loading conditions. There is no need to characterize the compressor, since conventional methods are capable of characterizing the device over its full operating range.

Electric assistance can impact the turbine flow also by generating unsteady effects. Because electric assistance significantly increases turbocharger acceleration, these rapid changes in turbine speed will cause rapid changes of turbine swallowing capacity and efficiency. This could generate low frequency unsteady effects in the turbine flow, which have to be investigated. The motor/generator could cause unsteady effects also at high frequency. This is because the torque of the motor/generator is not continuous but it fluctuates depending on the stator and rotor poles alignment. These high frequency oscillations will cause the turbine wheel to vibrate, and the impact of these vibrations on the turbine flow should also be investigated.

A further topic which has not been covered in the literature is how a switched reluctance motor/generator with a power output of over 5 kW performs at rotational speeds which approach 140,000 rev/min. In particular, the relative importance of the different losses that occur in the turbocharger is not clear. The author has been provided with an electrically assisted turbocharger prototype and it is necessary to prove that the device operates as expected, and to characterize the electrical machine performance in order to establish the likely engine transient response and fuel consumption benefits.

Other areas which have not been extensively covered in the literature include the electric assistance control methodology, the energy storage system, and the implementation of electrical assistance on multi-stage turbocharging systems. However, these topics are outside the scope of this PhD, and therefore are not covered in this thesis.

## 2.7 CHAPTER SUMMARY

In this chapter the literature relevant to electrically assisted turbochargers and diesel engine behaviour during transients has been summarized. Engine down-sizing and down-speeding have been found to be the main drivers to the development of electrically assisted

turbochargers, as reduced engine transient performance is the main limitation to how much an engine can be down-sized or down-speeded. The main parameters which affect diesel engine response have been found to be the turbocharger inertia, the matching of the turbocharger to the engine, the engine valve timing, the engine fuelling control and the manifolds volumes.

Electric assistance is a novel methodology to improve the turbocharged engine transient response, and it consists in coupling a motor/generator to the turbocharger to help accelerating the turbocharger rotor during engine transients. The novelty of this system is that it eases the matching of the turbocharger to the engine by adding an extra degree of freedom: the motor/generator torque. The main advantages of electric turbocharger assistance implementation have been found to be:

- Improved engine efficiency due to a higher degree of engine down-sizing and down-speeding, the possibility of matching the turbocharger for engine steady state efficiency, and turbocompounding
- Improved engine transient response thanks to a better turbocharger acceleration
- Improved low end engine torque thanks to the possibility of assisting the turbocharger in steady state
- Improved emissions due to the increased quantity of oxygen available during fuel combustion process
- Possibility of using electric assistance as part of the air management system

The chapter concludes by summarizing the available alternatives to electric turbocharger assistance and which areas need further research.

### 3. CHARACTERIZATION OF MOTOR/GENERATOR

This chapter describes the performance characterization of the switched reluctance motor/generator implemented in the electrically assisted turbocharger prototype. The scope of this testing is to obtain the power and efficiency characteristics of the electrical machine. The chapter is divided in two parts. The first part describes the measurement of the electromagnetic and frictional losses via a new experimental methodology which allows direct measurement of electrical machine torque. The second part describes the calculation of the rotor aerodynamic drag by means of three-dimensional computational fluid dynamics.

#### 3.1 MEASUREMENT OF ELECTROMAGNETIC AND FRICTIONAL LOSSES

##### 3.1.1 ELECTRICALLY ASSISTED TURBOCHARGER DETAILS

The electrically assisted turbocharger studied in this thesis is represented in **Figure 3.1**. The EM and its power electronics have been developed by two independent contractors of *Caterpillar*. The bearing housing is has been developed by *BorgWarner*, one of the project partners.

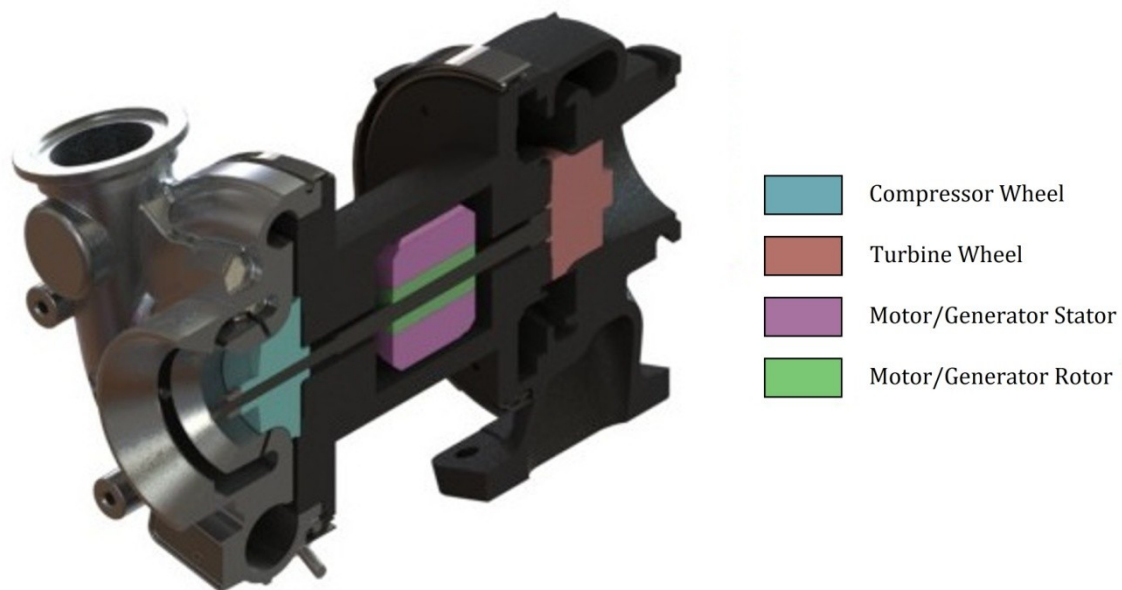


**Figure 3.1 - Representation of the electrically assisted turbocharger prototype under study**

The motor/generator is of the switched reluctance type and its rotor is mounted directly on the turbocharger shaft. The bearings are of the hydrodynamic type and consist of two journal bearings, one on each side of the electrical machine rotor, and one thrust bearing, placed on the compressor side of the turbocharger. The EM rotor diameter is 24 mm. The diameter is small as it is limited by the centrifugal stresses and aerodynamic drag at the maximum turbocharger speed (140,000 rev/min). The rotor length is 50 mm and it is constrained by the packaging of

the turbocharger. Despite the low rotor volume, the machine has been designed to produce a maximum, non-continuous power of 7.5 kW.

The fluid filling the gap between the stator and the rotor is air. There are two drain holes at the bottom of the machine to prevent the engine oil, which leaks from the shaft seals, accumulating inside the machine. The rotor is cooled mainly by heat conduction through the turbocharger shaft to the bearings, which are cooled by the lubrication oil flow. The stator is cooled by engine oil fed into the turbocharger at approximately ambient temperature from a dedicated inlet. This oil stream flows around the stator circumference and exits the turbocharger from an outlet port shared with the bearing lubrication oil stream. The stator cooling oil and the bearing lubrication oil are provided from different inlets as the temperature requirement for the two oil streams is different.

The electrical machine is a three-phase type and has six coils on the stator and four poles on the rotor. This configuration is economical to manufacture and provides a good power density. Moreover, because there are a total of 12 phase excitations per revolution, the torque ripple is low and at high frequency. The stator and rotor are laminated to reduce the eddy currents which occur when the phases are excited. The number of turns in the coils has been chosen to provide a high power output for a short time.

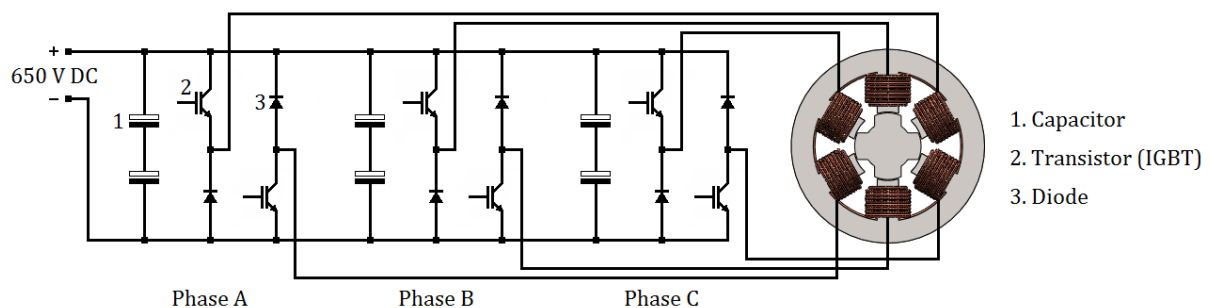


**Figure 3.2 - Asymmetric inverter power electronics arrangement as designed by subcontractor**

The electrical machine inverter, shown in **Figure 3.2**, converts the DC current into 3-phase AC current as required by the switched reluctance machine. This inverter is of the asymmetric type, and each phase is actuated by two insulated-gate bipolar transistors (IGBT). How this type of inverter works when coupled to a switched reluctance machine is described in **Section 2.4**. In summary, both phase transistors are turned on at a pre-determined rotor position to energize the phase coils. After a calibrated amount of time, the inverter goes in free-wheel mode. In this operation mode one of the transistors is turned off and, thanks to the coils inductance, the current recirculates through the other transistor and the corresponding diode. When the phase has to be turned off, also the second transistor is turned off and the excess current flows back to the power supply via the diodes (Ahn, 2011). If the voltage is measured across the coils of the

electrical machine, it would change in steps with magnitude equal to the magnitude of the voltage at the DC link, resulting in a square-shaped voltage waveform. The voltage would be +650 V in 'on' mode, 0 V in 'free-wheel' mode and -650 V in 'off' mode.

The firing of the three phases is controlled by a microprocessor. It turns on and off the transistors by reading lookup tables of 'on', 'free-wheel' and 'off' angles, whose inputs are shaft speed and torque demand. The rotor position and speed are provided by three *Hall Effect* sensors which are excited by a four-slot wheel mounted on the machine shaft. The microprocessor communicates with external devices through the Controller Area Network (CAN) protocol.

**Table 3.1 – Motor/generator and power electronics data**

<b>Machine type</b>	Switched Reluctance
<b>Number of phases</b>	3
<b>Number of stator poles</b>	6
<b>Number of rotor poles</b>	4
<b>Rotor diameter</b>	24 mm
<b>Rotor length</b>	50 mm
<b>Inverter type</b>	Asymmetric. Two transistors, two diodes and two capacitors for each phase, connected as shown in Figure 3.2. The transistors firing is determined by a microprocessor which calculates the rotor speed and position from the output of three hall effect sensors.
<b>Transistors type</b>	IGBT – International Rectifier IRG7PH35UD
<b>Diodes type</b>	Ultrafast recovery diode – STMicroelectronics STTH3012W
<b>Capacitors type</b>	Electrolytic 330 uF – Epcos B43504A9337M
<b>Cooling type</b>	Engine oil circulated around the machine stator, fed by the engine oil pump.

### 3.1.2 LOSSES OCCURRING IN AN ELECTRICALLY ASSISTED TURBOCHARGER

The inclusion of an electrical machine in a turbocharger introduces losses which are not present in a standard turbocharger. The power losses that occur in this particular electrically assisted turbocharger arrangement are the following:

- *Motor/generator rotor drag* – This is an electrical machine specific loss. It is caused by the high shear stress imposed on the air in the gap between the rotor and the stator.
- *Motor/generator copper loss* – This is the power loss caused by the resistance to the flow of charge through the copper windings. According to *Ohms Law*, this power loss is equal to  $I^2R$ , where R is the resistance.
- *Motor/generator iron losses* – These losses are generated by two separate physical mechanisms. One loss is caused by the eddy currents forming in the motor/generator stator and rotor. The second loss is caused by the magnetic hysteresis of the core material. Because there are no permanent magnets in the switched reluctance machine, the iron losses are zero when the motor/generator is off. This is one of the key advantages of this type of machine.

- *Motor/generator power electronics losses* – these losses correspond to the power consumed by the electrical machine inverter and control system. These losses are generally low and mainly occur in the transistors. Due to the low voltage drop across the selected IGBTs, which is approximately 2.3 V (International Rectifier Inc., 2010), the power electronics losses are expected to be around 100 W under full loading conditions.
- *Bearing friction* – These losses occur also in the standard turbocharger. Because the bearing system is the same for the assisted and non-assisted turbocharger, they are not expected to change significantly.
- *Aerodynamic losses in turbine and compressor* – Similarly to the bearing friction, these losses also occur in the standard turbocharger.

Only the frictional and electromagnetic losses are quantified in this chapter, as these are the losses related to the motor/generator, but the different sources of electromagnetic losses will not be separated. The turbine aerodynamic losses will be quantified in **Chapter 4** for steady state operation and the impact of motor/generator torque oscillations will be investigated in **Chapter 5**. The compressor losses are not quantified as an accurate efficiency map has been provided by the manufacturer.

### 3.1.3 MOTOR/GENERATOR CHARACTERIZATION OBJECTIVES

The focus of this investigation is to obtain performance data which allows to assess the impact of turbocharger assistance on engine transient response (**Chapter 6**), to provide data to the power electronics designer to optimize the motor/generator control lookup tables and to generate the performance maps required by the engine control algorithm which is being developed by *Loughborough University*. Moreover, a sensor-less electrical machine control algorithm is being developed by the power electronics contractor, and the test-rig is required to verify that it operates correctly with the physical hardware.

The objectives of the electrical machine testing are to:

- Develop a test-rig capable of measuring shaft torque to assist the development of the motor/generator
- Verify the correct operation of the motor/generator and power electronics up to the maximum turbocharger speed (140,000 rev/min)
- Measure the maximum electrical machine shaft power at different speeds both in motoring and in generating mode
- Characterize the efficiency of the motor/generator over different shaft powers and speeds



### *3.1.4 APPROACH TO MEET THE OBJECTIVES OF THE MOTOR/GENERATOR CHARACTERIZATION*

To verify the correct operation of the EM, the turbocharger shaft and bearing system have to be retained to verify that the electrical machine rotor attachment method is sufficiently strong to transfer the torque to the shaft and to verify that the rotordynamic behaviour is stable up to the maximum rotational speed. Moreover, as the shaft diameter is relatively large compared to the EM rotor diameter, the impact of the shaft on the rotor reluctance is expected to be significant, and modifying the turbocharger shaft or the attachment system could lead to a change in motor/generator performance. The bearing system has to be retained as this data is required to calibrate a bearing housing model described in **Chapter 6**. The stator cooling system has to be retained as well since it determines the maximum continuous power of the motor/generator and it is an integral part of the electrical machine.

As the majority of the turbocharger components have to be retained, it has been decided to design a torque measurement system which consists of modifications to one of the electrically assisted turbocharger prototypes, rather than designing and manufacturing a custom dynamometer. The technique implemented, which is described in the following section, also has the advantage of not requiring a new rotor-dynamics analysis, since the stable rotor configuration of the existing prototype is adopted.

The principal scope of this experiment is to characterize the motor/generator performance. As a result, this experimental technique is not designed to quantify individual power losses, so the efficiency maps produced contain all the losses that occur from the inverter DC link to the turbocharger shaft, including the bearing losses. The electromagnetic losses (i.e. the inverter, copper and iron losses) can be separated from the frictional losses by measuring the frictional moment separately (i.e. with no motor/generator torque) and subtracting it from the total moment.

In **Section 3.1.13**, two sets of results are presented. The minor differences between the two sets are in the torque measurement method and in the drive settings. The second set of data has been obtained with an improved torque measurement system which leads to higher measurement precision. Moreover, the drive settings in the second set of data are better refined and the maximum power and efficiency are higher. Both sets of data are presented because the maximum speed in the second experiment was limited to 80,000 rev/min due to vibration issues.

The novelty of the work presented in this chapter is in the development of the experimental methodology. No dynamometer capable of absorbing and producing over 7 kW at 140,000 rev/min, while being capable of measuring torques as low as 0.02 Nm, is commercially

available. Without this novel electrical machine experimental technique, the data required to assess ETA benefits, to develop an ETA specific engine control system and to develop the motor/generator controller would not be available.

### 3.1.5 MOTOR/GENERATOR CHARACTERIZATION METHODOLOGY

The idea behind this experimental methodology is to obtain the motor/generator shaft and electrical power, so that the efficiency can be calculated. The shaft power is obtained by measuring the shaft torque and angular velocity, while the electrical power is obtained by measuring the voltage and current at the DC link of the inverter. From these two powers, the motor/generator efficiency can be calculated via **Equation 3.1**.

$$\eta_{motoring} = \frac{\dot{W}_{shaft}}{-\dot{Q}_{elec}} = \frac{\tau\omega}{VI} \quad (3.1a)$$

$$\eta_{generating} = \frac{-\dot{Q}_{elec}}{\dot{W}_{shaft}} = \frac{VI}{\tau\omega} \quad (3.1b)$$

Note that the definition of efficiency changes depending on the operation mode of the electrical machine (i.e. motoring or generating). The efficiency map is formed by repeating the measurements over different electrical machine speeds and torque demands.

To run the experiment, power sources and loads are required both on the electrical and mechanical side of the machine. On the electrical side, a 3-phase AC to DC converter is utilized both as a power source and load. In motoring mode it feeds current from the national grid to the EM inverter and in generating mode it feeds the electricity produced back to the grid. This AC to DC converter only controls the voltage at the DC link of the electrical machine inverter and has no active role in the control of the electrical machine. Its role is purely to simulate the battery that would be mounted on the vehicle. The control of the electrical machine is done by the motor/generator's controller and inverter, which chop the DC current provided by the AC to DC converter into 3-phase AC current with the timing and frequency required by the motor/generator running conditions. More details on the control of the motor/generator are given in **Sections 2.4** and **3.1.1**.

On the mechanical side, the power source and load is the turbine, which is linked to the motor/generator rotor. In generating mode, air is pumped through the turbine to produce mechanical power. This power is regulated by adjusting the turbine inlet pressure via a control valve. In motoring mode, the mechanical power is absorbed via two different mechanisms. In one mechanism the power is dissipated as heat by the windage losses that occur in the turbine wheel. In the second mechanism the power absorption is increased by allowing air to flow from the turbine outlet to the turbine inlet. This occurs due to the centrifugal head across the turbine

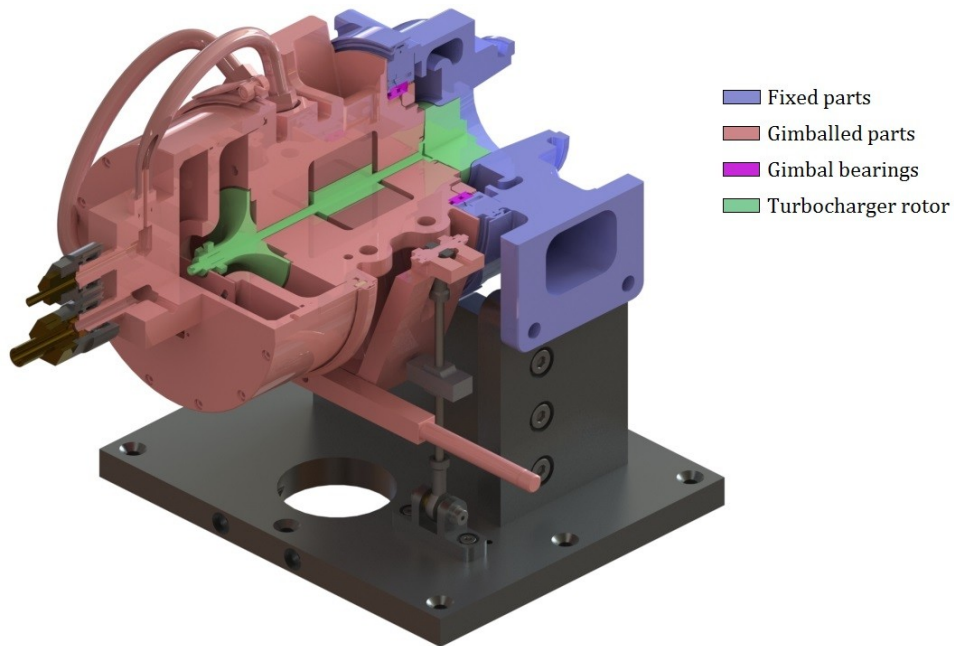


**Figure 3.3 – Section view of the modified electrically assisted turbocharger prototype. The motor/generator and bearing housing details are hidden**

wheel. When the turbine is absorbing energy via the first mechanism, the power dissipation is regulated by opening the flow control valves, since the air flow reduces the load. When the control valves are fully closed, the power is regulated by adjusting the reverse flow restriction. Maximum absorption is obtained with no reverse flow restriction.

As stated in the previous section, the existing turbocharger prototype has been modified to allow the testing of the EM. **Figure 3.3** shows how the turbocharger has been modified. The turbocharger bearing housing has been machined to place a pair of angular contact ball bearings between the bearing housing itself and the turbine volute, hence forming a gimbal system. Because the gimbal bearings are concentric to the motor/generator and the turbocharger is supported from the turbine volute, all the moments imposed on the bearing housing are reacted through the load-cell attached to its side. The compressor has been removed and the wheel has been substituted by a blank wheel. Since there is negligible load caused by the compressor, the only moments imposed on the bearing housing are due to the electrical machine and bearings. As a result, the reaction force measured by the load-cell corresponds to the electrical machine torque (including bearing losses) and the two can be related by knowing the distance between the load-cell attachment pin and the turbocharger shaft.

The free body diagrams of the turbocharger rotor and bearing housing in steady state operation are shown in **Figure 3.4**. In the top part of the figure the motor/generator is off. The torque generated by the gas flow through the turbine wheel is opposed only by the friction load, that is the sum of the EM rotor drag and the bearing load. Due to *Newton's Third Law*, a moment, equal

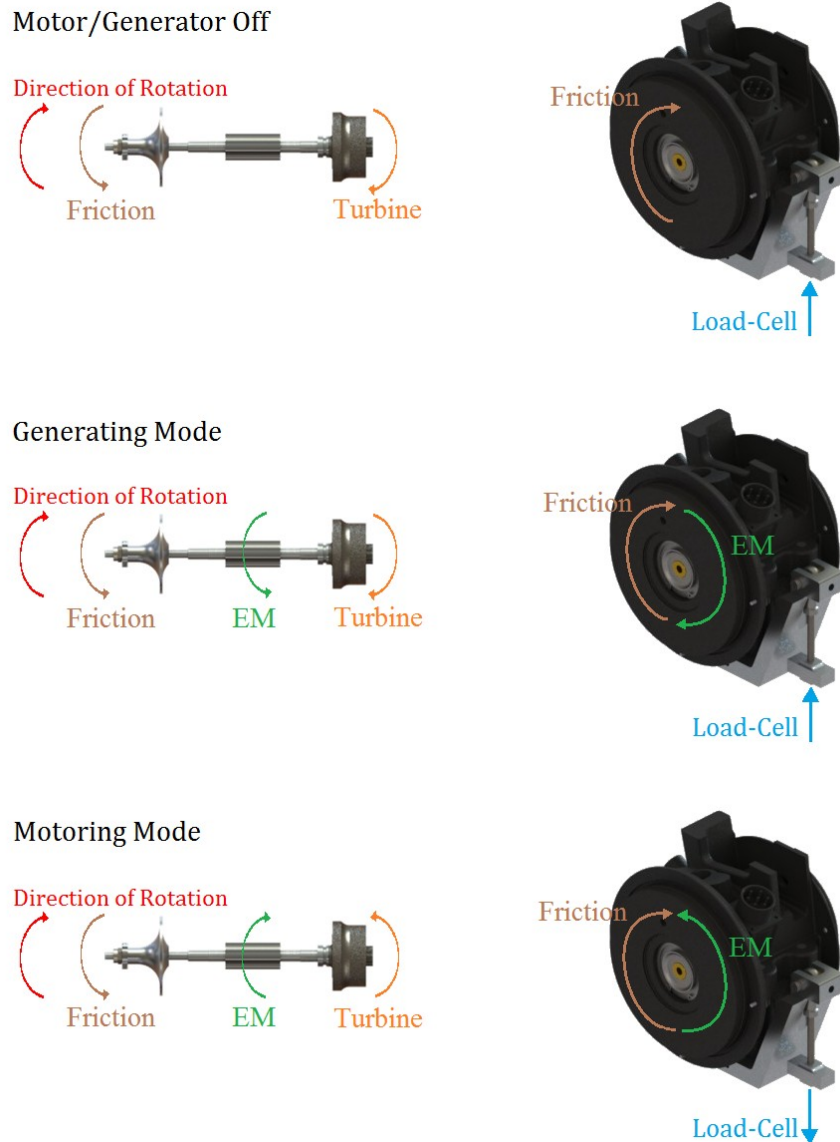


**Figure 3.4 – Free body diagrams showing the forces and moments acting on the turbocharger rotor and bearing housing during testing. Bearing housing is viewed from the compressor side**

and opposite to the friction load on the shaft, is imposed on the bearing housing, and this moment is reacted by the load-cell force. As a result, the torque calculated from the force measured by the load-cell is equal in magnitude to the friction load.

In the central part of **Figure 3.4** the electrical machine is operating in generating mode. In this case the turbine torque is opposed by both the friction load and the EM torque. The torque obtained from the load-cell reading is therefore equal in magnitude to the sum of these two moments. The bottom part of **Figure 3.4** shows the moments that occur when the machine is operating in motoring mode. In this case the motor/generator torque is opposed by the turbine windage load and bearing friction. Because the electrical machine torque and bearing friction load are opposing each other, the load-cell torque is equal in magnitude to the subtraction of these two moments.

It is clear from the free body diagrams that the efficiency maps obtained include the turbocharger bearing losses. Nevertheless, the pure electromagnetic efficiency can be obtained by taking two separate measurements at the same speed. The first measurement would be with the EM turned on and would give the algebraic sum of the electromagnetic torque and friction load. The second measurement would be with the machine off and would give the friction load. Provided that the lubrication oil flow conditions are identical, the friction load would not significantly change between the two readings and subtracting the two measurements would give the pure electromagnetic torque.

### 3.1.6 MOTOR/GENERATOR CHARACTERIZATION TEST-RIG LAYOUT

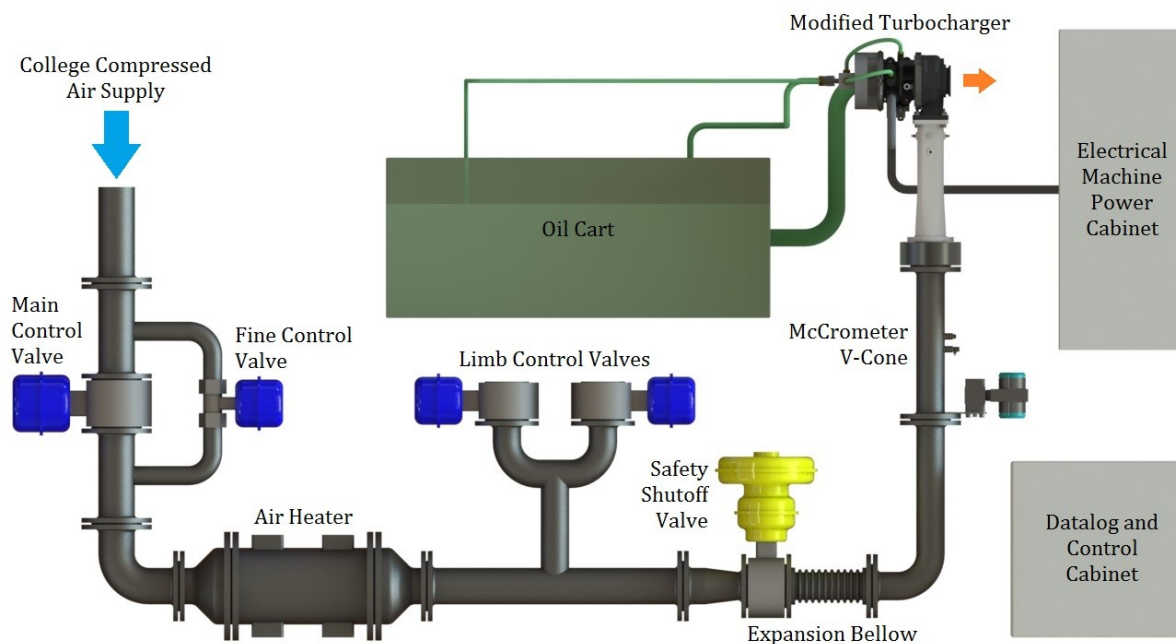


**Figure 3.5 – Representation of the motor/generator test-rig showing the principal components and how they are arranged**

The test-rig layout is shown in **Figure 3.5**. The compressed air is provided pre-filtered at a regulated pressure of 6 bar by the *Mechanical Engineering Department* central system. The flow is regulated by two control valves that operate in parallel. The main control valve is utilized when large changes in flow are required, while the fine control valve is used for the fine adjustments. Two additional control valves (limb control valves) are only opened when the turbine is acting as a load, so that turbine reverse flow can occur. The air temperature is increased and controlled by means of an electrical heater to avoid condensation within the turbine. Near the turbocharger, approximately 1.5 m upstream, there is the safety shutoff valve, which rapidly stops the flow in case of an emergency stop. There is no duct at the turbine outlet and the air is allowed to escape into the test-cell. The ambient pressure is maintained by the test-cell extraction system.

The test-rig has a dedicated oil cart to lubricate and cool the turbocharger, and a dedicated AC to DC converter to run the motor/generator.

### Oil Cart

The oil cart has been custom designed and manufactured by an external company based on the test-rig requirements. The cart has two outlets, one for the turbocharger bearings lubrication and one for the motor/generator stator cooling, and a combined oil return inlet.

The same oil is utilized for lubrication and cooling, but it is stored in two separate tanks which are connected by a pipe. The oil returning from the rig is fed into the cooling oil tank and the excess oil flows into the lubrication oil tank. The temperature of the cooling oil tank is not controlled. After being pressurized by the pump, the cooling oil flows through a heat exchanger and it exits the cart at approximately ambient temperature. The temperature of the lubrication oil tank is controlled by a heating circuit. In this circuit the oil is pressurised to 160 bar and then forced through an orifice. A remotely controlled valve is used to open or close the orifice bypass to maintain the tank temperature constant.

**Table 3.2 – Oil cart specifications**

<b>Maximum lubrication oil volume flow rate</b>	1.3 l/min
<b>Maximum lubrication oil exit pressure</b>	6 bar
<b>Maximum lubrication oil temperature</b>	120 °C
<b>Lubrication oil tank capacity</b>	35 l
<b>Maximum cooling oil volume flow rate</b>	11 l/min
<b>Maximum cooling oil exit pressure</b>	6 bar
<b>Cooling oil tank capacity</b>	35 l

Due to a design fault, the cart is only capable of reaching the maximum lubrication oil temperature if there is no water flow through the cooling oil heat exchanger. If water flows through the heat exchanger, the maximum temperature which can be maintained under all conditions is 50 °C.

### Active Rectifier

The active rectifier has been manufactured by *Emerson Control Techniques* and it is the *Unidrive SP3403* model. It converts the 3-phase 415 V, 50 Hz alternate current to the 650 V direct current required by the motor/generator inverter. When the electrical machine is operating in motoring mode, it feeds the energy from the AC side to the DC side. When the machine is operating in generating mode, it inverts the DC energy back to the national grid. The maximum current output is 25 A.

### Air Valves

The control valves are opened and closed by electrical actuators. The required opening is set by the operator in the control and data-log software (*LabVIEW*). The control computer

communicates with the data-logger inside the test-cell, which sends a 0 to 10 V output to the valves. The actuators have a built-in feedback controller so that the valves are opened by the correct amount. The actuators also send a 0 to 10 V feedback signal to the data-logger.

The control valves are of the ball type with linear opening area-angle relationship. The main control valve has a diameter of 5 in, while the fine control valve has a diameter of 2 in. The two limb valves have a diameter of 3 in.

The safety shutoff valve is opened and closed by a pneumatic/spring actuator controlled via a solenoid. The actuator is arranged in a normally closed configuration, which means that if there is no current through the solenoid, the gauge pressure in the pneumatic side of the actuator is zero and a spring maintains the valve closed. When the solenoid is energised, the actuator is pressurized and the valve opens. As soon as the current is stopped, the actuator is depressurized and the spring closes the valve. The shutting time is less than 0.5 s. Similarly to the other valves, the safety valve is also remotely controlled through the data-logger. The valve is a ball type and has a diameter of 3 in.

### **Air Heater**

The air heater is an *OSRAM Sylvania* electric heater. It has a maximum power of 72 kW and a maximum operating temperature of 600 °C. It is controlled by a *West 1600+* PID controller which receives air temperature feedback from a K-type thermocouple mounted just downstream of the heater. The required temperature is set remotely through the data-logger as a 0 to 10 V signal.

### *3.1.7 TORQUE MEASUREMENT*

#### **Load-cell**

To measure the reaction force on the bearing housing, an *Omegadyne LCM703-10* load-cell is used. This load-cell is of the strain gauge type and has a capacity of 10 kg. The linearity and hysteresis error are  $\pm 0.15\%$ , the repeatability error is  $\pm 0.05\%$  and the thermal error on the zero offset is  $\pm 0.009\%$  FS/°C. One of the main reasons to select this load-cell is its high rigidity, which minimizes the angular displacement of the bearing housing when loaded. The load-cell has a full scale deflection of 0.076 mm, which gives a bearing housing angular displacement of  $0.0055^\circ$  with 1 Nm loading.

#### **Initial Design**

The load-cell is positioned on one side of the turbocharger bearing housing, with the sensing axis aligned to the vertical axis, as shown in **Figure 3.6**. The load-cell is mechanically attached to the turbocharger support and bearing housing via two rods. One end of the rods is screwed

into the load-cell, while the other end is screwed into rod-end bearings. These bearings are necessary to prevent that a fraction of the motor/generator torque is reacted by the bending moment of the rods, which cannot be measured by the load-cell. The rods have a right hand thread on the load-cell side and a left hand thread on the rod-end bearing side. This allows to adjust the length of the load-cell assembly by rotating the rods, so that the bearing housing angular alignment can be easily adjusted. The rods are maintained in position by locking nuts.

The swivel centre point of the rod-end bearing attached to the turbocharger is positioned on the same horizontal plane as the turbocharger axis. This minimizes the angular displacement of the load-cell sensing axis that occurs when the gimbal system is loaded. The normal distance between the spherical bearing swivel point and the turbocharger axis is 90 mm.

The top rod-end bearing is not directly attached to the turbocharger, but to an aluminium arm bolted to the bottom of the bearing housing. The arm has large dimensions to minimize bending: it has a thickness of 15 mm and a width of 55 mm. This arm is necessary as no other attachment point is available. To calibrate the load-cell, a second arm is screwed to the top of the load-cell attachment arm. This calibration arm has a V shaped slot, cut at a normal distance from the gimbal axis of 200 mm, to which masses are attached during the calibration process.

The cooling and lubrication oil supply hoses are supported by a bracket and are attached to the back of the turbocharger. The bracket is dimensioned and positioned so that the portion of the hoses between the bracket and the turbocharger is parallel to the gimbal system axis. The hoses are attached to an aluminium block bolted to the compressor cover. This block has internal channels which route the two streams of oil to two other hoses, which are attached to the bearing housing oil inlets. To minimize the impact of the hoses bending on the measured force, the larger cooling oil hose is positioned on the turbocharger axis, while the smaller lubrication oil hose is positioned 35 mm above this axis.

The oil outlet points vertically downwards and its axis crosses perpendicularly the turbocharger axis. To remove the impact of the oil return hose bending on the measured torque, the hose is not mechanically attached to the outlet and the oil falls into it guided by a pipe. The oil is returned by gravity as the turbocharger sits higher than the oil cart. Because the oil enters the turbocharger axially and exits radially, the flow cannot impose any force on the load-cell.

The hoses that take the oil from the block at the back of the turbocharger to the bearing housing inlets are not fully rigid and could bend slightly with changing thermal conditions. As the hoses are made of multiple materials and the Young's Modulus to temperature relationship is not available for most of these materials, the bending amount cannot be easily estimated. However,



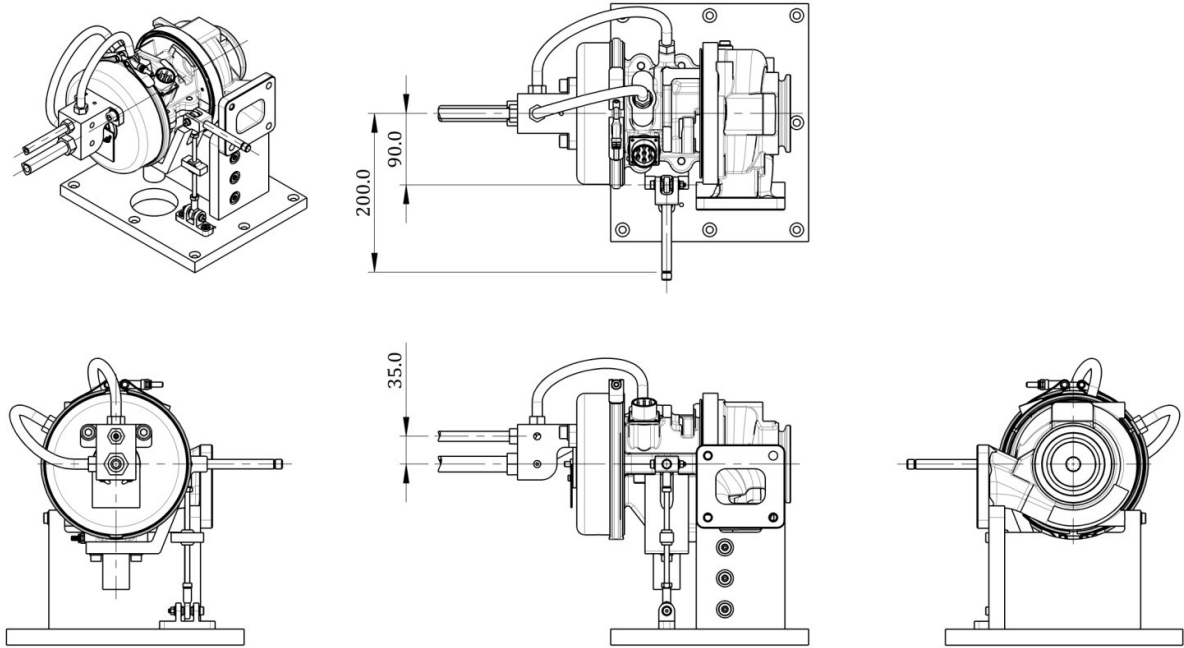


**Figure 3.6 - Assembly drawing of the initial version of the modified turbocharger. All the dimensions are in millimetres**

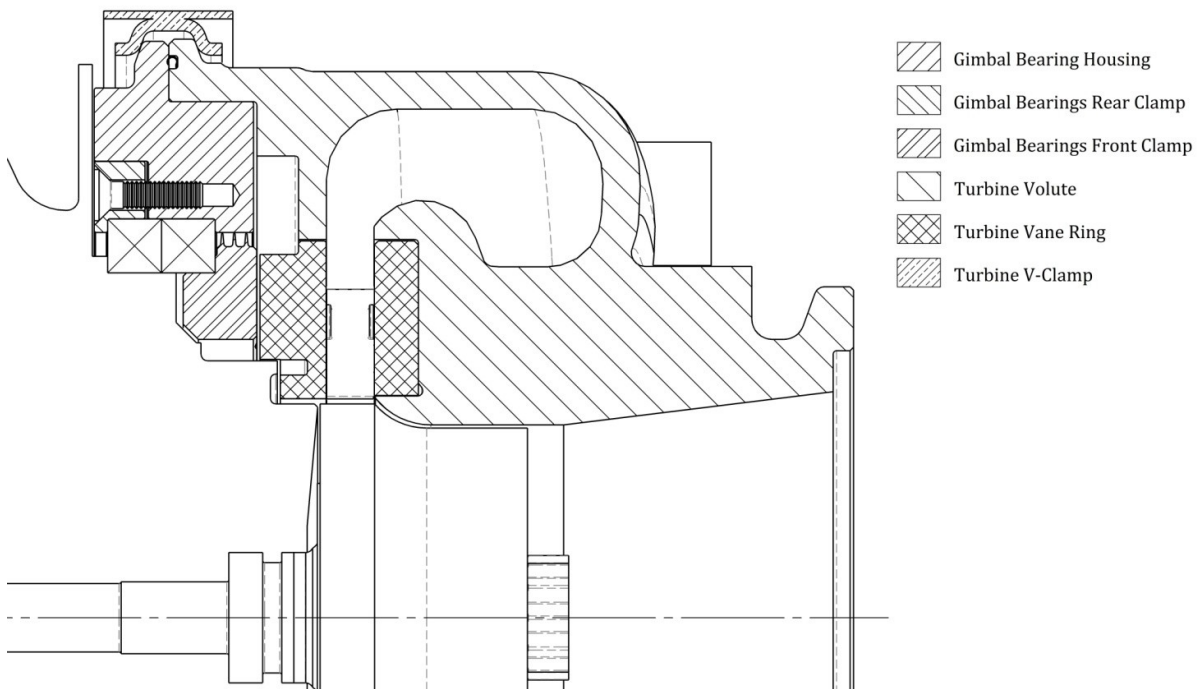


**Figure 3.7 - Cross sectional drawing of the initial version of the gimbal bearings and retaining system assembly, top view. The drawing plane does not cut through the turbocharger bearing housing as it is coincident with the bearing housing split plane. The turbocharger bearings and motor/generator details are hidden**

by making the conservative assumption that the hoses are shifted radially outwards by 5 mm, the change in moment about the turbocharger axis due to the weight of the hoses and oil is approximately 0.003 Nm. This is a small but non-negligible moment and is eliminated by

measuring the load-cell zero offset a few seconds after the torque is logged, when the turbocharger thermal conditions have not changed significantly.

**Figure 3.7** shows a cross sectional view of the gimbal system. The gimbal bearings consist of a pair of angular contact bearings manufactured by *Kaydon*, model *KB040AR0*. The external races of the bearings are clamped together by the gimbal bearing housing and the rear clamp. The gimbal bearing housing is clamped to the turbine volute by means of the standard turbine v-clamp. The inner races of the bearings are clamped to the turbocharger bearing housing by the front clamp. This clamp is bolted to the turbocharger bearing housing in a manner similar to the way in which the rear clamp is bolted to the gimbal bearing housing. The front clamp bolt is not shown as it is not on the same plane as the rear clamp bolt. A labyrinth seal is cut on the front clamp to reduce the air leakage through the gimbal system from the pressurized turbine volute. The turbine vane ring is bolted to the volute. The only point of contact between the fixed parts (turbine volute, vane ring, gimbal bearing housing and rear clamp) and the gimbaled parts (turbocharger bearing housing and front clamp) are the gimbal bearings.

Due to packaging constraints, the VGT actuation mechanism had to be removed to accommodate the gimbal bearings. The vanes have been maintained in position by a jig and the vanes pivots have been welded to the support rings. No material has penetrated in the flow volume and therefore the flow through the vanes is not affected by this modification.

### **Torque Measurement System Calibration**

The torque measurement system is calibrated by attaching masses to the calibration arm described above. These masses generate a moment about the gimbal bearings axis, similar to the moments generated by the electrical machine torque and turbocharger bearings friction during testing. The moment is calculated from the total weight attached to the calibration arm and the normal distance between the arm v-shaped slot and the gimbal axis (200 mm). The load-cell voltage output is directly correlated to this torque.

The system is calibrated both in loading and unloading conditions. The masses are first gradually added in 100 g steps up to a total mass of 300 g, to obtain the sensitivity curve under loading conditions. These masses are then removed, still in 100 g steps, to obtain the sensitivity curve under unloading conditions. By comparing the loading and unloading curve the non-linearity and hysteresis errors are found.

### **Issues with the Initial Design**

The preliminary testing revealed two major faults with this initial design. The first fault was caused by air leaking from the turbine volute through the gimbal system, which carried dust and

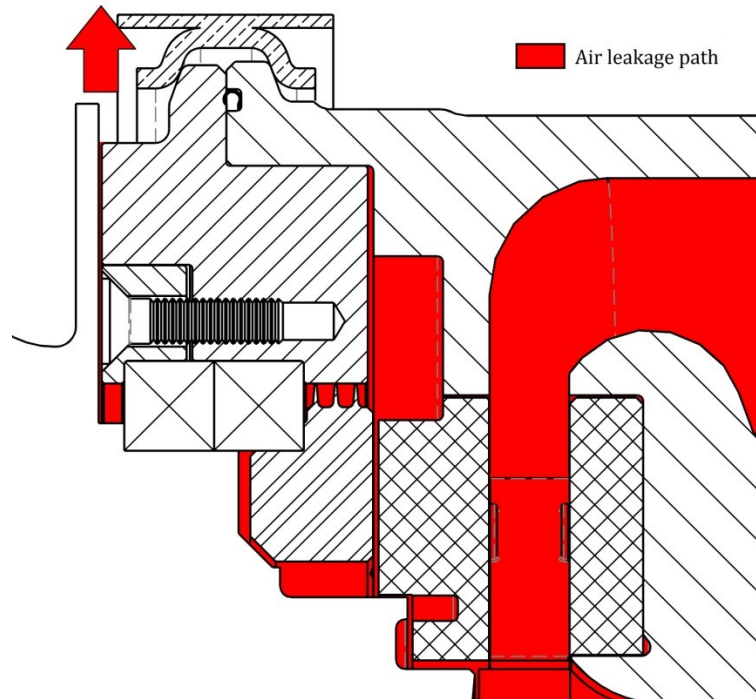


Figure 3.8 – Air leakage path shown on the cross sectional drawing of the initial version of the gimbal bearings and retaining system assembly. The air leakage path through the gimbal system and the pressurized turbine volume are shown in red. A labyrinth seal has been placed in front of the gimbal bearings to minimize the leakage

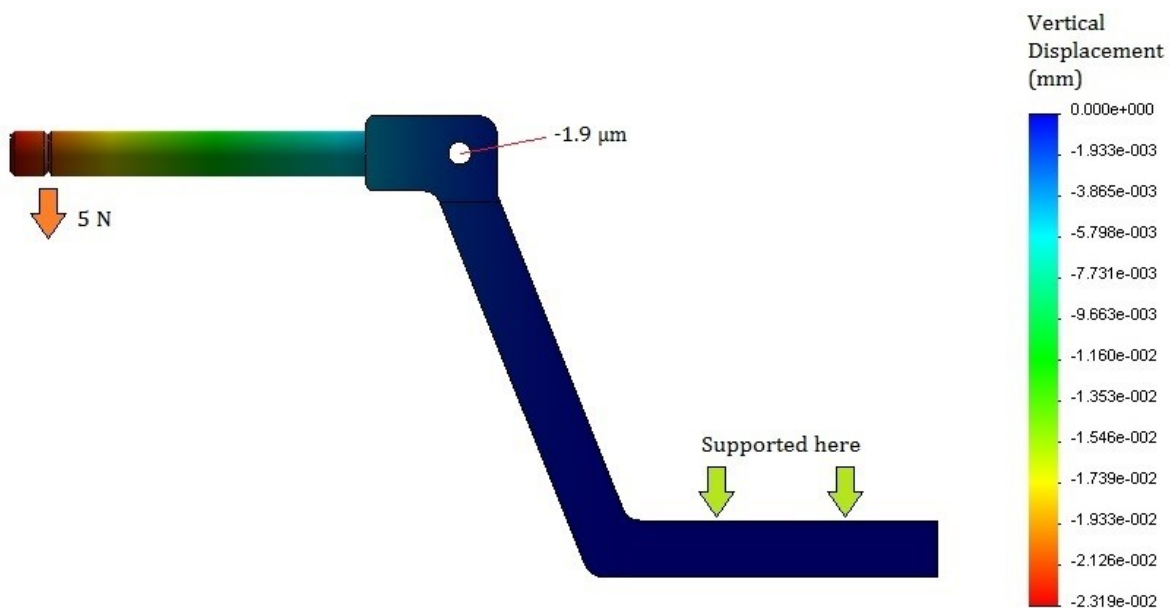


Figure 3.9 – Displacement results of the structural finite element analysis of the load-cell attachment arm. With a 5 N force on the calibration arm, equivalent to 1 Nm torque, the vertical displacement at the load-cell attachment point caused by the arm deformation is -1.9  $\mu\text{m}$

debris that get trapped in the bearings. This dust and debris caused the bearings stiction and friction to increase, affecting the torque measurement. **Figure 3.8** shows the air leakage path.

The second issue was caused by the load-cell arm deformation during the calibration process. Finite element analysis of the arm, shown in **Figure 3.9**, revealed that when masses are

attached to the calibration arm for an equivalent torque of 1 Nm, the arm bends by approximately  $1.9 \mu\text{m}$  at the load-cell attachment point. This  $1.9 \mu\text{m}$  is non-negligible, as it corresponds to 22% of the load-cell deflection when loaded by the same equivalent torque. Because some of the moment is reacted by the non-completely frictionless bearings, the arm bending causes the load-cell strain to be larger during the calibration process than when an equivalent moment is imposed on the bearing housing by the turbocharger bearings and motor/generator.

A further design fault was a large air leakage through the space between the front clamp and the turbocharger bearing housing. This air was passing through a cut-out in the turbocharger bearing housing which is required to accommodate the VGT actuation mechanism in the non-modified turbochargers (not shown in **Figure 3.8**). The leakage mass flow was large enough to affect the torque reading.

### Data Set 1 Gimbal Arrangement

To resolve the issue caused by the load-cell arm bending, the arm to which the masses are attached during the calibration process has been moved to the bottom of the turbocharger, as shown in **Figure 3.10**. The load-cell arm is still bending, but now the forces imposed on the arm during the calibration process are identical to the forces imposed by the motor/generator torque and turbocharger bearings friction during testing. For this reason, the arm bending is identical in both situations and therefore the load-cell output gradient obtained during the calibration process is correct.

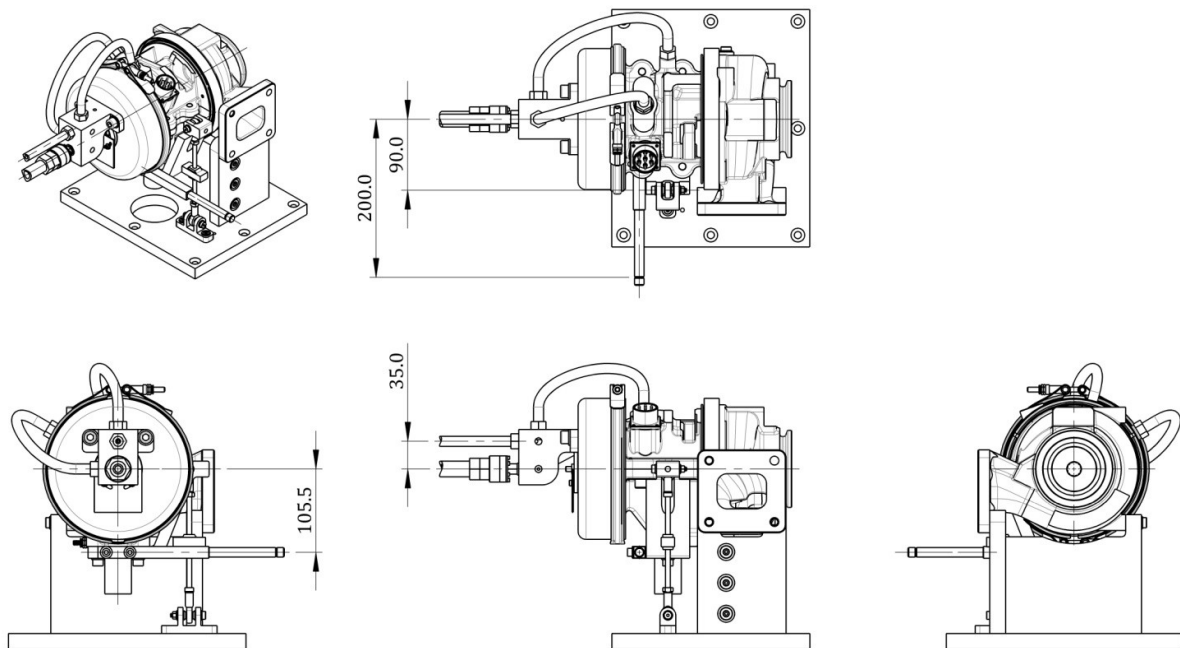


**Figure 3.10 - Assembly drawing of the Data Set 1 version of the modified turbocharger. The load-cell calibration arm is now attached to the bottom of the bearing housing. All the dimensions are in millimetres**

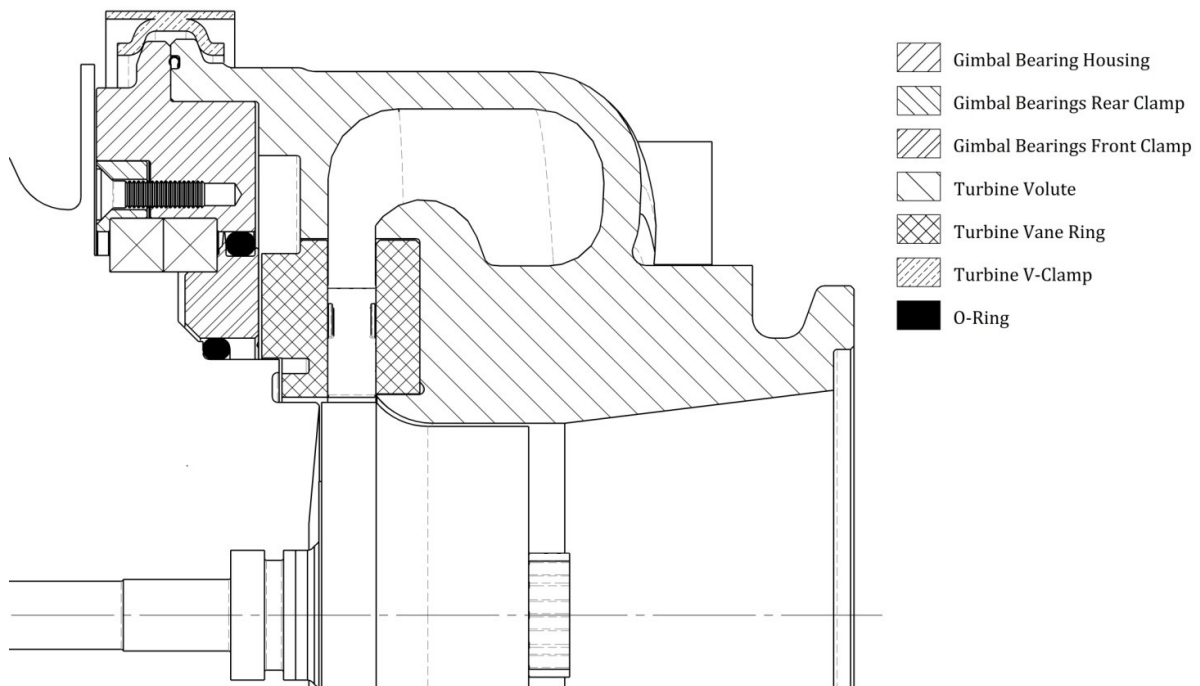


**Figure 3.11 – Cross sectional drawing of the Data Set 1 version of the gimbal bearings and retaining system assembly, top view. Two NBR o-rings have been inserted to stop the air leakage. The drawing plane does not cut through the turbocharger bearing housing as it is coincident with the bearing housing split plane. The turbocharger bearings and motor/generator details are hidden**

The air leakage issue has been solved by placing two o-rings as shown in **Figure 3.11**. The o-rings are made of Nitrile Butadiene Rubber (NBR) and are designed to withstand a maximum continuous temperature of 120° C. The smaller diameter o-ring has been inserted in the gap between the front clamp and turbocharger bearing housing, with no modifications to the two parts. The o-ring is kept in place by the higher air pressure on the turbine side. The larger diameter o-ring has been inserted between the front clamp and the gimbal bearing housing to stop debris getting trapped in the gimbal bearings. To provide space for the o-ring, the labyrinth seal on the front clamp has been removed and a groove has been cut to maintain the o-ring in place.

Since the larger diameter o-ring is pressed between the front clamp, which is part of the gimballed components, and the gimbal bearing housing, which is part of the fixed components, it resists the rotation of the turbocharger bearing housing. Its impact on the torque measurement has been estimated via finite element analysis (FEA), assuming no slippage, and the results are shown in **Figure 3.12**. The calculated o-ring equivalent torsional stiffness is 7.2% of the equivalent torsional stiffness of the load-cell and arm assembly. The stiffness of the o-ring simply adds to the combined load-cell and arm stiffness, resulting in a gentler load-cell output curve gradient. Because the load-cell is calibrated with the o-ring installed, the increased stiffness is accounted for during the calibration process and the o-ring does not directly generate a torque measurement error.

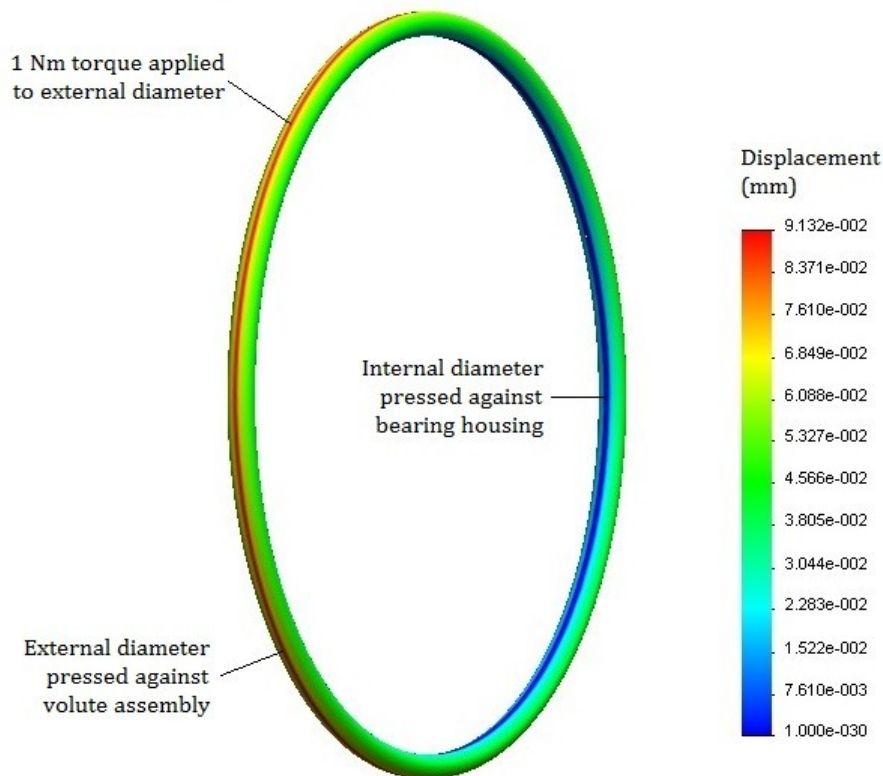


**Figure 3.12 – Displacement results of the structural finite element analysis of the NBR o-ring which blocks the flow through the gimbal bearings. These results show that if a 1 Nm torque is applied to the outer diameter of the o-ring, the resulting displacement is 0.0913 mm. This corresponds to a torsional stiffness of 10.8 Nm/deg, which is 6.8% of the total torsional stiffness**

What generates an error is the change of NBR elastic modulus with changing temperature. No accurate data has been found in the literature on the relationship between elastic modulus and temperature for this material, and the error cannot be quantified accurately. However, if the conservative assumption of a 50% change in modulus during testing is made, the torque measurement error generated would be only 3.4%.

Although NBR is an elastic polymer with non-linear properties, the material has been assumed to behave linearly as the deformations that occur due to the rotation of the bearing housing are very small. The validity of this assumption is confirmed by the linear load-cell output curve obtained with the o-ring in place. A further assumption made is that the o-ring does not slip on the contact surfaces. As the o-ring is pressed between the two surfaces, it imposes a radial force whose total magnitude has been estimated, through FEA, to be around 150 N. When a moment of 1 Nm, which is larger than the motor/generator maximum torque, is imposed on the bearing housing, the angular force that the o-ring has to sustain is only 1.2 N. Since this angular force is very small when compared to the radial force, the no slippage assumption is sensible.

A further modification to the test-rig is the addition of a bearing system for the cooling oil inlet hose, shown in **Figure 3.13**. This mechanism is composed of a ball bearing and a lip seal, and

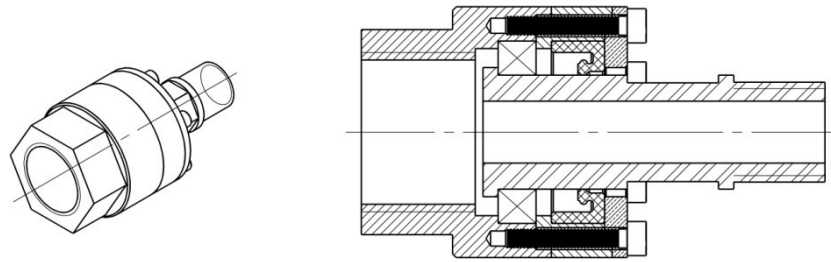


**Figure 3.13 – Assembly and cross sectional drawing of the cooling oil inlet hose attachment system. The inner part is bolted to the turbocharger and the outer part is bolted to the hose**

allows the hose to rotate about the turbocharger axis. The main reason to add this mechanism is to facilitate the installation of the hose, which can now be left attached to the adapter and bolted on the turbocharger without preloading the load-cell. This system is not installed on the lubrication oil hose as this hose is easier to install and, being of a smaller diameter, the load-cell preload caused by a non-perfect angular alignment is less significant.

This test-rig configuration has been utilized to obtain the first set of data. However, a few issues emerged during the testing. It has been found that the load-cell zero offset was drifting significantly during turbocharger cooling. This was caused by the fact that the turbocharger support and load-cell assembly were made of different materials and were subjected to different temperatures. As a result, the thermal expansion was different for the two parts and this caused the bearing housing to rotate. This rotation was resisted by the o-ring and gimbal bearings friction, which resulted in a change of load-cell strain and a drift in output voltage. This effect was minimized by recording the zero offset a few seconds after the measurement was taken. A second major issue was the hysteresis found during the load-cell calibration. This hysteresis was reduced compared to the initial set-up thanks to the cleaner gimbal bearings. However, the bearings were still heavily preloaded and therefore the friction was still relatively high. An additional issue was caused by an oil mist exiting the turbocharger from the rotor position sensor opening on the compressor cover. This oil mist was not causing any measurement error, but it was a health hazard. All the identified torque measurement errors that occur with this set-up have been estimated and included in the total error.

### **Data Set 2 Gimbal Arrangement**

The electric turbocharger assist has been further modified to resolve the issues encountered in the first testing iteration. To stop oil from escaping the turbocharger in the form of mist, a back cover has been added as shown in **Figure 3.14**. A drain hole has been drilled at the bottom of this cover to prevent oil accumulation.

A shim has been placed between the gimbal bearing housing and the rear clamp to reduce the bearing preload. As the shim material comes in a limited number of thicknesses, it has been



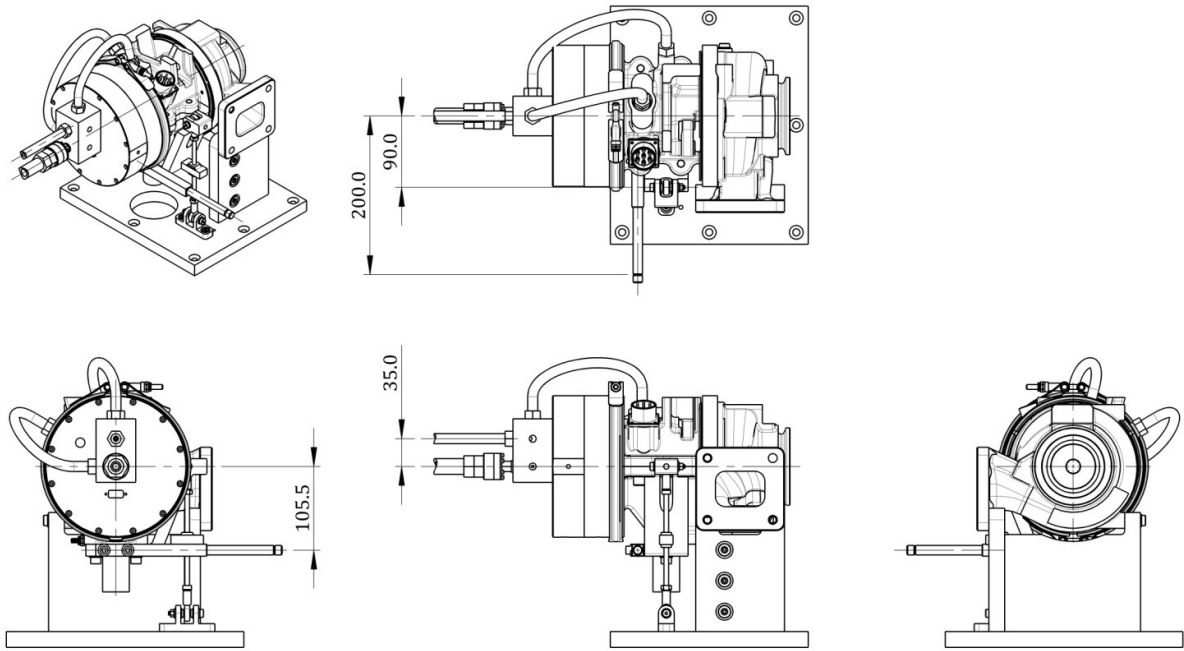


**Figure 3.14 - Assembly drawing of the Data Set 2 version of the modified turbocharger. The compressor cover opening has been closed to stop the oil from escaping in the form of mist. All the dimensions are in millimetres**

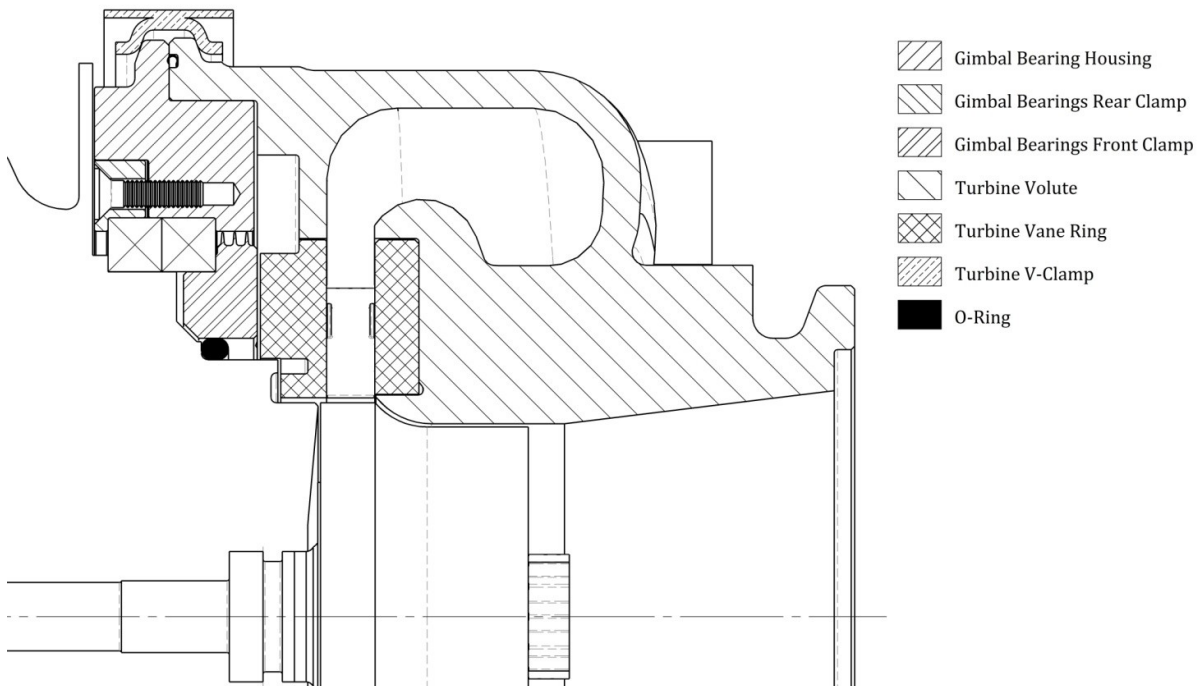


**Figure 3.15 - Cross sectional drawing of the Data Set 2 version of the gimbal bearings and retaining system assembly, top view. The large diameter o-ring has been replaced by a labyrinth seal. The drawing plane does not cut through the turbocharger bearing housing as it is coincident with the bearing housing split plane. The turbocharger bearings and motor/generator details are hidden**

selected so that its thickness was slightly lower than the clearance between the two parts. The rear clamp has then been carefully machined to remove some material from the bearing retaining step, so that the clearance is equal to the shim thickness (+10, -0  $\mu\text{m}$ ). This modification significantly reduced the gimbal bearings friction without introducing clearances.



The o-ring which sealed the gap between the gimbal bearing housing and front clamp has been replaced by a labyrinth seal, as shown in **Figure 3.15**. This reintroduced the initial problem of debris getting trapped in the gimbal bearings. However, the rate at which the load-cell output curve gradient changes over time is significantly lower than before and it is possible to test for up to two weeks with less than 5% change in gradient. As soon as the gradient exceeded 5% of the original gradient, the rig is disassembled and the bearings cleaned.

These two modifications significantly improved the torque measurement hysteresis and non-linearity, removed the o-ring stiffness change error and greatly reduced the load-cell offset drift. However, the gimbal system air leakage introduced an additional error. The air flowing out of the back of the volute exerts a force on the bearing housing which does not cross the gimbal axis. As a result, it generates a torque which is reacted through the load-cell, causing an error which is a function of the pressure ratio across the leakage path.

When the electromagnetic efficiency is obtained by subtracting the frictional losses from the total losses, a further error arises. This error is caused by the change in axial loading on the turbocharger thrust bearing due to the change in turbine inlet pressure. If the electrical machine operates in generating mode, the turbine power required to maintain the same turbocharger speed is higher than when the motor/generator is off. This higher power is achieved by increasing the turbine inlet pressure and, as a result, the frictional losses are increased due to the higher axial loading. The magnitude of the electromagnetic generating torque, obtained by subtracting the frictional torque from the total torque, is therefore overestimated. The motoring torque magnitude is also overestimated since it acts in the opposite direction of the frictional torque.

As described in the previous two paragraphs, this gimbal system set-up is not perfect and some errors still occur. These errors have been quantified and have been included in the uncertainty analysis as bias error (refer to *Uncertainty Analysis* part of **Section 3.1.13**). The resulting total systematic error was satisfactory and the gimbal system has not been further improved.

### *3.1.8 OTHER MEASUREMENTS REQUIRED TO CHARACTERIZE MOTOR/GENERATOR*

#### **Rotor Position and Speed Measurement**

The motor/generator rotor position sensor, constructed by the power electronics designer, is utilized to measure the turbocharger shaft position and speed. This sensor is composed of two parts: the wheel and the sensing board. The wheel has four slots and is made of low carbon steel. It is attached to the turbocharger shaft, clamped between the blank compressor wheel and the compressor nut. The sensing board is composed of three *Allegro ATS616 Hall Effect* sensors arranged in a semi-circular manner and spaced from each other by 45°. It is mounted

perpendicularly to the turbocharger shaft, with the *Hall Effect* sensors axis parallel to the turbocharger axis. The board includes a circuit which amplifies the *Hall Effect* sensors signals to reduce noise issues. The sensor is connected to the motor/generator controller, which provides a frequency signal output directly obtained from one of the *Allegro* sensors (hardwired). The turbocharger speed is calculated from this signal.

### **Voltage and Current Measurements**

The power electronics DC link voltage and current are measured by the inverter built-in sensors. The current sensor is a *LEM CASR 6-NP*, which has a range of 0 to 40 A, an accuracy of  $\pm 0.05$  A and a frequency bandwidth of 200 kHz ( $\pm 1$  dB). The voltage sensor has been custom built by the power electronics supplier utilizing an *Avago HCNR200-300E* linear optocoupler, which has a 0.01% of full scale non-linearity. The sensors output signals are not directly connected to the data-logger but are connected to the motor/generator controller, which does the analogue to digital conversion and sends the signal to the data-logger via the CAN bus as 16 bit unsigned words. The CAN bus signals have been calibrated with a *Voltech PM1000+* power meter to improve the sensor accuracy. The motor/generator phase currents are measured by means of the same current sensor utilized to measure the DC current.

When the second set of data was being collected, the DC link current was measured by means of an *Agilent U1241A* true RMS multimeter and logged manually. This meter has a current accuracy of  $\pm 0.6\%$  of the reading and a range of -10 to 10 A. The current was measured with this meter due to a fault of the inverter DC link current sensor.

### **Motor/Generator Stator Temperature Measurements**

The electrical machine stator temperature is measured by means of five T-type thermocouples with a 0.5 mm diameter. These thermocouples have been inserted in the coils during the winding process by the motor/generator manufacturer. No record of the exact position of the thermocouples has been provided and, for this reason, the five readings have been averaged during the error analysis.

### **Air Temperature, Pressure and Mass Flow Rate Measurements**

The turbine inlet air temperature is measured with a K-type thermocouple with the tip placed at the centre of the duct. The static pressure at the turbine inlet is measured with the *ScaniValve DSA3016* and the mass flow rate by means of a *McCrometer V-Cone*.

The ambient air temperature is measured by means of a K-type thermocouple. The thermocouple measurement has been verified with an *Oakton WD-03316-80*

thermometer/barometer. The ambient pressure is measured by means of a *Vaisala PTB110* barometer.

Because these measurements are not central to the motor/generator characterization and are identical to the turbine testing described in **Chapter 4**, the detailed description is provided in this other chapter.

### **Oil Temperature, Pressure and Volume Flow Rate Measurements**

The temperatures of the lubrication and cooling oil affect the bearing losses and electrical machine stator copper losses. For this reason, both temperatures are measured at the respective turbocharger oil inlets by means of two identical K-type thermocouples with a diameter of 1.5 mm. The oil temperature is also measured at the cart cooling and lubrication oil outlets and tanks. The four cart temperatures are measured by means of K-type thermocouples with a diameter of 3 mm.

Oil pressures are measured by means of two *Trafag NAT6.0A* pressure transmitters positioned at the oil cart outlets. These sensors have a range of 0 to 6 bar and a thermal error band of  $\pm 2\%$  of the full scale from  $-25$  to  $+85^\circ$  C. They are powered from a 24 V power supply and they provide an analogue output of 4 to 20 mA.

Two oval gear flow meters manufactured by *Titan Enterprises* are utilized to measure the oil volume flow rates. The *OG4* model is utilized to measure the cooling oil volume flow rate. This meter has a range of 0.25 to 50 l/min and an accuracy of 0.5% of the reading. The lubrication oil flow rate is measured with the *OG2* model which has a range of 0.03 to 4 l/min and an accuracy of 0.75% of the full scale. Both meters have built-in *Hall Effect* sensors to measure the oval gears rotational speed. The sensors are powered by a 5 V power supply and provide a frequency output.

The meters are positioned at the respective oil cart outlets. Because the measurements are in steady state and the temperature changes are small, the volume flow rate at the oil cart outlets is assumed to be equal to the volume flow rate at the turbocharger inlets.

### **Vibrations Measurement**

The vibrations of the turbocharger are monitored to detect bearing system failures. This is done by means of a *Monitran MTN/1100C* piezoelectric accelerometer. This accelerometer can detect accelerations in one axis, has a frequency range of 2 to 10,000 Hz and an acceleration range of  $-80$  to  $80$  g. The sensor is rigidly bolted on the compressor wheel cover, with the sensing axis crossing perpendicularly the turbocharger rotor axis. The sensor is mounted in this way to measure the vibrations caused by the rotary motion of the turbocharger rotor assembly. To

avoid aliasing effect due to the high order harmonics of the turbocharger speed, the sensor signal is filtered by a low pass filter with a cut-off frequency of 10,000 Hz.

### 3.1.9 DATA-LOGGER

The data-logger utilized for this testing is a *National Instruments CompactDAQ*. This data-logger is composed of a chassis and swappable modules which are specific to the type of measurement required. The chassis is a *NI cDAQ-9188* which can host up to eight different modules and communicates with the control computer via Ethernet.

Because the data-logger is positioned near the rig, inside the test-cell, the noise radiated from the electrical machine active rectifier could potentially disturb the Ethernet communication. To avoid noise issues, the computer and data-logger are directly connected by a shielded category 6a Ethernet cable with a crossover pin configuration. Moreover, as noise is also radiated through the laboratory electrical ground, both devices are powered from the same AC power source and share the same ground connection to avoid forming an earth loop between the test-rig and control computer. This is made possible by the fact that the chassis has two different ground connections insulated from each other. One earth connection is dedicated to the power supply and the second is dedicated to the sensors. The sensors earth is connected to the test-rig metallic bench and the sensors cable screens are connected either to the test-rig ground or to the data-logger ground. This connection arrangement prevents earth loops to be formed between the data-logger and test-rig which would generate noise in the signals.

The eight data-log modules inserted in the chassis are the following:

- *NI9201* – is an 8-channel single ended analogue voltage input module. The input range is from -10 to 10 V. The analogue to digital converter has a 12 bits resolution and an aggregate sampling rate of 500 kS/s.
- *NI9203* – is an 8-channel analogue current input module with an input range of -20 to 20 mA. The analogue to digital converter has a resolution of 16 bits and an aggregate sampling rate of 200 kS/s.
- *NI9205* – is a 32-channel single ended or 16-channel differential analogue voltage input module. The input range is from -10 to 10 V. The analogue to digital converter has a 16 bits resolution and an aggregate sampling rate of 250 kS/s.
- *NI9213* – is a 16-channel differential thermocouple module with cold junction compensation. It has an analogue to digital converter resolution of 24 bits and a maximum aggregate sampling rate of 1200 S/s.
- *NI9237* – is a 4-channel full-bridge strain gauge module. It has a built-in bridge excitation with a maximum voltage of 10 V. The analogue to digital converter has a

resolution of 24 bits and can sample all the channels simultaneously at a rate of 50 kS/s/ch.

- *NI9264* – is a 16-channel analogue output module with an output range of -10 to 10 V. The digital to analogue converter has a resolution of 16 bits and an update rate of 25 kS/s/ch.
- *NI9401* – is a digital counter module with 8 channels which can measure frequencies.
- *NI9862* – is a single-port high speed Controller Area Network (CAN) module.

**Table 3.3 – Data-logger connection details**

Module	Items Connected
NI9201	Main control valve feedback Fine control valve feedback Limb 1 control valve feedback Limb 2 control valve feedback
NI9203	McCrometer <i>V-Cone</i> differential pressure sensor Cooling oil pressure sensor Lubrication oil pressure sensor
NI9205	Accelerometer Barometer
NI9213	EM stator temperature 1 EM stator temperature 2 EM stator temperature 3 EM stator temperature 4 EM stator temperature 5 Turbine inlet air temperature <i>V-Cone</i> inlet air temperature Heater outlet air temperature Cooling oil turbocharger inlet temperature Cooling oil cart outlet temperature Cooling oil tank temperature Lubrication oil turbocharger inlet temperature Lubrication oil cart outlet temperature Lubrication oil tank temperature Ambient temperature
NI9237	Load-cell
NI9264	Control valves opening set-point Heater temperature set-point Heater on/off control Safety shutoff valve control Oil cart heating circuit control
NI9401	Turbocharger speed sensor Cooling oil mass flow rate sensor Lubrication oil mass flow rate sensor
NI9862	Motor/generator controller (CAN bus)

Not all the data is logged via the *NI cDAQ*. The *ScaniValve* pressure measurement device has a built-in data-logger which reads and processes the air pressure data. The motor/generator phase currents are logged via an *Agilent Technologies DSO1004A* oscilloscope which has a sampling frequency of 1 GSa/s/ch.

### 3.1.10 DATA-LOG AND CONTROL SOFTWARE

The data-log and control software is run in the *Microsoft Windows* based control computer located outside the test-cell. The program is written in *NI LabVIEW* environment, which is

specifically designed to work with *National Instruments* data-loggers. The main scope of this software is to allow communication between the *CompactDAQ* data-logger and the control computer so that data can be transferred between the two devices. In addition, the program displays the collected and written data on the computer screens, both in numerical and graphical format, so that it can be easily monitored by the user.

The program is divided in six main areas:

- Sensors signals reading and conditioning – reads the raw data sampled by the data-logger and transforms it to the required data format.
- Data-logging – it averages the data over 5 s and it stores it into a *Microsoft Excel spreadsheet*.
- Air and oil control – allows the user to control the valves opening, the air and lubrication oil temperature, and to open or close the safety shutoff valve.
- Emergency shutdown – automatically shuts off the test-rig if one of the monitored parameters exceeds the imposed limits or if the emergency button within the program is pressed by the user.
- Communication with motor/generator controller – allows the user to log electrical machine data such as DC link voltage and current, and to set motor/generator control variables such as torque demand or operation mode.
- Communication with the *ScaniValve* pressure measurement system – Allows the user to control the *ScaniValve* and reads the pressure data.

### *3.1.11 MOTOR/GENERATOR CHARACTERIZATION PROCEDURE*

When a new test session begins, the oil system and turbocharger have to be warmed-up before running the machine. The warm-up procedure is done by running the oil with the heating circuit on until the required lubrication oil temperature at the turbocharger inlet is reached. This temperature is then maintained approximately constant by the control software, which turns on and off the heating circuit so that the temperature stays within a tolerance of  $\pm 0.5^\circ\text{C}$ . The oil is circulated at this constant temperature for 30 min to ensure that all the components have reached a steady temperature. Once the warm-up procedure is completed, the load-cell is calibrated, and this is done by following the procedure described in **Section 3.1.7**.

The next step is to warm-up the air heater and pipes. This is done by opening the main control valve so that air flows through the heater and pipe system. The heater is turned on and the PID controller maintains the exit temperature constant at  $70^\circ\text{C}$ . This procedure finishes once the temperature at the turbine inlet reaches a constant value. During this procedure the turbocharger runs at low speed ( $<40,000\text{ rev/min}$ ).

Once the pre-testing procedures are complete, the data collection can start. This is done through the following procedure:

1. The turbocharger is run to the desired speed ( $\pm 1,000$  rev/min) by gradually opening the control valves and increasing the electrical machine torque demand.
2. Once the desired torque demand is set and the desired speed is reached, the data is logged by the data-log software.
3. The turbocharger is rapidly stopped and the load-cell offset is recorded.
4. Within one minute from when the turbocharger is stopped, it is run again to the same speed ( $\pm 500$  rev/min) with the motor/generator turned off.
5. The data is logged.
6. The turbocharger is rapidly stopped and the load-cell offset is recorded.

To reduce the random experimental error, points 1 to 6 are repeated three times for each torque and speed combination tested. The points plotted in the efficiency maps correspond to the average of these three measurements. The measurements are not taken in a well defined sequence, as it has been found that the measurements' order does not have any impact on the efficiency calculated.

This motor/generator has a low number of windings because it is designed to run in a non-continuous manner. This means that the stator windings heat up rapidly due to the relatively high copper losses and the electrical machine temperature cannot be easily controlled. In the worst case scenario, the average stator temperature can vary by up to  $20^{\circ}$  C between repeated measurement points. This leads to a scatter in copper losses of up to 7% at the maximum machine power, which translates to an efficiency random error of  $\pm 0.5\%$ .

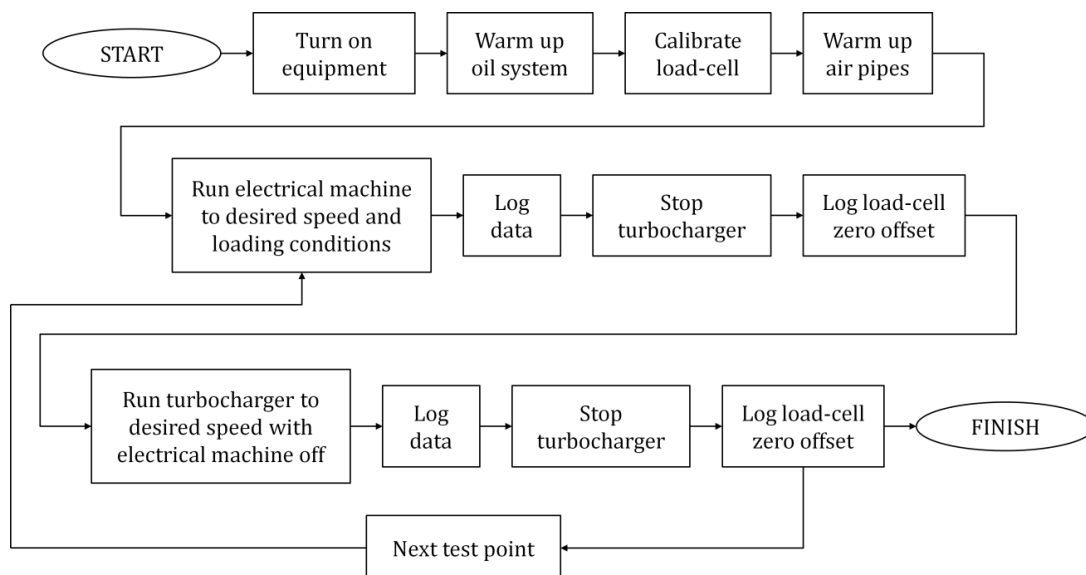


**Figure 3.16 – Motor/generator testing procedure flowchart**

The load-cell offset has been found to vary depending on the bearing housing temperature, as explained in **Section 3.1.7**. For this reason, the turbocharger is stopped rapidly as soon as the software has finished logging the data. Because the turbocharger cooling occurs over a time span of several minutes, recording the offset a few seconds (typically <10 s) after the load is measured significantly reduces the torque error.

### 3.1.12 EMERGENCY TEST-RIG SHUTDOWN

In case of emergency, the user can shut down the test-rig either manually or through the control software. Outside the test-cell there is a control box which is hardwired to the safety shutoff valve, active rectifier and air heater. When the emergency button on this control box is pressed, the valve closes and the power to the air heater and motor/generator is cut. This control box is independent of the control software and is only used if this software crashes. On the control box there are also switches to shut these devices individually. The heater has a separate controller connected in series with the PID controller that cuts the power if the temperature limit of 130° C is exceeded.

An emergency stop button is also present in the *LabVIEW* virtual panel. When this button is pressed, the safety valve is immediately closed and the power to the air heater is cut. The software emergency stop also shuts the control valves to avoid the risk of over-speeding the turbocharger when the safety valve is opened again. If the electrical machine is operating in motoring mode the machine is turned off immediately. If it is operating in generating mode, the machine is turned off only when the turbocharger speed drops below 20,000 rev/min. This occurs to avoid turbocharger over-speeds that could take place if the electrical machine load is removed before the safety valve is shut. In addition, the generating power increases the turbocharger deceleration and this helps reducing turbocharger damage in case of oil supply failure.

The control software automatically shuts the test-rig off if it detects a turbocharger over-speed, bearing failure (vibrations), oil system failure or motor/generator overheating. If excessive air temperature is detected, the software turns off the heater only. The variable monitored and the emergency shutdown activation limits are listed in **Table 3.4**.

**Table 3.4 – Automatic system shutdown conditions**

Monitored Variable	Shutdown Condition
Turbocharger speed	>140,000 rev/min
Vibrations	>4.5 mm/s
Lubrication oil pressure	<2.5 bar
Lubrication oil mass flow rate	<0.7 kg/min
EM stator max temperature	>140° C
Air heater exit temperature	>130° C



### 3.1.13 MOTOR/GENERATOR CHARACTERIZATION RESULTS AND DISCUSSION

Two sets of data are presented in this section. The first set of data has been obtained with the version of the torque measurement system described in the *Data Set 1 Gimbal Arrangement* part of **Section 3.1.7**, which includes an o-ring to stop compressed air from leaking through the bearings of the gimbal system. The second set of data has been obtained with the latest version of the torque measurement system, which is more accurate than the first version. A further difference between the two data sets is in the control system of the motor/generator. The control system parameters in *Data Set 2* are more refined compared to the parameters in *Data Set 1*, and therefore there are differences in motor/generator performance. In addition, the two sets have been produced with two different machines, but of identical design. This is because the journal bearings of the first assisted turbocharger prototype failed, causing unreparable damage to the device. Since the two motor/generators are identical, no significant changes in performance are expected to occur. Both sets of data have been included because *Data Set 2* only covers the machine performance up to a speed of 80,000 rev/min due to vibration issues.

The data produced by this experiment has been used to produce three efficiency maps for each data set. One map includes both the electromagnetic losses that occur in the electrical machine and power electronics, and the frictional losses that occur within the turbocharger bearing housing. The other map only includes the electromagnetic losses. A third map, which includes the electromagnetic losses and the rotor aerodynamic drag loss, is presented in the **Section 3.2**. **Table 3.5** lists all the performance maps presented in this chapter.

**Table 3.5 – List of the motor/generator efficiency maps presented in this chapter**

	<b>Data Set 1</b> O-ring to stop leakage through gimbal bearings, high torque uncertainty, control parameters not fully refined	<b>Data Set 2</b> Labyrinth seal to stop leakage through gimbal bearings, improved torque uncertainty, control parameters better refined
<b>Total Efficiency</b> Includes electromagnetic, bearings and rotor drag losses	Figure 3.17	Figure 3.18
<b>Electromagnetic Efficiency</b> Includes electromagnetic losses only	Figure 3.20	Figure 3.21
<b>Electromagnetic + Windage Efficiency</b> Includes electromagnetic and rotor drag losses	Figure 3.26	Figure 3.27

#### **Total Efficiency Data**

**Figure 3.17** and **Figure 3.18** show the motor/generator total efficiency, which includes the turbocharger frictional losses, as a function of rotational speed and output shaft power. These results show that the frictional load magnitude is similar to the motor/generator electromagnetic torque magnitude. This is indicated by the negative efficiency obtained when the machine operates in motoring mode under certain loading conditions. The negative

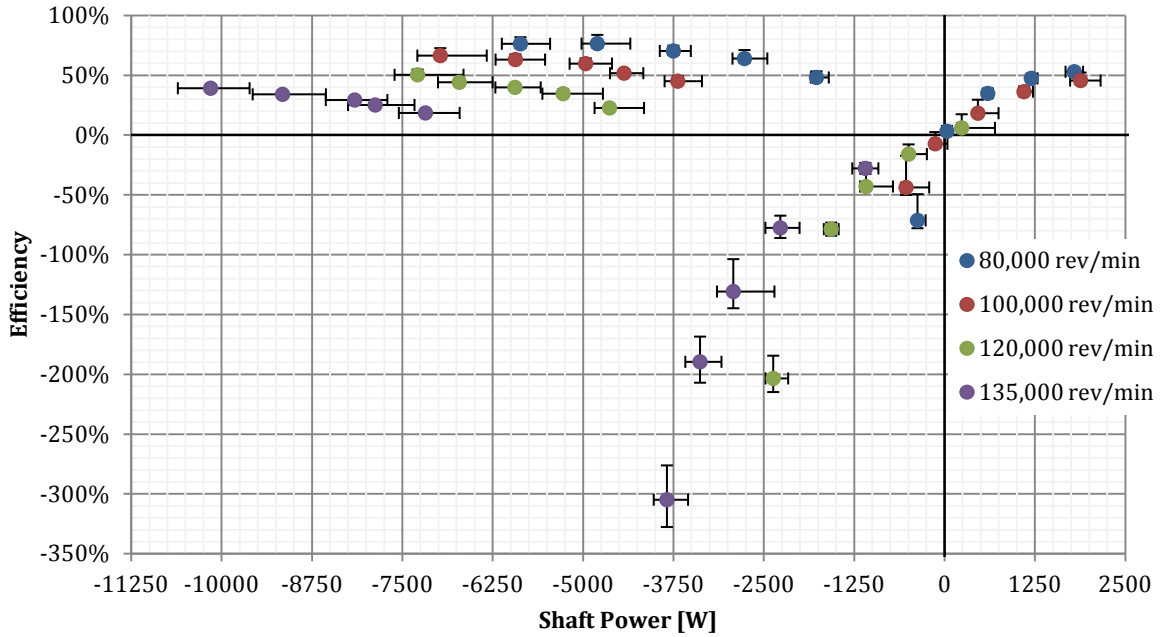


Figure 3.17 - Data Set 1 motor/generator efficiency plotted against shaft power output. Frictional losses included (turbocharger bearing load and motor/generator rotor drag)

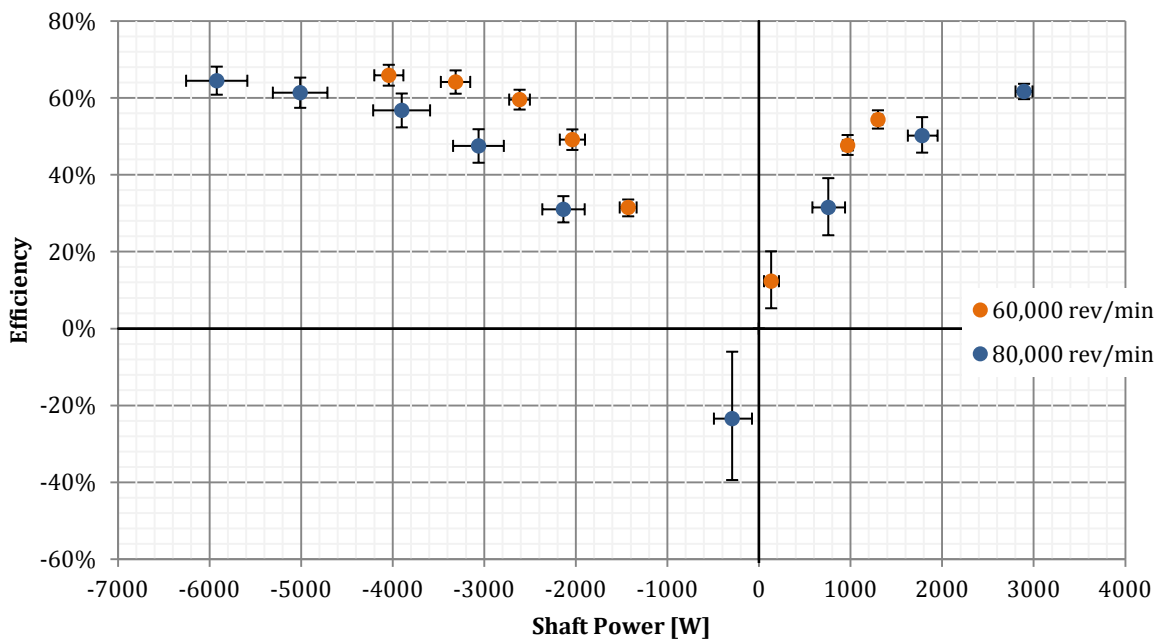
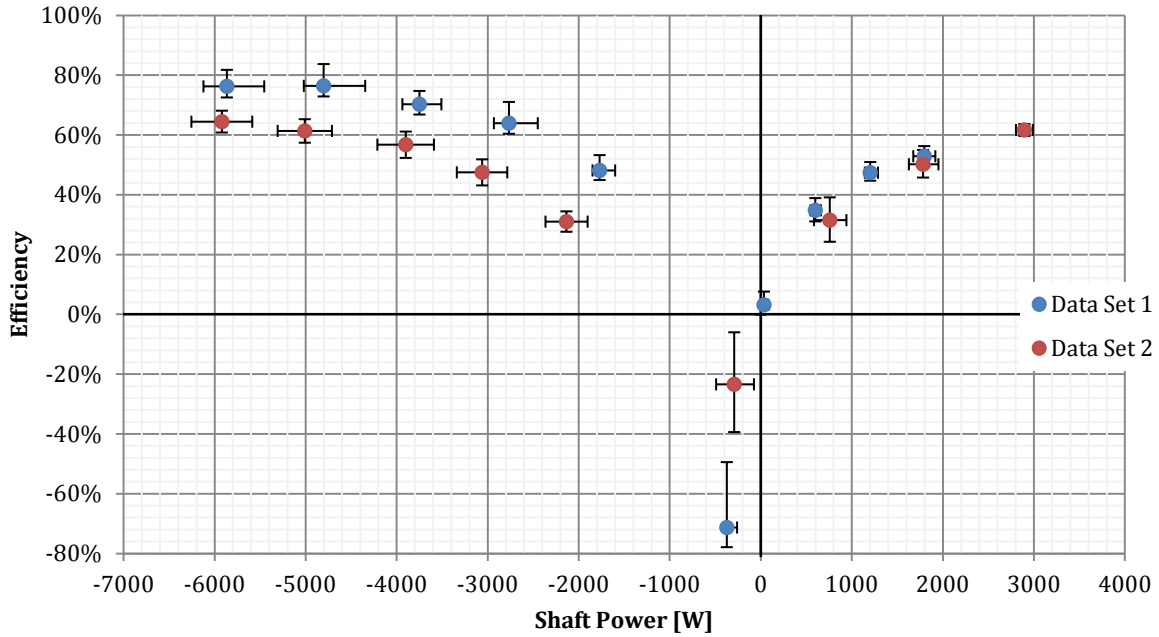


Figure 3.18 - Data Set 2 motor/generator efficiency plotted against shaft power output. Frictional losses included (turbocharger bearing load and motor/generator rotor drag)

efficiency occurs when the bearing load exceeds the electromagnetic torque, causing a negative shaft power. At 135,000 rev/min the motoring efficiency is always below zero, indicating that bearing load is always larger than the electromagnetic torque. Due to the different generator efficiency definition (**Equation 3.1**), negative efficiency does not occur in generating mode. However, the frictional losses cause the generating efficiency to be low.



**Figure 3.19 – Comparison of Data Set 1 and Data Set 2 motor/generator efficiency at 80,000 rev/min. Frictional losses included (turbocharger bearing load and motor/generator rotor drag)**

The frictional losses are higher in this experimental set-up than when the turbocharger is installed on an engine. This is mainly due to the fault in the oil cart heating system, which resulted in approximately 60° C lower lubrication oil temperature at the turbocharger inlet. This causes higher oil viscosity and therefore higher bearing losses when compared to the typical values occurring when the turbocharger is mounted on an engine. Nevertheless, these results are important since the thermal and loading conditions are known, and therefore it has been possible to utilize this data to calibrate the bearing losses model described in **Chapter 6**. Moreover, these results show the accuracy level of the test-rig when the efficiency is obtained from a single torque measurement.

**Figure 3.19** compares the *Data Set 1* (initial EM controller calibration) and *Data Set 2* (Improved test-rig and EM controller calibration) efficiency at 80,000 rev/min. The power achieved is higher in *Data Set 2* both in motoring and generating mode. However, the efficiency in *Data Set 2* is lower when the machine operates in generating mode. As it will be seen in the following section, this is not caused by a lower electromagnetic efficiency, but by a lower mechanical efficiency. The reason for the different mechanical losses is that the two sets of data have been generated utilizing two different assisted turbocharger prototypes and that the oil utilized to lubricate the turbochargers has oxidised over time, resulting in increased viscosity.

### **Electromagnetic Efficiency Data**

It must be noted that the turbocharger bearings on the assisted and non-assisted turbocharger are the same. As a result, the bearing losses are also present in the standard turbocharger and

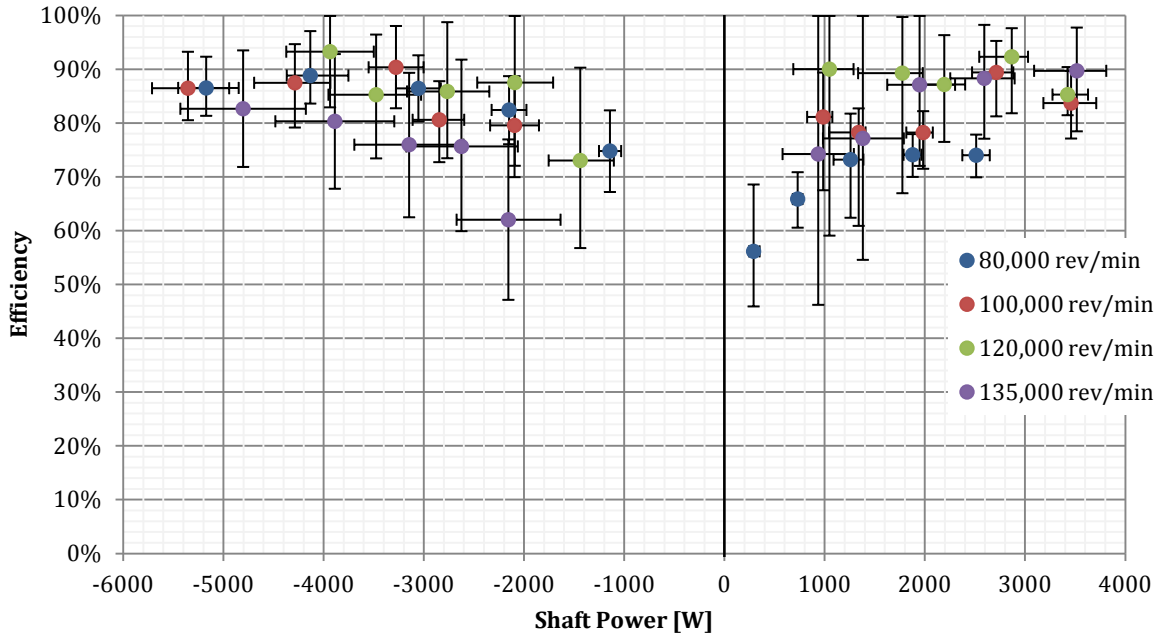


**Figure 3.20 – Data Set 1 motor/generator efficiency plotted against shaft power output. Frictional losses not included (turbocharger bearing load and motor/generator rotor drag)**

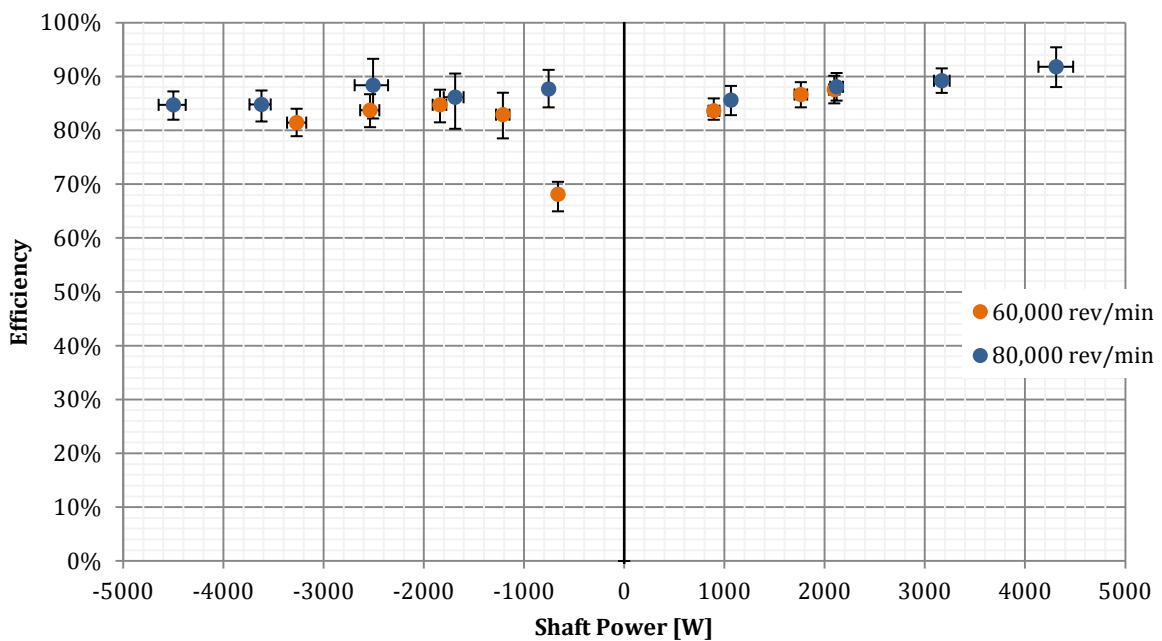


**Figure 3.21 – Data Set 2 motor/generator efficiency plotted against shaft power output. Frictional losses not included (turbocharger bearing load and motor/generator rotor drag)**

therefore they should only be included in the turbocharger mechanical efficiency. The pure electromagnetic efficiency, which only includes the power electronics, copper and iron losses, provides a better indication of how much of the electrical energy consumed is utilized to assist the turbocharger. The electromagnetic efficiency maps for the two data sets are shown in

**Figure 3.20** and **Figure 3.21**. Note that the frictional power losses have also been subtracted from the shaft power.

In *Data Set 1* the peak efficiency is 93% and is achieved at a speed of 120,000 rev/min, while in *Data Set 2* the peak efficiency is 92% and is achieved at a speed of 80,000 rev/min. No clear correlation between efficiency and speed can be seen, and the efficiency differences between speed lines in *Data Set 1* are probably due to the not fully optimized control parameters.

Both data sets show that the efficiency drops rapidly as the shaft power approaches zero. This effect is caused by the fact that not all the energy which is transferred from the electrical power source to the magnetic field is turned into mechanical power. When the transistors that control the phase are turned off, the excess energy is returned to the power supply via the diodes (Ahn, 2011) (refer to **Figure 2.20**). However, not all the energy stored in the magnetic field is either converted to mechanical power or returned to the power supply. Part of this energy is turned into heat by copper and iron losses. The instantaneous copper power loss is given by:

$$\dot{W}_{copper} = I^2 R \quad (3.2)$$

Amar and Kaczmarek (1995) give an equation for the eddy currents cycle average power loss that occurs in the stator and rotor:

$$\dot{W}_{eddy} = \frac{\sigma}{f} \frac{h^2}{12\rho} \frac{1}{T} \int_0^T \dot{B}^2 dt \quad (3.3)$$

In **Equation 3.3**  $\sigma$  is the lamination conductivity,  $f$  is the current switching frequency,  $h$  is the lamination thickness,  $\rho$  is the lamination density and  $T$  is the current switching time period.  $B$  is the magnetic flux density, which is a function of the current in the coils, number of turns in the coils, the iron cross sectional area and the magnetic circuit reluctance (Hughes, 2006):

$$B = \frac{NI}{AR} \quad (3.4)$$

These equations show that both the copper and the eddy current losses are a function of the current in the coils, i.e. on the energy stored in the magnetic field. As explained in **Section 2.4**, part of the energy stored in the magnetic field is turned into mechanical energy, part of it is returned to the power source and the remaining part is turned into heat by the copper and iron losses. Therefore, if the portion of the returned energy is high relative to the portion of energy turned into mechanical energy, the copper and eddy current losses would be proportionally high due to the high current in the coils. Because of the method adopted to control the electrical machine's inverter, when the motor/generator power is reduced, the ratio between the

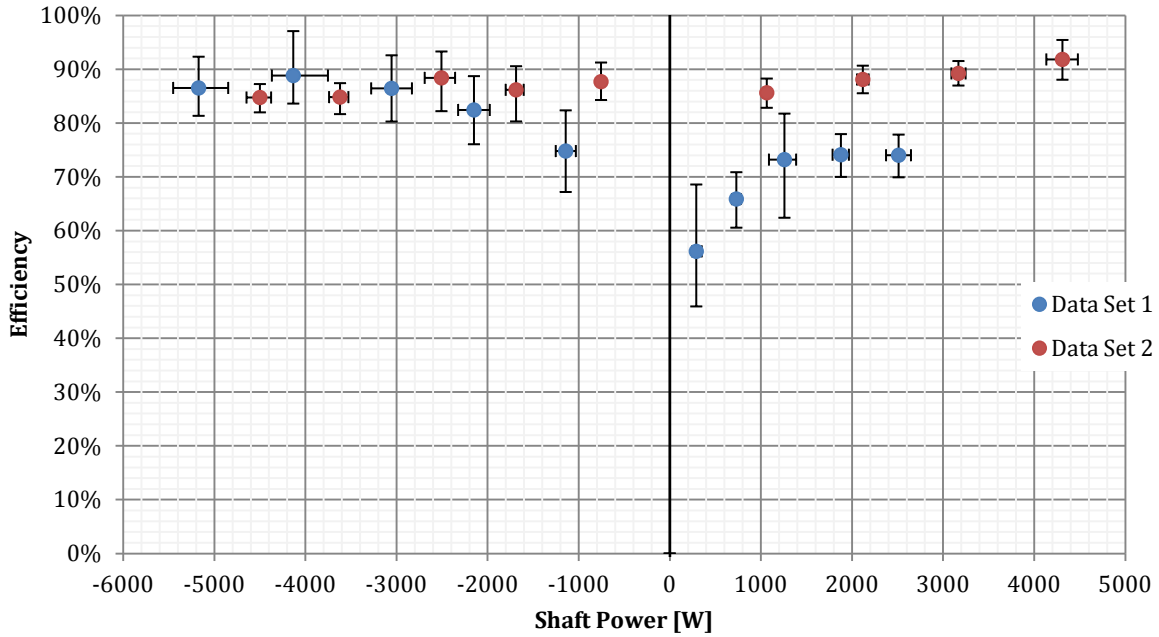


**Figure 3.22 – Comparison of Data Set 1 and Data Set 2 motor/generator efficiency at 80,000 rev/min. Frictional losses not included (turbocharger bearing load and motor/generator rotor drag)**

produced mechanical energy and the returned energy drops. As a consequence, the copper and eddy current losses increase relative to the shaft power and the efficiency falls.

The explanation given above is also valid when the machine operates in generating mode, as the copper and iron losses mechanisms are identical. The difference between the generating mode and motoring mode is that in generating mode the amount of energy returned to the power supply is larger than the amount of energy supplied to the magnetic field. The efficiency drops because the ratio between the mechanical energy extracted and the supplied energy is reduced.

By observing **Figure 3.22** it can be seen that the main difference between the two data sets, apart from the different error magnitude, is in the efficiency and power obtained in motoring mode at 80,000 rev/min. In *Data Set 1*, the efficiency and power achieved are lower compared to *Data Set 2* since the ‘on’, ‘free-wheel’ and ‘off’ angles were all occurring early. The reason why this was causing poor performance can be understood by observing the equation which describes the instantaneous torque production in motoring mode, which is given by Soares and Costa Branco (2001) (modified for a single phase):

$$\tau = \frac{1}{2} \frac{dL}{d\theta} I^2 \quad (3.5)$$

With an early ‘on’ angle, the current starts increasing when the stator and rotor poles are not overlapping and the inductance gradient is zero, resulting in no torque being produced. The energy supplied by the power source is stored in the magnetic field and part of it is converted to

heat by iron and copper losses. Eventually the inductance starts increasing and some of the energy stored in the magnetic field is converted to mechanical energy. However, because the ‘off’ angle is also occurring early, a large fraction of the magnetic energy is returned to the power source and therefore the electromagnetic losses are relatively high compared to the power produced. The low power is caused by the low efficiency and by the fact that only part of the angular region where the inductance gradient is positive is exploited to produce torque. In *Data Set 2* the firing angles have been delayed resulting in a more powerful and efficient motor/generator.

The electromagnetic efficiency does not include the motor/generator rotor drag loss which occurs only in the assisted version of the turbocharger. As a result, the electromagnetic efficiency overestimates the fraction of energy which is utilized to assist the turbocharger. Nevertheless, this data is important because it allows a better understanding of the electromagnetic losses and allowed a more accurate calibration of the inverter firing angles.

### Uncertainty Analysis

In this experimental methodology the efficiency and the shaft power are not measured directly, but are calculated from variables such as turbocharger speed and bearing housing reaction torque. Efficiency and shaft power are therefore known as derived variables and the parameters from which they are calculated are the independent variables. **Equation 3.6** represents the relationship between the two types of variables.

$$y = f(x_1, x_2, x_3, \dots, x_N) \quad (3.6)$$

Both bias and precision error are present in the independent variables. The bias is the difference between the mean of the measurements and the true value. Therefore, by definition, this component of the error cannot be found by taking multiple measurements and it has to be estimated either by comparing the results of different measurement methodologies or by applying judgement (Abernethy, Benedict and Dowdell, 1985). Since no alternative measurement methodologies were available, the bias has been estimated for each independent variable by dividing the systematic error into different components. The magnitude of each component has been estimated individually and the total bias for the independent variable has been obtained through the root sum square method, as recommended by Abernethy et al. (1985):

$$B_x = \sqrt{\sum_{j=1}^{N_{comp}} b_j^2} \quad (3.7)$$

In this equation  $B_x$  represents the total bias for independent variable  $x$ ,  $b$  represents the individual component of  $B_x$  and  $N_{comp}$  is the total number of components. The asymmetry of the bias has been maintained by summing the negative and positive parts of the error components separately.

The systematic error is propagated to the derived variable by differentiating the derived variable function with respect to the independent variable to which the bias applies. The total bias of the derived variable is found by the root sum square method:

$$B_y = \sqrt{\sum_{i=1}^{N_x} \left( \frac{\partial y}{\partial x_i} B_{x_i} \right)^2} \quad (3.8)$$

In this equation  $N_x$  is the total number of independent variables  $x$  in the function that describes the derived variable  $y$ . Because the torque bias error obtained is highly asymmetrical, the positive and negative parts of the error have been propagated individually to maintain the asymmetry in the error. This has been done by summing all the positive components of  $B_y$  (i.e.  $\partial y / \partial x_i B_{x_i}$ ) to find the positive part of the error and all the negative components to find the negative part.

The precision error has been calculated directly from the derived variables and the error propagation technique has not been implemented. It is possible to do this because the rotational speed, torque, voltage and current are all logged simultaneously and the measurements are repeated three times for each machine running condition (refer to **Section 3.1.11**). The derived variable is calculated for each measurement set and the error is computed as recommended by Kirkup (1994):

$$P_y = \frac{y_{max} - y_{min}}{N_{meas}} \quad (3.9)$$

The random error is calculated following this methodology because the exact speed and load cannot be replicated when the measurements are repeated. If the precision error is calculated for the independent variables and then propagated to the derived variable, it would be inflated by the fact that the loading conditions are not homogeneous. For example, if measurement set A occurs at a slightly higher load than measurement B, the electrical current of measurement A would also be larger than in measurement B and the difference in computed efficiency is not large. However, if the precision error is calculated for the torque and current and propagated to the efficiency, the resulting efficiency error would be significantly larger than the difference between efficiency A and efficiency B. It is important to note that this technique still captures both the error caused by the non repeatability of the loading conditions and the error caused by the precision of the measurement.



As stated in **Section 3.1.11**, the electromagnetic efficiency is found by subtracting the torques from two different measurements. The first measurement occurs with the motor/generator turned on while the second measurement occurs with the electrical machine turned off. Because the turbocharger thermal conditions during the two measurements are similar, the electromagnetic efficiency is calculated for each measurement pair and the error is calculated directly from the derived variables as above. Because the electrical power is calculated only from the first measurement, the efficiency precision error fully captures the torque random error caused by the difference in rotational speed between the two measurements.

To be consistent with the precision error estimation technique, the mean of the derived variables plotted in the result charts is not calculated from the mean of the independent variables, but by averaging the values of the derived variables calculated from the individual measurements set. The difference between the values obtained with the two different techniques has been found to be at least one order of magnitude smaller than the total error.

The bias and precision error are combined together by the root sum square method to obtain a single error value:

$$\varepsilon_y = \sqrt{B_y^2 + P_y^2} \quad (3.10)$$

#### *Torque Measurement Bias*

The torque measurement bias is not identical for the two data sets as they have been obtained with different versions of the torque measurement system. For *Data Set 1* the components of the systematic random error are the following:

- Hysteresis and non-linearity caused by gimbal bearings friction, o-ring non-linear behaviour and load-cell accuracy
- Geometric tolerances of calibration arm
- Load-cell zero offset drift
- O-ring stiffness variation with temperature
- Thrust bearing friction variation due to change in axial load (applies only to electromagnetic efficiency)

For *Data Set 2* the bias components are:

- Hysteresis and non-linearity caused by gimbal bearings friction and load-cell accuracy (extensively reduced)
- Geometric tolerances of calibration arm

- Load-cell zero offset drift (extensively reduced)
- Error caused by air leakage
- Thrust bearing friction variation due to change in axial load (applies only to electromagnetic efficiency)

The hysteresis and non-linearity of the torque measurement system has been estimated from the results of the calibration process. The system has been calibrated both under loading and unloading conditions and the error has been taken as the maximum difference between the torque value given by the sensitivity line and the actual torque applied to the bearing housing. In *Data Set 1* this error is  $\pm 4\%$  of the reading and in *Data Set 2* is  $\pm 0.5\%$  of the reading. These errors have been specified relative to the reading as the load cell zero offset voltage is logged for every single measurement.

The horizontal distance between the gimbal axis and the point where the load-cell calibration weights are attached is not exactly 200 mm but has a manufacturing tolerance. This causes an error during the calibration process which is proportional to the geometrical tolerance. This error has been found to be  $\pm 0.14\%$  of the reading.

The load-cell zero offset drift error has been estimated for each individual measurement. This has been done by calculating the gradient of the drift where the offset is measured, and by extrapolating this gradient to the time when the torque is logged. Because the measurements are repeated three times, the three estimated errors have been averaged.

As explained in the *Data Set 1 Gimbal Arrangement* part of **Section 3.1.7**, the o-ring stiffness changes with temperature. However, data which describes the relation between the NBR elastic modulus and temperature has not been found and the exact error cannot be calculated. To overcome this issue, the conservative assumption of 50% change in stiffness is made, and the resulting error is  $\pm 1.7\%$  of the reading.

The air leakage which occurs with the *Data Set 2* gimbal arrangement exerts a force on the bearing housing and therefore generates an error. Because this error is a function of the turbine pressure, it has been estimated by pressurizing the turbine volute with the outlet blocked and by logging both the load-cell output and turbine inlet pressure. This function has been found to change every time the test-rig is disassembled and reassembled, so this test has been repeated several times and the most conservative positive and negative gradient functions have been selected. The resulting error function is the following:

$$b_{leak} = 0.075(PR - 1) \quad (3.11)$$

In this equation PR is the ratio between the static pressure at the nozzles outlet and the ambient pressure. The static pressure has been estimated from the flow area, the mass flow rate, and by assuming no stagnation pressure and heat loss in the turbine.

The electromagnetic torque error due to the variation of thrust bearing axial load with turbine pressure has been estimated via the calibrated turbine and bearing housing models described in **Chapter 6**. The logged turbine inlet pressure and rotational speed have been added to the model as boundary conditions to obtain the bearing load as a function of inlet pressure. The difference in bearing load between the run with the motor/generator on and the run with the motor/generator off has been calculated for every measurement pair and, because the measurements have been repeated three times (three measurement pairs), the three estimated errors have been averaged.

#### *Voltage and Current Measurements Bias*

The voltage and current measurement bias have been assumed to be equal to the linearity accuracy of the built-in sensors plus the accuracy of the calibrator and, for *Data Set 2* current measurements, to the accuracy quoted by the meter manufacturer. The current bias is therefore  $\pm 0.05$  A plus  $\pm 0.1\%$  of the reading for *Data Set 1* and  $\pm 0.6\%$  of the reading for *Data Set 2*. The optocoupler utilized to measure the voltage has a reported linearity of  $\pm 0.01\%$  of the reading. To be conservative, the measurement error has been assumed to be  $\pm 0.2\%$  of the reading.

In addition to the errors listed above, there is an electrical power systematic error caused by the non consistent temperature during testing which results in non consistent copper losses. This error has been estimated for each data point from the copper resistivity-temperature relationship, the difference between the measured mean stator temperature and a reference temperature ( $60^\circ$  C), and by making the conservative assumption that the copper losses are equal to the full motor/generator power loss. This assumption has been made because the copper losses could not be calculated, since the high frequency resistance (i.e. the resistance including conductor skin effects) is not known and because the phase currents have been logged only in *Data Set 2*.

#### **Possible Improvements**

This experimental methodology could be improved by replacing the angular contact ball bearings utilized to form the gimbal system with hydrostatic or aerostatic bearings. These solutions would have completely removed the gimbal system stiction and therefore it would have significantly reduced the torque measurement non-linearity and hysteresis. Moreover, it would have eliminated the load-cell zero offset drift. This solution has not been implemented

due to the prohibitive cost of these custom made bearings, packaging difficulties, and concerns regarding bearings seizure due to thermal expansion.

A further improvement would be the addition of a shaft axial preloading system to ensure that the shaft axial displacement remains constant during testing. Such a system would ensure constant thrust bearing friction and would reduce the bias error of the electromagnetic efficiency.

A custom turbocharger bearing housing could have been machined to allow measuring the reaction torque of the motor/generator stator. This would have separated the bearing losses from the other losses, including the motor/generator rotor drag. As a result, it would have been possible to directly obtain an electrical machine efficiency map which includes the rotor drag losses. However, the cooling system, which is an integral part of the motor/generator, would have had to be modified and a separate test-rig would have had to be manufactured to measure the bearing losses.

## 3.2 COMPUTATIONAL ESTIMATION OF MOTOR/GENERATOR ROTOR DRAG

This section covers the calculation of the motor/generator rotor drag loss via computational fluid dynamics analysis. The reason to estimate this loss via CFD software is that the torque measurement system has not been designed to separate the bearing losses from the rotor drag loss.

The objective of this section is to generate an efficiency map for the electrical machine which includes only the losses introduced by the motor/generator. This is achieved by combining the electromagnetic losses measured in the previous section with the rotor drag loss estimated computationally in this section.

### 3.2.1 MOTOR/GENERATOR ROTOR DRAG ESTIMATION METHODOLOGY

The shear stresses and pressure on the motor/generator rotor have been computed via *Ansys CFX*, which is a commercial CFD program. This program is composed by a solver, which solves the unsteady Navier-Stokes equations in their conservative form (Ansys Inc., 2012), meshing software and post-processing software.

The fluid around the rotor is air and the flow has been modelled in three dimensions. The flow domain includes the gap between the rotor and the stator, and the volumes around the rotor collars. This domain has been divided in four slices (4-pole rotor) and only one slice has been simulated to allow a finer mesh. The rotational periodicity assumption is made, which means that the model assumes that the flow across the two symmetry planes is identical. Turbulence has been modelled through the k- $\epsilon$  model.

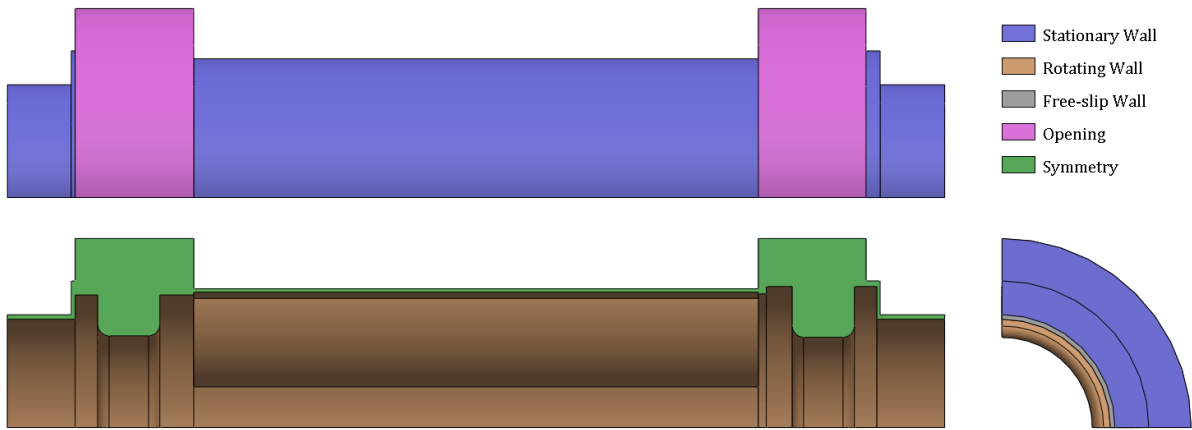


**Figure 3.23 – Boundary conditions of the computational fluid dynamics model of the motor/generator air gap**

The mesh has been generated with the *Ansys* meshing software. It is an unstructured tetrahedral mesh with a specified cell size of 0.15 mm at the rotor, collars and stator faces. At the rotor edges the mesh has been refined by an order of two (i.e. 0.075 mm cell size). The total number of nodes is 633,668, while the total number of elements is 3,444,746. A cell size sensitivity study utilizing a simplified air gap model has been performed to determine the trade-off between computational time and accuracy. The simplified model consisted of the volume of the gap between two concentric cylinders with a difference in radius equal to the motor/generator air gap. The results of this sensitivity study are shown in **Table 3.6**. Because drag difference between the selected mesh and the finest mesh is approximately 5%, a  $\pm 5\%$  error has been assumed.

**Table 3.6 – Results of the motor/generator CFD model elements size sensitivity study**

Elements Number	Nominal Element Size [m]	Fraction of Air Gap Size	Torque [Nm]
7780	3.00E-04	100%	-7.83E-05
59241	1.50E-04	50%	-6.88E-05
197838	1.00E-04	33%	-7.05E-05
487360	7.50E-05	25%	-7.20E-05

The rotor, collars, stator and bearing housing faces have been modelled as no-slip wall boundary conditions with a specified surface roughness of 6.3  $\mu\text{m}$  (roughness average). The rotor and collars faces have been set to rotate about the machine axis. The surfaces temperature has been set to 100° C. Because this temperature value is not supported by experimental data, the actual surfaces temperatures are not know. The drag uncertainty has been estimated by assuming that the surfaces temperatures lay in the 50° C to 150° C range and that the drag uncertainty is proportional to the change of air viscosity in this temperature range. This resulted in an uncertainty of +9.4%, -9.8%. The outermost bearing housing surfaces on either side of the stator have been modelled as constant pressure boundary conditions with a pressure of 1 atm. This is to account for the openings in the bearing housing required to drain the oil which leaks into the motor/generator.

Initial steady state simulations revealed that full solution convergence could not be achieved due to the existence of non-stable secondary flow. As a result, the flow has been resolved through a transient analysis. The simulation time has been set to the time required to complete three revolutions and the time step has been set to the time required by the rotor to rotate by  $10^\circ$ . During the last revolution the rotor drag was found to be oscillating in a stable manner and therefore it has been assumed that the rotor drag is the average drag over this last revolution. The flow has been integrated over time through a *Second Order Backward Euler* numerical scheme. Three different rotational speeds have been simulated: 60,000 rev/min, 100,000 rev/min and 140,000 rev/min.

### 3.2.2 MOTOR/GENERATOR ROTOR DRAG ESTIMATION RESULTS AND DISCUSSION

The results obtained from this computational study are shown in **Figure 3.24**, where the rotor drag loss is plotted as a function of rotational speed. The maximum power loss is 63.4 W and occurs at a speed of 140,000 rev/min. This loss is not large as it is about 1.2% of the maximum machine power. On the other hand, it is not negligible as it is 7.1% of the maximum measured power loss at that speed.

The computed rotor drag loss has been combined with the measured electromagnetic losses to produce the efficiency maps shown in **Figure 3.26** for *Data Set 1*, and in **Figure 3.27** for *Data Set 2*. The difference between these plots and the electromagnetic efficiency plots is small. The main differences can be seen at low motor/generator shaft powers, where the rotor drag losses are proportionally more important. In *Data Set 1* at 135,000 rev/min, where the largest rotor drag loss occurs, the average drop in efficiency for the measured points is approximately 2%.

**Figure 3.25** shows how the motor/generator power loss is divided into electromagnetic and rotor drag losses at 60,000 rev/min (part a) and 80,000 rev/min (part b). It can be noted that,

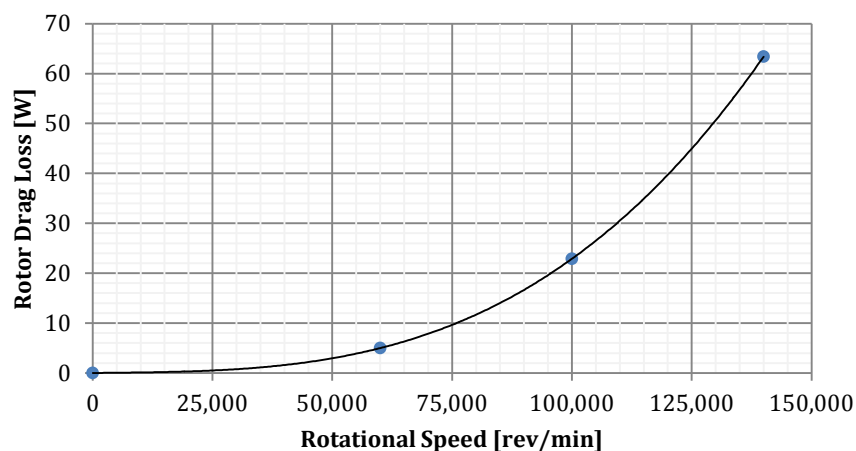


**Figure 3.24** - Results of the computational fluid dynamics analysis, showing the motor/generator rotor drag loss as a function of rotational speed. The error is +14.4%/-14.8% (non-symmetric)

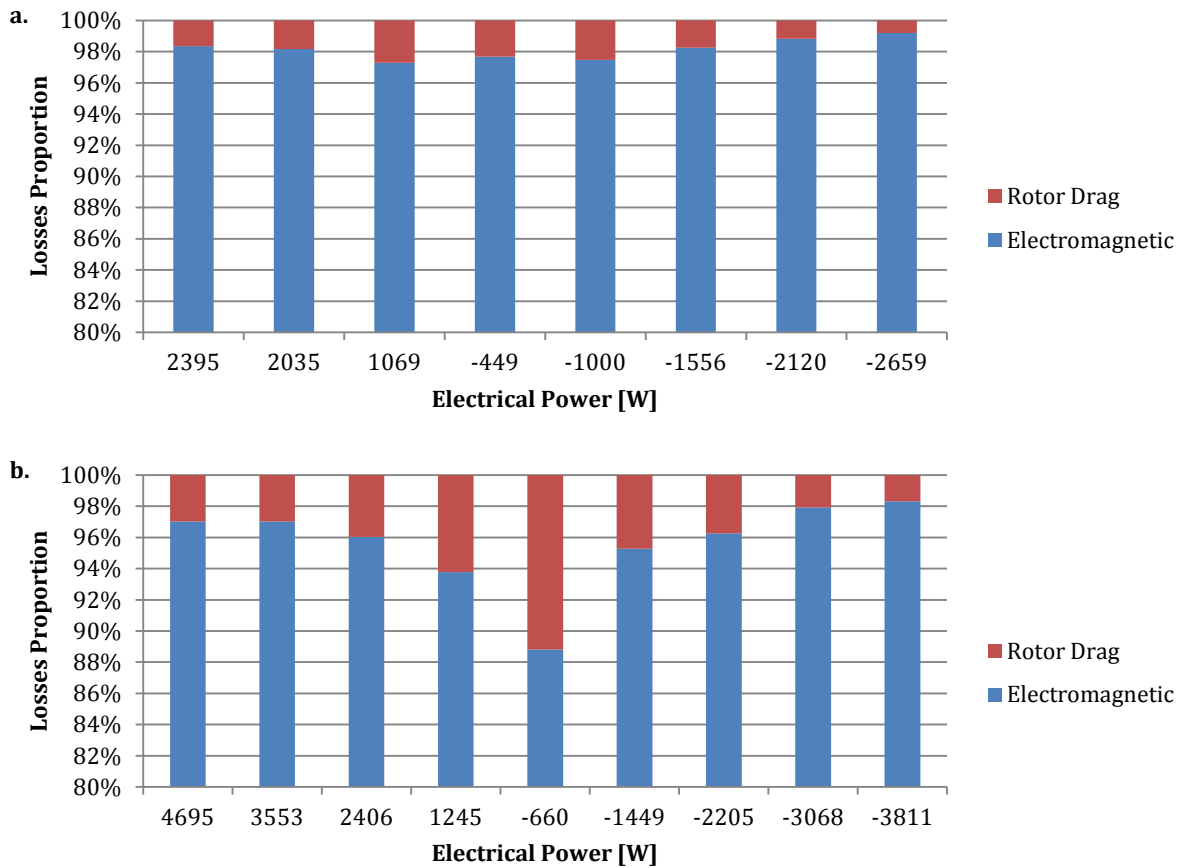


**Figure 3.25 – Rotor drag loss and electromagnetic losses proportions for Data Set 2. In part a the rotational speed is 60,000 rev/min, while in part b is 80,000 rev/min. Note that the vertical axis scale starts at 80%**

the rotor drag loss is always a small fraction of the total loss (vertical axis scale starts at 80%), but at low motor/generator powers it becomes more important. The reason for this latter observation is that the rotor drag losses are independent of machine power, while the electromagnetic losses increase with increasing electrical power. This figure also shows that the rotor drag loss is more dependent on the rotational speed than the electromagnetic losses, and therefore they become relatively more important as the turbocharger speed increases.

The reason for the low rotor drag losses is to be found in the small rotor diameter and the large air gap between the rotor and the stator. Ignoring the fact that the rotor has cut-outs and therefore is not circular, an equation which describes the drag on the rotor can be derived from the definition of viscosity, assuming a linear velocity gradient and no slip boundary conditions.

$$\tau = \mu \frac{\omega l_{rot} d_{rot}^3 \pi}{4h_{gap}} \tag{3.12}$$

This equations states that the drag is inversely proportional to the air gap height and proportional to the cube of the rotor diameter. However, a large air gap increases the reluctance of the magnetic path (Hughes, 2006) which results in a reduction of the inductance gradient.

According to **Equation 3.5**, this causes a lower maximum torque and, because the copper losses become relatively more important, lower efficiency. Consequently, the air gap height has to be optimized for efficiency within the limits imposed by torque requirements and manufacturing tolerances. The rotor diameter has to be minimized to minimize the moment of inertia and drag losses. However, a small rotor results in smaller arc lengths and, therefore, higher reluctance. This reduces the machine torque and efficiency in a similar way to a large air gap. Consequently, the rotor diameter also has to be optimized for efficiency within the constraints imposed by torque requirements and centrifugal stresses. In this geometry optimization the turbocharger duty cycle plays a fundamental role, since the rotor drag loss occurs whenever the turbocharger is running, while the electromagnetic losses occur only when the motor/generator windings are excited.

The uncertainty caused by the unknown boundaries temperatures and the uncertainty caused by the mesh limitations, estimated in **Section 3.2.1**, have been added together. The total error is approximately  $\pm 15\%$  and, although this error might seem large, the resulting motor/generator efficiency error in the worst case scenario is less than  $\pm 1\%$ . Moreover, a 10 W uncertainty is negligible when compared to the maximum engine power of 180 kW and the resulting engine efficiency error is also negligible. As a result, it is appropriate to estimate the rotor drag losses computationally.

The motor/generator maximum power shown in **Figure 3.26** and **Figure 3.27** is small when compared to the turbine power, which can reach approximately 50 kW. Despite this small power, this electrical machine is capable of improving engine transient response, as the majority of the turbine power is consumed by the compressor and only a small fraction is used to accelerate the turbocharger. In *Data Set 2* the maximum torque achieved is 0.54 Nm and, if all this torque is utilized to accelerate the turbocharger, it results in an angular acceleration of  $6500 \text{ rad/s}^2$ . According to the compressor map, this acceleration translates to a time to increase the boost pressure from 1.5 bar to 2.5 bar of less than 1 s. It is clear from this basic calculation that this motor/generator is suitable to improve turbocharged engine transient response. A detailed computational analysis of engine transient response, with and without electric turbocharger assistance, will be presented in **Chapter 6**.

The maximum generating power is only 3% of the engine maximum power and can only be achieved for a short period of time. As a consequence, this motor/generator is not capable of exploiting the full benefits of electric turbocompounding. If continuous turbocompounding is implemented, with the generating power limited to the maximum continuous power, the electrical machine would always be running at the maximum temperature and it would not be



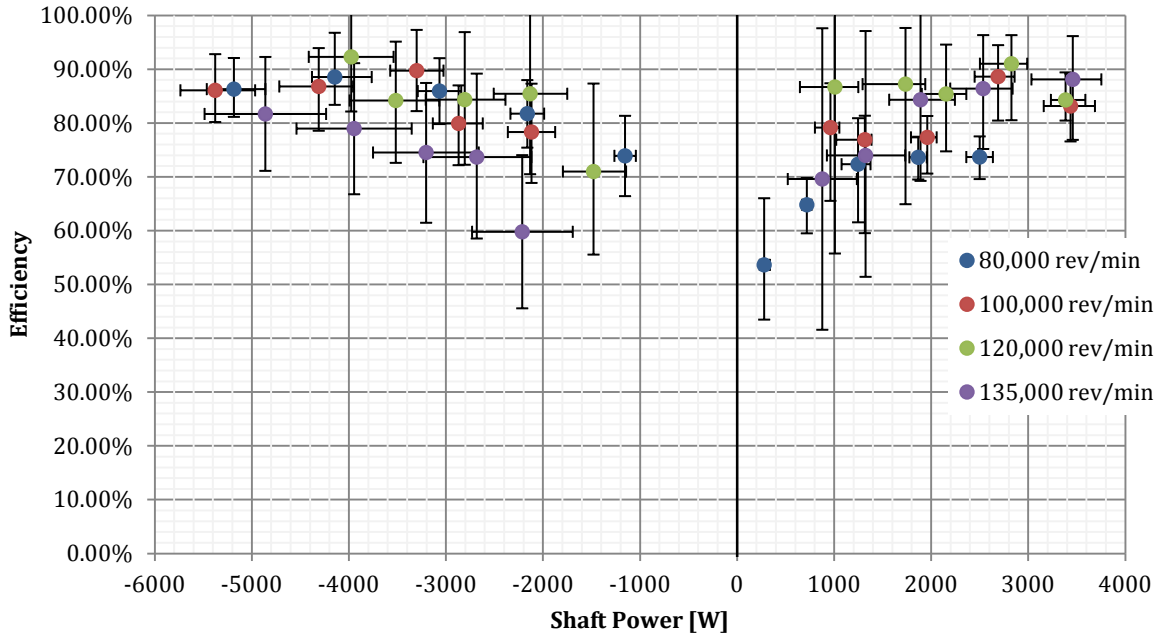


Figure 3.26 – Data Set 1 motor/generator efficiency plotted against shaft power output. Bearing losses not included

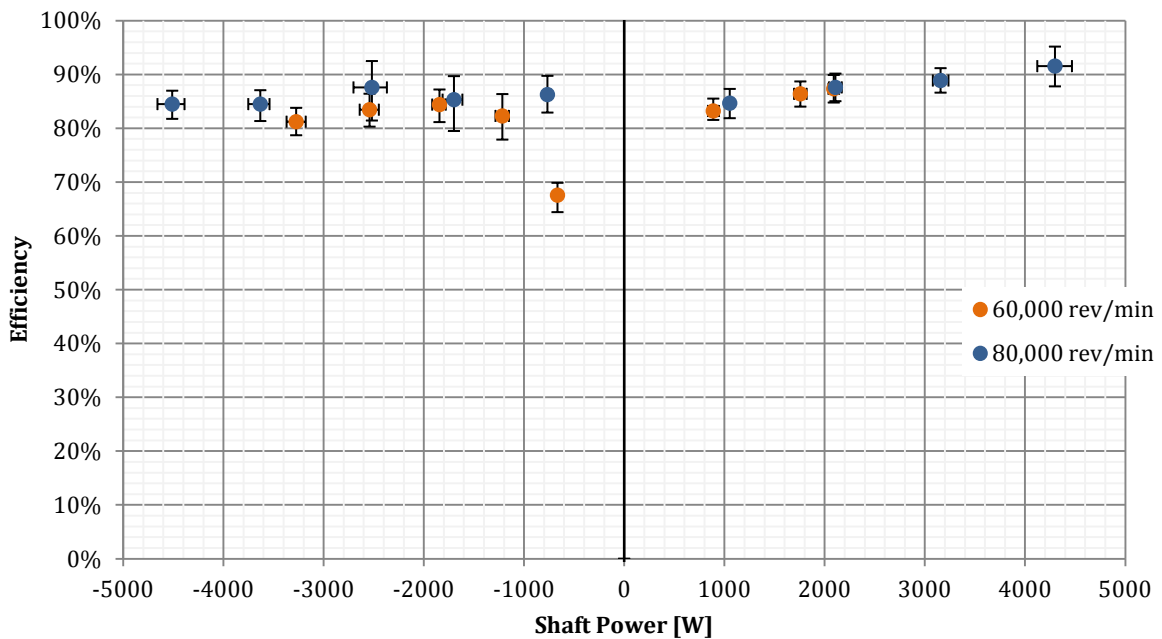


Figure 3.27 – Data Set 2 motor/generator efficiency plotted against shaft power output. Bearing losses not included

able to provide the maximum motoring power during engine transients. It is therefore clear that this motor/generator is not suitable for this scope. Nevertheless, this machine can be used to recuperate part of the turbocharger shaft kinetic energy by decelerating it when the engine load is decreased. A higher number of winding and a more effective cooling system would improve the maximum continuous power of this machine.

After obtaining *Data Set 1*, the motor/generator controller has been recalibrated aiming at achieving a maximum torque of 0.56 Nm, constant up to a speed of 80,000 rev/min, and a maximum power of 5300 W. In *Data Set 2* the maximum generating torque matched the requirements, while the motoring torque has increased, but it has not been possible to measure the maximum motoring torque due to the limited loading capabilities at low speeds. However, the maximum measured value is 0.51 Nm for an 80% torque demand and therefore it is likely that the maximum motoring torque requirement is achieved or exceeded. Although higher speeds could not be tested, it is safe to assume that the power requirements would also be met. This is justified by the fact that the power requirements have been met in generating mode in *Data Set 1* and because these requirements have been specified utilizing inductance data measured by the power electronics subcontractor during the inverter commissioning. Moreover, the maximum power is limited by the fact that the control algorithm is not designed to run in continuous current mode (phase currents never drop to 0 A), which means that the power is software limited rather than hardware limited.

The experimental methodology selected allowed to meet all the objectives stated at the beginning of the chapter. The test-rig has been successfully utilized to collect shaft torque, rotational speed, inverter current and voltage to characterize the motor/generator maximum torque and efficiency. This proved that the motor/generator is capable of efficiently producing torque up to a speed of 135,000 rev/min and that it is capable of running up to 140,000 rev/min. Moreover, this testing methodology also allows to characterize the turbocharger turbine as described in **Chapter 4**.

The work presented in this chapter is particularly important because it describes a novel experimental technique which allowed the testing of a fast switched reluctance motor/generator. Because no dynamometer capable of the required power and speed ratings is available, without this experimental technique it would have not been possible to tune the machine firing angles to obtain the required torque and efficiency compromise. Moreover, the efficiency data generated by this experiment is being utilized by *Loughborough University* in the electric assistance management system that they are developing. Finally this efficiency data will be utilized in the computational study presented in **Chapter 6**, where the electric assistance benefits in terms of engine transient response will be estimated.

### 3.3 CHAPTER SUMMARY

In this chapter a prototype of an electrically assisted turbocharger is tested by means of a novel experimental methodology to obtain the motor/generator power and efficiency characteristics. The machine has been first tested with non optimized control parameters and the data of this

first characterization has been utilized by the controller designer to tune the firing angles. The machine has been characterized a second time, with an improved torque measurement system, to obtain the efficiency characteristics with the optimized control parameters. Due to a vibration issue, in the second characterization it has not been possible to test the motor/generator up to the maximum speed. The motor/generator rotor drag loss has been estimated computationally via *Ansys CFX* because this testing methodology did not allow to separate this loss from the bearing losses.

All the objectives have been met and the main conclusions are:

- This motor/generator operates correctly up to a rotational speed of 140,000 rev/min
- The maximum torque achieved in motoring mode is 0.51 Nm and in generating mode is 0.54 Nm. However, the full motoring torque could not be measured due to limited loading capacity at low speeds and the maximum motoring torque is higher than 0.51 Nm.
- The maximum efficiency is 91.6% and has been achieved in motoring mode at 80,000 rev/min. In the second data set, where the firing angles are optimized, the efficiency is always greater than 80%, except for one point at low generating power
- The rotor drag loss is 63.4 W at 140,000 rev/min and is a small compared to the electromagnetic losses

## 4. STEADY STATE CHARACTERIZATION OF TURBINE

In this chapter, the turbocharger turbine mass flow rate and efficiency experimental characterization is described. The turbine performance has been characterized for three different vanes openings, over a total to static pressure ratio range of 1.00 to 1.96 and over an equivalent hot conditions (923 K) rotational speed range of 80,000 rev/min to 140,000 rev/min. To extrapolate the turbine maps to higher pressure ratios and lower rotational speeds, and to interpolate between tested vanes openings, a turbine mean-line model has been built.

### 4.1 EXPERIMENTAL TURBINE CHARACTERIZATION

#### 4.1.1 TURBOCHARGER TURBINE DESCRIPTION

The turbine of the electrically assisted turbocharger prototype is of the radial inflow type with a single entry. The flow enters the volute in the radial direction, passes through the nozzles and rotor, and exits in the axial direction. This turbine has variable geometry capabilities achieved by altering the angle of the vanes, and thus changing the rotor inlet incidence angle. The vanes are rigidly attached to pivots, which are rotated by an electrical actuator. The turbine wheel diameter is 63 mm.

#### 4.1.2 TURBINE CHARACTERIZATION OBJECTIVES

The turbine characteristics provided by the turbocharger manufacturer were measured on a hot gas stand utilizing the compressor as a loading device. The turbine power is obtained by measuring the change in enthalpy across the compressor and making the assumption that the



**Figure 4.1 - 3D drawing of the turbine tested. The volute has been cut to show the vanes and the rotor, which are coloured in red**

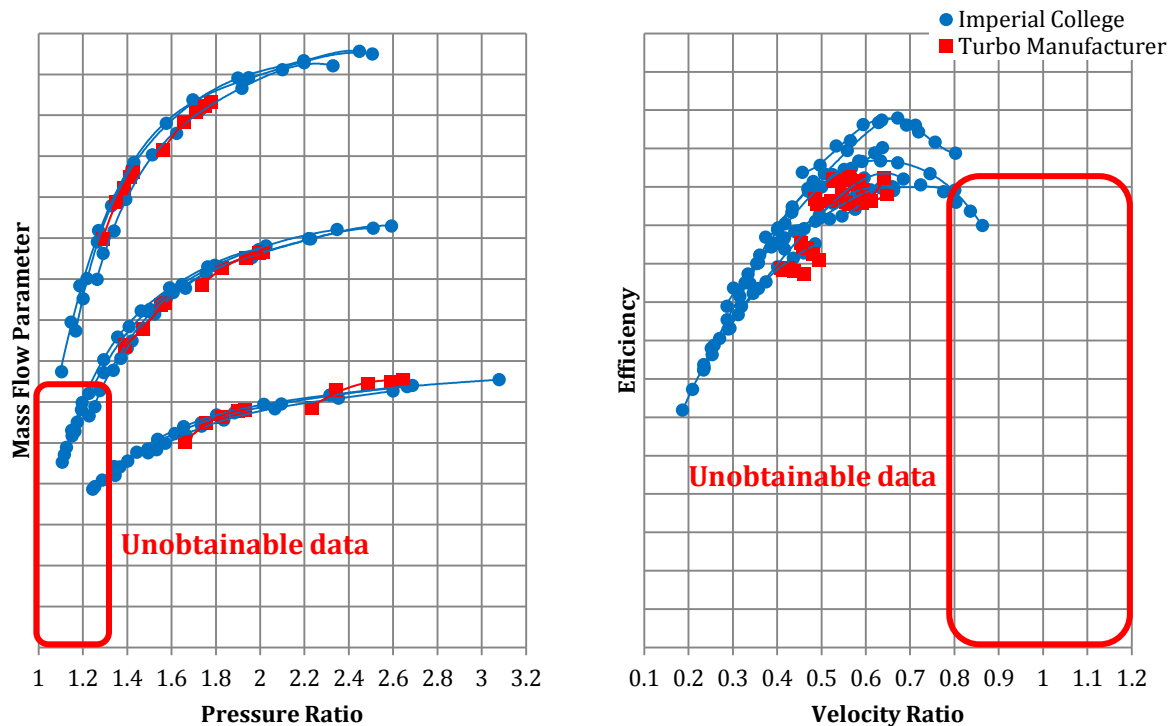


**Figure 4.2** - Typical turbine mass flow parameter and efficiency maps. The red lines represent the typical data obtained by testing the turbine on a hot gas stand utilizing the compressor as a loading device. The blue lines represent the typical data obtained with the Imperial College dynamometer. Even the Imperial College testing facility is not capable of characterizing the turbine down to zero mass flow rate

turbine and compressor power magnitudes are equal. This methodology has three major drawbacks. The most important of these issues is that the turbine maps produced cover a narrow pressure ratio range, due to the loading limitations imposed by compressor surge and choking. The second issue is that thermal and turbocharger bearing losses are included in the efficiency produced, hiding the true aerodynamic performance. The third drawback is that the bias and precision error of the efficiencies measured via this methodology are high, and the efficiency values are highly scattered. Typical turbine performance maps obtained via this testing methodology are shown in **Figure 4.2** (red lines).

An eddy current dynamometer, specifically designed to test turbocharger turbines, is available at *Imperial College London*. This dynamometer is capable of a wider loading range than the compressor, as it is not limited by surge or choking. In fact, it can extend the width of the turbine maps by up to five times, as shown in **Figure 4.2**. The turbine power is directly found by measuring the shaft torque and rotational speed, greatly reducing the scatter in the efficiency data. The torque measurement system is arranged so that the bearing losses are not included in the efficiency map. In addition, by testing the turbine in cold flow conditions, the thermal losses are also removed from the performance maps. More information on this dynamometer is provided by Szymko (2006).

Although this dynamometer greatly improves the turbine maps, it has two major negative aspects. The first problem is that the speed is limited to 63,000 rev/min, and, as a consequence, the full speed range of this turbine cannot be tested. The second issue is that, even when the load is set to a minimum, the turbine is always loaded by the bearings friction. In addition the dynamometer cannot motor the turbine, so that the speed cannot be maintained even with extremely low pressure ratios. This means that there is a region of the turbine maps that cannot be characterized. This region is at low pressure ratios (high velocity ratios) and is marked in **Figure 4.2**. These turbine operating conditions are expected to occur when the engine is at idle and the turbocharger is accelerated via the motor/generator. Very limited data or information on the turbine behaviour at these conditions has been published in the literature and, therefore, the turbine has to be experimentally characterized in this operating range.

The turbine characteristics need to be measured via an alternative methodology to produce improved and extended turbine maps. The following objectives have been set:

- Characterize the turbine mass flow rate and efficiency for different vanes openings
- Characterize and study the turbine behaviour at low pressure ratios and high rotational speeds

Due to the large number of possible VGT openings and rotational speeds combinations, it has been decided to limit the testing speed-lines to the following openings and speeds:

- Three VGT openings: 30%, 60% and 100%
- Four rotational speeds: equivalent to 80,000 rev/min, 100,000 rev/min, 120,000 rev/min and 140,000 rev/min in hot conditions (923 K)

#### *4.1.3 APPROACH TO MEET THE OBJECTIVES OF THE TURBINE CHARACTERIZATION*

To meet the objectives, the test-rig described in **Chapter 3**, which has been designed to characterize both the motor/generator and the turbine, is utilized. This test-rig can cover the full speed range of the turbine and can motor it to overcome the frictional and turbine losses, so that the required speed is maintained even with a pressure ratio of one. The only drawback of this solution is that the generating power is limited, resulting in low maximum pressure ratios. This issue is overcome by extrapolating the data via a mean-line model, described in the second part of this chapter.

#### *4.1.4 NON-DIMENSIONAL PARAMETERS*

The turbine operating conditions have been non-dimensionalized, so that the testing conditions can be related to the operating conditions via a similitude analysis. This is common practice in

the turbomachinery industry and is achieved through the Buckingham Pi theorem (Japikse and Baines, 1994). This theorem states that a relation between  $n$  parameters with  $m$  fundamental dimensions:

$$q_1 = f(q_2, q_3, \dots, q_n) \Rightarrow 0 = g(q_1, q_2, q_3, \dots, q_n) \quad (4.1)$$

Can be transformed to an equivalent relation between  $n-m$  independent dimensionless ratios (Fox, McDonald and Pritchard, 2004):

$$0 = G(\Pi_1, \Pi_2, \dots, \Pi_{n-m}) \quad (4.2)$$

The independent parameters which describe the flow in a turbocharger turbine can be collected in the following function:

$$0 = g(d_{rot}, N, \dot{m}, P_{0 in}, P_{out}, T_{0 in}, T_{0 out}, R, \gamma, \mu) \quad (4.3)$$

The dimensionless ratios resulting from the application of the Buckingham Pi theorem are:

$$\Pi_1 = \frac{T_{0 out}}{T_{0 in}} \quad (4.4)$$

$$\Pi_2 = \frac{\dot{m} \sqrt{RT_{0 in}}}{P_{0 in} d_{rot}^2} \quad (4.5)$$

$$\Pi_3 = \frac{P_{out}}{P_{0 in}} \quad (4.6)$$

$$\Pi_4 = \frac{N d_{rot}}{\sqrt{RT_{0 in}}} \quad (4.7)$$

$$\Pi_5 = \frac{\mu \sqrt{RT_{0 in}}}{d_{rot} P_{0 in}} \quad (4.8)$$

$$\Pi_6 = \gamma \quad (4.9)$$

$\Pi_1$  is the temperature ratio;  $\Pi_2$  is the dimensionless mass flow rate;  $\Pi_3$  is the inverse of the pressure ratio;  $\Pi_4$  is the dimensionless rotational speed and  $\Pi_6$  is the ratio of specific heats. It can be shown that the total to static efficiency is a function of the temperature ratio,  $\Pi_1$ , of the total to static pressure ratio,  $\Pi_3$ , and of the specific heats ratio,  $\Pi_6$ :

$$\eta_{ts} = \frac{\dot{W}}{\dot{W}_{is}} = \frac{T_{0 in} - T_{0 out}}{T_{0 in} - T_{is out}} = \frac{1 - \frac{T_{0 out}}{T_{0 in}}}{1 - \left(\frac{P_{out}}{P_{0 in}}\right)^{\frac{\gamma-1}{\gamma}}} = \frac{1 - \Pi_1}{1 - (\Pi_3)^{\frac{\Pi_6-1}{\Pi_6}}} \quad (4.10)$$

$\Pi_4$  can be divided by  $\Pi_5$  to obtain the turbine Reynolds's number:

$$Re = \frac{d_{rot} P_{0 in}}{\mu \sqrt{RT_{0 in}}} \frac{Nd_{rot}}{\sqrt{RT_{0 in}}} = \frac{\rho_{0 in} U_{rot} d_{rot}}{\mu} \quad (4.11)$$

In a turbocharger turbine, the efficiency and dimensionless mass flow are found to be a very weak function of the Reynolds number. In addition, it is impractical to match this parameter and its effects are ignored (Japikse and Baines, 1994). The effects of compressibility, which is a function of the specific heats ratio, are also weak, especially at low pressure ratios, and are ignored as well. The efficiency and dimensionless mass flow are considered to be only a function of the pressure ratio and dimensionless speed:

$$\eta_{ts} \approx F_1 \left( \frac{P_{0 in}}{P_{out}}, \frac{Nd_{rot}}{\sqrt{RT_{0 in}}} \right) \quad (4.12)$$

$$\frac{\dot{m} \sqrt{RT_{0 in}}}{P_{0 in} d_{rot}^2} \approx F_2 \left( \frac{P_{0 in}}{P_{out}}, \frac{Nd_{rot}}{\sqrt{RT_{0 in}}} \right) \quad (4.13)$$

Automotive turbocharger turbines are usually tested with no geometry scaling. Fresh and combusted air have a very similar molar mass and, as a result, a very similar gas constant. For these reasons, the non-dimensional mass flow and speed are usually simplified to the dimensional mass flow and speed parameters:

$$MFP = \frac{\dot{m} \sqrt{T_{0 in}}}{P_{0 in}} \quad (4.14)$$

$$SP = \frac{N}{\sqrt{T_{0 in}}} \quad (4.15)$$

The isentropic efficiency is not often plotted as a function of pressure ratio, but as a function of velocity ratio. The velocity ratio is the ratio between the blade tip speed (at the rotor inlet) and the isentropic velocity, which is the velocity achieved in an adiabatic nozzle with a pressure ratio identical to the turbine pressure ratio.

$$VR = \frac{U_{rot}}{C_{is}} = \frac{Nd_{rot}\pi}{\sqrt{2c_p T_{0 in} \left[ 1 - \left( \frac{P_{out}}{P_{0 in}} \right)^{\frac{\gamma-1}{\gamma}} \right]}} = \frac{\Pi_4 \pi}{\sqrt{2 \frac{\Pi_6}{\Pi_6^{-1}} \left[ 1 - (\Pi_3)^{\frac{\Pi_6-1}{\Pi_6}} \right]}} \quad (4.16)$$

By plotting **Equation 4.16**, it can be seen that the velocity ratio is a very weak function of the specific heats ratio and the change caused by the difference in specific heats ratio between fresh and combusted air is negligible. Consequently:

$$\eta_{ts} \approx F_3 \left( \frac{U_{rot}}{C_{is}}, \frac{Nd_{rot}}{\sqrt{RT_{0 in}}} \right) \quad (4.17)$$



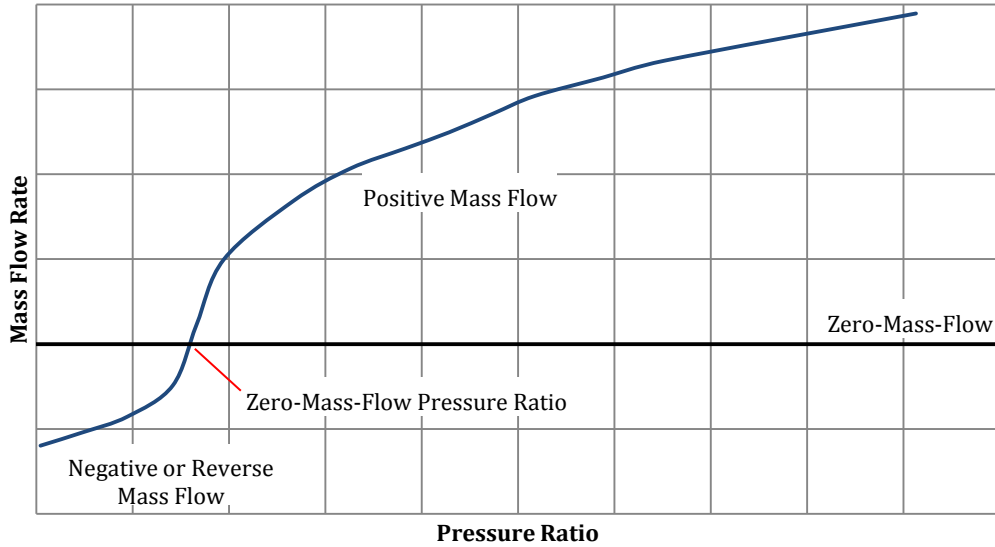


**Figure 4.3 – Expected turbine mass flow rate results**

The turbine studied in this thesis is a variable geometry type. However, this analysis assumes geometric similarity and therefore the nozzles effective area is not included in the analysis. This variable affects both the non-dimensional mass flow and the efficiency, therefore it cannot be neglected. This issue is dealt with by mapping turbine performance at fixed nozzles positions, i.e. the mapping procedure is repeated for each desired vanes opening.

Reverse mass flow is expected to occur at low pressure ratios due to the centrifugal head within the turbine wheel, as it is shown in **Figure 4.3**. In these conditions the turbine is effectively acting as a compressor. Consequently, the turbine performance parameters change to the compressor performance parameters:

$$SP_{rev} = \frac{N}{\sqrt{T_{0 out}}} \quad (4.18)$$

$$PR_{tt rev} = \frac{P_{0 in}}{P_{0 out}} \quad (4.19)$$

$$MFP_{rev} = -\frac{\dot{m}\sqrt{T_{0 out}}}{P_{0 out}} \quad (4.20)$$

$$\eta_{tt rev} = \frac{\dot{W}_{is}}{\dot{W}} = \frac{T_{0 is in} - T_{0 out}}{T_{0 in} - T_{0 out}} \quad (4.21)$$

Note that the subscripts *in* and *out* still refer to the inlet and outlet of the turbine. The velocity ratio is not shown because the turbine cannot be compared to a nozzle when reverse mass flow occurs, since the turbine is not expanding the flow, but compressing it.

#### 4.1.5 VELOCITY TRIANGLES

It is common practice to analyze the turbine flow in terms of velocity triangles. The velocity triangles are triangles formed by the absolute velocity vector,  $C$ , the relative velocity vector,  $W$ , and the rotor velocity vector,  $U$ , at different locations within the turbine. The relative velocity is the flow velocity relative to the rotor velocity.  $\alpha$  is the angle between the absolute velocity vector and the radial/axial direction.  $\beta$  is the angle between the relative velocity vector and the radial/axial direction. **Figure 4.4** shows typical velocity triangles for a radial turbine. The sign convention is that the velocities and angles which are in the same direction of the rotor velocity are positive. For example, the  $\beta$  angle at the rotor outlet shown in **Figure 4.4** is negative.

#### 4.1.6 TURBINE CHARACTERIZATION METHODOLOGY

The idea behind this experiment is to obtain the mass flow rate parameter and total to static efficiency as a function of the speed parameter, pressure ratio and vanes opening (in the case of efficiency, also as a function of velocity ratio). To achieve this, the variables required to calculate these derived parameters have to be measured over a range of turbine loading and speed

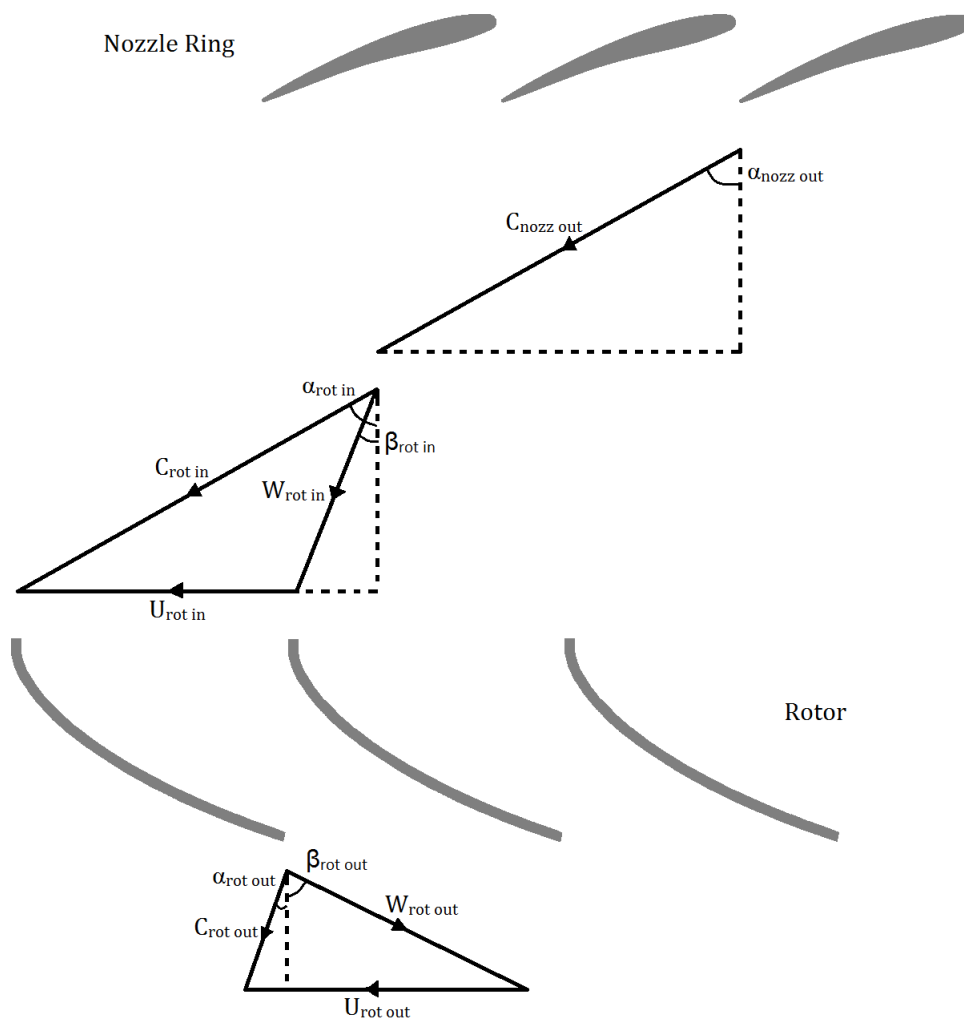


**Figure 4.4 – Typical velocity triangles for a radial turbine**

### Generating Mode

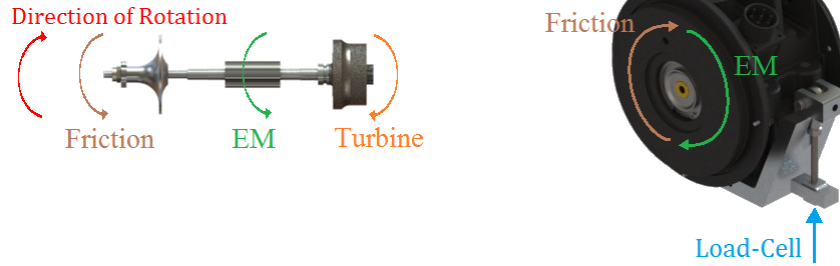


**Figure 4.5 – Free body diagrams of the modified turbocharger rotor and bearing housing showing the moments and forces that occur during testing. The electrical machine torque is shown in the generating direction**

conditions and over a number of vanes openings. According to the equations derived in **Section 4.1.4**, these variables are the steady state mass flow rate, the inlet and outlet temperature, the inlet and outlet pressure, and the rotational speed. However, in this experiment the efficiency is obtained by calculating the actual work via the turbine torque rather than via the temperature ratio, as shown in **Equation 4.22**. As a result, the turbine torque is measured instead of the outlet temperature.

$$\eta_{ts} = \frac{\dot{W}}{\dot{W}_{is}} = \frac{\omega\tau}{\dot{m}c_p T_{0in} \left[ 1 - \left( \frac{P_{out}}{P_{oin}} \right)^{\frac{\gamma-1}{\gamma}} \right]} \quad (4.22)$$

The turbine torque is measured by means of the gimbal system described in **Chapter 3**. As it can be seen from **Figure 4.5**, the moments caused by the motor/generator and the frictional load are reacted via the load-cell. As a consequence, the force measured by the load-cell is equal to the total moment divided by the normal distance between the load-cell sensing axis and the gimbal system axis. **Figure 4.5** also shows that the sum of the friction and motor/generator moments is equal to the turbine torque. Therefore, the turbine torque is proportional to the load-cell output, as demonstrated by **Equation 4.23**.

$$\tau_{turb} = \tau_{frict} + \tau_{EM} = rF_{LC} \quad (4.23)$$

The novelty in this experimental technique is that the electrical machine is not only used to load the turbine, but is also utilized to motor it. This allows to extend the performance maps down to a pressure ratio of one by progressively shifting the turbine operating conditions to the following map regions:

1. The region where the turbine power is positive, but of a lower magnitude than the power consumed by the bearing housing (or dynamometer) frictional losses

2. The region where the turbine power is negative because its losses are larger than the power extracted from the flow
3. The region where the turbine flow is reversed and the turbine operates as a low efficiency compressor

#### 4.1.7 VANES SETTINGS

Since the VGT mechanism of this turbine allows an infinite number of vanes openings, it has been decided to map turbine performance for only three different openings. These selected openings correspond to 100%, 60% and 30% of the nozzles effective flow area when the mechanism is set to the fully open position. The effective flow area is given by:

$$A_{nozz} = 2\pi r_{nozz\ out} h_{nozz} \cos(\alpha_{nozz\ out}) \quad (4.24)$$

In the equation above,  $r_{nozz\ out}$  is the radial distance between the turbocharger rotor axis and the trailing edge of the nozzles,  $h_{nozz}$  is the height of the nozzles and  $\alpha_{nozz\ out}$  is the nozzles exit flow angle as given in **Figure 4.4**.

Since the nozzles actuation mechanism had to be removed to insert the gimbal bearings, three different nozzle rings have been manufactured by welding the nozzles in position. To ensure accurate and uniform vanes openings, a jig has been utilized to fix the nozzles in place. The nozzles pivots have then been welded to the supporting rings, in such a way that no welding material protruded in the flow area.

#### 4.1.8 TURBINE CHARACTERIZATION TEST-RIG LAYOUT

The rig layout, instrumentation and data-logging system are identical to the motor/generator testing and are described in **Chapter 3**. The main components of the rig are the modified turbocharger, the oil cart to lubricate and cool the turbocharger, the active rectifier to provide power to the motor/generator or return power to the national grid, and the air heater and valves to control the turbine flow.

The only modification to the test-rig is the addition of a turbine exit duct. This duct has an internal diameter of 69.8 mm, which is equal to the volute exit duct diameter, and a length of 810 mm. The scope of this duct is to guide the flow exiting the turbine, so that the static exit pressure can be measured.

#### 4.1.9 TURBINE CHARACTERIZATION MEASUREMENTS

##### **Shaft Torque and Rotational Speed Measurements**

The shaft torque is measured via the gimbal mechanism described in the *Data-Set 2 Gimbal Arrangement* part of **Section 3.1.7**. With this arrangement the gimbal system is sealed via a

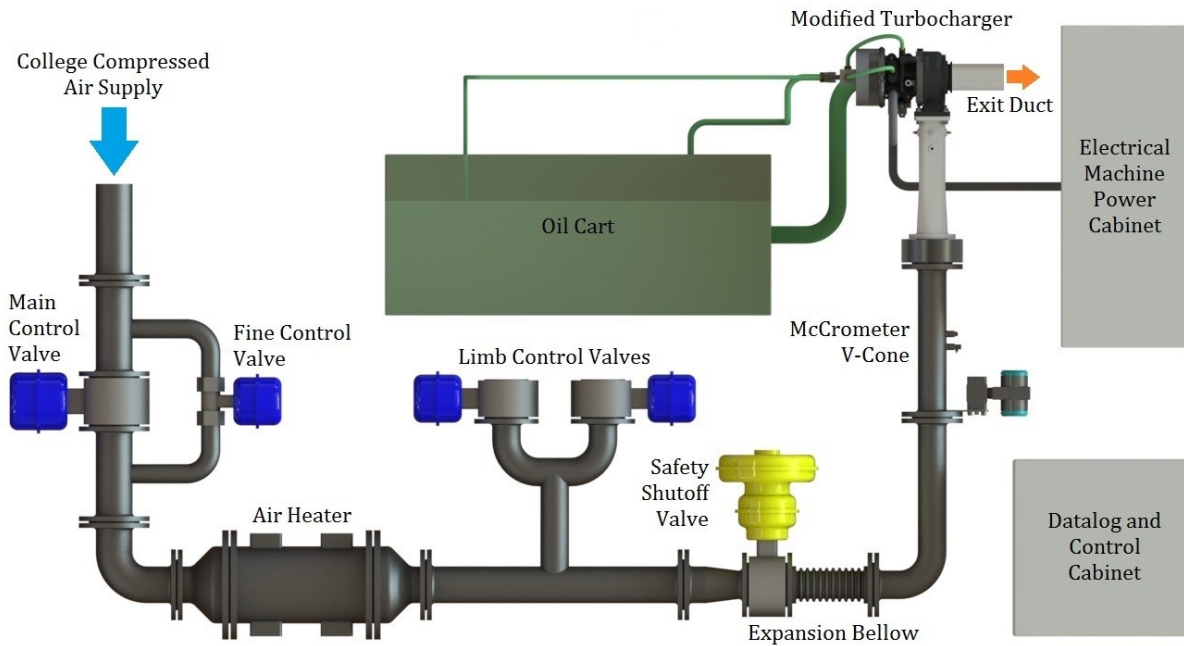


**Figure 4.6 – Representation of the turbine test-rig showing the principal components and how they are arranged**

labyrinth seal and therefore the seal does not constrain the rotation of the bearing housing. The drawback is that a small air leakage occurs and this has to be taken in account when the bias error is calculated. The rotational speed is measured via a *Hall Effect* sensor and a slotted wheel attached to the turbocharger shaft.

### **Air Temperature Measurements**

The turbine inlet and outlet air temperatures are measured by means of mineral insulated stainless steel thermocouples with a diameter of 1.5 mm. The thermocouples cross perpendicularly the flow and the tip is placed at the centre of the respective ducts. The position of the thermocouples relative to the turbine housing is shown in **Figure 4.7**. The inlet thermocouple is of the K-type, while the outlet thermocouple is of the T-type. The K-type thermocouple is suitable to measure temperatures up to 1100° C and has an accuracy of  $\pm 1.5^\circ$  C. The T-type thermocouple is suitable to measure temperatures up to 400° C and has an accuracy of  $\pm 0.5^\circ$  C. The thermocouples did not require calibration.

Because the thermocouples protrude in the flow and interact with it, the temperature they measure is neither the stagnation nor the static temperature, and is known as the recovery temperature. This temperature is related to the stagnation and static temperatures via a recovery factor, described by Hakeem and Khezzar (1994).

$$T_{meas} = T + r(T_0 - T) \quad (4.25)$$

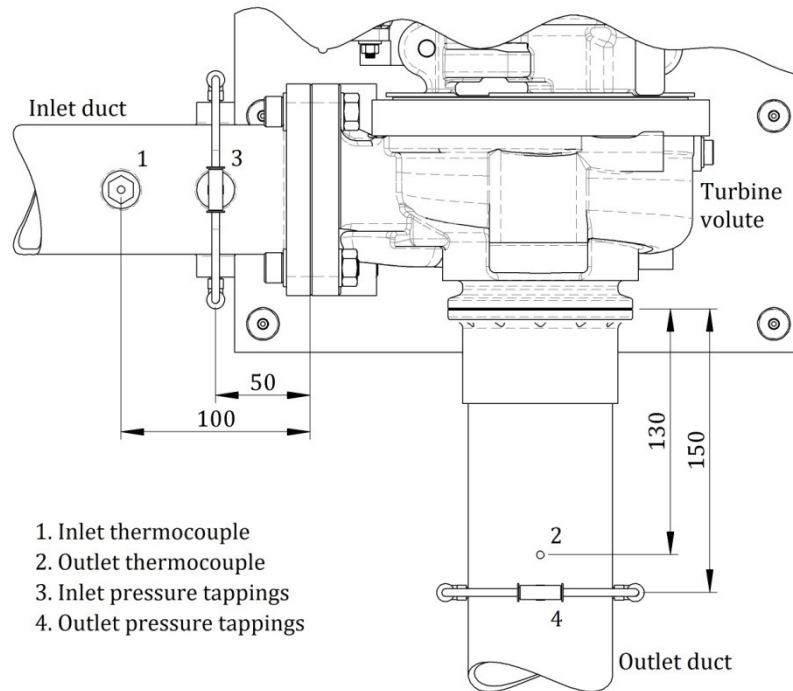


**Figure 4.7 - Location of the inlet and outlet pressure tapplings and thermocouples relative to the turbine housing for the steady state turbine test**

The recovery factor for thermocouples identical to the thermocouples utilized in this experiment has been measured, as a function of the Mach number, by Szymko (2006). For this reason, the measurement has not been repeated, and the same recovery factor function has been applied to the temperature data collected in this experiment. Below 0.2 Mach number, a fixed recovery factor of 0.8 is applied. This corresponds to the recovery factor measured by Szymko at 0.2 Mach number. Below this Mach number, the difference between the static and stagnation temperatures is small, resulting in highly scattered recovery factor data. As it will be seen in the *Uncertainty Analysis* part of **Section 4.1.11**, the error resulting from this approximation is significantly less than the thermocouple measurement uncertainty.

### **Air Pressure Measurements**

The turbine inlet and outlet air static pressures are measured with a *ScaniValve DSA3016/8D* pressure measurement module mounted in a *DSAENCL4000* enclosure. The *DSA3016/8D* contains eight temperature compensated piezoresistive pressure sensors and is factory calibrated. It has a range of 0 to 7 bar and an accuracy of 0.05% of the full scale reading. The enclosure contains a data-logger with a 16 bit analogue to digital converter and communicates the pressure values, in engineering units, directly to the control computer.

The static pressure is measured by drilling four 3 mm diameter holes equally spaced around the circumference of the duct. These four pressure tapplings are connected together via an annular chamber formed by 4 mm OD polyurethane tubes joined together by T-shape junctions. The

same polyurethane tubing is utilized to connect the two annular chambers to their respective sensor. The exact positioning of the pressure tapings is shown in **Figure 4.7**.

The inlet pressure tapings are positioned upstream of the volume entrance to avoid the disturbances generated by the imperfect duct and volute alignment. These disturbances would affect the pressure measurement and generate an error. The distance between the pressure tapings and the volute entrance has been set so that it is approximately 50 times the size of the duct misalignment.

For the same reason, the outlet pressure tapings have been drilled downstream of the volute exit. In this case the disturbances are caused by the shape and rotation of the turbine wheel. The distance between the wheel nose and the pressure tapings has been set to 2.7 times the rotor exit tip diameter and about 7.5 times the wheel nose diameter.

### Air Mass Flow Measurements

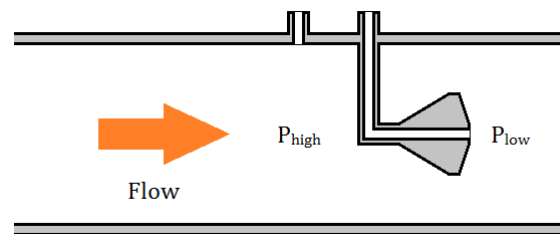


**Figure 4.8 - McCrometer V-Cone schematic**

The turbine air mass flow rate is measured via a 3" ID *McCrometer V-Cone* placed 460 mm upstream of the turbine inlet. The *V-Cone* is a differential pressure flow meter and it consists of a cone positioned at the centre of the pipe with the tip facing the flow. The static pressure is measured both ahead of the cone and at the back face of the cone. The difference between the two pressures can be correlated to the mass flow via the following equation (McCrometer Inc., 2011):

$$\dot{m} = C_d k_1 \left[ 1 + 2\alpha \left( \frac{9}{5} T - 527.67 \right) \right] \left[ 1 - \left( 0.649 + 0.696 k_2^4 \right) \frac{\Delta P 10^{-3}}{\gamma P} \right] \sqrt{\Delta P 348.338 \frac{S_g P}{Z T}} \quad (4.26)$$

In this equation  $C_d$  is a discharge coefficient,  $k_1$  and  $\beta$  are constants which describe the device geometry,  $\alpha$  is the material thermal expansion coefficient,  $S_g$  is the gas specific gravity, and  $Z$  is the gas compressibility.  $C_d$ ,  $k_1$  and  $\beta$  are provided by the manufacturer.  $T$  is the temperature of the flow entering the *V-Cone* and has to be measured at the device inlet.  $P$  is the static pressure ahead of the cone and  $\Delta P$  is the difference between  $P$  and the pressure on the back face of the cone.

The cone is designed to straighten the flow, so that the flow entering the device does not need to be fully developed. For this reason, the *V-Cone* requires only two pipe diameters (150 mm) length of straight duct upstream and one diameter (75 mm) downstream. This is a clear advantage over orifice plates, which typically require at least ten pipe diameters length of straight pipe upstream. Moreover, the cone also straightens the flow downstream of the device, improving the quality of the flow entering the turbine.

The *V-Cone* is calibrated by the manufacturer. It has an accuracy of  $\pm 0.5\%$  of the reading and a repeatability of  $\pm 0.1\%$  of the reading. The relationship described by **Equation 4.26** is valid down to a Reynolds number of 8,000, which corresponds to a mass flow rate of approximately 10 g/s for this turbine and *V-Cone* size combination. Special calibration is required for lower mass flow rates.

The differential pressure is measured via a *Siemens Sitrans P DS III* differential pressure transmitter, which has a range of 0 to 60 mbar. This sensor has been calibrated by means of a *Druck DPI 610* pressure calibrator and it has been found to have an accuracy of  $\pm 0.3$  mbar ( $\pm 0.5\%$  of full scale). At high mass flow rates, above 170 g/s, the differential pressure is measured via the *ScaniValve*. The static pressure ahead of the cone is always measured via the *ScaniValve*.

The temperature is measured via a K-type thermocouple identical to the one utilized to measure the turbine inlet temperature. Due to the low Mach number and the low *V-Cone* reading sensitivity to temperature, the recovery effects are neglected and the measured temperature is assumed to be the stagnation temperature.

### **Ambient Conditions**

The ambient pressure is measured by means of a *Vaisala PTB110* barometer positioned at the centre of the test-cell, away from the turbine outlet and test-cell extraction system. This barometer has a range of 800 to 1100 mbar and an accuracy of  $\pm 0.3$  mbar. It has a 0 to 5 V voltage output and is connected to the *NI cDAQ* data-logger. No calibration has been necessary as the device is calibrated at the factory. The ambient temperature is measured by means of a K-type thermocouple.

### **Other Measurements**

Other quantities have been measured with the sole purpose of detecting faults in the system. The oil cart operation has been monitored by measuring the oil temperature at different locations in the circuits, the mass flow rates of both the cooling and lubricating oil streams and the pressures at the cart outlets. The turbocharger bearings have been monitored by measuring



the vibrations of the bearing housing. The operation of the motor/generator has been monitored by measuring the windings temperatures and the DC link voltage and current. Details on these measurements and the test-rig safety system can be found in **Chapter 3**.

#### 4.1.10 TURBINE CHARACTERIZATION PROCEDURE

The experimental procedure can be divided in two parts. The first part consists of the test-rig preparation procedure and has to be repeated every time a new test session begins. The second part consists of the data collection procedure.

When a new test session begins, the rig oil system has to be warmed-up. This is achieved by circulating the oil in the system, without running the turbocharger. The lubrication oil heating circuit controller is set to maintain 50° C. Once all the oil and motor/generator temperature readings have stabilized, the torque measurement system is calibrated following the procedure outlined in **Chapter 3**. The final step in the rig preparation consists of the air heater and pipes warm-up, which is achieved by running air through the turbine with the air heater on. The air flow is set so that the turbocharger speed does not exceed 30,000 rev/min, and the air temperature is maintained at 60° C by the heater controller.

After the test-rig preparation is completed, the turbine performance data can be collected through the following procedure:

1. The desired turbine speed parameter and loading conditions are reached by gradually opening the air control valves and/or energizing the motor/generator
2. When the turbine inlet air temperature and rotational speed stabilize to the desired value, the sensors outputs are logged
3. The turbocharger rotor is rapidly stopped by cutting the air flow and electrical power
4. The load-cell zero offset is logged as soon as the turbocharger rotor stops

This procedure is repeated three times for each point on the turbine maps and the quantities obtained are averaged. The order in which the data is collected is changed in a random manner

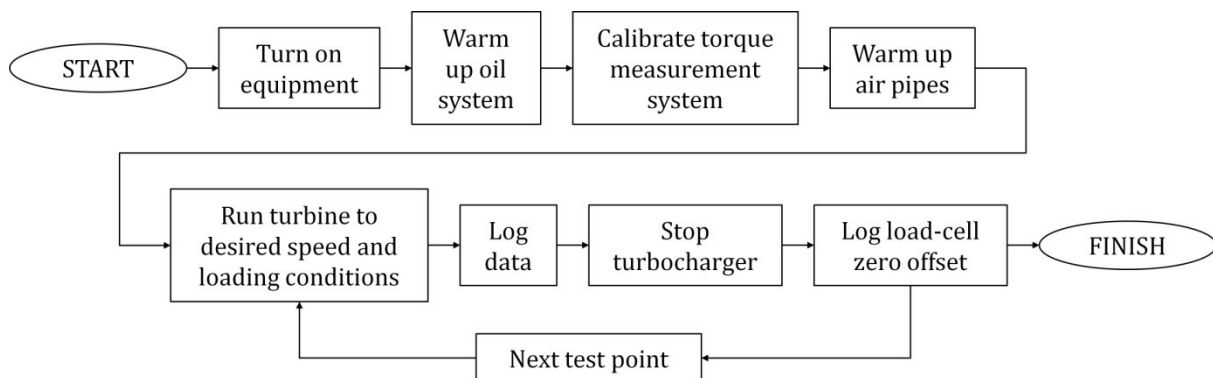


**Figure 4.9 – Steady state turbine testing procedure flowchart**

to observe if it affects the data. No correlation between turbine performance and data collection order has been found, proving that the bias is either small or it does not vary with time.

The load-cell zero offset is recorded after logging the performance data since it has been found to vary with the turbocharger support and load-cell arm temperatures. If the load-cell zero offset is measured a few seconds (typically < 10 s) after the performance data is logged, the rig thermal conditions are approximately the same as when the data is logged, and the load-cell offset is correct. A small error still occurs as the thermal conditions are not exactly identical, and this is taken into account in the uncertainty analysis.

Because the *V-Cone* can measure mass flow only in one direction, at low pressure ratios the device is reinstalled in the reverse direction to measure negative mass flow rate. In these operating conditions, the flow is controlled by adjusting a valve which lets the air escape back into the test-cell. The turbocharger rotational speed is controlled by adjusting the electrical machine motoring power.

#### *4.1.11 TURBINE CHARACTERIZATION RESULTS AND DISCUSSION*

In this section the steady state turbine characterisation results are shown. To make the discussion easier to follow, the data is presented in three subsequent stages. In the first stage, only one speed-line is presented (3292 rev/min/ $\sqrt{K}$  speed parameter and 60% VGT opening) and the mass flow and efficiency trends with pressure ratio are discussed. In the second stage, the other speed-lines of the 60% VGT opening are shown and the effects of rotational speed are discussed. In the last stage, the full data set is presented and the impact of VGT on turbine performance is discussed.

#### **Impact of Pressure Ratio on Turbine Performance**

The mass flow parameter and total to static efficiency curves for a speed parameter of 3292 rev/min/ $\sqrt{K}$  and a VGT opening of 60% are shown in **Figure 4.10** and **Figure 4.11**. By observing these figures, the following comments can be made:

- The mass flow parameter increases with increasing pressure ratio
- The mass flow parameter line crosses the abscissa at a pressure ratio which is higher than one. Below this critical pressure ratio, reverse mass flow occurs
- The efficiency drops rapidly with increasing velocity ratio and, above a critical value, it becomes negative
- The efficiency drops in an asymptotic manner (asymptote parallel to the ordinate)

The mass flow parameter trend in the positive mass flow portion of **Figure 4.10** is always observed in turbine performance maps. The mass flow rate parameter increases with pressure

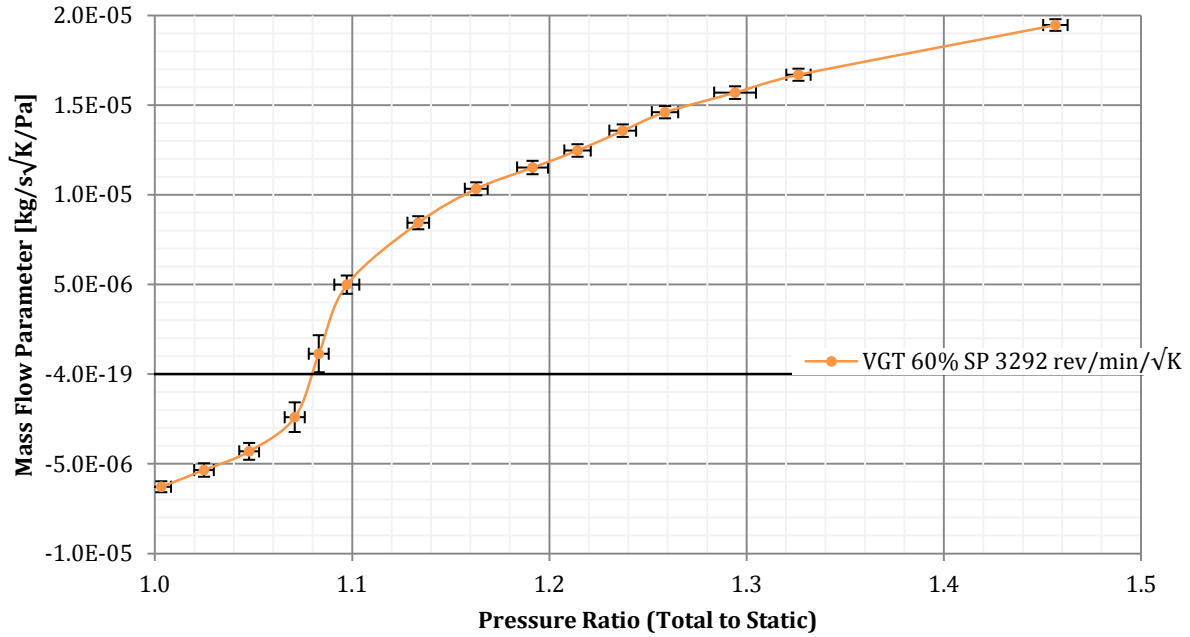


Figure 4.10 – Collected turbine mass flow data. Showing only one speed-line of the 60% VGT opening. The mass flow parameter definition is given by Equation 4.14, the pressure ratio definition is given by Equation 4.6 and the speed parameter definition is given by Equation 4.15

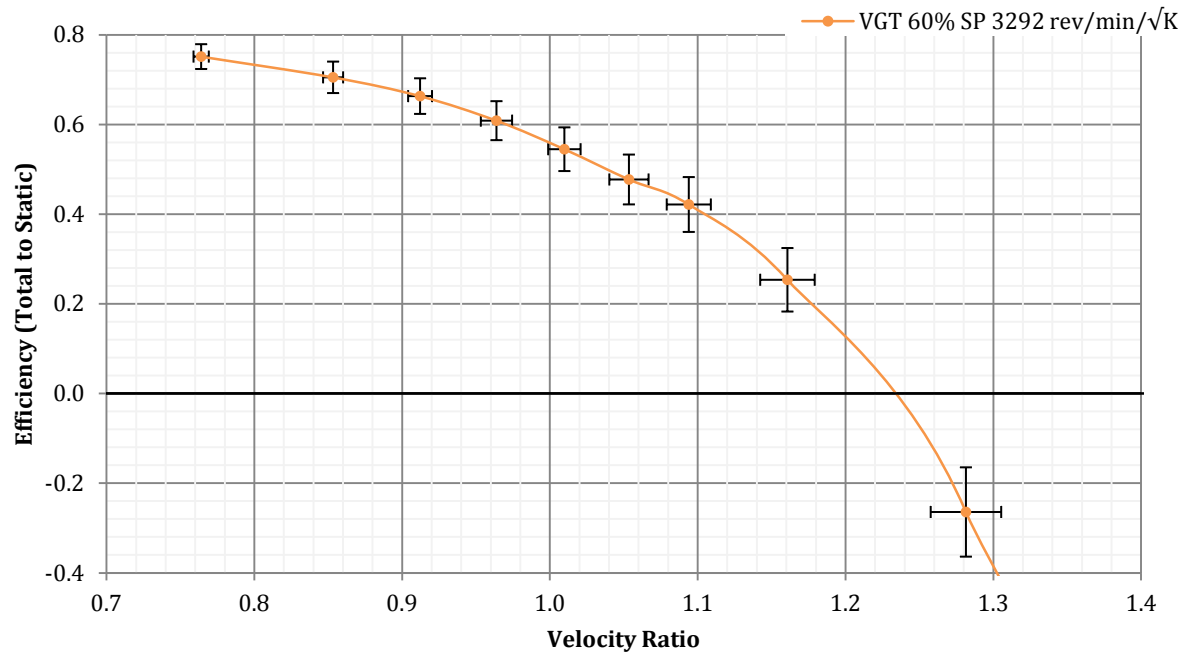


Figure 4.11 – Collected turbine total to static efficiency data. Showing only one speed-line of the 60% VGT opening. The total to static efficiency definition is given by Equation 4.10, the velocity ratio definition is given by Equation 4.16 and the speed parameter definition is given by Equation 4.15

ratio, since a greater pressure ratio causes a greater change in momentum. This results in a higher flow speed and hence a higher mass flow rate.

The fact that the mass flow parameter drops to zero at a pressure ratio which is higher than one, and that reverse mass flow occurs below this pressure ratio are the key findings of this

experiment. The cause of these effects is the centrifugal head generated by the rotation of the working fluid around the turbocharger axis. Because the working fluid has a finite mass, to achieve the centripetal acceleration a force is required, and this is provided by a pressure gradient in the radial direction. If the pressure ratio is less than the zero-mass-flow critical value, the centripetal force acting on the mass inside the rotor passages has a lower magnitude than the centrifugal body force. This force imbalance causes reverse mass flow, which is observed in **Figure 4.10** and **Figure 4.12**.

An equation to estimate the zero-mass-flow pressure ratio can be derived by considering the force balance on a rotating fluid element in polar coordinates. This analysis results in the following relationship between pressure and the radius of rotation:

$$\frac{dP}{dr} = Pr \frac{\omega^2}{RT} \quad (4.27)$$

If **Equation 4.27** is integrated between the rotor blades outlet tip radius and the nozzles trailing edge radius, assuming a forced vortex with a rotational velocity equal to the rotor velocity and no mass flowing through the turbine, the following equation can be obtained:

$$\frac{P_{0 in}}{P_{out}} \approx \frac{P_{nozz out}}{P_{rot out}} \approx \exp\left(\frac{\omega^2 (r_{nozz out}^2 - r_{rot out tip}^2)}{2RT}\right) \quad (4.28)$$

For this turbine geometry, **Equation 4.28** predicts a pressure ratio value of 1.12, which is similar to the measured value, 1.08, but they are not perfectly equal. The main reason for the difference is that the vortex is a forced vortex only within the rotor passages, and not in the stator-rotor gap. **Equation 4.28** is effectively assuming that the tangential velocity at the nozzles outlet is equal to the wheel rotational speed multiplied by the normal distance between the turbocharger shaft axis and the nozzles trailing edge (i.e. nozzles outlet radius), but the actual tangential velocity would be lower than that due to friction. As a result, the pressure ratio is overestimated.

**Equation 4.28** is important because it proves that the zero-mass-flow pressure ratio does not depend on the testing conditions. By observing this equation, it can be seen that the pressure ratio is only a function of the dimensionless rotational speed,  $\omega/\sqrt{RT}$ , and the turbine geometry. Consequently, if the turbine was tested in hot conditions, the zero-mass-flow pressure ratio value measured would be the same as the value measured in this experiment.

The reason why the efficiency drops to negative values with increasing velocity ratio can be understood by observing the *Euler Turbomachinery Equation* (**Equation 4.29**). This relationship

states that the specific work increases as the flow tangential velocity difference between the rotor inlet and the rotor outlet increases (refer to **Figure 4.4**).

$$w = U_{in}C_{\theta in} - U_{out}C_{\theta out} = \omega(r_{in}C_{\theta in} - r_{out}C_{\theta out}) \quad (4.29)$$

The velocity ratio is the ratio between the blade speed and the flow velocity at the throat of an isentropic nozzle which has the same pressure ratio as the turbine. For the purpose of this explanation, the velocity ratio can be assimilated to a ratio between the blade velocity and the flow velocity:

$$VR = \frac{U_{rot in}}{C_{is}} = \frac{Nd_{rot in}\pi}{\sqrt{2c_p T_{in} \left[ 1 - \left( \frac{P_{out}}{P_{in}} \right)^{\frac{\gamma-1}{\gamma}} \right]}} \sim \frac{\text{Blade velocity}}{\text{Flow velocity}} \quad (4.30)$$

If the blade velocity is maintained constant and the velocity ratio is increased by decreasing the pressure ratio, the rotor inlet tangential velocity, which is given by **Equation 4.31**, would drop. This is because the tangential velocity is proportional to the total velocity, as the nozzle angle for a given VGT position is fixed (refer to **Figure 4.4**).

$$C_{\theta rot in} = C_{rot in} \sin \alpha_{nozz out} \quad (4.31)$$

As the rotor inlet flow velocity drops, the rotor outlet flow tangential velocity, which is given by **Equation 4.32**, increases. The reason for this is that the relative flow velocity reduces and because the rotor outlet angle is negative and fixed.

$$C_{\theta rot out} = U_{rot out} + W_{rot out} \sin \beta_{rot out} \quad (4.32)$$

From the *Euler Turbomachinery Equation* (**Equation 4.29**) it can be seen that the consequence of these velocity changes is that the specific work reduces and becomes negative. What is happening is that, as the velocity ratio increases, the rotor becomes less effective in transforming the inlet flow kinetic energy into useful work. When the velocity ratio exceeds a critical value, the efficiency becomes negative because the rotor increases the flow kinetic energy.

The last observation made on **Figure 4.11** is that the efficiency line approaches a vertical asymptote. This asymptote occurs because the zero-mass-flow pressure ratio is higher than one. This can be understood by studying the efficiency definition given by **Equation 4.22** and the velocity ratio definition given by **Equation 4.30**. From the efficiency definition it can be seen that if the mass flow rate is zero and the actual work is finite, the efficiency is infinite. From the velocity ratio definition it can be seen that if the zero-mass-flow pressure is one, the

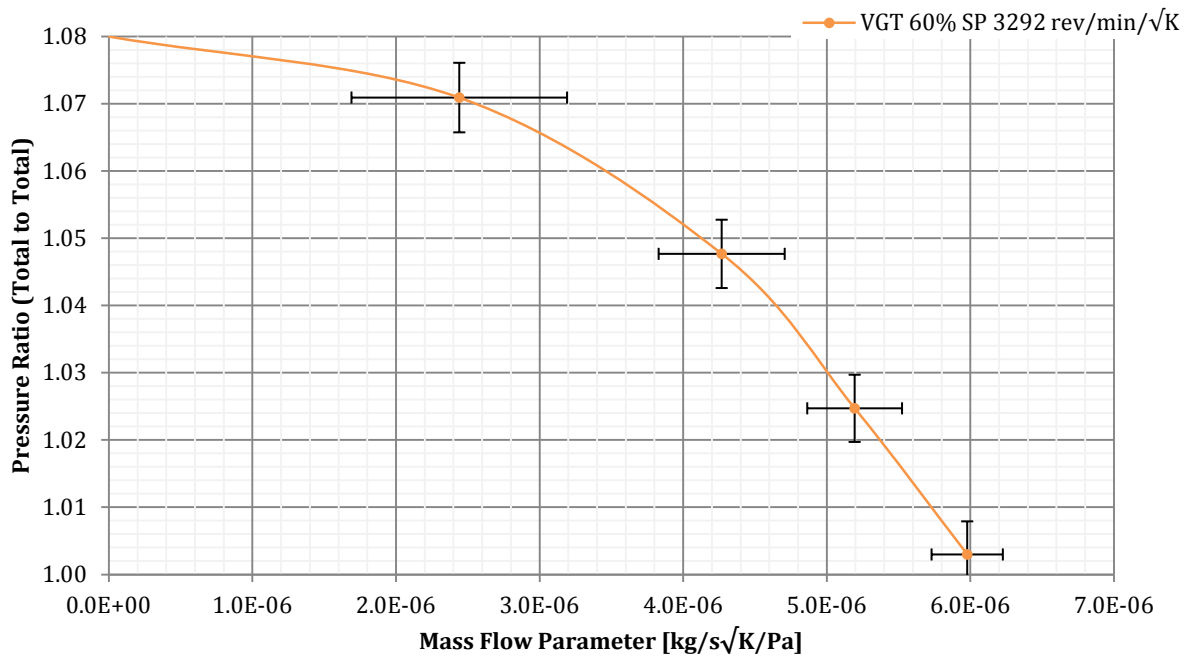


Figure 4.12 – Collected turbine mass flow data in reverse flow conditions. Showing only one speed-line of the 60% VGT opening. The total to total pressure ratio definition is given by Equation 4.19, the mass flow parameter definition is given by Equation 4.20 and the speed parameter definition is given by Equation 4.18

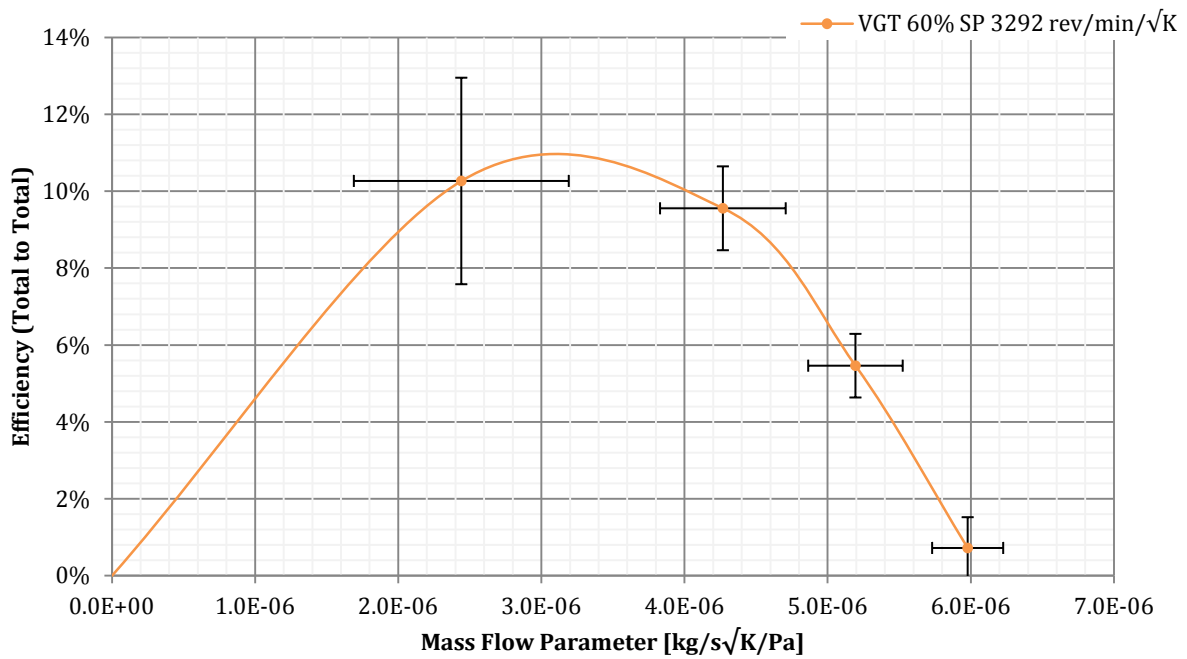
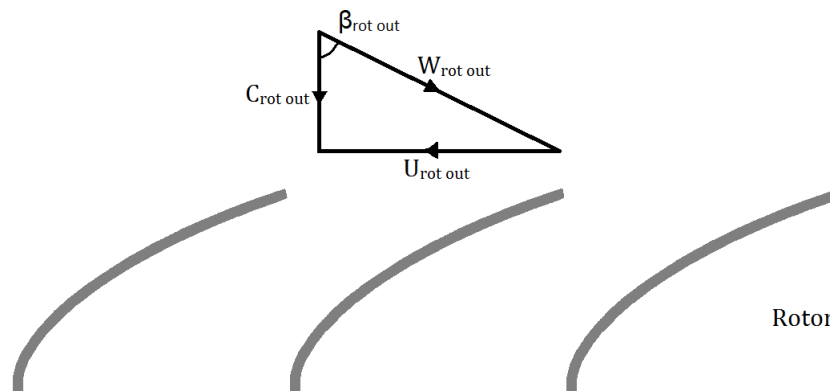


Figure 4.13 – Collected turbine total to total efficiency data in reverse flow conditions. Showing only one speed-line of the 60% VGT opening. The total to total efficiency definition is given by Equation 4.21, the mass flow parameter definition is given by Equation 4.20 and the speed parameter definition is given by Equation 4.18

corresponding velocity ratio would be infinity and no asymptote would exist. However, since this pressure ratio is higher than one, the asymptote exists and can be calculated. For this speed-line, which has a zero-mass-flow pressure ratio of 1.08, the asymptote occurs at a velocity

ratio of 1.64. At this velocity ratio the efficiency would be negative infinity, since the actual work is negative due to the frictional losses that occur even with no mass flow.

The reverse mass flow data is plotted as a compressor mass flow map in **Figure 4.12** and as a compressor efficiency map in **Figure 4.13**. The main comment which can be made on these plots is that the turbine does not surge as a compressor. Compressor surge consists of a cyclic flow reversal which occurs due to periodic flow detachment and reattachment within the compressor impeller. Compressor surge occurs when the mass flow rate drops below a critical value which depends on the pressure ratio across the device. The reason why the turbine does not surge when reverse flow occurs is due to the exit angle of the rotor blades, which cause a very negative incidence angle when reverse mass flow occurs (refer to **Figure 4.14**). This poor incidence angle causes a large flow separation within the rotor under all reverse flow conditions. Because the flow is always separated, it does not cyclically detach and reattach, so the turbine always operates in a stable manner. The large flow separation also explains the poor efficiency shown in **Figure 4.13**.



**Figure 4.14 - Turbine rotor outlet velocity triangle in reverse mass flow conditions**

The reason why the reverse flow efficiency drops to zero when the mass flow is zero and when the mass flow reaches the maximum value can be understood from the definition of total to total compressor efficiency, given by **Equation 4.21**. This equation states that the efficiency is zero when the isentropic work is zero. This condition occurs when there is no flow through the device and when the pressure ratio through the device is zero. This latter condition coincides with the maximum mass flow rate, as shown by **Figure 4.12**, and this is why the efficiency drops to zero at the maximum reverse mass flow rate.

### **Impact of Rotational Speed on Turbine Performance**

In the previous section only the pressure ratio effects on the mass flow parameter and total to static efficiency have been discussed. Three other speed-lines have been tested for this vanes opening (60%) and the results are plotted in **Figure 4.15**, for mass flow parameter, and in

**Figure 4.16**, for efficiency. The reverse mass flow data is plotted as a compressor mass flow map in **Figure 4.17**. The reverse flow efficiency data is shown in **Appendix A**. From the plots shown in this section, the following observations on the speed effects can be made:

- The mass flow parameter decreases with increasing speed parameter
- The zero-mass-flow pressure ratio increases with increasing speed parameter
- The magnitude of the reverse mass flow increases with increasing speed parameter
- The velocity ratio value at which the efficiency vertical asymptote occurs depends on the speed parameter

These observations are all caused by the impact that the rotational speed has on the centrifugal head. The mass flow rate drops as the rotational speed increases because the centrifugal body force acting on the fluid is proportional to the square of the rotational speed. This means that as the speed increases, an increasing fraction of the pressure ratio is utilized to overcome this body force, rather than accelerating the flow radially/axially or overcoming the frictional losses. This causes the observed reduction of mass flow rate. For the same reason, the magnitude of the reverse mass flow rate, which is driven by this centrifugal body force, rises as the rotational speed increases, as it can be observed in **Figure 4.17**.

The zero-mass-flow pressure ratio is also affected by the centrifugal head and it increases with the square of the rotational speed (**Equation 4.28**). As explained in the previous section, this zero-mass-flow pressure ratio also affects the velocity ratio at which the efficiency asymptote

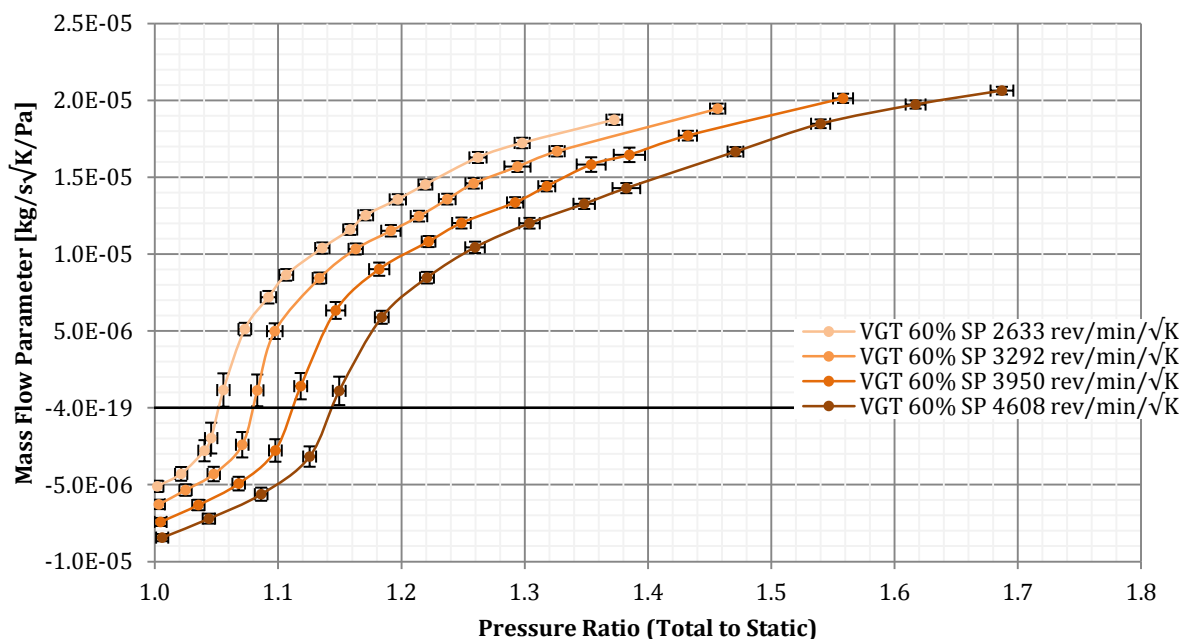


**Figure 4.15** - Collected turbine mass flow data. Showing only the speed-lines of the 60% VGT opening. The mass flow parameter definition is given by Equation 4.14, the pressure ratio definition is given by Equation 4.6 and the speed parameter definition is given by Equation 4.15



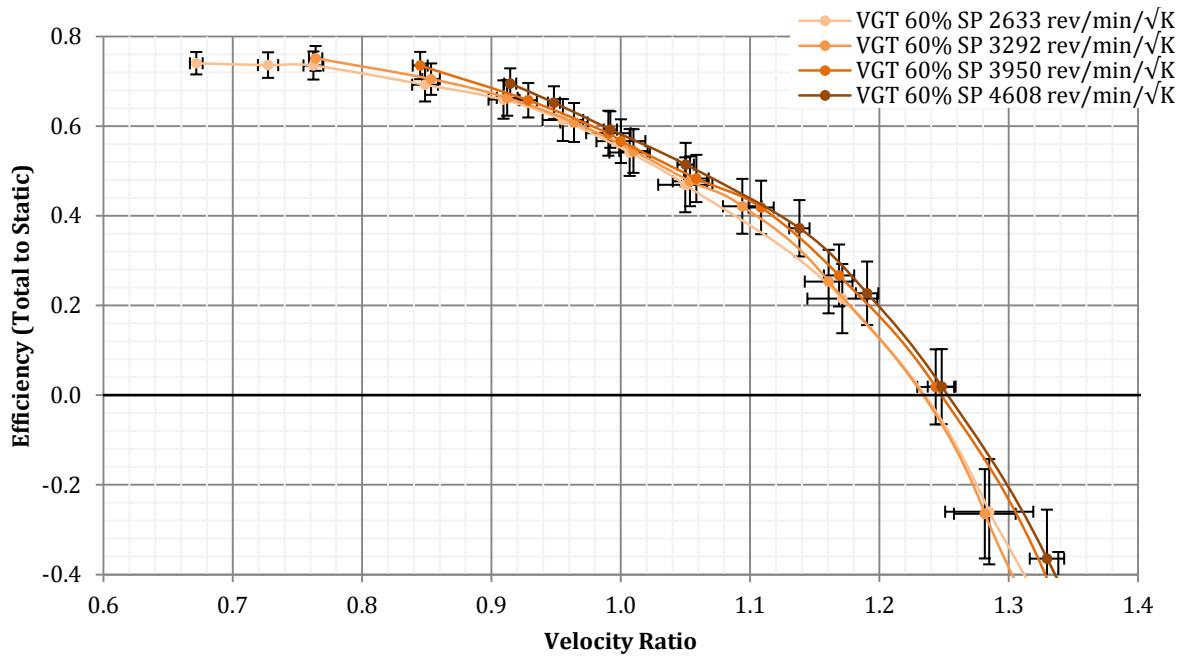


Figure 4.16 - Collected turbine total to static efficiency data. Showing only the speed-lines of the 60% VGT opening. The total to static efficiency definition is given by Equation 4.10, the velocity ratio definition is given by Equation 4.16 and the speed parameter definition is given by Equation 4.15

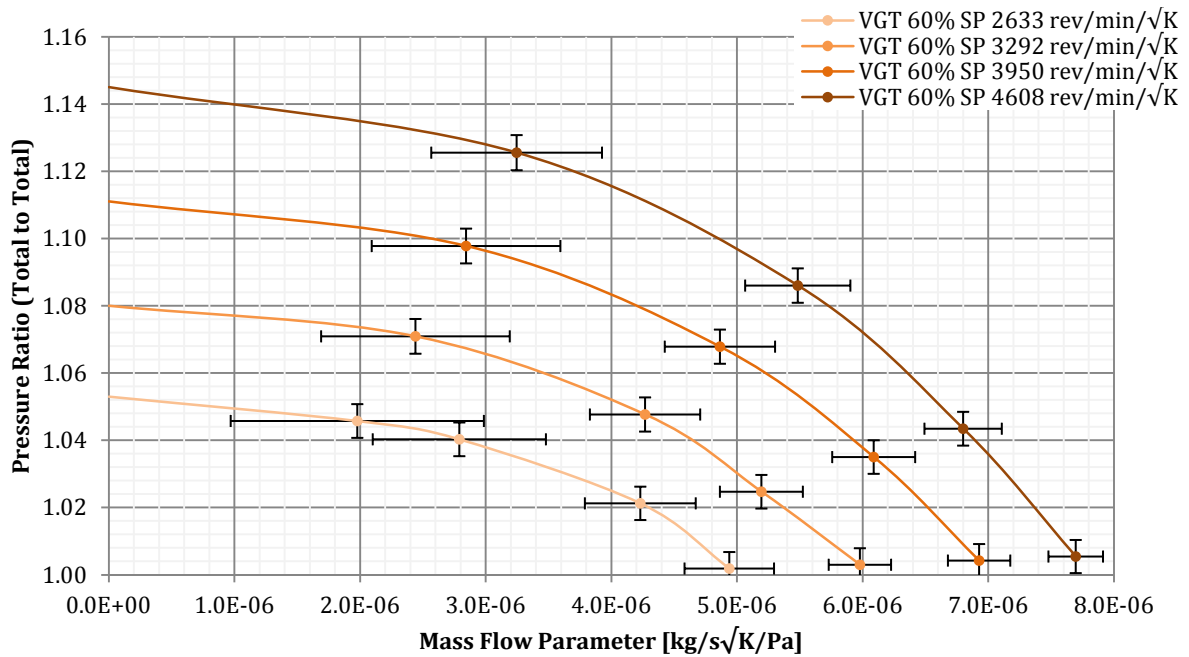


Figure 4.17 - Collected turbine mass flow data in reverse flow conditions. Showing only the speed-lines of the 60% VGT opening. The total to total pressure ratio definition is given by Equation 4.19, the mass flow parameter definition is given by Equation 4.20 and the speed parameter definition is given by Equation 4.18

occurs. This is because the efficiency goes to negative infinity when there is no mass flow (Equation 4.22) and the velocity ratio is a function of the pressure ratio (Equation 4.30). For this reason, the critical velocity ratio reduces as the rotational speed rises.

A further observation which can be made is that the efficiency does not drop with increasing speed parameter, despite the increase in centrifugal head. This rise in centrifugal head increases the work required to overcome the centrifugal body force on a fluid particle. However, **Figure 4.16** shows that the efficiency does not drop as the speed increases, which means that this work done on the fluid particle is converted into work done on the turbine wheel.

How this occurs can be understood by considering a fluid particle which is moving radially inwards at constant radial velocity in a turbine rotor designed to maintain the tangential velocity constant. In this system there is no change of speed and therefore the particle kinetic energy is also constant. Two forces are acting on this particle:  $F_{rad}$ , which is pushing the particle radially inwards, and  $F_{\theta}$ , which is pushing the particle against the tangential velocity.  $F_{rad}$  is equal and opposite to the centrifugal body force acting on the particle:

$$F_{rad} = ma = m \frac{C_{\theta}^2}{r} \quad (4.33)$$

$F_{\theta}$  can be obtained from the conservation of angular momentum:

$$L = (L + dL) + \tau dt = (L + dL) - F_{\theta} r \frac{-dr}{C_{rad}} \quad (4.34)$$

$$F_{\theta} = -\frac{dL}{dr} \frac{C_{rad}}{r} = -m C_{\theta} \frac{C_{rad}}{r} \quad (4.35)$$

The work done by  $F_{rad}$  as the particle moves radially by  $dr$  is:

$$dW_{rad} = F_{rad} dr = m \frac{C_{\theta}^2}{r} dr \quad (4.36)$$

The work done by  $F_{\theta}$  during the same time period is given by:

$$dW_{\theta} = F_{\theta} d(\theta r) = -m C_{\theta} \frac{C_{rad}}{r} C_{\theta} \frac{dr}{C_{rad}} = -m \frac{C_{\theta}^2}{r} dr = -dW_{rad} \quad (4.37)$$

Please note that the above derivation is simplified by the fact that the velocity is constant. The work done by the axial force is equal and opposite to the work done by the radial force. This means that the work done to overcome the centrifugal head is turned into work done by the fluid particle on the rotor blade and is not turned into thermal energy. This is an idealized situation as viscous effects are not considered and because a real rotor is designed to reduce the tangential speed. Nevertheless, this simple derivation explains well why the efficiency is not negatively affected by the centrifugal head.

## Impact of Vanes Angle on Turbine Performance

The complete results are shown in **Figure 4.18** for the mass flow rate parameter and in **Figure 4.19** for the total to static efficiency. The reverse mass flow data is plotted as a compressor mass flow map in **Figure 4.20**. The reverse flow efficiency data is shown in **Appendix A**. By observing the plots presented in this section, a few remarks on the impact of vanes opening on turbine performance can be made:

- The mass flow parameter increases with increasing vanes opening
- The zero-mass-flow pressure ratio decreases with increasing vanes opening
- The magnitude of the reverse mass flow increases with increasing vanes opening
- The efficiency has a peak at a velocity ratio of approximately 0.65
- The peak efficiency is affected by the nozzle angle and, with a 30% VGT opening, by the speed parameter. The most efficient VGT opening is 60%
- The gap between the efficiency speed-lines is small for a large VGT opening and large for a small VGT opening
- The velocity ratio value at which the efficiency asymptote occurs depends on the nozzle angle

It is clear from **Figure 4.18** that the vanes opening is the variable which most affects the mass flow rate parameter. When the vanes are closed, the flow angle increases (i.e. the tangential velocity component becomes more important relative to the radial component) and, although the nozzles tip radius increases, the effective nozzles throat area reduces. This throat area

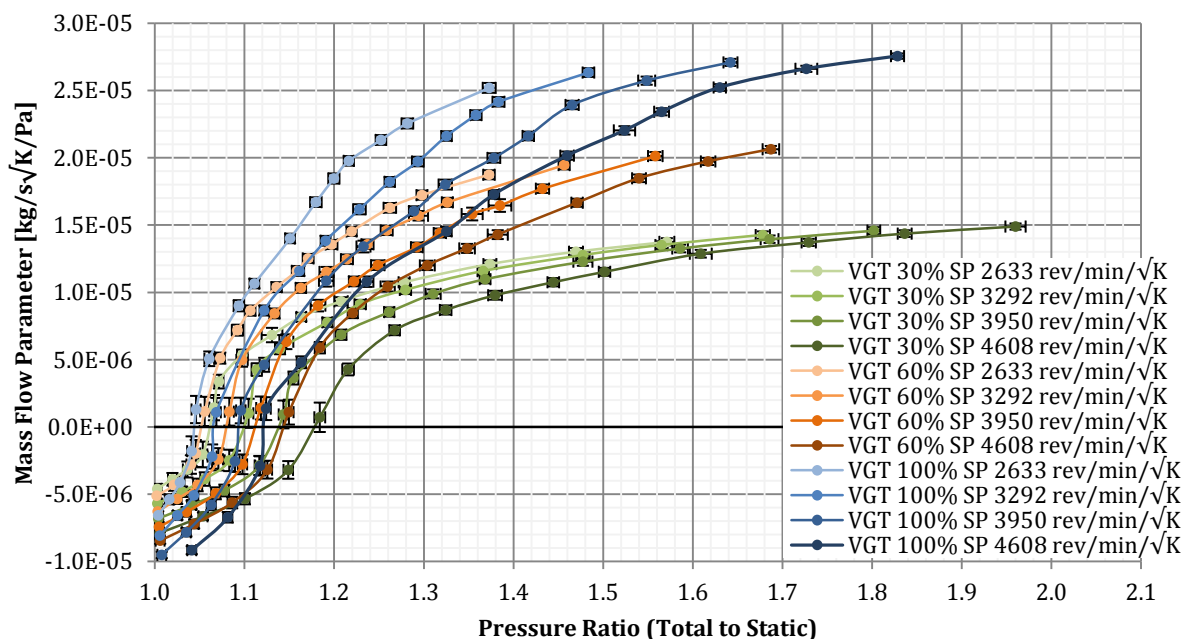


**Figure 4.18 – Collected turbine mass flow data. Showing the full data set. The mass flow parameter definition is given by Equation 4.14, the pressure ratio definition is given by Equation 4.6 and the speed parameter definition is given by Equation 4.15**

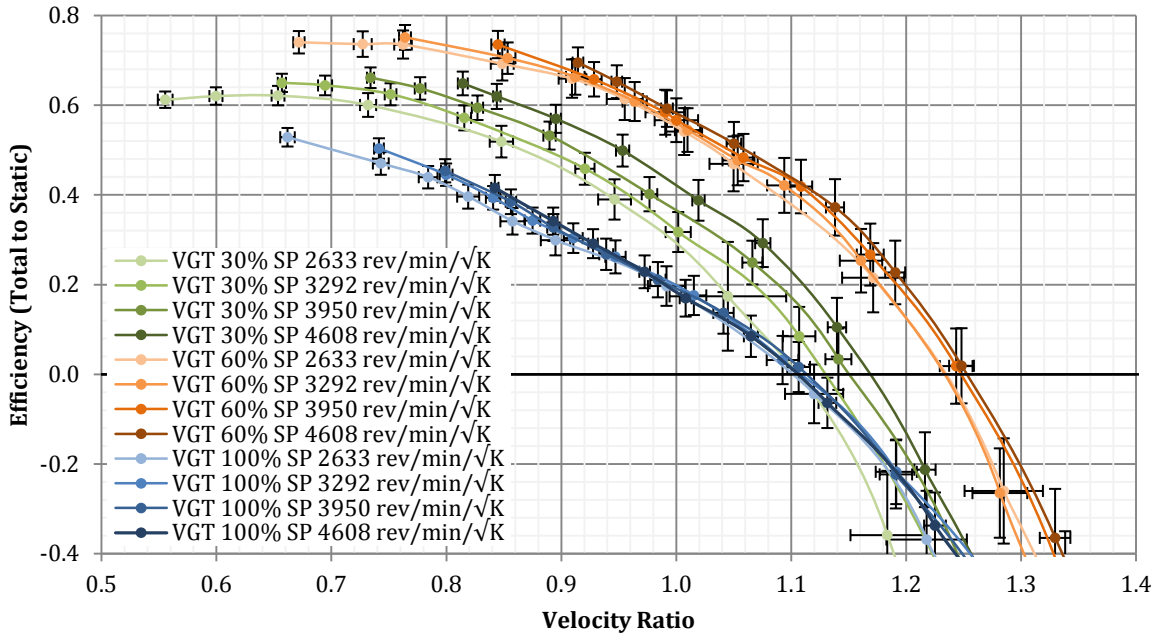


Figure 4.19 – Collected turbine total to static efficiency data. Showing the full data set. The total to static efficiency definition is given by Equation 4.10, the velocity ratio definition is given by Equation 4.16 and the speed parameter definition is given by Equation 4.15

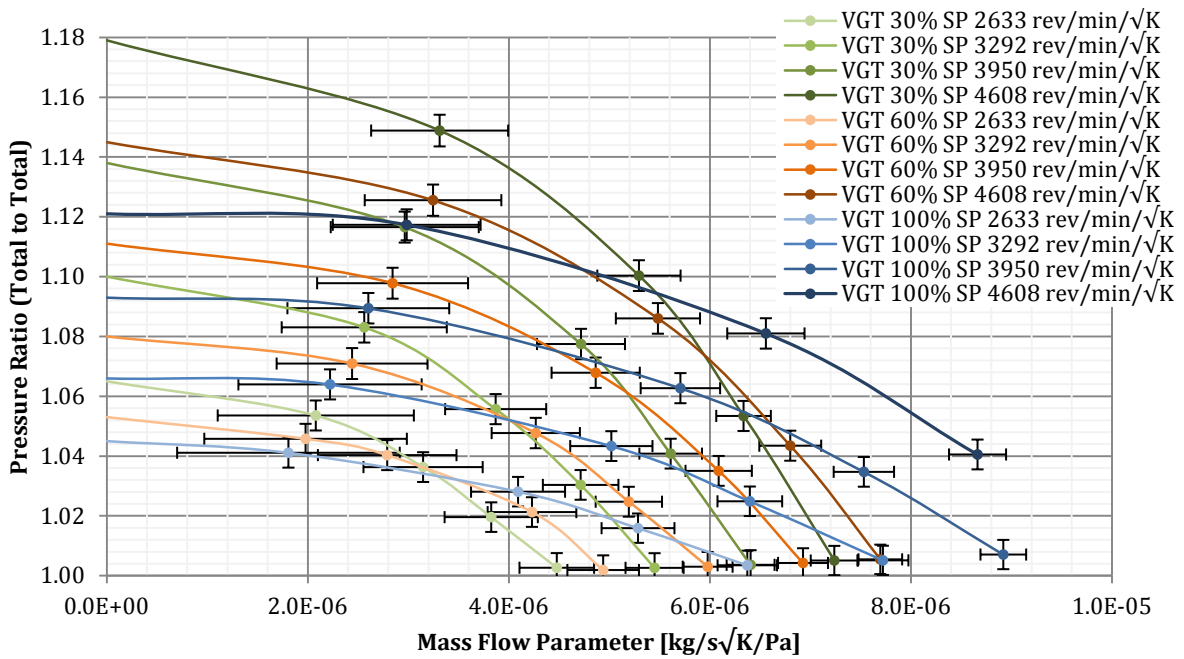


Figure 4.20 – Collected turbine mass flow data in reverse flow conditions. Showing the full data set. The total to total pressure ratio definition is given by Equation 4.19, the mass flow parameter definition is given by Equation 4.20 and the speed parameter definition is given by Equation 4.18

reduction is what causes the reduction of mass flow rate.

The zero-mass-flow pressure ratio and the magnitude of the reverse mass flow are also influenced by the vanes opening. The two variables are not affected in the same manner, as a smaller opening causes a larger zero-mass-flow pressure ratio, but a lower maximum reverse

mass flow rate (**Figure 4.20**). The reason why the zero-mass-flow pressure ratio increases with decreasing vanes opening is found in the nozzle pivoting mechanism. Because the nozzles are not pivoted about the outlet tip but about the centre, the radial gap between the rotor inlet and nozzles exit increases with decreasing VGT opening. This causes the diameter of the vortex generated by the wheel rotation to be larger, as the gas is free to rotate in the gap between the stator and rotor, and the pressure ratio increases (**Equation 4.28**). The reason why the reverse mass flow decreases with decreasing vanes opening is found in the nozzles angle. When reverse flow occurs, it approaches the nozzles perpendicularly. This generates a flow separation which restricts the effective nozzles throat area and reduces the mass flow. As the vanes are opened, the incidence angle improves, the flow area enlarges and the reverse mass flow magnitude increases.

The *Euler Turbomachinery Equation* (**Equation 4.30**) can explain why the efficiency peaks at a velocity ratio of approximately 0.65. The efficiency will be highest when the outlet swirl is zero, because, at this point, the energy lost via the outlet in the form of kinetic energy is minimized. In a well designed turbine, the stator is designed so that the optimum rotor incidence angle coincides with the zero outlet swirl point. Combining these conditions with the *Euler Turbomachinery Equation*, the definition of total to static efficiency and the equation of isentropic work, the following equation is obtained:

$$\left(\frac{U_{in}}{C_{is}}\right)_{opt} = \sqrt{\eta_{ts} \frac{\tan \alpha_{in} - \tan(\beta_{in})_{opt}}{2 \tan \alpha_{in}}} \quad (4.38)$$

In a typical radial turbine the optimum rotor incidence angle is in the range of  $-20^\circ$  to  $-30^\circ$  (Japikse and Baines, 1994). Assuming that the rotor inlet angle is equal to the nozzle angle, that the optimal incidence angle is  $-25^\circ$  and that the peak efficiency can be extrapolated from the data obtained, **Equation 4.38** leads to the velocity ratio values shown in **Table 4.1**. For the 60% VGT opening, the predicted peak efficiency velocity ratio approximately coincides with the actual peak efficiency velocity ratio of the lowest speed-line.

A good agreement is shown also by the two lowest speed-lines of the 30% VGT opening. However, despite this good agreement, the incidence angle at the peak efficiency of these speed-lines is not optimal. In this case, **Equation 4.38** does not predict the peak efficiency velocity ratio, but the velocity ratio at which the outlet swirl would be zero if the incidence angle was  $-25^\circ$ . **Equation 4.38** is still useful to understand why the efficiency peaks at around that velocity ratio value. The incidence angle of the lowest speed-line of the 30% opening is  $33.8^\circ$  when the exit swirl is zero. If this value is inserted into **Equation 4.38**, the equation yields a velocity ratio value of 0.51. The calculated incidence angle is far off from the optimal incidence angle and,

therefore, the incidence loss significantly reduces the efficiency. As a result, the peak efficiency cannot occur at 0.51 velocity ratio, as it must be the result of a trade-off between the optimal exit tangential velocity and the optimal incidence angle. The incidence angle improves as the flow speed reduces relative to the blade speed. For this reason, the peak efficiency occurs at a velocity ratio which is higher than 0.51.

**Table 4.1 - Predicted peak efficiency velocity ratio (left part), predicted incidence angle at peak efficiency velocity ratio (central part), and predicted exit kinetic energy as a fraction of isentropic work at peak efficiency velocity ratio (right part)**

VGT	$\alpha_{rot\ in}$	Peak $\eta_{ts}$	Peak $\eta_{ts}$ VR	Incidence Angle				Exit KE/ $W_{is}$ with fixed $\beta_{rot\ out}$			
				$U_{in} = 158\ m/s$	$U_{in} = 197\ m/s$	$U_{in} = 237\ m/s$	$U_{in} = 266\ m/s$	$U_{in} = 158\ m/s$	$U_{in} = 197\ m/s$	$U_{in} = 237\ m/s$	$U_{in} = 266\ m/s$
100%	39.4	0.55	0.63	-59.6	-61.6	-63.8	-65.4	0.06	0.08	0.11	0.15
60%	63.3	0.75	0.67	-32.7	-40.7	-48.7	-53.9	0.05	0.06	0.07	0.08
30%	74.4	0.70	0.62	33.8	14.3	-15.2	-35.4	0.04	0.04	0.04	0.05

The reason why the peak efficiency drops at 100% VGT opening can be understood by deriving an equation for the pressure ratio required to achieve the optimal incidence angle with no exit swirl:

$$\left(\frac{P_{0\ in}}{P_{out}}\right)_{opt} = \left(1 - \frac{1}{\eta_{ts} c_p} \frac{U_{in}^2}{T_{0\ in}} \frac{\tan \alpha_{in}}{\tan \alpha_{in} - \tan(\beta_{in})_{opt}}\right)^{\frac{\gamma}{1-\gamma}} \quad (4.39)$$

This equation is obtained following an approach similar to the derivation of the optimal velocity ratio: starting from the *Euler Turbomachinery Equation* and assuming zero exit swirl. It is clear that for a given speed parameter, stator geometry and gas properties, only one optimal pressure ratio exists. However, this equation is derived assuming that there is no exit swirl, so it implies that the exit relative flow angle is always adjusted to achieve this. In a real machine, such as the one being studied, the rotor exit angle is fixed and this implies that, for a given speed parameter, the situation where the exit swirl is zero and the incidence angle is optimal can be achieved for only one nozzle angle.

By combining **Equation 4.39** with the conservation of mass, the incidence angle that results when the exit swirl is zero can be calculated for given speed parameter, turbine geometry and gas properties. This has been done for all the combinations of speed parameter and vanes position tested and are summarized in **Table 4.1**. The 60% opening is the opening that has the incidence angle closest to the optimal value over the speed range tested and this is why it shows the highest efficiency. The 30% opening is also close to the optimum incidence angle at the two highest speeds, but the testing pressure ratio range was not enough to cover the peak efficiency of these two speed-lines. The 100% opening has the worst incidence angles and this is why it

shows the lowest efficiency. **Table 4.1** also shows the outlet kinetic energy as a fraction of the isentropic work. The 100% opening is penalized also in this case, since it has the highest mass flow rate.

**Table 4.1** provides an explanation of why the efficiency speed-lines are very close to each other for the full opening vanes position and far apart for the 30% opening. The change in incidence angle with changing speed is much larger for the 30% opening (changes by  $69.2^\circ$ ) than for the 100% (changes by  $5.8^\circ$ ). This means that for the 30% opening the angle changes from a very poor angle ( $+33.8^\circ$ ) to an almost optimal angle ( $-35.4^\circ$ ), hence the peak efficiency is a strong function of speed. On the contrary, for the 100% opening the incidence angle is consistently poor ( $-59.6^\circ$  to  $-65.4^\circ$ ). As a result, the efficiency is not significantly affected by speed.

### **Disadvantages of Cold Flow Testing**

This turbine has been tested with an inlet temperature of about  $60^\circ\text{C}$ , while on an engine it operates at approximately  $650^\circ\text{C}$ . The main drawback caused by this is the lack of heat transfer in the turbine. This heat loss, which would mainly occur in the volute as in this region the flow is slow and the surface area is large, would result in a reduction of efficiency. Nevertheless, the turbocharger solid parts have a non-negligible thermal inertia. Therefore, even if the heat loss is included in the efficiency map, this would not be correct, as the heat loss is a function of the previous turbocharger states. To correctly account for the thermal loss, a dynamic heat transfer model should be included in the turbocharger model.

A further error is caused by the different mechanical clearances that occur in cold conditions. In particular, the radial gap between the rotor blades and the shroud has a non-negligible effect on the turbine efficiency, since a secondary flow occurs in this gap. This flow is driven by the difference in pressure between the suction and pressure faces of the blades. The exact thermal deformation of the turbine assembly is difficult to predict without a finite element analysis, due to the complex shape of the rotor and volute. Moreover, there is a lack of data on how the change in gap affects performance.

Because air is not a perfect gas, the specific heats ratio is a function of temperature. This implies that the specific heats ratio in cold conditions is not the same as in hot conditions. As a result, the gas compressibility is different and this affects turbine performance. The differences are particularly noticeable at high pressure ratios, where the Mach number is higher. The impact of the specific heats ratio mismatch has been estimated via the mean-line model described in the second part of this chapter and the results have been plotted in **Figure 4.21**. The efficiency has a maximum discrepancy of approximately 1%, while the mass flow rate has a maximum discrepancy of approximately 2%. For the pressure ratio range achieved during testing, the

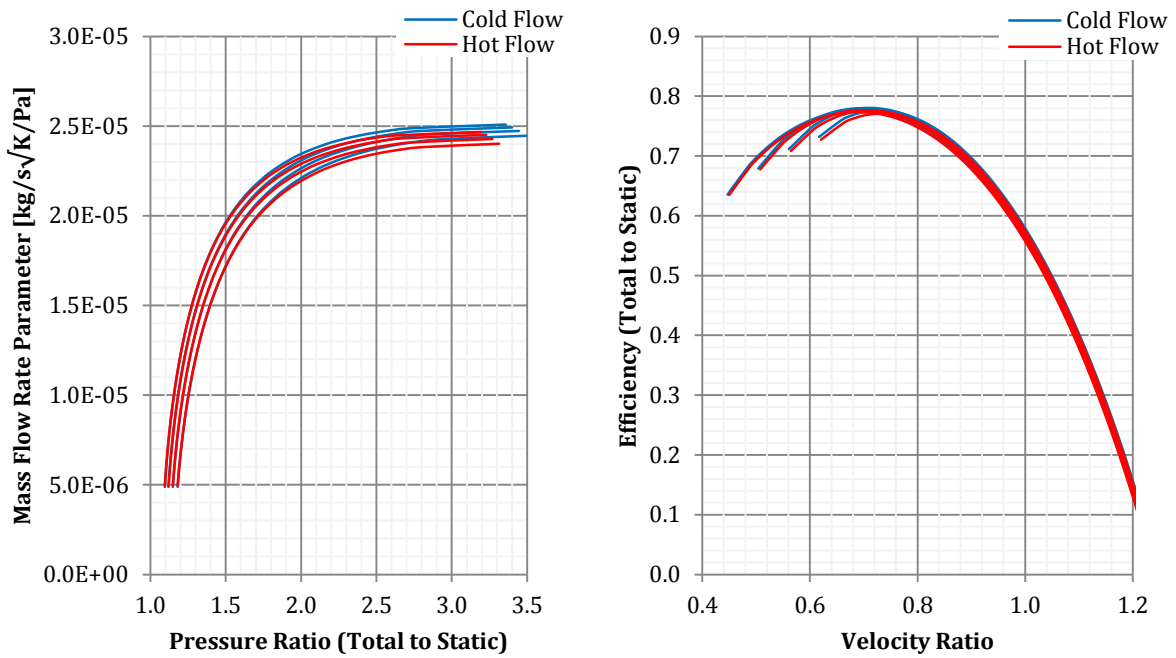


**Figure 4.21 – Gas compressibility impact on turbine performance. Results obtained via the mean-line model described in the following section**

actual maximum mass flow rate discrepancy is less than 1%. These discrepancies are of a smaller magnitude than the experimental error. This means that the specific heats ratio difference is acceptable. In fact, it is standard practice to neglect the gas compressibility differences when testing in cold conditions.

Similarly to the specific heats ratio, the cold flow Reynolds number cannot be matched to the hot flow Reynolds number. The minimum mass flow parameter required to have turbulent flow at the turbine inlet is  $6.38 \times 10^{-7}$  kg/s√K/Pa in cold conditions and  $2.11 \times 10^{-6}$  kg/s√K/Pa in hot conditions. This implies that, for the large majority of the measured map points, the flow would be turbulent both in cold and hot conditions, so in neither cases there would be a laminar to turbulent transition inside the turbine, and the differences in Reynolds Number become less important.

The Reynolds Number still affects the frictional losses in the turbine passages. However, it has to be considered that the cold flow and hot flow Reynolds numbers always have the same order of magnitude and that the frictional losses are not as important as the incidence loss or the exit swirl loss. Moreover, because the pressure loss due to friction is proportional to the square of the flow speed, the frictional losses are more important at high Reynolds numbers and are likely to be small in the pressure ratio range achieved in this experiment. In addition, from the Moody diagram it can be seen that at high flow speeds the friction factor is a weak function of the Reynolds number. Therefore, even relatively large changes in Reynolds number cause small changes in frictional losses. From the considerations above, it is clear that the performance



discrepancies caused by the variations in Reynolds number are relatively small. However, the actual changes in friction are difficult to estimate since the flow in the turbine passages is not fully developed.

These disadvantages of cold flow testing are minor when compared to the benefits of this testing technique. The main advantage is that it was possible to directly measure the shaft output torque and speed, rather than calculating the power from the inlet and outlet temperature of the compressor. This means that the experimental error is smaller and that it was possible to separate the aerodynamic losses from the bearing and thermal losses. In addition, because it was possible to utilize the motor/generator as the loading device, the maps width was not limited by the compressor surge and choking limitations, and it has been possible to test down to a pressure ratio of one. In any case, all the features of the maps discussed in this chapter are due to aerodynamic effects that would occur also in hot conditions. This means that the significance of the results is not diminished by the fact that the testing temperature does not match the exhaust gases temperature.

### **Significance of Results**

This new experimental set-up allowed to expand the turbine maps in the low pressure ratio region over the maps produced by the dynamometer designed by Szymko (2006) and to test up to the maximum turbine rotational speed. This allowed to observe features of the turbine maps that were not possible to observe with previous experimental techniques. The main findings of this experiment are:

- At low pressure ratios, the centrifugal force acting on the gas inside the turbine plays a key role in determining the turbine performance
- The mass flow rate speed-lines cross the abscissa at a pressure ratio higher than one because the centrifugal body force needs to be compensated by the surface force caused by the pressure difference
- Below this zero-mass-flow pressure ratio, reverse mass flow occurs. This reverse mass flow is driven by the centrifugal force
- The zero-mass-flow pressure ratio increases with the nozzle tip diameter because the diameter of the vortex generated by the turbine wheel rotation is constrained by this dimension
- The maximum reverse mass flow magnitude depends on the angle at which the flow approaches the nozzles. The larger this angle is, the larger is the flow separation and the smaller the effective flow area becomes

- At low pressure ratios (i.e. high velocity ratios) the efficiency is negative because the rotor increases the flow kinetic energy instead of reducing it
- When the mass flow rate is zero, the efficiency tends to negative infinity

This work is important because there is no information in the literature that explains how a radial turbine operates in these conditions. Typical commercial turbine maps extrapolation software assumes that the zero-mass-flow pressure ratio is one, and this leads to non-negligible errors during engine simulations (Pesiridis, Salim and Martinez-Botas, 2012) During an engine transient, the turbine provides the majority of the power required to accelerate the turbocharger, even when electric assistance is present. Therefore it is very important to feed into the turbine models accurate experimental data, in order to accurately predict the engine transient performance.

In addition, this data shows that turbine maps extrapolation software can be improved by implementing a correlation which determines the zero-mass-flow pressure ratio. This correlation could take a form similar to **Equation 4.28** but with the addition of empirical corrections. Such a correlation would not only improve the prediction of the mass flow parameter map, but also the efficiency map, since the efficiency asymptote occurs at the zero-mass-flow pressure ratio.

In a real engine application, the reverse mass flow can only occur during an engine transient and with electric assistance present. This is because the exhaust manifold fills very rapidly with no or reverse turbine mass flow, so that these conditions cannot occur in steady state. Electric assistance is also necessary, because the change in turbocharger speed required to produce reverse mass flow cannot be driven by an increase in turbine pressure ratio, but it needs to be driven by an external power source. The electric assistance must also be significantly powerful, as it needs to rapidly accelerate the turbocharger with minimal increase in exhaust manifold pressure. For these reasons, the electric assistance under study is unlikely to cause reverse mass flow, but it is likely to cause a shift in turbine operation to the lower end of the performance maps, where experimental data was still not available.

### **Uncertainty Analysis**

The bias propagation, precision error estimation, and bias and precision error combination are identical to **Chapter 3** and will not be discussed here. However, only a few measurements are identical to the electrical machine testing and in this section the sources of bias for these new measurements are discussed.

### *Inlet and Outlet Temperatures*

The temperatures have been measured through thermocouples. This measuring technique has two sources of bias:

- Accuracy of thermocouples – The accuracy of the sensor is  $\pm 1.5^\circ \text{C}$  for the inlet temperature, where a K-type thermocouple has been utilized, and  $\pm 0.5^\circ \text{C}$  for the outlet temperature, where a T-type thermocouple has been used.
- Recovery factor error – The recovery factor error has been assumed to be  $\pm 0.1$ , which is a conservative assumption, and the resulting temperature error has been obtained by differentiating **Equation 4.25** with respect to recovery factor. Because the difference between computed static and stagnation temperatures is typically low due to the low flow speeds, the temperature error due to recovery factor uncertainty never exceeds  $\pm 0.15^\circ \text{C}$ .

### *Inlet and Outlet Pressure*

The inlet pressure is calculated by summing the gauge pressure measured via the *ScaniValve* pressure meter and the ambient pressure measured via the *Vaisala* barometer. Therefore, the sources of bias are:

- Accuracy of pressure meter –  $\pm 350 \text{ Pa}$
- Accuracy of barometer –  $\pm 30 \text{ Pa}$

By combining the two errors via the root sum square method, the resulting total error is  $\pm 351 \text{ Pa}$

### *Mass Flow Rate*

The mass flow rate is measured via a *McCrometer V-Cone*, which is a differential pressure device. Due to the nature of the meter, the mass flow measurement depends on other measurements such as pressures and temperatures. The sources of bias are:

- Accuracy of the *V-Cone* – The accuracy of the *V-Cone* is provided by the manufacturer and is  $\pm 0.5\%$  of the reading.
- Accuracy of the pressure and temperature readings – The *V-Cone* relays on measurements from the differential pressure meter, the pressure meter, the barometer and the thermocouple. The errors caused by the uncertainties associated to the pressure and temperature measurements are calculated by differentiating the *V-Cone* mass flow equation, **Equation 4.26**, with respect to the relevant measurement.
- Leakage flow – A further bias source is a small leakage which occurs inside the turbine (maximum  $10 \text{ g/s}$  with a pressure ratio of 1.9). The air tightness of the system has been

tested every time the rig was rebuilt and the leakage has been found to be a function of the turbine pressure ratio. Because the leakage is very consistent, the mass flow rate measurement is corrected by subtracting the leakage mass flow from the original measurement. However, the leakage mass flow Reynolds number is always smaller than the minimum Reynolds number at which the *V-Cone* is accurate. As a result, the error has been conservatively assumed to be  $\pm 100\%$  of the reading when the Reynolds number is zero, and to decrease linearly down to  $\pm 1\%$  at a Reynolds number of 8,000.

### *Torque*

The torque bias sources are identical to these of the electrical machine testing (*Data Set 2*) and are covered in **Chapter 3**. To summarize, the main sources are:

- Hysteresis and non-linearity caused by gimbal bearings friction and load-cell accuracy
- Geometric tolerances of load-cell calibration arm
- Load-cell zero offset drift
- Torque imposed on bearing housing by leaking air

### **Experiment Improvements**

There are some improvements that could be done on the test-rig to enhance the data produced. The most important of these improvements would be an increase in motor/generator power. Currently, the maximum achievable pressure ratio is 1.96 for a VGT opening of 30% and a speed parameter of 4608 rev/min/ $\sqrt{K}$ , and only 1.37 for a VGT opening of 100% and a speed parameter of 2633 rev/min/ $\sqrt{K}$ . If the power absorption capabilities of the electrical machine were increased, it would be possible to characterize the turbine up to choking conditions, reducing the amount of extrapolation required.

To reduce the air leakage, the volume on the bearing housing side of the gimbal bearings could be pressurized. The pressure could be forced to be equal to the turbine pressure via a valve and a PI controller. The feedback for the controller could be from pressure tappings on both sides of the gimbal bearings labyrinth seal (refer to **Figure 3.15**). To avoid an increase in torque error due to the increased flow of air escaping from the gimbal bearing, a second labyrinth seal could be cut in the passage between the volute back face and the bearing housing.

To improve the torque measurement, the current angular contact ball bearings utilized for the gimbal system could be replaced by aerostatic or hydrostatic bearings, as discussed in **Chapter 3**. These non-contact bearings would remove the stiction, and improve the torque measurement hysteresis and zero offset drift.

## 4.2 TURBINE MAPS EXTRAPOLATION

In **Chapter 6** the ETA impact on the engine is studied via an engine model. Accurate and complete turbine performance data is required by this engine model in order to predict the engine transient response. The maps produced in the previous section do not cover the full operation range as the maximum turbine pressure ratio achieved during testing was limited by the relatively low power absorption capabilities of the motor/generator. Consequently, the turbine maps have to be extrapolated to cover the full turbine operating range.

Commercially available extrapolation software is not suitable for this task. This is because not all the assumptions on turbine off-design operation performance made by these programs are valid, as it has been discussed in **Section 4.1.11**. It is therefore necessary to generate a physics based extrapolation technique which is capable of predicting the off-design operation performance.

The objectives of this section are to:

- Predict turbine performance at high pressure ratios (lower velocity ratios)
- Predict turbine performance at low speed parameters
- Interpolate turbine performance between tested VGT openings

### 4.2.1 TURBINE MEAN-LINE MODEL

It has been decided to extrapolate the maps by generating a mean-line model of the turbine. A mean-line model is a one-dimensional, steady state model which computes the flow average properties at discrete locations within the turbine. This model applies the conservation of mass, conservation of energy, the *Euler Turbomachinery Equation*, isentropic flow relations and empirical loss models.

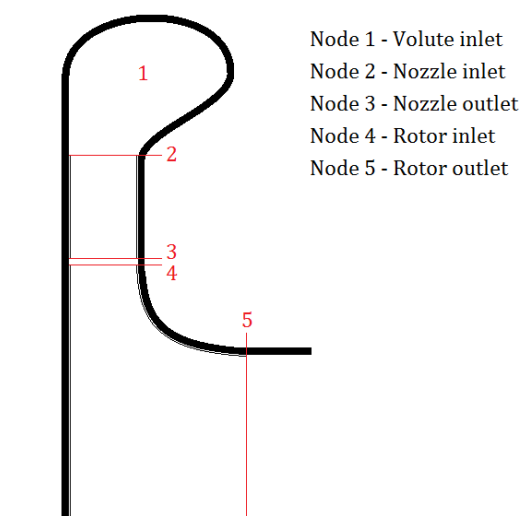
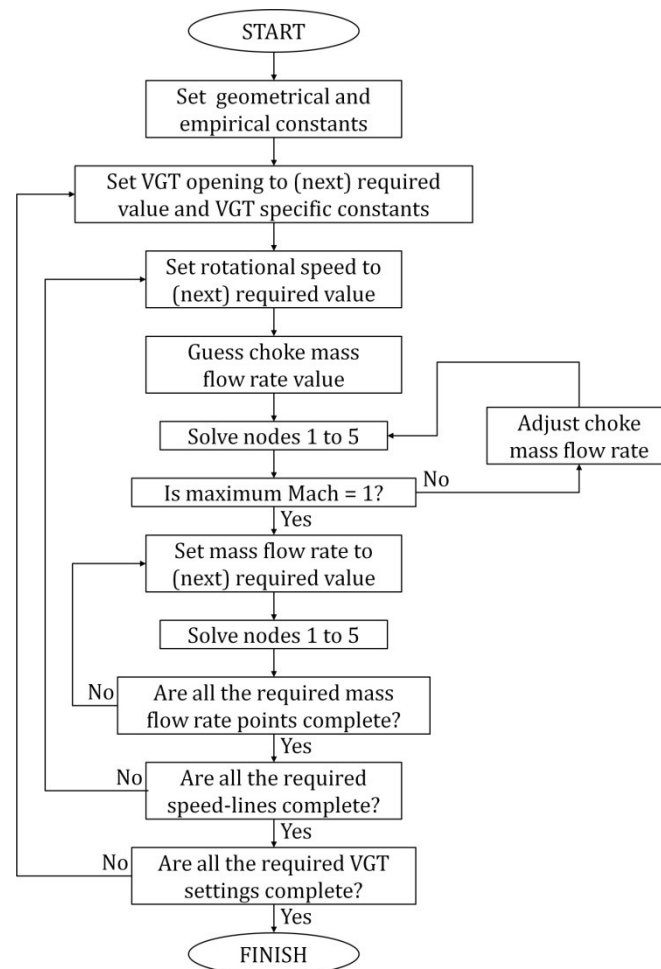


Figure 4.22 - Sketch of the turbine cross section which shows the location of the mean-line model nodes

Romagnoli (2010) has demonstrated that by adopting a particular set of empirical loss models, the off-design operation performance of the turbine can be predicted with sufficient accuracy. It has therefore been decided to adopt a similar modelling approach and a similar set of loss models to build a new, more flexible code.

The model computes the mean flow properties at five different locations within the turbine. These locations are shown in **Figure 4.22**. *Node 1* is placed at the volute inlet, *Node 2* is coincident with the inlet of the nozzles, *Node 3* is placed at the nozzles exit, *Node 4* is coincident with the rotor inlet, and *Node 5* is placed at the rotor outlet.

**Figure 4.23** shows how the model works. The model starts the simulation by reading the constants set by the user which describe the turbine geometry, losses, inlet flow thermodynamic properties and data range required. The model then sets the first VGT opening and rotational speed that have to be simulated, according to the data range required by the user. The actual turbine simulation starts when the choking conditions are computed. The code first sets an initial mass flow rate and calculates the Mach number for all the nodes. It calculates the difference between the choked flow Mach number, one, and the maximum Mach number in the



**Figure 4.23 - Structure of the turbine mean-line model**

turbine and utilizes this difference to compute a new mass flow rate. This iterative process continues until the maximum Mach number converges to one.

Once the choking conditions are known, turbine performance is calculated for a discrete number of mass flow rates up to the choking mass flow rate. When the speed-line is complete, the process above is repeated for the other speed-lines until all the speed-lines required for a single VGT opening are complete. This process is then repeated for all the desired vanes openings.

The model computes the pressure ratio for a given mass flow rate by considering the working fluid as an ideal and calorically perfect gas. The radial or axial velocity is computed for each node from the mass flow rate, the area normal to the velocity component, the density and a blockage factor which accounts for the growth of the boundary layer, as suggested by Japikse and Baines (1994):

$$C_{n\ rad/ax} = \frac{\dot{m}}{A_n B_n \rho_n} \quad (4.40)$$

The tangential velocity component is computed from, depending on the node, the nozzles angle, the rotor angle or the conservation of angular momentum. The total velocity is computed from trigonometric relations. The static properties are computed from the Mach number via isentropic relations. At every node it is necessary to iterate over the Mach number as the equations cannot be arranged in an explicit order. The heat transfer in the turbine is neglected as the model has been designed to extrapolate maps generated in cold flow conditions. As a result, the stagnation enthalpy and temperature drop only in the rotor, while they are constant in the rest of the turbine.

#### *Node 1 – Volute Inlet*

At this location the inlet stagnation conditions are set by the user. The fluid is assumed to be flowing tangentially so that the radial velocity is zero and the tangential velocity (axial relative to the inlet duct) is computed via **Equation 4.40**.

#### *Node 2 – Nozzles Inlet*

In this node the stagnation temperature is equal to that of *Node 1*, but the stagnation pressure drops due to friction. The drop in stagnation pressure is computed from the following equation, proposed by Japikse and Baines (1994):

$$k_{pl2} = \frac{P_{01} - P_{02}}{P_{02} - P_2} \quad (4.41)$$

The radial component of the flow velocity is computed via **Equation 4.40** and the tangential velocity is obtained by applying the conservation of tangential momentum. A tangential momentum loss factor is introduced to account for the frictional losses inside the volute, as suggested by Japikse and Baines (1994):

$$C_{\theta 2} = SC_{\theta 1} \frac{r_1}{r_2} \quad (4.42)$$

#### *Node 3 – Nozzles Outlet*

At the nozzles outlet the stagnation pressure loss is modelled by applying **Equation 4.41** to this node. The radial velocity component is obtained as in the other nodes and the tangential velocity is calculated from the flow angle. The flow angle is not equal to the nozzles angle and is given by:

$$\alpha_3 = \alpha_{nozz} + \alpha_{3 dev} \quad (4.43)$$

Many relations have been published in the literature to calculate the deviation angle. One of the most utilized is the one published by Mizumachi et al. (1979). However, in this model the deviation angle is calibrated directly, since the scope is to extrapolate the maps and not to predict a full turbine map with no existing experimental data. Because the large majority of nozzle flow angle deviation correlations are only geometry dependant and not flow dependant, this deviation angle is assumed to be fixed for a given VGT opening.

#### *Node 4 – Rotor Inlet*

The tangential velocity at *Node 4* is computed from the conservation of angular momentum, and no empirical loss factor is included:

$$C_{\theta 4} = C_{\theta 3} \frac{r_3}{r_4} \quad (4.44)$$

The loss of stagnation pressure between *Nodes 3* and *4* is computed via an equation proposed by Meitner and Glassman (1983):

$$P_{03} - P_{04} = \frac{4f_4 l_{34} \rho_4 C_4^2}{2D_{h4}} \quad (4.45)$$

In this equation the friction factor,  $f_4$ , is a function of the Reynolds number.  $l_{34}$  and  $D_{h4}$  are, respectively, the flow path length between *Node 3* and *4* and an hydraulic diameter.

#### *Node 5 – Rotor Outlet*

At this node the stagnation enthalpy and temperature are not constant as at the other nodes but drop as work is done by the fluid on the rotor blades. This drop is modelled via the *Euler Turbomachinery Equation*.



Several losses occur in the rotor and they must be accurately estimated to determine the flow properties at the rotor outlet. The most important of these losses is the incidence loss, which is caused by the non-ideal angle at which the flow approaches the rotor. The optimum incidence angle is computed via a relation proposed by Stanitz (1952):

$$i_{opt} = \tan^{-1} \left[ \frac{-1.98 \tan \alpha_4}{Z(1-1.98/Z)} \right] \quad (4.46)$$

In this equation  $Z$  represents the number of rotor blades. This optimal incidence angle is used to compute the loss of kinetic energy via a relation proposed by Mizumachi et al. (1979), which is based on the work of Wasserbauer and Glassman (1975):

$$L_{inc} = k_{inc} [W_4 \sin(\beta_4 - \beta_{rot\ in} - i_{opt})]^2 \quad \text{when } |\beta_4 - \beta_{rot\ in} - i_{opt}| < \pi/4 \quad (4.47a)$$

$$L_{inc} = k_{inc} [W_4 (0.5 + |\beta_4 - \beta_{rot\ in} - i_{opt}| - \pi/4)]^2 \quad \text{when } |\beta_4 - \beta_{rot\ in} - i_{opt}| > \pi/4 \quad (4.47b)$$

A second important loss is the rotor passage loss. This loss occurs due to secondary flows and friction in the rotor passage. This loss is also dependent on the incidence angle. In fact, the separation between this loss and the incidence loss is not clear, but the best results are achieved when both these losses are included (Japikse and Baines, 1994). This passage loss is calculated via an equation proposed by Futral and Wasserbauer (1965):

$$L_{pass} = \frac{1}{2} k_{pass} (W_4^2 \cos^2 |\beta_4 - \beta_{rot\ in} - i_{opt}| + W_5^2) \quad (4.48)$$

A further loss is caused by the rotor blades tip leakage. Because the blades are not touching the shroud, a secondary flow is driven through the tip gap by the pressure difference between the pressure and suction sides of the blade. This loss is calculated via a relation proposed by Rodgers (1978), where the drop in total to total efficiency is computed from **Equation 4.49**. In this equation  $h$  is the blade height and  $\varepsilon$  is the clearance height.

$$\Delta\eta_{tt} = k_{cl\ 4} (\varepsilon_4/h_4) + k_{cl\ 5} (\varepsilon_5/h_5) \quad (4.49)$$

The last major loss related to the rotor is the disk friction loss. This loss is caused by the drag on the back face of the rotor and is modelled via an equation proposed by Meitner and Glassman (1983):

$$L_{df} = \frac{0.02125 U_4^2 \rho_4^2}{\dot{m} (U_4 \rho_4 r_4 / \mu)^{0.2}} \quad (4.50)$$

The relative tangential velocity is computed from the flow relative exit angle via trigonometric relations. The relative tangential velocity is added to the blade speed to compute the actual

tangential velocity. The flow relative exit angle is obtained from the rotor exit angle and a fixed angle deviation:

$$\beta_5 = \beta_{rot\ out} + \beta_{5\ dev} \quad (4.51)$$

The deviation angle actually depends on the velocity ratio and the turbocharger rotational speed (Japikse and Baines, 1994). However, it has not been possible to find a model which describes how the angle deviates. A good match is obtained by maintaining this deviation angle fixed, and only changing it when the VGT opening is changed.

### Mean-Line Model Calibration

The new structure allowed the model to converge to the results rapidly enough so that an automatic calibration algorithm could be implemented. The chosen calibration algorithm iteratively calculates the performance maps for a range of possible coefficient values, which are stored in a matrix that has the same number of dimensions as the number of coefficients to be calibrated. The algorithm calculates the average mass flow and efficiency error for each combination of coefficients present in the matrix and then selects the set of coefficients which results in the minimum mean error. The matrix is centred around this set of coefficients and the range of the coefficients is reduced by a fixed factor (a factor of 0.9 worked well in this case). The process described above is repeated until the calculated performances stop changing significantly. This matrix based algorithm takes significantly more computation time than a derivative based algorithm, but it is more likely of finding a global minimum error rather than a local minimum error.

Because not all the coefficients could be calibrated, the model sensitivity to each of the empirical coefficients has been studied and the 8 coefficients which most affect the model have been selected. These coefficients are the volute pressure loss coefficient,  $k_{pl2}$ ; the nozzle pressure loss coefficient,  $k_{pl3}$ ; the nozzle outlet deviation angle,  $\alpha_{deviation3}$ ; the nozzles outlet blockage factor  $B_3$ ; the incidence angle loss coefficient,  $k_{inc}$ ; the rotor passage loss coefficient,  $k_{pass}$ ; the rotor outlet deviation angle,  $\beta_{deviation5}$ ; and the rotor outlet blockage factor,  $B_5$ . All the other coefficients have been set to the values recommended in the literature.

#### 4.2.2 FURTHER DATA INTERPOLATION AND EXTRAPOLATION

The turbine mean-line model has two major limitations:

- At very low mass flow rates the model cannot match the experimental data since the empirical losses models are not valid at these extreme operating conditions
- This mean-line model is not capable of predicting turbine performance beyond choking conditions

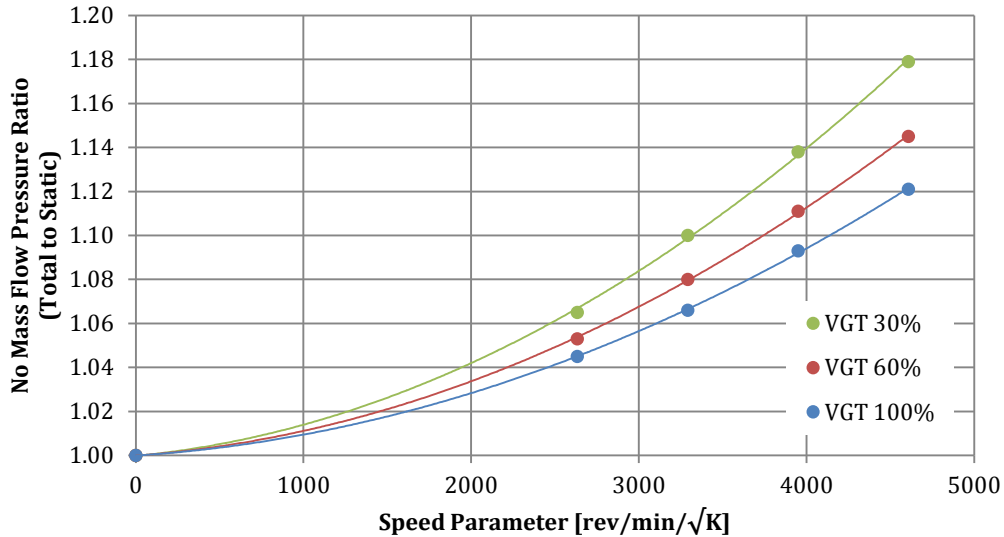


Figure 4.24 – Turbine zero-mass-flow pressure ratio interpolation over rotational speed

To overcome the issue at low pressure ratios, the data is interpolated between the minimum mass flow at which the model matches the experimental data and the point where the mass flow is zero. This zero-mass-flow point is directly obtained by interpolating the experimental data. The zero-mass-flow pressure ratio is plotted against rotational speed and a quadratic line is fitted in the data, as shown in **Figure 4.24**.

The output of the model is extrapolated beyond choking conditions by making two assumptions. The first assumption is that the mass flow rate parameter is constant beyond the choking point. The second assumption is that the efficiency drops to zero at a velocity ratio of zero. Both these assumptions are commonly made by commercial extrapolation software. The mass flow rate lines are obtained by extending the lines generated by the model with horizontal lines. The efficiency lines are obtained by fitting a cubic line between the data generated by the model and the zero-mass-flow/zero-velocity-ratio point.

A further issue is caused by the lack of data between the tested vanes openings. Not enough VGT settings have been tested to obtain satisfactory results when the data is directly interpolated between the different settings. As a result, it has been decided to interpolate the turbine data utilizing the mean-line model. This is achieved by linearly interpolating the empirical loss factors with respect to nozzle angle and by measuring the new nozzle angles and radiuses via a CAD model. The interpolated maps are then generated by running the mean-line model with these interpolated loss factors and the measured geometry.

The maps are not extrapolated to negative mass flow rate as initial simulations showed that this particular electrically assisted turbocharger is not sufficiently powerful to drive the turbine to these operating conditions.

#### 4.2.3 TURBINE MAPS EXTRAPOLATION RESULTS AND DISCUSSION

The results of the mean-line model calibration process are shown in **Figure 4.25** for the mass flow parameter and in **Figure 4.26** for the total to static efficiency. These figures demonstrate that the model is capable of matching the experimental data well. A small error occurs around the peak efficiency for the 60% VGT opening, where the model overestimates the efficiency by approximately 2%. Nevertheless, this error is acceptable as the efficiency lines predicted by the

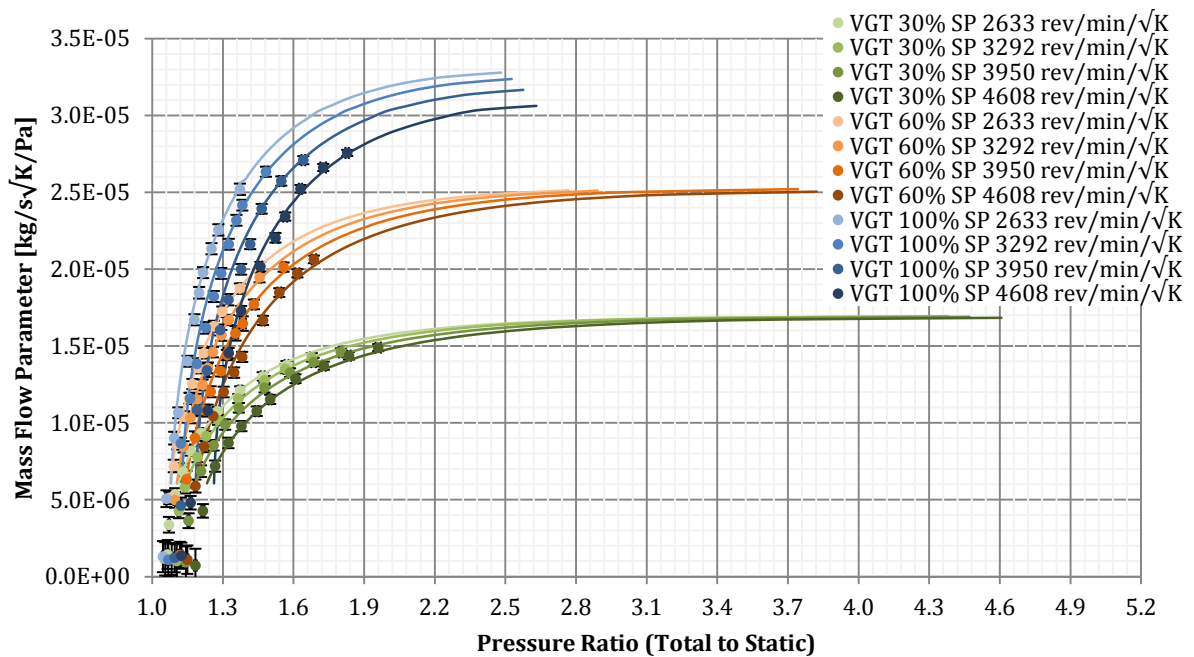


**Figure 4.25** – Mass flow parameter results of the turbine mean-line model. The continuous lines represent the model output and the dots represent the experimental data

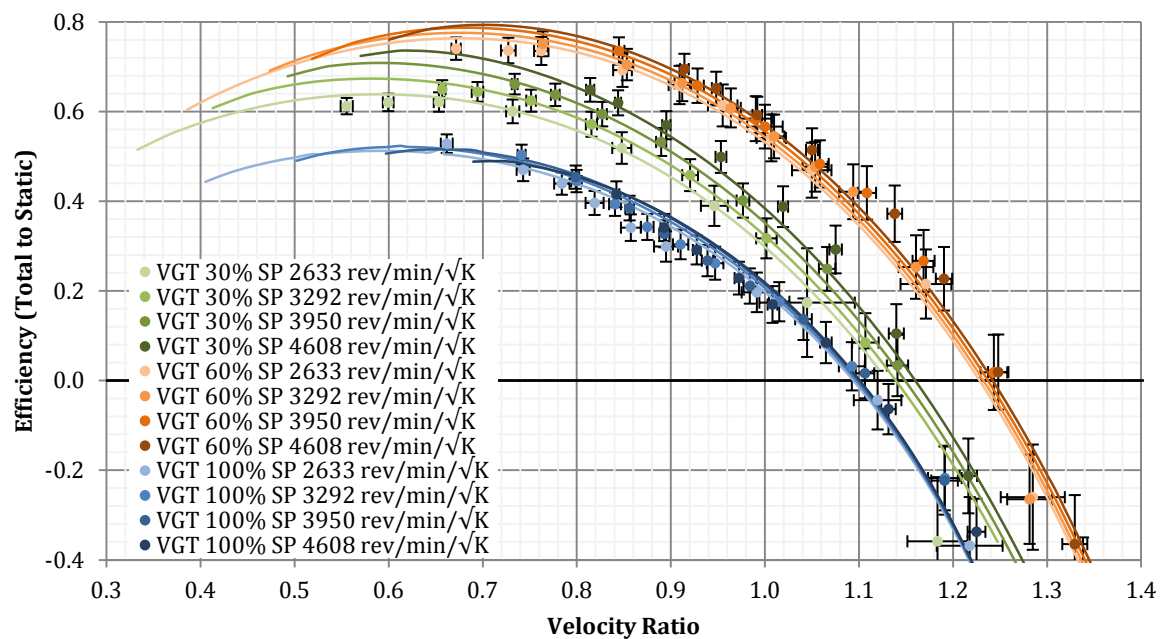


**Figure 4.26** – Total to static efficiency results of the turbine mean-line model. The continuous lines represent the model output and the dots represent the experimental data

model pass through the experimental data error bars. Small errors occur also with a VGT opening of 30% at a pressure ratio of approximately 2. In this map area, the mass flow rate is underestimated by 3.5% and the error line just misses the error box. At the same pressure ratio, the efficiency is overestimated by approximately 2.5%, and also in this case the predicted line just misses the error bars.

The discrepancies between the model and the actual turbine behaviour would probably lead to specific fuel consumption and transient response errors during the engine simulations. However, the discrepancies shown by these results are small (< 4%) and would lead to even smaller errors in the predicted engine performance. It is common to achieve specific fuel consumption errors of less than 1% even utilizing the highly scattered maps produced by the turbocharger manufacturer (**Figure 4.2**), so it is likely that a 2.5% error in turbine efficiency would have a small impact on the engine simulations. The discrepancies in mass flow rate are less important as during the engine simulations the turbocharger speed is controlled via a PID controller which adjusts the VGT opening.

**Table 4.2 - Calibrated turbine mean-line model empirical coefficients**

VGT	Nozzle Angle $\alpha_3$	Volute Pressure Loss $k_{pl2}$	Nozzle Pressure Loss $k_{pl3}$	Nozzle Blockage $B_3$	Nozzle Deviation Angle $\alpha_{3dev}$	Incidence Loss $k_{inc}$	Rotor Passage Loss $k_{pass4}$	Rotor Deviation Angle $\beta_{5dev}$	Rotor Blockage $B_5$
100%	39.4°	0.30	0.20	0.95	0.0°	0.91	0.00	17.8°	0.75
60%	63.3°	0.15	0.12	0.97	0.3°	0.92	0.00	10.0°	0.95
30%	74.4°	0.95	0.45	0.95	-5.3°	1.10	0.00	2.7°	0.90

The calibrated coefficients of the empirical loss models are shown in **Table 4.2**. Minimum stator stagnation pressure losses and blockage occur at 60% vanes opening, which indicate that the smoothest flow occurs with this vanes setting. The 100% opening leads to higher pressure losses in the volute and in the nozzles, probably due to a poor nozzle inlet incidence angle. The stator pressure loss coefficients are even higher for the 30% VGT opening. The reasons for this are that the nozzles inlet angle and volute A/R ratio are optimized for the 60% opening. At 30% opening, the nozzles incidence angle is poor and possibly leads to flow separation near the nozzles inlet. The nozzle flow deviation angle for the 30% opening is also larger than for the other openings. The reason for this is that the nozzle passage length reduces as the vanes are closed, reducing the turning capacity of the vanes. The fact that the deviation angle is negative indicates that the flow approaches the vanes with a larger angle than the vanes angle.

The deviation angle at the rotor is large and positive, which means that the rotor is underturning the flow. Because the deviation angle represents an average value, the fact that it increases as the VGT opening increases shows that the rotor becomes less effective in turning the flow as the average mass flow increases. The rotor blockage factor indicates that a flow

separation could occur with the 100% opening as the average blockage factor is lower for this opening (higher degree of blockage).

**Table 4.2** shows that the rotor passage loss is always zero. This is probably due to the fact that it is difficult to separate the passage loss from the incidence loss, as both losses depend on the incidence angle. The fact that the passage loss is always zero indicates that the secondary flow losses occurring in the rotor are better modelled via the incidence loss model.

**Figure 4.27** and **Figure 4.28** represent part of the extrapolated/interpolated data. The data has been extrapolated up to a pressure ratio of 5. As explained in the previous section, the interpolation between tested VGT openings has been achieved by linearly interpolating the loss coefficients and by running the mean-line model with the interpolated coefficients. This linear interpolation is not ideal as the coefficients do not necessarily change linearly with nozzle angle between the calibrated coefficients. Nevertheless, the efficiency maps obtained by interpolating the loss coefficients are smooth and do not show unrealistic abrupt changes as the maps obtained by directly interpolating the data do.

A further limitation of the model is that the empirical losses coefficients are maintained constant over the full turbine operating range and change only with nozzle angle. This is fine for most of the coefficients, which fit into loss models designed to predict the off-design operation losses from their respective constant coefficient. However, the blockage factors and rotor outlet deviation angle change depending on the operation conditions of the turbine. Romagnoli (2010) has made the same assumptions and has shown that off-design performance can be well

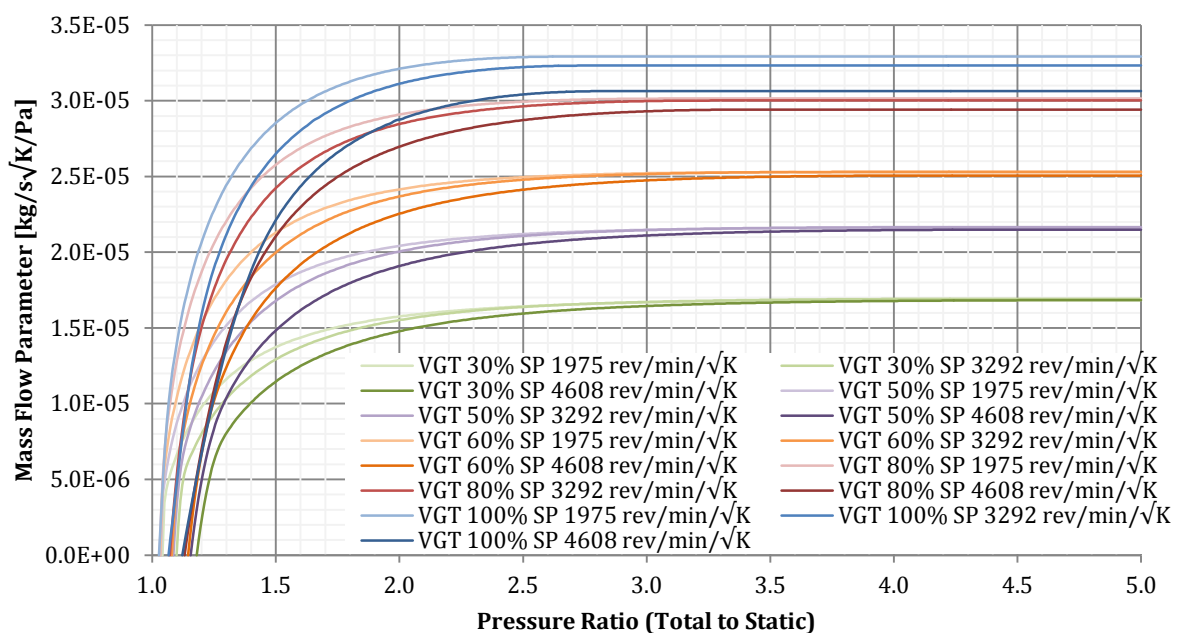


**Figure 4.27 – Turbine mass flow parameter extrapolation results**

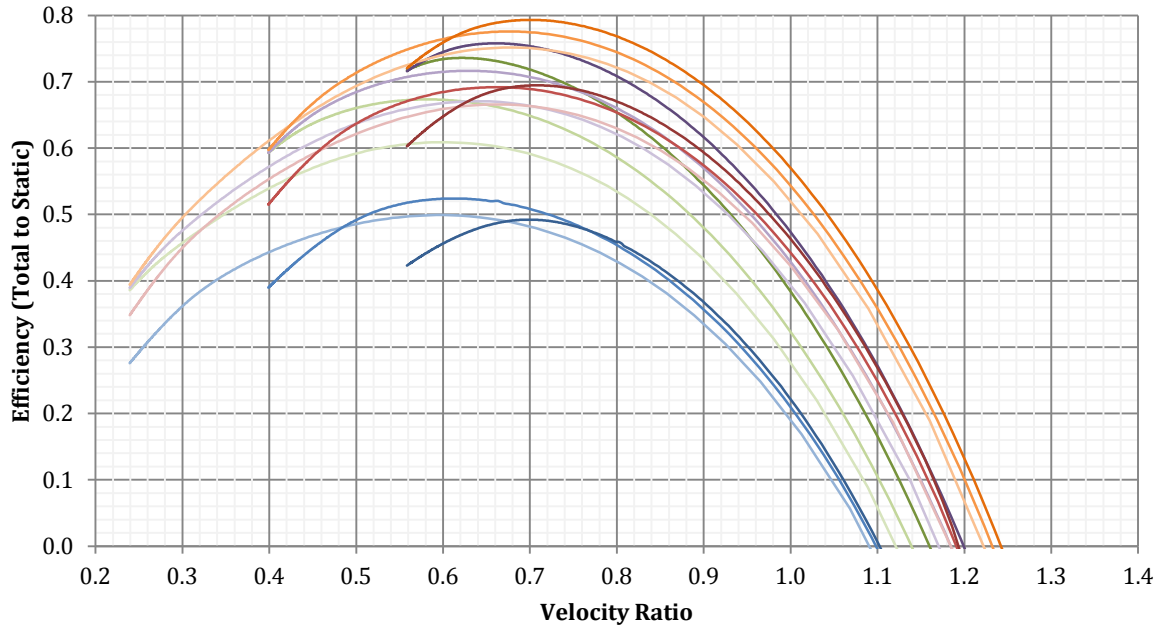


**Figure 4.28 – Turbine total to static efficiency extrapolation results**

predicted even with fixed coefficients. In any case, the mean-line model provides a map extrapolation which is based on physics, and is likely to produce more accurate data than a simple mathematical extrapolation.

To extrapolate the efficiency maps beyond choking conditions it has been necessary to assume that the efficiency speed-lines converge to the origin of the efficiency versus velocity ratio plot. This is a common assumption made in commercial software and in the literature it can be found a large number of validated turbocharged engine models that employ turbine maps extrapolated by making this assumption. The advantage over commercial software is that the amount of extrapolation required is less than on standard turbocharger maps, as the mean-line model predicts the maps up to the choking conditions. Typical turbine maps do not cover the turbine range up to choking conditions, especially at low test speeds.

### 4.3 CHAPTER SUMMARY

In this chapter the turbocharger turbine has been characterized experimentally via a novel experimental technique. This technique consists of employing the electric assistance motor/generator as a loading device, and to directly measure the turbine torque via a gimbal system and a load-cell. The advantage of utilizing a motor/generator as a loading device is that it can be utilized in motoring mode to overcome the frictional and turbine losses so that the turbine can be characterized down to a pressure ratio of 1.00. The main findings are that:

- The mass flow rate does not fall to zero at a pressure ratio of one, but at a higher pressure ratio. This is due to the centrifugal force acting on the fluid.

- Reverse mass flow, driven by the centrifugal force, occurs below the zero-mass-flow pressure ratio.
- If the blade tip speed is significantly higher than the flow tangential velocity, the rotor increases the flow kinetic energy instead of reducing it. For this reason, at low pressure ratios (i.e. high velocity ratios) the efficiency is negative.

These findings are important because electric assistance drives the turbine towards this low pressure ratio region during engine transients. Commercial turbine maps extrapolation software makes the assumption that the mass flow rate falls to zero at a pressure ratio of one, but this experiment demonstrate that this is not the case. Without this set of data, significant errors would occur during engine simulations with electric assistance.

In the second part of the chapter the turbine maps are extrapolated to higher pressure ratios and lower speeds via a mean-line model. This mean-line model is capable of matching the experimental data well, with peak efficiency errors of less than 3%. This indicates that this physics based extrapolation provides more accurate data than commercial extrapolation software, which does not consider the turbine physics. The data collected in this chapter is fed into the engine model described in **Chapter 6**, where engine transient response is studied via a one-dimensional model.



## 5. MOTOR/GENERATOR DRIVEN TURBINE UNSTEADY EFFECTS

In this chapter the unsteady effects on the turbine flow caused by the electric assistance are studied. Two different experimental studies are completed employing the gas stand facility described in the previous chapters. In the first study, the turbine speed is changed by powering the motor/generator without changing the flow control valves settings. The aim is to understand if this speed transient can generate any unsteady effect in the exhaust and turbine flow. In the second part of the chapter, the flow entering and exiting the turbine is studied via fast response pressure sensors to understand if the oscillating nature of the motor/generator torque could cause pressure fluctuations in the turbine flow.

### 5.1 TRANSIENT TURBINE TESTING

In this thesis, the unsteady effects are defined as the deviations of turbine performance from the steady state performance which occur when the turbine speed or pressure ratio is changed rapidly. Unsteady effects can be caused by turbocharger speed transients, engine loading transients, exhaust pressure pulsations generated by the opening and closing of the exhaust valves, pressure pulsations produced by the turbine rotor and stator interaction, and, in the case of electrically assisted turbochargers, pressure fluctuations caused by the oscillating torque of the motor/generator. The different frequencies at which these unsteady effects occur are shown in **Figure 5.1**.

This section of the chapter is focused on the unsteady effects caused by the turbocharger speed transients. It is important to study these speed transient effects since an electrically assisted turbocharger is capable of accelerating significantly more quickly than a standard turbocharger. We have seen in **Chapter 4** that the mass flow rate and efficiency characteristics of a turbine are a strong function of the rotational speed. Because of this, the fast turbocharger acceleration

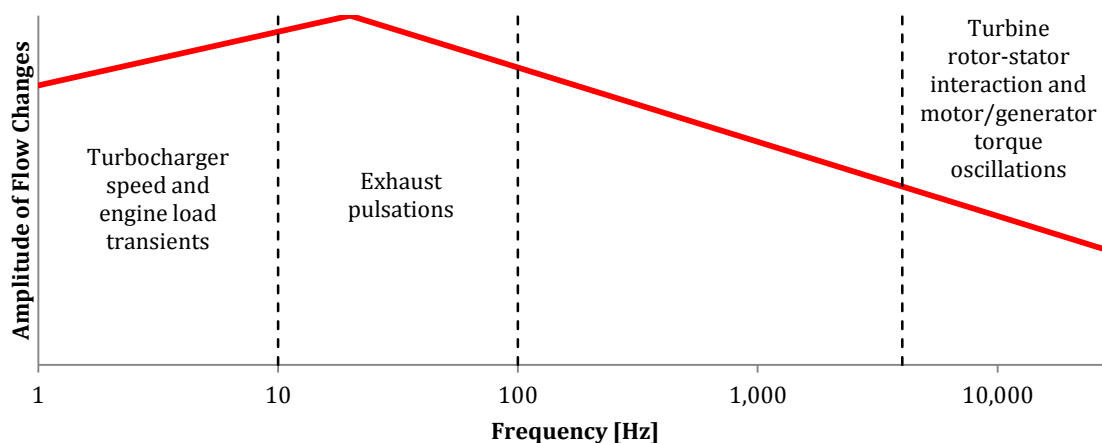


**Figure 5.1 – Graph showing the relative importance and frequency content of the different sources of flow unsteadiness in an automotive turbocharger turbine (Copeland et al., 2012)**

could generate unsteady flow effects within the turbine and exhaust manifold. These unsteady effects have to be evaluated to understand if they can adversely affect the effectiveness of electric assistance in improving the transient response of the engine.

Upon reading the relevant literature, it is clear that there is a lack of information concerning transient effects on turbine performance. Consequently, the objectives of this study are to:

- Observe if the turbine performance deviates from the steady state performance when the turbocharger is accelerated via the motor/generator
- Understand if these unsteady effects could impact the transient response of a turbocharged diesel engine

Note that the objectives of this investigation are not to study how the turbine performs on an actual engine, but to study how externally driven accelerations impact the mass flow rate and efficiency of the turbine. Therefore the unsteady effects caused by the turbine acceleration have to be studied in isolation. How the turbocharger turbine performs when mounted on an engine will be studied in **Chapter 6**, where different engine transients are simulated via a 1-dimensional engine model. Because the unsteady effects observed in this section are mainly caused by the filling and emptying of the exhaust manifold, which is one order of magnitude larger than the turbine volume, these effects will be captured also by a one-dimensional engine model.

#### *5.1.1 TRANSIENT TURBINE TESTING TEST-RIG LAYOUT*

The test-rig utilized to test the turbine in transient conditions is a modified version of the test-rig developed to characterize the turbine in steady state. The main modification consists of the replacement of the safety shutdown valve with a control valve, as shown in **Figure 5.2**. This control valve is operated to control the flow going through the turbine, while the valves upstream are set to the fully open position.

The reason to reposition the valve employed to control the flow nearer to the turbine is to isolate the turbine and the portion of the pipe-work downstream of the valve from the rest of the laboratory pipe-work. The isolation from the upstream pipe-work occurs because the pressure upstream of the valve is regulated to approximately 6 bar, and therefore the pressure ratio across the control valve is always above the critical choke pressure ratio. This means that the valve is always choked for this experiment and, for constant valve inlet pressure, the mass flow rate is maintained constant. This is a good approximation of an engine, where the mass flow rate is mainly a function of the engine speed.

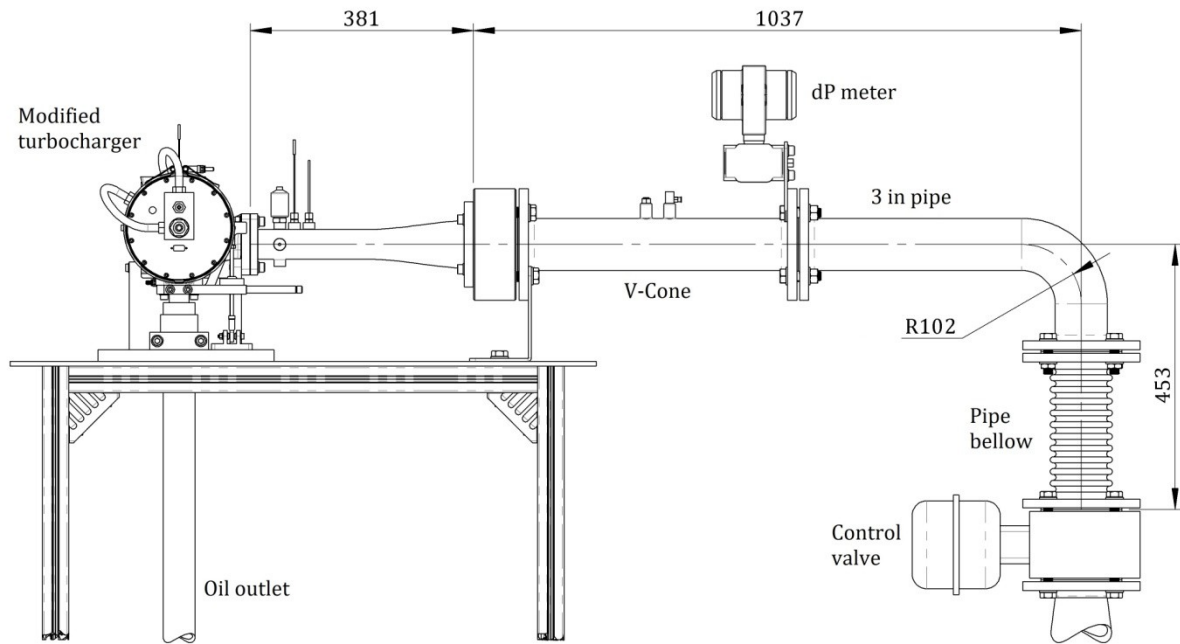


**Figure 5.2 - Drawing of the test-rig modified for transient turbine testing**

The volume of the pipe-work downstream of the control valve is approximately  $7 \times 10^{-3} \text{ m}^3$  and it is similar to the volume of an exhaust manifold for this turbocharger application. The volume of the pipe-work has to be similar to the manifold volume because the unsteady effects shown in the results section are affected by this volume. Initial testing with the control valve in the original position resulted in strong unsteady effects being recorded.

The shaft torque, shaft speed and inlet temperature measurements are identical to the steady state turbine testing described in **Chapter 4**. The position of the inlet thermocouple has been moved by 25 mm and the new position is shown in **Figure 5.3**. The inlet and outlet pressure, and the mass flow rate measurements methods have been changed as the previous methods are only suitable for steady state conditions.

### **Transient Torque Measurement**

The reaction torque on the bearing housing is measured via the system utilized for the motor/generator characterization and for the turbine steady state characterization (second data set), which is described in **Chapter 3**. However, during a transient the reaction torque on the bearing housing is not equal to the turbine torque, as a fraction of the torque produced by the turbine is utilized to accelerate the turbocharger rotor. This fraction can be calculated via *Newton's Second Law* by differentiating the rotational speed. The torque utilized to accelerate the turbo is added to the torque measured via the load-cell to obtain the turbine torque.

$$\tau_{turb} = \tau_{LC} + I \frac{d\omega}{dt} \quad (5.1)$$

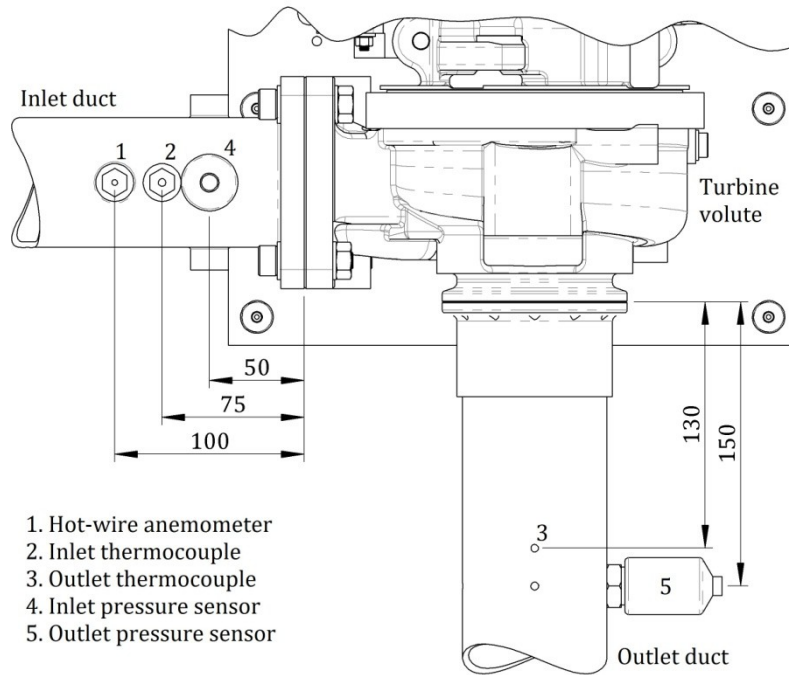


**Figure 5.3 – Location of the hot-wire anemometer, pressure sensors and thermocouples relative to the turbine housing for the turbine transient test**

### **Transient Inlet and Outlet Pressure Measurements**

The inlet and outlet pressure is measured via two strain gauge *Schaevitz P704* pressure transducers, which have a range of 0 to 3.5 bar gauge and a maximum hysteresis and non-repeatability of  $\pm 0.3\%$  F.R.O. The advantage of this sensor model is that it has a natural frequency which is higher than 2.5 kHz (depends on range), and therefore it is suitable to measure transient pressure changes.

The sensors are installed as shown in **Figure 5.3**. The annular chambers have been removed as the filling and emptying of these chambers could have potentially affected the results. This means that the pressure is measured from a single tapping at each location. This should not affect the results as the pressure is expected to be uniform around the flow area circumference. The outlet pressure sensor is mounted with the sensing axis parallel to the ground, as the vibrations are expected to have a larger magnitude in the vertical direction. The inlet pressure sensor is mounted near the turbocharger support, where the vibrations are expected to be lower.

### **Transient Mass Flow Rate Measurement**

The mass flow rate is measured via a constant temperature anemometer. A constant temperature anemometer is composed of two parts: the hot-wire probe and the circuitry which maintains the temperature constant. When the probe is immersed in a cooler flow, the flow will remove heat from the probe. The rate of heat transfer is a function of the flow velocity. The

probe is powered via a Wheatstone bridge and an amplifier is utilized to maintain the bridge balanced (i.e. the resistance of the probe is maintained equal to the resistance of the other resistive elements that form the Wheatstone bridge), as shown in **Figure 5.4**. Because the cooling effect will tend to change the resistance of the probe, the amplifier adjusts the voltage so that the resistance is maintained constant. The change in voltage is therefore a function of the flow velocity and the correlation takes the form of (Newton, 2014):

$$\left(\frac{T_{wire}-T_{ref}}{T_{wire}-T_{fluid}}\right)^{1+k_3} \left(\frac{T_{ref}}{T_{fluid}}\right)^{0.83} V^2 = k_1 + k_2 \left(\rho C \left(\frac{T_{ref}}{T_{fluid}}\right)^{0.73}\right)^{k_4} \quad (5.2)$$

In this equation  $k_1$ ,  $k_2$ ,  $k_3$  and  $k_4$  are constants that have to be calibrated,  $V$  is the voltage across the Wheatstone bridge, and  $T_{ref}$  is a reference temperature.

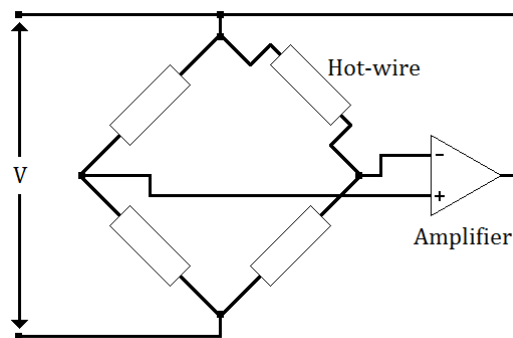


**Figure 5.4 – Circuitry of the constant temperature anemometer (Dantec Dynamics A/S, 2013)**

Because the mass flow rate is not expected to change significantly during the transients, as the volumes are relatively small and the control valve is maintained choked, the velocity profile in the pipe is assumed to not vary over the experiment mass flow rate range. By making this assumption, the centreline velocity and density is proportional to the mass flow rate. The constants of the equation above are therefore directly calibrated in steady state against the mass flow rate obtained via the *V-Cone*.

The hot-wire system is manufactured by *DantecDynamics* and is the *miniCTA* model. The probe has a wire diameter of 5  $\mu\text{m}$  and is installed at the centre of the inlet pipe, 100 mm upstream the turbine inlet (**Figure 5.3**). This system has a bandwidth of 10 kHz, so it is suitable to measure the instantaneous mass flow rate, which changes at a considerably lower frequency.

### 5.1.2 TURBINE TRANSIENT CYCLE

The transient turbocharger speed cycle has been designed to be representative of the speed transients that occur when the turbocharger is installed on an engine. A typical turbocharger transient speed trace is shown in **Figure 5.5**. The speed increases from just over 60% of the maximum turbocharger speed to over 90% in approximately 2 s. Consequently, the transient

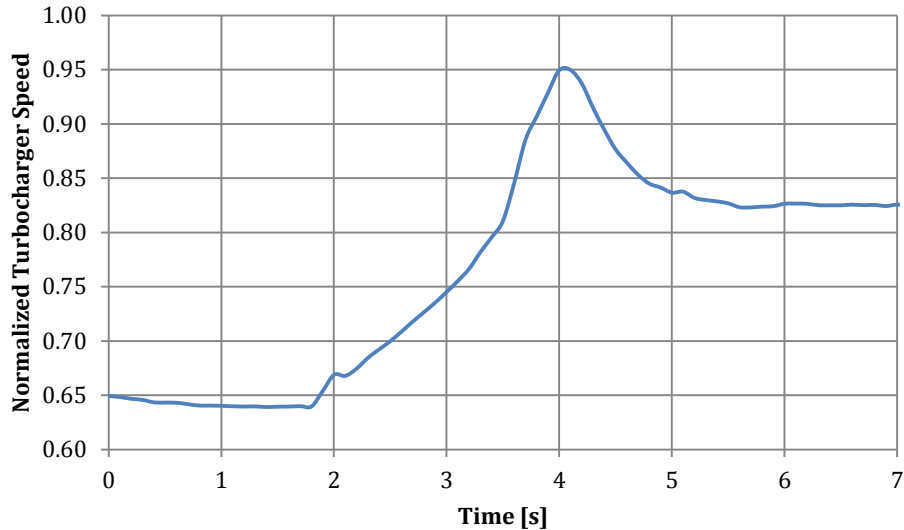


**Figure 5.5 – Typical VGT turbocharger speed trace during an engine load increase transient**

cycles in this experiment are designed so that the turbocharger speed parameter changes approximately from 2633 rev/min/ $\sqrt{K}$  to 4608 rev/min/ $\sqrt{K}$ , which corresponds to a speed change from approximately 60% to 100% of the maximum speed. The actual acceleration does not need to be matched, as an electrically assisted turbocharger accelerates more than a standard turbocharger, and the acceleration is determined by the motor/generator performance.

Four turbine speed transients are generated by powering the motor/generator without changing the settings of the air flow control valve. These four transients occur in two different cycles: *Cycle A*, where the electrical machine is operated in motoring mode, and *Cycle B*, where the electrical machine is operated in generating mode. **Figure 5.6** shows how the motor/generator is operated during the cycles.

*Cycle A* begins with the turbine running in steady state at a speed parameter of 2633 rev/min/ $\sqrt{K}$ , which is the minimum speed parameter for which steady state data has been obtained in **Chapter 4**. The electrical machine is initially off and, to generate the speed transient, it is powered in motoring mode with a torque setting of 60%. This torque setting has been chosen so that the speed parameter reached at the end of the transient is similar to the maximum speed parameter tested in steady state (4608 rev/min/ $\sqrt{K}$ ). A few seconds after the speed has stabilized (typically 5 s), the motor is turned off and the turbocharger decelerates down to the initial speed.

*Cycle B* begins at a speed parameter of 4608 rev/min/ $\sqrt{K}$  and with the motor/generator off. The electrical machine is powered in generating mode with a torque setting of 70%, so that the speed parameter drops to 2633 rev/min/ $\sqrt{K}$ . After few seconds, the motor/generator is de-

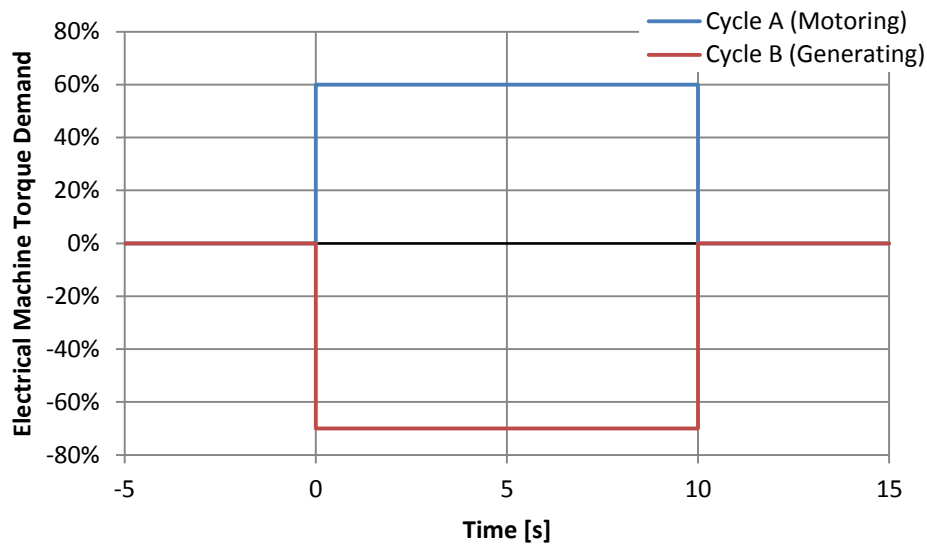


**Figure 5.6 – Motor/generator torque demand for Cycle A (motoring) and Cycle B (generating)**

energised so that the turbocharger accelerates to the initial speed parameter. Because *Cycle B* starts at a higher speed parameter than in *Cycle A*, where the bearing housing frictional load is higher, the average load in *Cycle B* is higher than in *Cycle A*.

### 5.1.3 TURBINE TRANSIENT TESTING PROCEDURE

The test-rig preparation is similar to the turbine steady state characterization. The oil system is first warmed-up, the torque measurement system is calibrated (refer to **Chapter 3**) and the air pipes are warmed-up. When the rig is ready, the data is collected via the following procedure:

1. The turbocharger speed is adjusted via the control valve until the required speed parameter is reached.
2. When the turbine inlet air temperature and rotational speed stabilize to the desired value, the sensors output logging is started.
3. The motor/generator is powered to produce the speed transient.
4. The motor/generator is turned off as soon as the first transient ends.
5. When the second transient is complete, the data-logging is stopped.
6. The turbocharger is rapidly stopped by cutting the air flow.
7. The load-cell zero offset is logged as soon as the turbocharger rotor stops.

This procedure is repeated three times for *Cycle A* and three times for *Cycle B*. The results are averaged to reduce the precision error.

The load-cell zero offset is logged after the data is collected to minimize the impact of the offset drift caused by the different thermal deformation of the turbocharger support and load-cell assembly. If the load-cell drift is measured a few seconds after the data is logged (typically >10

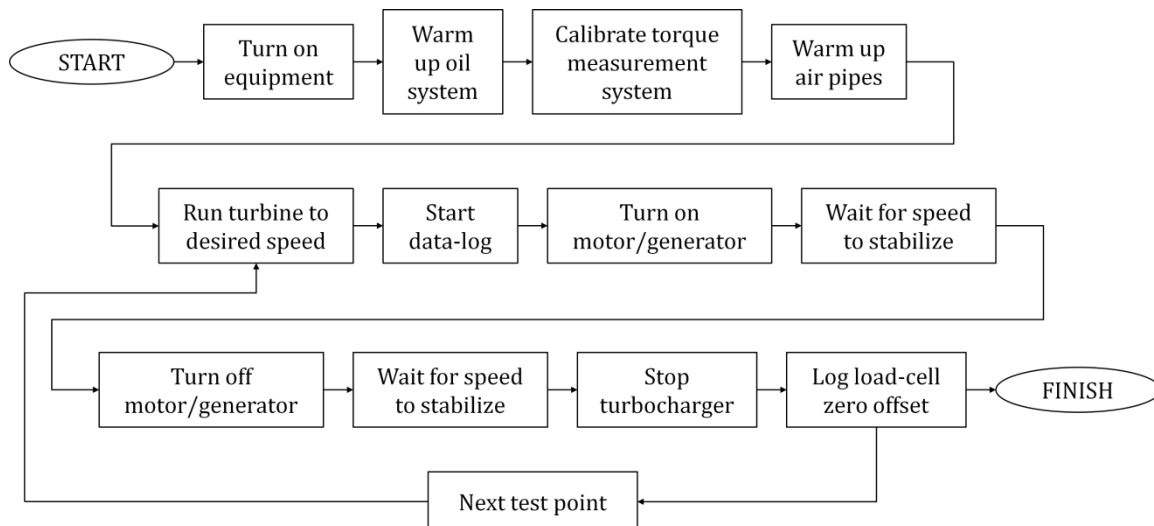


**Figure 5.7 – Transient turbine testing procedure flowchart**

s), the thermal conditions do not change significantly due to the high thermal inertia of the system. Because the cycles take less than 20 s to complete, the support and load-cell assembly thermal conditions do not change significantly during the cycle. The error caused by this offset drift has been estimated in the uncertainty analysis section.

#### 5.1.4 TURBINE TRANSIENT DATA FILTERING

During the transients, the data has been logged with a high sampling frequency to avoid phase shifts caused by the anti-aliasing filters. This made software data filtering necessary to remove the following noises:

1. Electrical noise – affecting all the measured quantities
2. Turbulence – affecting the pressure measurements and the anemometer measurements
3. Vibrations – affecting mainly the load-cell reading, but could also affect the pressure sensors and anemometer

**Table 5.1 – Turbine transient data filter parameters**

<b>Filter Type</b>	Low Pass Finite Impulse Response
<b>Frequency at Pass Band Start</b>	10 Hz
<b>Frequency at Stop Band End</b>	14 Hz
<b>Allowable Ripple in Pass Band</b>	0.0001 dB
<b>Stop Band Attenuation</b>	60 dB

The filtering of the data has been achieved in *MATLAB*, utilizing the *filtfilt* function (The MathWorks Inc., 2013). This function filters the data both in the forward and reverse direction, so that the resulting phase shift is zero (Oppenheim and Schaffer, 1989). The actual filter is a finite impulse response (FIR) low pass filter. The filter has been generated by *MATLAB* according to the specifications described in **Table 5.1**. To determine the stop band end frequency, a *Fast Fourier Transform* analysis has been carried out on the measurements signals.



It has been found that the load-cell output has high amplitude oscillations occurring at 14 Hz. To remove these output oscillations, the stop band end frequency has been set to match the frequency of the oscillations. These load-cell output oscillations were probably caused by the load-cell assembly and bearing housing acting as a mass-spring system.

#### 5.1.5 TURBINE AND AIR PIPE EQUIVALENT VOLUME AND ASSISTANCE TORQUE

In this experiment the flow through the turbine has a temperature of roughly 330 K. However, when the turbocharger is installed on a diesel engine, the flow temperature would be around 900 K. This means that to replicate the results obtained here in hot flow conditions (i.e. the same traces on the efficiency and mass flow rate parameter maps), the pipe volume and assistance torque would need to be different.

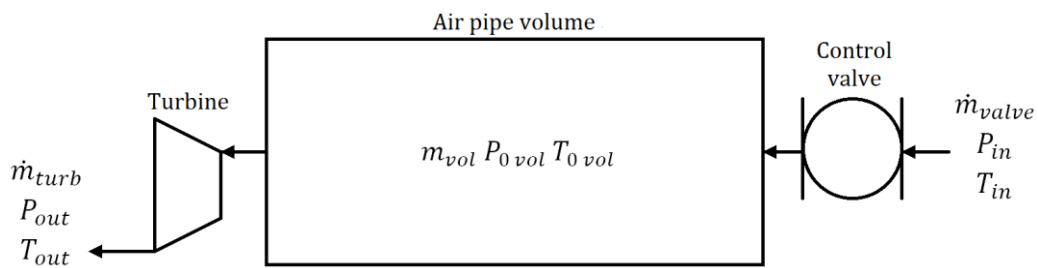


Figure 5.8 – Schematic of the turbine transient testing test-rig

A basic relation which describes how the equivalent volume and torque would change with testing temperature can be obtained by modelling the pipe between the control valve and turbine as a control volume (**Figure 5.8**). This control volume has one inlet, which is the control valve, and one outlet, which is the turbine. We know from **Chapter 4** that the turbine steady state efficiency and mass flow rate parameter can be approximated to be a function of only the pressure ratio and the speed parameter. Therefore, if the turbine behaves in a quasi-steady manner, to obtain the same mass flow parameter and efficiency traces in cold and hot flow, the only constraint is that the pressure ratio and the speed parameter time traces must be identical in both conditions. This means that to have matching time traces, the initial pressure ratio and speed parameter must be the same and the pressure ratio and speed parameter time derivatives must be identical at any moment in time:

$$(PR)_{hot,t=0} = (PR)_{cold,t=0} \quad (5.3a)$$

$$\left(\frac{dPR}{dt}\right)_{hot} = \left(\frac{dPR}{dt}\right)_{cold} \quad (5.3b)$$

$$(SP)_{hot,t=0} = (SP)_{cold,t=0} \quad (5.4a)$$

$$\left(\frac{dSP}{dt}\right)_{hot} = \left(\frac{dSP}{dt}\right)_{cold} \quad (5.4b)$$

By modelling air as an ideal gas, we can see that if the valve inlet temperature is constant, air has been flowing through the volume for a sufficiently long time and the volume is adiabatic:

$$P_{0\ vol} = \frac{m_{vol}RT_{0\ vol}}{V} \quad (5.5)$$

$$T_{0\ vol} = T_{0\ in} \quad (5.6)$$

$$\frac{dP_{0\ vol}}{dt} = \frac{dm_{vol}}{dt} \frac{RT_{0\ in}}{V} \quad (5.7)$$

The control volume mass time derivative is found via the conservation of mass:

$$\frac{dm_{vol}}{dt} = \dot{m}_{valve} - \dot{m}_{turb} \quad (5.8)$$

The mass flow rates can be described from the respective mass flow parameters:

$$MFP_{valve} = \frac{\dot{m}_{valve}\sqrt{RT_{0\ in}}}{P_{0\ in}d_{valve}^2} \quad (5.9a)$$

$$MFP_{turb} = \frac{\dot{m}_{turb}\sqrt{RT_{0\ vol}}}{P_{0\ vol}d_{rot}^2} \quad (5.9b)$$

By inserting **Equations 5.7, 5.8** and **5.9** into **Equation 5.3b**, assuming that the turbine outlet pressure is constant, the following equation is obtained:

$$\left( (MFP_{valve}P_{0\ in}d_{valve}^2 - MFP_{turb}P_{0\ vol}d_{rot}^2) \frac{\sqrt{RT_{0\ in}}}{V} \right)_{hot} = \left( (MFP_{valve}P_{0\ in}d_{valve}^2 - MFP_{turb}P_{0\ vol}d_{rot}^2) \frac{\sqrt{RT_{0\ in}}}{V} \right)_{cold} \quad (5.10)$$

If the conditions described in **Equations 5.3** and **5.4** are met and the turbine behaves in a quasi-steady manner, the mass flow parameters in hot conditions are identical to these in cold conditions at any moment in time. In addition, if the valve inlet pressure, valve diameter and turbine rotor diameter are maintained constant, **Equation 5.10** can be simplified to a relation between the volume ratio and the temperature ratio:

$$\frac{V_{hot}}{V_{cold}} = \sqrt{\frac{T_{0\ in\ hot}}{T_{0\ in\ cold}}} \quad (5.11)$$

**Equation 5.11** gives the required volume to obtain the same pressure ratio, mass flow parameter and efficiency loops obtained in this study when the inlet temperature is different. This means that if the testing is carried out at 923 K (turbo manufacturer reference temperature), the volume required to replicate the cold testing results is 1.67 larger than the

volume in this test. In other words, this means that the unsteady effects are amplified by testing in cold conditions.

**Equation 5.11** is not the only condition necessary to replicate the turbine performance traces in hot conditions. The electrical machine torque has to be different as well to achieve the same speed parameter traces. To find an equation which describes the equivalent hot conditions torque, the derivative of the speed parameter has to be found:

$$\frac{dSP}{dt} = \frac{d\omega}{dt} \frac{30}{\pi\sqrt{T_{vol}}} = \frac{\tau}{I} \frac{30}{\pi\sqrt{T_{vol}}} \quad (5.12)$$

If **Equation 5.12** is inserted into **Equation 5.4**, a relation which describes how the torque should change with temperature is found:

$$\frac{\tau_{hot}}{\tau_{cold}} = \sqrt{\frac{T_{0 \text{ in hot}}}{T_{0 \text{ in cold}}}} \quad (5.13)$$

Similarly to the volume, the equivalent torque in hot conditions is 1.67 the torque in cold conditions. This means that the equivalent hot conditions torque applied in *Cycle A* is 100% and in *Cycle B* is 117%. It is important to note that, to obtain the same performance transient traces in hot and in cold conditions, both **Equation 5.11** and **5.13** must be true.

To derive these relations it has been assumed that the turbine behaves in a quasi-steady manner. This might seem contradictory, as the scope of this experiment is to observe how turbine performance deviates from quasi-steady performance. The reason why this assumption has been made is that the unsteady effects that will be observed in the following section are mainly the results of the filling and emptying of the exhaust manifold volume, which is an order of magnitude larger than the turbine volute volume. As the unsteady effects observed are relatively small, the turbine is expected to operate in a quasi-steady manner. The relations obtained here provide a good indication of how well the unsteady effects observed via this experiment represent the unsteady effects that occur on a real engine.

#### 5.1.6 TURBINE TRANSIENT TESTING RESULTS AND DISCUSSION

This experiment produced two sets of results: the mass flow parameter traces plotted on the turbine mass flow map shown in **Figure 5.10** and the total to static efficiency traces plotted on the turbine efficiency map as shown in **Figure 5.11**. The speed parameter time traces are shown in **Figure 5.9**.

**Figure 5.10** and **Figure 5.11** show that the system does not behave in a steady manner, as the acceleration and deceleration traces on the maps do not overlap. When the turbine accelerates,

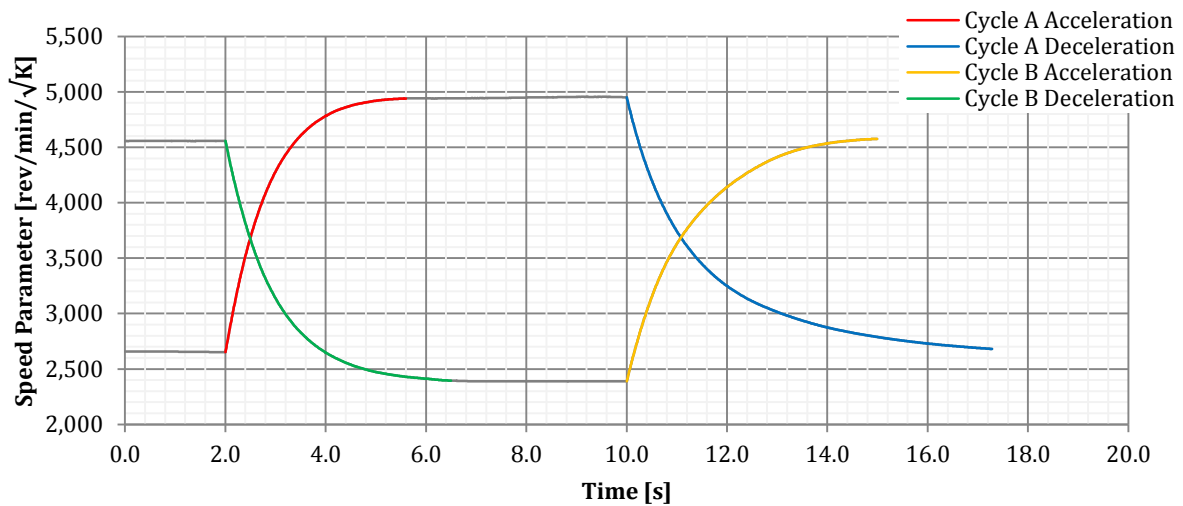


**Figure 5.9 - Turbine rotational speed traces obtained from the transient test. In Cycle A the electrical machine operates in motoring mode and in Cycle B it operates in generating mode**

both the mass flow parameter and efficiency tend to drop. When the turbine decelerates, the opposite occurs, and the efficiency and mass flow rate tend to be higher.

These unsteady effects are caused by the finite amount of time required to fill the pipe-work volume and the impact that the turbine rotational speed has on its swallowing capacity. By observing the steady state turbine mass flow rate map, it can be seen that as the speed increases, the turbine mass flow parameter reduces. Because the flow rate of mass entering the system via the control valve is fixed (the valve is choked), when the speed increases some mass starts to accumulate in the pipe and turbine volute. As a result, the pressure rises until the mass flow through the turbine matches the mass flow through the valve. If the turbine speed changes slowly, the difference between the turbine mass flow rate and the valve mass flow rate is small and the system behaves in a quasi-steady manner. However, if the turbine speed changes rapidly, as in these cases, the pressure ratio lags behind the speed, since a finite amount of time is required to fill the pipe volume. When the turbocharger decelerates, the opposite occurs. The pressure ratio drop lags behind the speed drop, as it requires a finite amount of time to expel the extra mass stored in the pipe.

It is clear from the mechanism described in the previous paragraph that these unsteady effects are caused by both the pipe and turbine volute volumes. The pipe is expected to contribute the most to these effects, as its volume is one order of magnitude larger than the turbine volume.

This filling and emptying of the volute and pipe causes both the transient mass flow and efficiency to drop (relative to their quasi-steady value) when the turbocharger accelerates and to rise when the turbocharger decelerates. During the acceleration this would result in a drop of

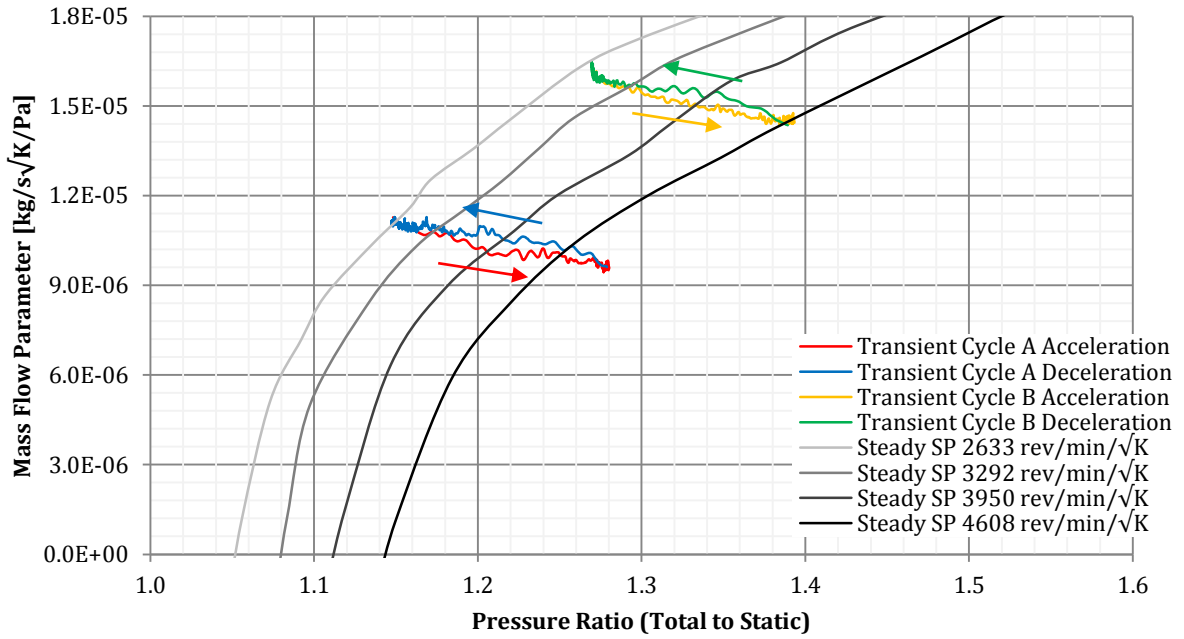


Figure 5.10 – Mass flow parameter traces during the turbine speed transients obtained from the transient test. In Cycle A the electrical machine operates in motoring mode and in Cycle B it operates in generating mode

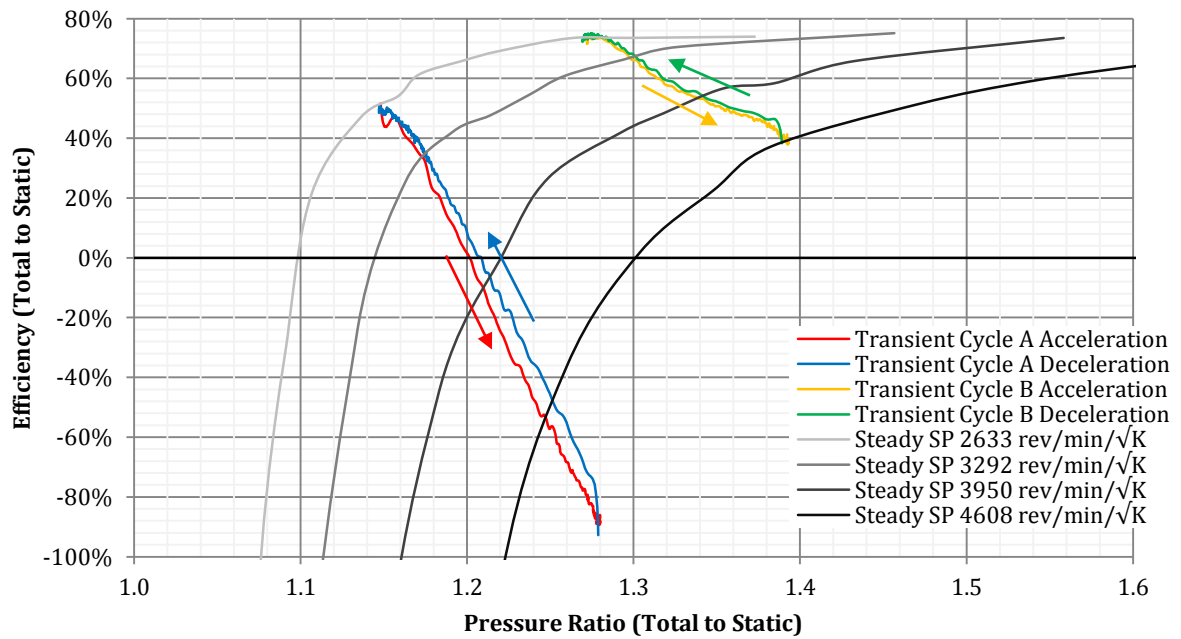


Figure 5.11 – Total to static efficiency traces during the turbine speed transients obtained from the transient test. In Cycle A the electrical machine operates in motoring mode and in Cycle B it operates in generating mode

turbine power. This would adversely affect transient response, as the power available to accelerate the turbocharger, given by **Equation 5.14**, is reduced.

$$\dot{W}_{acc} = \dot{W}_{turb} + \dot{W}_{EM} - \dot{W}_{comp} \quad (5.14)$$

The higher turbine efficiency achieved by forcing the deceleration of the turbocharger would result in an increase of exhaust energy recovery. The higher mass flow rate would result in faster exhaust manifold emptying, which would translate in lower exhaust back pressure and engine pumping losses. A further advantage of forcing the deceleration of the turbo is that part of the kinetic energy stored in the shaft is recovered. These three advantages indicate that forced turbocharger deceleration would result in a more efficient engine operation, and this should be taken into account when designing the electric assistance control system.

In this experiment it was not possible to generate a transient at higher pressure ratios, as the loading range was limited by the bearing losses. At these higher pressure ratios the steady state efficiency tends to decrease as the speed reduces. Therefore, forcing the deceleration is expected to cause the efficiency to drop compared to the quasi-steady value at these loading conditions. As a result, the exhaust energy recovered during the transient would decrease, but the pumping losses are still expected to be reduced and the turbocharger shaft kinetic energy would still be recovered.

It can be observed from **Figure 5.10** and **Figure 5.11** that the mass flow parameter and efficiency traces include ripples. These ripples are not caused by pressure waves travelling in the pipe-work because they can only be observed in the mass flow rate signal and not in the pressure signals. They cannot be caused by large eddies occurring in the flow either, since these ripples would occur at frequencies of the order of  $10^2$  Hz, and therefore are filtered out. The source of the ripples is not a flow unsteady effect, but it could be caused by the non-repeatability of the anemometer reading or fluctuations in the ground voltage. In fact, the amplitude of these ripples corresponds to the mass flow parameter precision error given in **Table 5.2**.

The scope of this experiment was to understand what happens to the turbine flow when the turbine is accelerated via the assistance power. It would have not been possible to meet this objective if the turbine was tested on a real engine, because the fluctuations caused by the turbine speed change would have been covered by other pressure and mass flow fluctuations occurring in the exhaust flow. The exhaust flow would be pulsating due to the opening and closing of the exhaust poppet valves and the mass flow rate would not be fixed, but it would increase as the turbocharger speed, and thus the compressor speed, increases. This experiment has the advantage of separating the unsteady effects caused by the turbine speed change from the unsteady effects caused by the rest of the engine. Although this experiment cannot perfectly mimic the engine behaviour, the results obtained via this experiment are important because they demonstrate experimentally that there is a filling and emptying effect in the exhaust

manifold which adversely affects the effectiveness of the electric assistance in improving engine transient response. The impact of these unsteady effects on engine transient response will be considered in **Chapter 6**, where a 1D engine model is utilized to study the impact of the electric assistance on the engine. It is possible to assess these unsteady effects computationally because the turbine operating point deviation from the quasi-steady point is mainly caused by the filling and emptying of the exhaust manifold, which is captured by a 1D engine model.

### **Uncertainty Analysis**

The uncertainty of the results is calculated with a method similar to the motor/generator and turbine steady state testing, where the bias is estimated for each independent variable and is propagated to the derived variables by differentiating the derived variables functions and adding the contribution of individual independent variables via the root sum squared method. The precision error is calculated from the scatter of the time synchronized derived variables, following the same method outlined in **Chapter 3**.

#### *Rotational Speed*

In this experiment we are interested in the instantaneous speed of the turbine. The speed is calculated from the passing frequency of the sensor wheel cut-outs. However, the sensor wheel gaps have a combined angular tolerance of  $\pm 0.2^\circ$ , and this would result in speed fluctuations of  $\pm 0.22\%$ . A further error arises from the finite sampling frequency of the data-logger. The data-logger manufacturer quotes a maximum digital pulse width measurement error of  $\pm 100$  ns. This measurement error would result in a speed error of only  $\pm 0.06\%$  at the maximum testing speed. The maximum combined rotational speed error would be  $\pm 0.23\%$  of the reading (RSS method).

Nevertheless, the data plotted in this chapter is filtered via a low pass filter, which reduces the error to zero. This is because the filter pass band frequency is much lower than the passing frequency of the sensor wheel cut-outs, so that the random speed value oscillations around the actual speed value are damped by the filter.

#### *Torque*

The torque is measured by summing the load-cell reading to the torque obtained from the rotor acceleration. As a result, the torque measurement has the same bias components of the steady state testing, plus the errors caused by the acceleration and the inertia uncertainty.

The bias components of the load-cell reading are: the hysteresis and non-linearity caused by gimbal bearings friction and load-cell accuracy, the geometric tolerances of load-cell calibration arm, the load-cell zero offset drift, and the torque imposed on bearing housing by leaking air.

The torque obtained from the rotor acceleration has two bias components. The first component is caused by the speed uncertainty discussed above, but this error is reduced to zero by filtering. The second error is caused by the uncertainty in the inertia quoted by the manufacturer, which is  $\pm 1\%$ .

For the results shown in this chapter, the mean combined bias is  $\pm 0.014$  Nm in *Cycle A* and  $\pm 0.016$  Nm in *Cycle B*. The maximum combined bias is  $\pm 0.022$  Nm in *Cycle A* and  $\pm 0.024$  Nm in *Cycle B*.

#### *Mass Flow Rate*

The bias in mass flow rate is estimated from the calibration process of the hotwire anemometer and is 7 g/s. This error includes the bias generated by assuming that the flow velocity profile across the pipe does not change with mass flow rate. The anemometer bias error must be summed to the bias of the *V-Cone* which is utilized to calibrate the anemometer, which is 3 g/s. A further source of error is the leakage that occurs through the gimbal bearings of the torque measurement system (refer to **Section 3.1.7**). For the results shown in this chapter, in both cycles the mean and maximum combined bias is  $\pm 0.0079$  kg/s and 0.0080 kg/s respectively.

#### *Inlet and Outlet Pressure*

The sensors utilized to measure the inlet and outlet pressures have a poorer accuracy than the *ScaniValve* system utilized in steady state. The maximum hysteresis and non-linearity error of the sensors is 1050 Pa and, combined to the barometer error of 30 Pa it gives a total bias of 1050 Pa (barometer error contribution is negligible when components are summed via RSS method).

#### *Inlet Temperature*

The thermocouple accuracy is 1.5 K. The uncertainty in the recovery factor causes a further systematic error which depends on the flow velocity. In addition to these errors, the thermocouple will not be able to pick up instantaneous temperature changes due to its thermal inertia. The temperature changes would be caused by the changes in flow velocity and by the pressure ratio change across the control valve (Joule-Thomson effect). The mean combined bias is  $\pm 1.5$  K in *Cycle A* and  $\pm 1.6$  K in *Cycle B*. The maximum combined bias is  $\pm 1.6$  K in both cycles.

#### *Derived Variables*

The bias in the derived variables has been calculated by differentiating the derived variables functions with respect to each independent variable and by multiplying this derivative by the bias of the independent variable. The individual contributions have been summed together via the root sum squared method. The precision error has been found by time synchronizing the



repeated measurements and by calculating the derived variable scatter at every time step. The precision error has been calculated from the scatter via **Equation 3.9**. The maximum uncertainty for each derived variable is given in **Table 5.2**.

**Table 5.2 - Transient turbine testing results uncertainty**

	Derived Variable	Systematic Error ( $\pm$ )		Precision Error ( $\pm$ )		Total Error ( $\pm$ ) (RSS)	
		Mean	Max	Mean	Max	Mean	Max
Cycle A	Pressure Ratio (Total to Static)	0.016	0.016	0.0022	0.0049	0.016	0.017
	Speed Parameter [rev/min/ $\sqrt{K}$ ]	8.3	12	19	47	21	49
	Mass Flow Parameter [kg/s $\sqrt{K}$ /Pa]	$1.2 \times 10^{-6}$	$1.2 \times 10^{-6}$	$1.1 \times 10^{-7}$	$3.4 \times 10^{-7}$	$1.2 \times 10^{-6}$	$1.3 \times 10^{-6}$
	Efficiency (Total to Static)	0.10	0.17	0.018	0.083	0.11	0.19
Cycle B	Pressure Ratio (Total to Static)	0.017	0.017	0.0059	0.0087	0.018	0.019
	Speed Parameter [rev/min/ $\sqrt{K}$ ]	7.6	11	36	44	37	45
	Mass Flow Parameter [kg/s $\sqrt{K}$ /Pa]	$1.1 \times 10^{-6}$	$1.1 \times 10^{-6}$	$9.9 \times 10^{-8}$	$3.7 \times 10^{-7}$	$1.1 \times 10^{-6}$	$1.2 \times 10^{-6}$
	Efficiency (Total to Static)	0.067	0.071	0.0057	0.025	0.067	0.075

### Experiment Improvements

This experiment is well suited to study the filling and emptying effect in a qualitative manner and it allowed to fully meet the objectives of the study. There is no reason to improve the accuracy of the measurements as the experiment is qualitative by nature, since the results of this experiment cannot be utilized to accurately quantify the impact of the exhaust manifold filling and emptying on engine transient response. The only improvement would be to use Pitot tubes to measure the mass flow rate and to use more than one probe at different locations in the flow cross section. This is expected to improve the mass flow rate measurement accuracy and thus make the mass flow rate loop clearer.

## 5.2 MOTOR/GENERATOR OSCILLATING TORQUE IMPACT ON TURBINE FLOW

In the previous section of this chapter, the unsteady effects caused by the low frequency turbine speed transients have been studied. In this second section, the focus shifts on the right side of the frequency spectrum represented in **Figure 5.1**. Here the unsteady effects caused by the high frequency motor/generator torque oscillations are studied.

The motor/generator implemented in this assisted turbocharger does not produce a continuous torque. For a switched reluctance machine, such as the one implemented in this assisted turbocharger, the torque varies depending on the alignment between the rotor and stator poles, and the current in the windings, as shown in **Equation 5.15**.

$$\tau = \frac{1}{2} \frac{dL}{d\theta} I^2 \quad (5.15)$$

The individual phase torque can oscillate from zero, which occurs when the poles do not overlap so there is no change in inductance; to a maximum value, which occurs when the current reaches a peak. In some situations, the torque can also become of the opposite sign to what is expected (i.e. negative in motoring mode and positive in generating mode). This situation occurs

if current is present in the windings when the inductance gradient is of the incorrect sign. Because this electrical machine has 6 stator poles and 4 rotor poles, the torque will oscillate 12 times each rotor revolution. Since the arc length of both the stator and rotor poles is approximately equal to 30°, no significant phase torque overlap is expected to occur.

The motor/generator torque fluctuations cause the turbocharger rotor to cyclically accelerate and decelerate. This speed fluctuation could generate pressure waves in the turbine flow and, if these pressure waves are sufficiently strong, they might affect turbine performance. The objectives of this study are therefore to:

- Analyze the pressure waves at the inlet and outlet of the turbine
- Understand if the motor/generator generates pressure waves of significant amplitude
- Understand if these pressure waves could affect turbine performance

### 5.2.1 IMPACT OF OSCILLATING TORQUE INVESTIGATION DESCRIPTION

In this experiment the turbocharger is run at constant speed and the inlet and outlet pressures are measured via high frequency pressure sensors. The data collected by the sensors is processed by performing a *Fast Fourier Transform* to obtain its frequency spectrum. The spectrums obtained with the motor/generator powered are then compared to the spectrums obtained with the motor/generator unpowered. If the torque oscillations of the electrical machine cause any pressure wave, it will be clearly seen as a spectrum peak which is only present when the motor/generator is on.

Different motor/generator torque and turbine speed parameter combinations are tested. When the electrical machine is powered in generating mode the torque is set to 100%, as this torque setting causes the largest rotor speed oscillations. Ideally, the motoring torque would also be set to 100%. However, the turbine and motor/generator are only loaded by the frictional losses in the bearing housing, and therefore it has only been possible to power the motor/generator in motoring mode at the maximum speed parameter and only with a 50% torque setting. At lower speeds it was not possible to power the turbine torque in motoring mode while having significant turbine flow. The combinations of turbine speed parameters and turbine speeds tested are summarized in **Table 5.3**.

**Table 5.3 – Rotational speed and loading conditions tested during the motor/generator torque oscillations impact investigation**

Turbine Speed Parameter [rev/min/√K]	Motor/Generator Torque Settings Tested
2633	0%, -100%
3292	0%, -100%
3950	0%, -100%
4608	+50%, 0%, -100%

This experiment is carried out in cold flow conditions. This means that, to obtain the same speed parameter which would be obtained in hot conditions, the turbine speed is lower. However, the frequency of the oscillations is proportional to the actual turbocharger speed and not to the turbine speed parameter, hence the oscillations in this experiment will have a lower frequency than on the engine (1.67 times lower with an exhaust temperature of 923 K). Moreover, because the motor/generator torque is constant up to about 90,000 rev/min and then drops, for the three highest speeds tested the torque oscillations have a larger magnitude than on the engine. This is a favourable situation, since this test represents a worst case scenario.

The pressure sensors are positioned near the turbocharger, therefore it is likely that they will be subjected to significant electrical noise radiated from the motor/generator and vibrations caused by the pulling effect that the electrical machine stator has on the rotor. Both the electrical noise and mechanical vibrations will disturb the sensor measurement and the frequency of these disturbances would have the same frequency of the pressure waves generated by the oscillating torque (12 times the rotational speed). To differentiate between noise and actual pressure waves, the test is run twice for each speed and assistance torque combination: once with the pressure sensor free to sense the flow and once with the passage between the sensor and the flow blocked, but with the sensor installed in the same location. By comparing the FFTs obtained with the sensors free and blocked, it is possible to understand if the peaks observed are caused by actual pressure waves or by noise.

### 5.2.2 IMPACT OF OSCILLATING TORQUE INVESTIGATION TEST-RIG

The test-rig utilized in this experiment is the same utilized in the turbine transient motoring test (**Figure 5.2**), and is described earlier in this chapter. The only modification consists of the replacement of the *Schaevitz* pressure sensors with *Kulite XCQ-062* piezo-resistive pressure sensors. The new sensors are installed at the same location of the *Schaevitz* sensors, which is shown in **Figure 5.3**. These *Kulite* miniature differential pressure sensors have a frequency range of 0 to 300 kHz, so they are suitable to measure the high frequency pressure waves generated by the electrical machine. These sensors also have low sensitivity to mechanical vibrations, only  $3 \times 10^{-4}\%$  FS/g. The maximum combined non-linearity, hysteresis and repeatability of these sensors is  $\pm 0.5\%$  FSO and the pressure range is 0 to 3.5 bar. The sensors are connected to the *NI 9237 CompactDAQ* data-logger module, which has a built-in power supply and anti-aliasing filter.

When the sensors have to be blocked, they are screwed into small steel cylinders which have a threaded cavity. These cylinders are then screwed into the pressure sensors holes in the pipe.

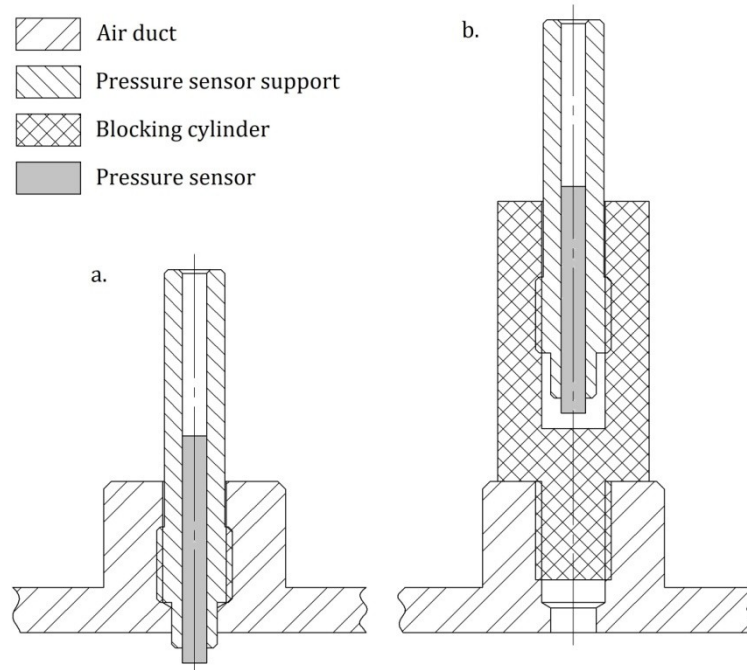


**Figure 5.12 – schematic showing how the miniature pressure sensors are mounted. In part a. the sensor is free and in part b. the sensor is blocked**

This allows to mount the pressure sensor approximately in the same position of when it is not blocked.

The sensors are not mounted flush to the pipe internal surface, but are protruding into the flow by approximately 2 to 3 mm. This means that the pressure acting on the sensors is not the static pressure, but is between the static and the stagnation pressure. This is unimportant as we are not interested in the actual pressure value, but on the frequency content of the pressure oscillations.

### 5.2.3 IMPACT OF OSCILLATING TORQUE INVESTIGATION EXPERIMENTAL PROCEDURE

The test-rig preparation is similar to the other turbine related experiments. However, since the turbine torque is not measured in this experiment, the torque measurement system is not

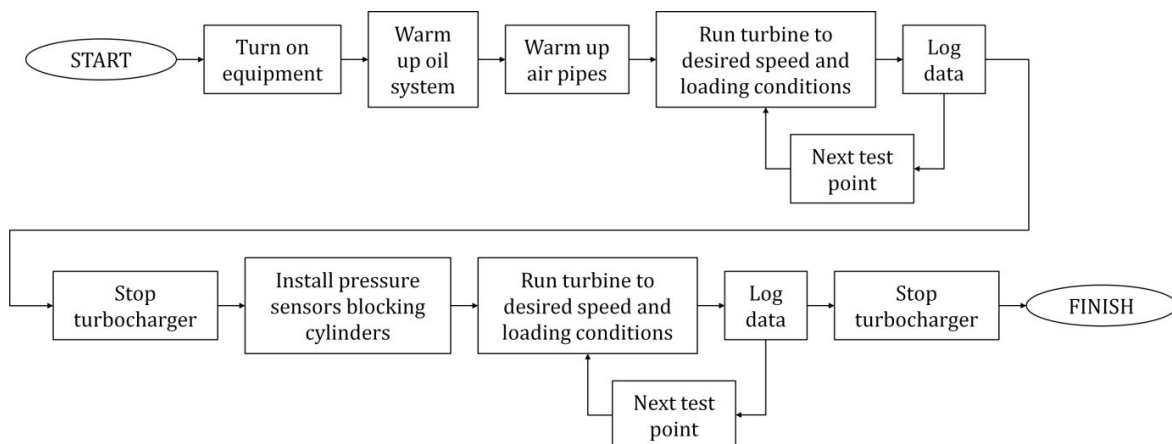


**Figure 5.13 – Motor/generator oscillating torque impact on turbine flow testing procedure flowchart**

calibrated. The data collection procedure is also simpler than in other experiments, as the turbocharger does not need to be stopped to log the load-cell zero offset. The data is first collected with the sensors free to sense the flow for all the combinations of motor/generator torque setting and turbine speed parameter given in **Table 5.3**. Then the sensors are blocked, and the noise data is collected. **Figure 5.13** shows the experiment procedure flowchart.

#### *5.2.4 IMPACT OF OSCILLATING TORQUE INVESTIGATION RESULTS AND DISCUSSION*

In this section the data obtained for the 4608 rev/min/ $\sqrt{K}$  speed parameter is presented. This speed parameter is the only speed condition at which it has been possible to test both in motoring and generating mode. The data obtained at the lower rotational speed is not presented in this section as it does not show features different from the features shown here, so it does not contribute to the understanding of the electrical machine oscillating torque effects. The frequency spectrums obtained from the lower speed data can be found in **Appendix B**.

The frequency spectrums of the pressure data collected in the experiment are shown in **Figure 5.14** for the inlet pressure and in **Figure 5.15** for the outlet pressure. By observing these figures, the following comments can be made:

- When the electrical machine operates in generating mode, no amplitude peak can be observed at the 12<sup>th</sup> rotor speed harmonic, which is the fundamental motor/generator torque frequency. On the contrary, in motoring mode a peak at the 12<sup>th</sup> rotor speed harmonic can be observed both at the inlet and at the outlet of the turbine, but these peaks have low amplitude.
- The pressure fluctuations occurring at the blade passing frequency (10<sup>th</sup> rotational speed harmonic, the rotor has ten blades) are dominant.
- The results are not caused by the effect of electrical noise or mechanical vibrations on the sensors and sensor cabling, as when the sensors are blocked the same frequency spectrum features cannot be observed.

The reason why the pressure fluctuations at the motor/generator torque oscillation frequency are small can be understood by looking at the mechanism by which the rotor speed oscillations generate pressure waves. When the turbine rotor vibrates, its blades impose an oscillatory displacement on the fluid particles in contact with the blades surfaces. This generates pressure waves in the flow and the amplitude of these pressure waves is a function of the vibration velocity. If the magnitude of the rotor speed fluctuations is calculated by assuming a sinusoidal torque fluctuation, the resulting peak-to-peak speed oscillation at the rotor inlet tip is only 0.0128 m/s when the turbine rotational speed is 84,000 rev/min. This speed fluctuation is not

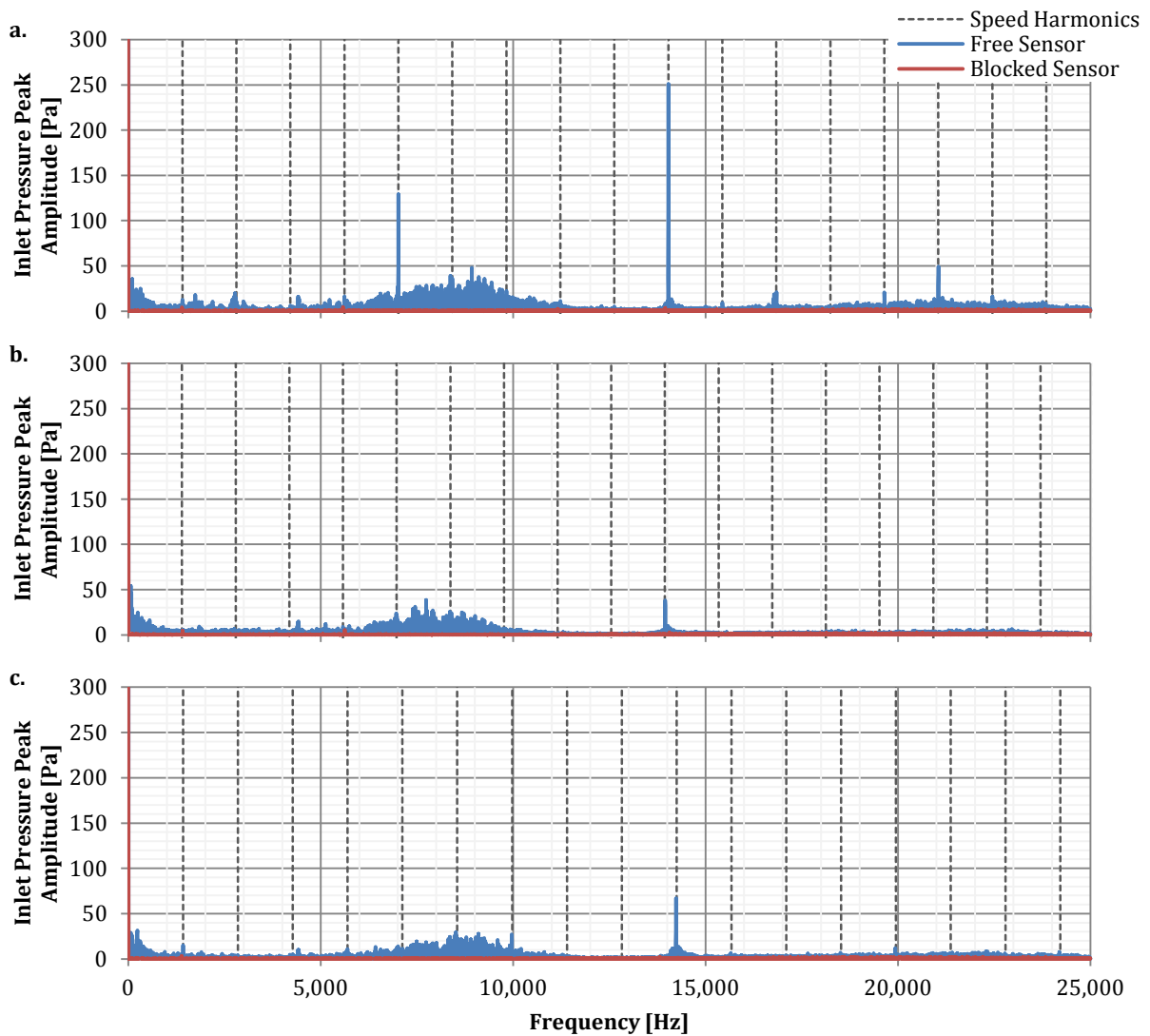


**Figure 5.14 – Frequency spectrum of the inlet pressure signal. In part a. the electrical machine is operating in motoring mode with a 50% torque demand, in part b the electrical machine is operating in generating mode with a 100% torque demand and in part c. the electrical machine is off**

large and therefore it generates pressure waves whose amplitude is not sufficiently high to be observed when the electrical machine operates in generating mode.

Pressure fluctuations can only be observed at the 12<sup>th</sup> rotational speed harmonic when the electrical machine operates in motoring mode. In this situation the turbine is weakly loaded and the mass flow rate is only 60 g/s. The reason why the pressure fluctuations can only be observed when the mass flow rate is low, is that turbulence dissipates the sound energy into heat (Howe, 1984). Because the flow turbulent kinetic energy increases as the mass flow rate increases, as shown in **Table 5.4**, the pressure fluctuations caused by the motor/generator are dissipated faster at high turbine loading. This also explains why the magnitude of the amplitude peaks at the blade passing frequency drops as the turbine loading increases.

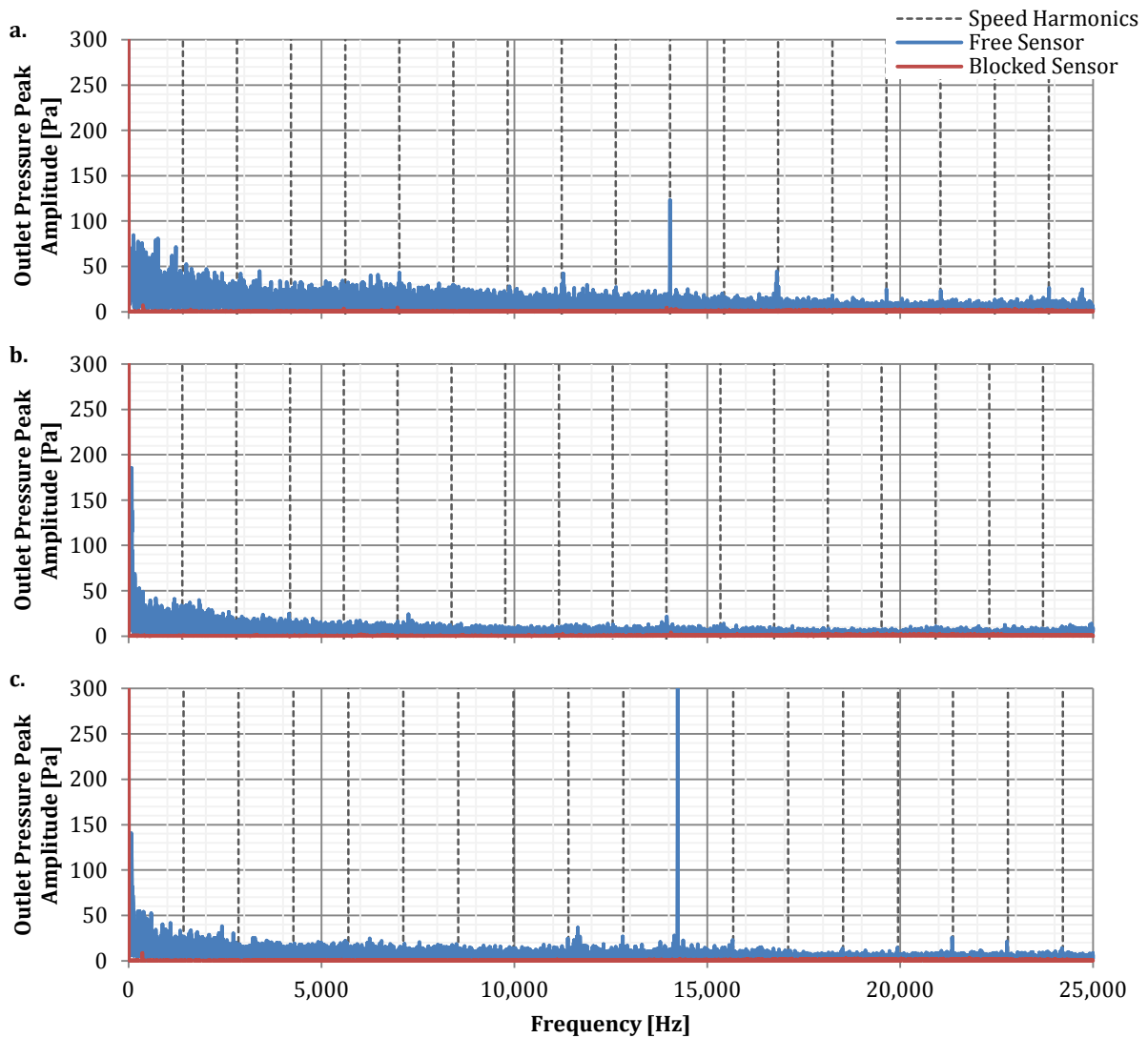


**Figure 5.15 – Frequency spectrum of the outlet pressure signal. In part a. the electrical machine is operating in motoring mode with a 50% torque demand, in part b the electrical machine is operating in generating mode with a 100% torque demand and in part c. the electrical machine is off**

The turbulent kinetic energy is given by **Equation 5.16**. In this equation  $u'$ ,  $v'$  and  $k'$  are the amplitude of the velocity oscillations in the x, y and z axes. These velocity oscillations are caused by the turbulent motion of the flow and are defined as the instantaneous deviation from the mean flow velocity.

$$KE_{turbol} = \frac{1}{2} (\overline{u'^2} + \overline{v'^2} + \overline{k'^2}) \quad (5.16)$$

**Table 5.4** shows the values of the turbulent kinetic energy at the pipe centre. These values have been obtained via the hot-wire anemometer described in the previous section.

**Table 5.4 – Turbulent kinetic energy at pipe centre for different turbine loading conditions**

Loading Condition	Turbulent Kinetic Energy at Pipe Centre (100 to 10,000 Hz)
50% Motoring	1.709 J/kg
0%	3.522 J/kg
100% Generating	4.938 J/kg

The pressure oscillations observed when the machine operates in motoring mode might not be entirely caused by the rotor vibration, but also by the mechanical vibration of the turbine stator and ducts. The vibrations caused by the oscillating motor/generator stator reaction torque are transmitted from the bearing housing to the turbine volute and air ducts, so that these components are also vibrating. Similarly to the turbine rotor vibrations, the vibrating movement of the internal surfaces of the stator and ducts generate pressure waves in the flow. The actual vibration amplitude at the 12<sup>th</sup> speed harmonic is not known, as the accelerometer implemented to measure the bearing housing vibrations has a maximum measuring frequency of 10 kHz. Nevertheless, at lower speeds the bearing housing vibration magnitude at the 12<sup>th</sup> speed harmonic is only 0.0003 m/s, which is 43 times lower than the rotor vibration, and this vibration magnitude is not expected to increase as the rotational speed increases. Consequently, the major source of the pressure oscillations observed at the motor/generator torque ripple frequency is the rotor vibration. This is confirmed by a feature of **Figure 5.14a**, where the amplitude of the pressure waves at the 1<sup>st</sup> speed harmonic is lower than the pressure waves occurring at the 12<sup>th</sup> speed harmonic, despite the fact that the amplitude of the vibrations occurring at this lower frequency is 15 times higher than the amplitude of the bearing housing vibrations occurring at the motor/generator torque oscillation frequency.

The pressure waves amplitude peak at the 10<sup>th</sup> rotor speed harmonic is caused by the turbine rotor-stator interaction and, because it is not caused by the motor/generator, it occurs also when this device is off. The peak caused by the stator-rotor interaction always occurs at the 10<sup>th</sup> rotor speed harmonic because this frequency corresponds to the blade passing frequency (10 rotor blades). This means that the frequency of the rotor-stator interaction is always similar to the frequency of the motor/generator oscillating torque. However, these two sources generate pressure waves of very different amplitude, as the amplitude of the blade passing frequency peaks is always several times larger than the amplitude of the oscillating torque frequency peaks.

In **Figure 5.14** three other peaks can be observed when the motor/generator operates in motoring mode: at the 5<sup>th</sup> rotor speed harmonic, at the 14<sup>th</sup> rotor speed harmonic and at the 15<sup>th</sup> speed harmonic. It is not clear what is causing the peak at the 5<sup>th</sup> speed harmonic, but it cannot be caused by the motor/generator, as it cannot impose an oscillating torque or force on the system at that frequency. Although the electrical machine can vibrate at frequencies different from the 12<sup>th</sup> speed harmonic due to the possible magnetic imbalance, the frequencies it can generate are always even, as shown in **Table 5.5**, since the electrical machine has six stator poles and four rotor poles. Moreover, the accelerometer readings do not show a peak in amplitude at that frequency, while they do show a high amplitude peak at the 12<sup>th</sup> rotor speed



harmonic when lower speeds are tested. This peak cannot be caused by the interaction between the pulsations at the blade passing frequency and the motor/generator torque pulsations either, as this interaction would produce an amplitude peak at the 2<sup>nd</sup> harmonic of the rotor speed. This is because the pulsations generated by the rotor-stator interaction and the pulsations generated by the motor/generator align twice per revolution. This amplitude peak occurring at the 5<sup>th</sup> rotor speed harmonic is probably generated by an air column resonance, as smaller peaks can be observed at the same frequency also with different loadings and rotational speeds. The peak at the 15<sup>th</sup> speed harmonic is the 3<sup>rd</sup> harmonic of the peak observed at the 5<sup>th</sup> speed harmonic. The peak at the 14<sup>th</sup> speed harmonic is also not caused by the motor/generator, as a peak at the same rotational speed harmonic can also be observed when the electrical machine is off.

**Table 5.5 - Frequencies of electrical machine force and torque oscillations**

	<b>Radial Force Fluctuations Frequencies</b>	<b>Angular Torque Fluctuations Frequencies</b>
Normal motor/generator operation	No fluctuations	Speed x12 and harmonics
One stator pole of different length or damaged coil	Speed x4 and harmonics	Speed x4 and harmonics
One rotor pole of different length	Speed x6 and harmonics	Speed x6 and harmonics
Weaker or stronger phase	No fluctuations	Speed x4 and harmonics
Stator eccentricity	Speed x12 and harmonics	No fluctuations
Rotor eccentricity (unaligned with poles and mechanically balanced)	Speed x12 and harmonics	No fluctuations

The results of this experiment indicate that the electrical machine torque oscillations cause fluctuations in rotor speed, which in turn generate low amplitude pressure waves in the turbine flow. As the peak-to-peak speed oscillation at the rotor inlet tip has been calculated to be only 0.0128 m/s, the change in incidence angle within an oscillation cycle is negligible and this fluctuation is very unlikely to cause any change to the inlet incidence loss, which is the dominant loss in a turbocharger radial turbine. This vibration could affect the laminar to turbulent transition of the boundary layer forming on the rotor blades and thus affecting the rotor passage loss. However, the flow entering the rotor is turbulent and this would force the laminar to turbulent transition to occur near the leading edge, a phenomenon called “bypass transition” (Martinez-Botas, 1993), (Newton, 2014). In addition, the boundary layer is already disturbed by the much stronger pressure pulsations caused by stator and rotor interaction, which occur at a frequency similar to the rotor oscillation frequency. Because of these two flow features, the weak rotor oscillations are unlikely to further shift the boundary layer laminar to turbulent transition point and thus the friction losses inside the rotor cannot be significantly affected.

From this study, it can be concluded that the motor/generator torque oscillations have a negligible impact on turbine performance because:

- Pressure fluctuations at the motor/generator oscillating torque frequency cannot be observed when the electrical machine operates in generating mode.
- Low amplitude fluctuations at the motor/generator oscillating torque frequency can only be observed in motoring mode, where the mass flow rate through the turbine is only approximately 60 g/s. The amplitude of these oscillations at the turbine inlet is 12 times lower than the amplitude of the oscillations occurring at the blade passing frequency, at the outlet it is 3 times lower.
- Because the turbine is tested in cold flow conditions, the amplitude of the rotor displacement oscillations is amplified by the higher motor/generator torque and by the lower oscillation frequency.

### 5.3 CHAPTER SUMMARY

The turbine flow unsteady effects caused by the turbocharger electric assistance have been studied in this chapter to understand if they can impact turbine performance. The electric assistance generates unsteady effects via two different mechanisms: by increasing the turbocharger acceleration capability and by causing the turbine rotor to vibrate due to the oscillating nature of motor/generator torque.

The first section of the chapter is focused on the low frequency unsteady effects caused by the turbine speed transient. The turbine has been characterized on a gas stand while the rotational speed was rapidly changed via the electric assistance. The mass flow rate through the flow control valve has been maintained constant by keeping the valve choked. The volume of the pipe-work between the control valve and turbine is representative of the exhaust manifold volume. The main findings are that:

- The turbine operating point deviates from the quasi-steady operation point during the transient
- During an acceleration event, the efficiency and mass flow rate tend to drop, and this could negatively impact the turbocharger acceleration due to the reduced turbine power
- The deviation from the quasi-steady operation is caused by the filling and emptying of the turbine volute and exhaust manifold (represented by the volume between the control valve and the turbine). The exhaust manifold volume is the major contributor, as its volume is one order of magnitude larger than the turbine volute volume

These results are important because they show that the low frequency unsteady effects caused by the turbine acceleration could have an impact on engine transient performance. This impact will be analyzed in **Chapter 6**, where different engine transients are simulated via a one-

dimensional engine model. Although the data obtained in this experiment will not be fed into the engine model, the understanding gained from this experiment will help to analyze the simulated engine transients.

In the second section of this chapter, the high frequency unsteady effects caused by the motor/generator oscillating torque have been investigated. The turbine has been tested on a gas stand with different levels of motor/generator power, and the turbine inlet and outlet pressures have been analyzed in the frequency domain. The main finding is that the pressure fluctuations caused by the motor/generator oscillating torque have low amplitude, and it is possible to observe these fluctuations only when the machine operates in motoring mode. In the discussion of the results it has been argued that:

- The changes in turbine blade tip speed are not sufficiently large to affect the rotor incidence loss, which is the dominant turbine loss
- The low amplitude pressure oscillations generated by the motor/generator cannot significantly affect the location of the laminar to turbulent transition and therefore they cannot significantly affect the rotor passage loss.

The results of this second experiment are important because they show that the torque oscillations have a negligible impact on turbine performance. This means that the transient assistance and regenerating capabilities of the system are not significantly affected by the motor/generator torque oscillations.

## 6. STEADY AND UNSTEADY IMPACT OF TURBOCHARGER ASSIST ON DIESEL ENGINE

In this chapter a low order model of an off-road 6-cylinder, 7-liters diesel engine is described. This model has been validated against engine and turbocharger experimental data, both in steady and transient conditions. Different boost levels have been simulated in steady state conditions to study the impact on engine brake specific fuel consumption. Engine load steps have been simulated to study the impact of electric turbocharger assistance on the engine dynamics.

### 6.1 TURBOCHARGED DIESEL ENGINE MODEL DESCRIPTION

#### 6.1.1 ENGINE AND TURBOCHARGER DETAILS

The engine modelled consists of a 6-cylinder, 7-liter diesel engine with single stage turbocharging and intercooling. This engine is designed for off-road applications such as construction machinery, mining machinery and power generators. These types of applications require a constant engine speed with fast torque transient response.

The turbocharger can either be assisted or non-assisted. The non-assisted turbocharger consists of a centrifugal compressor powered by the radial turbine described in **Chapter 4** and **5**. The compressor and turbine are connected together by a single shaft supported by two hydrodynamic journal bearings and a thrust bearing. The assisted turbocharger version has the same turbine, compressor and bearing system as the non-assisted version, but it includes the motor/generator described in **Chapter 3**.

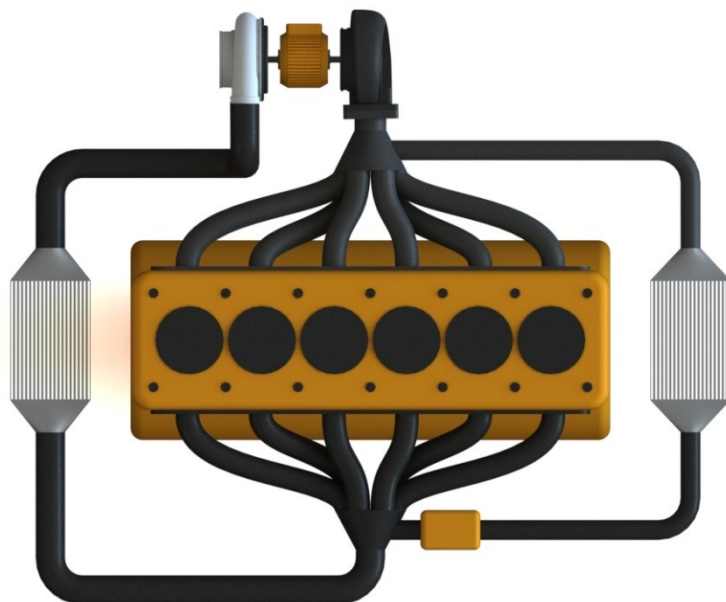


Figure 6.1 – Representation of the turbocharged diesel engine modelled

The engine is equipped with an exhaust gas recirculation (EGR) system to reduce NOx emissions. This system is of the high pressure type where the gases are driven by pressure pulsations in the exhaust manifold. The quantity of exhaust gases recirculated is controlled by a valve governed by the engine control module (ECM). In the EGR loop there is a one way valve to prevent reverse flow.

**Table 6.1 - Engine specifications**

<b>Cycle</b>	4-stroke diesel
<b>Displacement</b>	7.01 L
<b>Bore</b>	105 mm
<b>Stroke</b>	135 mm
<b>Compression ratio</b>	16.5
<b>Nominal speed</b>	1800 rev/min
<b>Engine inertia (including flywheel)</b>	1.481 kg m <sup>2</sup>
<b>Dynamometer inertia</b>	1.250 kg m <sup>2</sup>
<b>Turbocharger inertia</b>	70.71 kg mm <sup>2</sup>
<b>Electrically assisted turbocharger inertia</b>	82.71 kg mm <sup>2</sup>
<b>Motor/Generator max shaft power</b>	5.39 kW

### 6.1.2 DYNASTY ENVIRONMENT

*Dynasty* is a multi-purpose dynamic simulation program proprietary to *Caterpillar* (Caterpillar Inc., 2013). It allows the development of gas, hydraulic, electrical and mechanical models through a graphical interface. It includes prebuilt models such as combustion chambers, engine crankcase, inertias, 1D ducts, volumes, coolers, turbine and compressors.

*Dynasty* simulates the system dynamics by integrating over time the partial differential equations which describe the model by means of an *Adams-Moulton* numerical technique (Cellier and Kofman, 2006).

### 6.1.3 CUSTOM COMPONENTS MODELS

The sub-models described in this section have been created by the author. These sub-models have been built within the *Dynasty* environment utilizing mathematical operators and lookup tables.

#### **Turbine Model**

The turbocharger turbine has been modelled by means of the efficiency and the mass flow rate maps presented in **Chapter 4**. The inputs to the maps are total to static pressure ratio  $PR = P_{0\ in}/P_{is\ out}$ , speed parameter  $SP = N/\sqrt{T_{0\ in}}$ , and vanes opening. The output of the mass flow rate map is mass flow rate parameter  $MFP = \dot{m}\sqrt{T_{0\ in}}/P_{0\ in}$ , while the output of the efficiency map is total-to-static efficiency  $\eta_{ts} = \tau\omega/\dot{W}_{is}$ .

By knowing the inlet total temperature and pressure, the actual mass flow is computed from the definition of the mass flow rate parameter. The turbine exit temperature is computed from the following equation:

$$T_{0\ out} = T_{0\ in} \left[ 1 + \eta_{ts} \left( PR^{\frac{1-\gamma}{\gamma}} - 1 \right) \right] \quad (6.1)$$

The turbine torque is obtained from the conservation of energy:

$$\tau = \frac{\dot{m} c_p (T_{0\ in} - T_{0\ out})}{\omega} \quad (6.2)$$

The turbine model also estimates the axial force on the shaft which is required by the bearing housing model. The axial force is calculated via the equation below, which is derived by summing the forces acting on the compressor and turbine wheels.

$$F_{ax} = \frac{8\pi P_{in} R T_{in}}{\omega^2} \left( 1 - e^{\frac{\omega^2}{8RT_{in}} (r_{shaft}^2 - r_{tip\ in}^2)} \right) - \frac{\dot{m}^2}{\rho_{out} A_{out}} - P_{out} r_{tip\ out}^2 \pi - 2\pi \left[ \frac{P_{in} - P_{out}}{r_{tip\ in} - r_{tip\ out}} \frac{(r_{tip\ in}^3 - r_{tip\ out}^3)}{3} + \left( P_{out} - \frac{P_{in} - P_{out}}{r_{tip\ in} - r_{tip\ out}} R_{tip\ out} \right) \frac{(r_{tip\ in}^2 - r_{tip\ out}^2)}{2} \right] \quad (6.3)$$

The first term represents the force on the back of the rotor, the second term is the force imposed by the change in axial momentum of the turbine gases, the third term represents the force imposed by the outlet pressure and the last term represents the force imposed by the pressure on the turbine shroud. The subscripts “in” and “out” refer to the inlet and outlet of the turbine rotor.

The rotor inlet Mach number is required to calculate the static flow properties through isentropic relations. This Mach number is given by:

$$M_{in} = \frac{\dot{m}}{\rho_{in} A_{flow\ in\ max} X_{VGT} \sqrt{\gamma R T_{in}}} \quad (6.4)$$

In **Equation 6.4** the area is the effective maximum flow area at the nozzle outlet  $A_{flow\ in\ max} = 2r_{tip\ nozzle\ max} \pi h \cos(\alpha_{nozzle\ max})$ , which is multiplied by the VGT opening fraction to find the actual effective flow area. The gas specific heat constants are obtained from the JANAF tables.

### Motor/Generator Model

The motor/generator has been modelled following a quasi-steady approach. The machine torque range is obtained from two different functions of shaft angular velocity, one for motoring and one for generating. These maps are taken from the motor/generator controller settings and have been validated in **Chapter 3**. The model assumes that the torque required is delivered instantaneously as long as it is within the machine torque range.

The electrical energy consumed or produced is obtained from an efficiency map whose inputs are motor/generator shaft angular velocity and output power. The efficiency map implemented is the one obtained in **Chapter 3**.

The rotor drag load is computed from a function of angular velocity. This function has been obtained from the CFD analysis described in **Chapter 3**. The model includes an inertia which accounts for the increase in inertia due to the longer shaft and motor/generator rotor.

#### 6.1.4 DYNASTY BUILT-IN COMPONENT MODELS

The sub-models described in this section are built-in within *Dynasty*. These sub-models are combined together by the user to form dynamic models of engines or other machines.

##### **Compressor Model**

The compressor model calculates torque and mass flow rate from non-dimensional performance maps and inlet and outlet flow properties. This model obeys the conservation of mass, conservation of atoms and conservation of energy laws from which it calculates the outlet temperature and gas composition. The compressor maps have been provided by the turbocharger manufacturer.

This model considers the heat loss through the scroll and computes it via an empirical relation for convective heat transfer. This empirical relation requires the compressor outlet diameter and the scroll internal surface area. A heat transfer factor is available to tune this heat loss.

The axial force imposed on the turbocharger shaft by the compressor rotor is computed from the inlet and outlet pressures and rotor dimensions. These dimensions have been measured directly from the compressor and consist of the shaft diameter, inlet and outlet blade tip diameter and the impeller nose diameter. No calibration constant is required.

##### **Bearing Housing Model**

The bearing housing model is based on Petroff's approximate method (Ugural, 2003) where the thrust bearing load is a function of axial displacement. It is a physics based model, so bearings clearances, diameters and lengths are required to compute the frictional power loss.

This model is capable of calculating bearing losses in transient conditions. To achieve this it computes the instantaneous shaft axial displacement from a one-dimensional linear motion model. The data it requires consists of a stiffness coefficient, a damping coefficient and the mass of the full turbocharger rotor assembly.

The convective heat transfer from the oil to the bearings is computed via the Nusselt number obtained from a Prandtl number and a Reynolds number. The constants of the algebraic expression relating these non-dimensional numbers can be tuned.

### **Combustion Chamber Model**

The *Dynasty* combustion chamber model contains a single-zone combustion model and a heat loss model. It computes the force exerted on the piston by knowing the instantaneous pressure and the cylinder bore. The model obeys the laws of conservation of mass, conservation of atoms and conservation of energy. Cylinder blow-by is ignored.

The single-zone combustion model computes the instantaneous heat release rate from the quantity of fuel and oxygen available in the cylinder at that precise time. The rate at which fuel and air mix together is accounted for through a mixing rate factor, which is a quadratic function of fuel jet velocity parameter ( $JVP = v_{jet}/\sqrt{P_{cyl}}$ ). The constants of this function are calibrated by the user as they depend on engine and injector geometries. The combustion model also computes the ignition delay by means of an *Arrhenius* type equation and the fuel cetane number. The model assumes that all the fuel is burned inside the combustion chamber.

The heat loss model considers both the convective and conductive heat transfer. The thermal conductivity, thermal diffusivity, surface area and effective thickness of the cylinder head, liner and piston are required to calculate conductive thermal resistance. The convective heat transfer model is based on the work of Woschni (1967). To calculate the convection resistance, the model needs to know the combustion chamber surface area, cylinder bore and the swirl momentum. The swirl momentum is found by integrating over time the net rate of momentum change, which is computed from the cylinder valves mass flows and inlet swirl velocity. This last quantity is given as a function of inlet valve mass flow which is found experimentally by *Caterpillar*.

### **Cylinder Valves and Camshaft**

The flow through the cylinder valves is computed via the method given by both Heywood (1988) and Ferguson and Kirkpatrick (2001). This method requires the valve diameter, the lift, which is given as a function of crankshaft angle, and the discharge coefficient, which is given as a function of valve lift. The valve lift function has been obtained from the camshaft geometry while the discharge coefficient has been measured experimentally by the engine manufacturer. No valve bouncing is assumed.

The model also computes the heat loss through the valve and port. To calculate the heat transfer across the valve it requires the valve equivalent thickness, valve face thermal conductivity, valve



thermal diffusivity and the stem thermal resistance. For the heat transfer through the port it requires the diameter and length of the port, the wall thickness, thermal conductivity, density and specific heat of the wall.

### **Engine Crankcase Model**

The engine crankcase model computes the kinematics of the crankshaft, pistons and connecting rods and calculates the output torque. To account for the friction losses, a friction mean effective pressure (FMEP) map, measured experimentally from the engine manufacturer, has been provided. The geometrical data which it requires consists of the connecting rods length, the pistons stroke and the firing order. A value for the engine inertia is required to calculate angular accelerations.

### **Ducts**

*Dynasty* includes duct type elements that can model the flow in quasi-one-dimension. This means that the gas only flows along one-dimension but the flow cross sectional area can vary. The duct model obeys the conservation of mass, atoms, energy and momentum laws, but it cannot model supersonic flow. The cross sectional area is assumed to vary linearly across the element and therefore the model only needs the inlet and outlet diameters and the length of the duct. Multiple elements can be joined together to model more complex duct shapes.

The duct elements can compute the convective and conductive heat transfer from the gas to ambient. The internal and external convection thermal resistance is calculated from empirical relations, while the conductive thermal resistance is computed from *Fourier's Law*. The required geometrical and material properties of the wall are the thickness, roughness, density, heat capacity and conductivity.

The duct type element has been used to model the manifolds runners, the duct between the intake and the compressor, the duct between the compressor and the intercooler, the duct between the intercooler and the intake manifold, the duct between the exhaust manifold and the turbine, the duct between the turbine and the exhaust, the duct between the exhaust manifold and the EGR cooler, the duct between the EGR cooler and the EGR valve, and the duct between the EGR valve and the intake manifold.

### **Volumes**

The engine volumes that cannot be represented as ducts are modelled with volume type elements. These elements are zero dimensional, which means that they do not model the momentum equation and that the fluid properties within the element are homogeneous. The elements obey the conservation of mass, atoms and energy laws.

The volume elements can compute the heat transfer from the gas to ambient in a similar way to the duct elements. The internal convective thermal resistance is estimated via an empirical relation which requires a characteristic length and diameter to calculate a characteristic Reynolds number. To account for non-cylindrical volume shapes the user has to calibrate a heat loss factor.

The engine components which have been modelled as volume elements are the inlet and exhaust manifolds and the volume inside the EGR valve.

### **Valves and Nozzles**

Valves and nozzles have been modelled as orifice plates with a constant discharge coefficient. Nozzle elements have been used to model sharp changes in duct diameters. Valves have been utilized to model the intake pressure loss, intercooler pressure loss and exhaust back pressure.

### **Coolers**

*Dynasty* includes a cooler model which computes the heat transfer from an effectiveness map, the air and coolant mass flow rates, and the temperatures of the fluids.

### **Inertias**

Inertias are used to compute shafts accelerations through *Newton's Second Law of Motion*. The accelerations are then integrated over time to obtain the angular velocity.

## **6.2 TURBOCHARGED DIESEL ENGINE MODEL VALIDATION**

The *Dynasty* engine model has been validated by comparing the simulation results against experimental data. The combustion chamber model has been calibrated separately by matching experimental in-cylinder pressure traces. The calibrated combustion chamber model has then been inserted in a complete engine model to validate the air system. The turbocharger transient behaviour has been validated by comparing the simulation results against the experimental data presented in **Chapter 5**.

### *6.2.1 COMBUSTION CHAMBER VALIDATION*

To validate the combustion chamber model, a simplified single-cylinder engine model has been generated. This model includes modified intake and exhaust manifolds with the runners of the missing cylinders removed. Pressures and temperatures have been specified at the intake manifold inlet and exhaust manifold outlet. A simplified EGR loop has also been included. In this loop the temperature and mass flow rate at the EGR valve outlet have been imposed as boundary conditions.

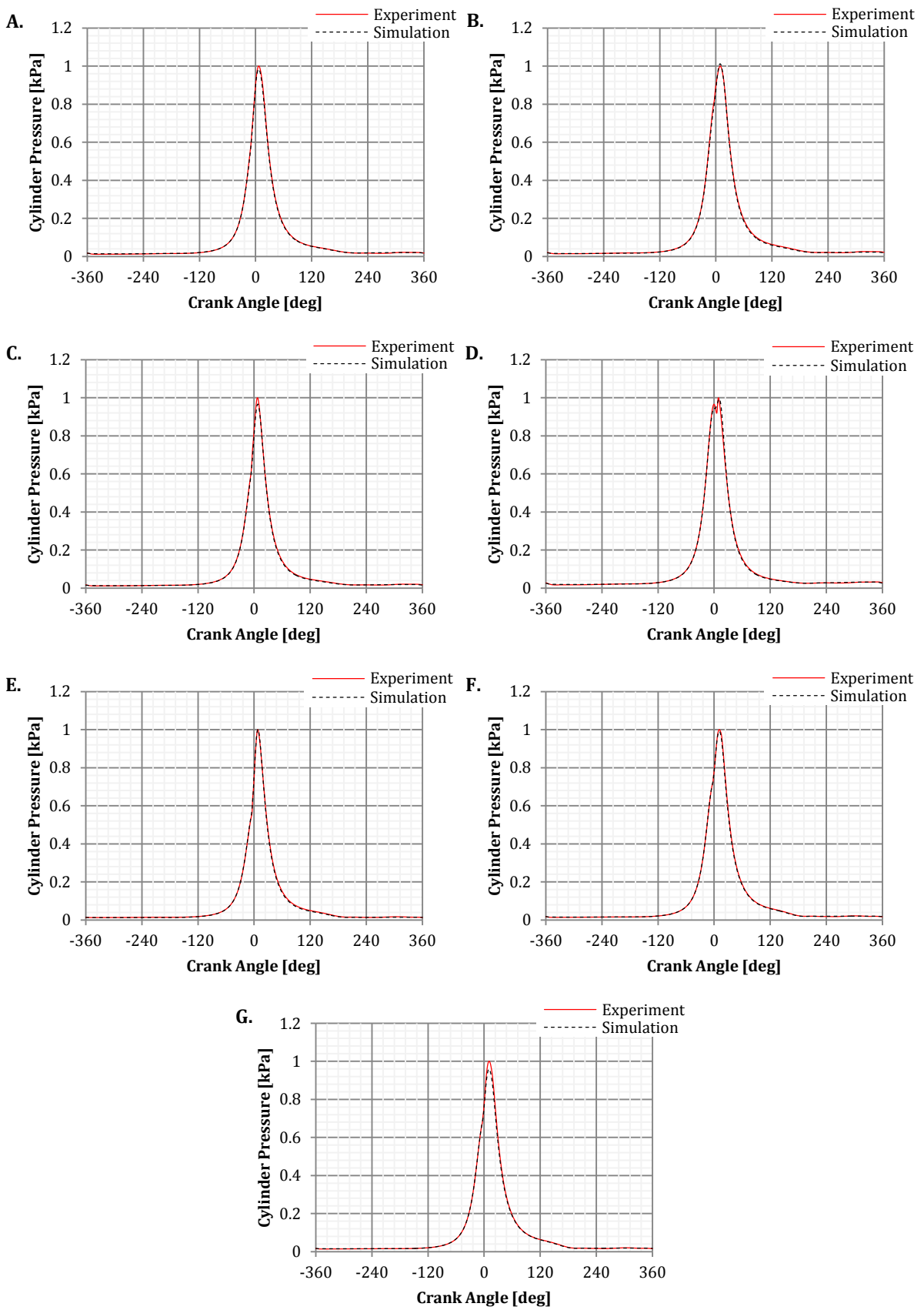


Figure 6.2 - Experiment and simulation in-cylinder pressure traces for seven different engine loading conditions

The experimental data has been provided by *Caterpillar* in the form of in-cylinder pressure traces and averaged quantities for seven different engine loading conditions. This data has been obtained from an engine identical to the one installed at *Loughborough University*, but with different intake and exhaust ducts lengths and diameters. As the air system was different from the engine modelled, this data has been used to validate the combustion model only.

Start of injection, injection duration and injected fuel quantity have been obtained from the experimental data and have not been modified. No option is given to adjust the ignition delay as the model is unaffected by cylinder geometry and has been calibrated by *Dynasty* developers. A fuel Cetane number is required and this has been set to 51 which is the minimum specified by the European standard EN590:2004 (European Committee for Standardization, 2004).

The combustion heat release rate shape has been calibrated by altering the mixing rate factor function defined in **Section 6.1.4**. The coefficients of this function have been obtained by directly calibrating the mixing rate factor for each engine loading condition and by fitting a second order polynomial to the data. The mixing rate factor can be related to the pace at which fuel is mixed with air, but it is a model specific parameter and it is not a physical quantity. For this reason, it is standard practice in *Caterpillar* to tune this variable in preference to adjusting injection parameters. The results shown are those obtained by running the model with the mixing rate factor function, and not with the individually calibrated mixing rate factors.

Despite the fact that a heat transfer scaling factor is available to tune the cylinder heat loss, no tuning has been necessary. Since the Biot number is low, the good match was mainly due to the validity of the Woshny model and the quality of the swirl data provided by *Caterpillar*.

**Table 6.2 - Numerical results of the combustion chamber validation**

	Point A	Point B	Point C	Point D	Point E	Point F	Point G
<b>Engine Torque [Nm]</b>	767	576	383	77	544	811	1049
<b>Engine Speed [rev/min]</b>	2202	2202	2202	2202	1350	1300	1250
<b>Peak Cylinder Pressure Error</b>	-1.37%	0.49%	-3.46%	-0.46%	-0.22%	-1.01%	-4.21%
<b>IMEP Error</b>	-1.66%	0.10%	-2.41%	3.50%	-3.38%	-3.61%	-3.63%
<b>Exhaust Temperature Error</b>	1.03%	0.65%	-0.08%	-1.55%	1.34%	2.92%	5.15%
<b>Mass Flow Rate Error</b>	1.27%	1.16%	1.34%	1.85%	5.20%	2.76%	2.44%

**Table 6.2** and **Figure 6.2** show the simulation results comparison with the experimental data. Under most engine loading conditions, the peak cylinder pressure and indicated mean effective pressure (IMEP) tend to be on the low side, while exhaust port temperatures tend to be on the high side. These parameters have been found to be highly sensitive to the injection timing, and therefore to the start of combustion, which indicates that the small differences are likely to be caused by a minor overestimate of the ignition delay. The reason for this overestimate could be that the fuel has a higher Cetane number than the one specified in the model. Nevertheless, the

majority of the errors are within  $\pm 5\%$  even at the maximum engine speed (points A to D), which shows that the time dependant ignition delay and combustion models are well calibrated.

Since the engine has been modelled as a single cylinder, the pulsations in the manifolds and runners could not be correctly replicated. Nevertheless, the error in mass flow rate is small, indicating that the impact on the combustion process is low.

### 6.2.2 COMPLETE TURBOCHARGED ENGINE VALIDATION

The complete engine has been validated by comparing average flow properties against experimental data provided by *Loughborough University*. The experimental data consists of average gas pressures, temperatures and flows at different engine locations and under nine different engine loading conditions.

The data did not include in-cylinder pressure measurements and therefore it could not be used to validate the combustion sub-model. However, the engine block, cylinders, head, manifolds and ECM are identical to the engine tested by *Caterpillar*. Since no differences in the combustion process of the two engines are expected, the previously validated combustion chamber sub-model has been inserted in the full engine model with no further tuning.

The air system has been set-up by modelling the pipes with 1D duct-type elements of different diameters and, where abrupt changes in diameter occur, with nozzle-type elements. Parameters such as diameters, lengths, wall thicknesses and materials have been obtained from installation drawings. The injection timing, duration and rates have been provided by the ECM and have not been modified. The effectiveness of the coolers has been estimated from the experimental data and has been inserted into the model as a function of gases mass flow rates. The effectiveness functions have then been tuned with minor adjustments to improve the temperature matching. The other parameters which have been tuned to improve the model-experiment matching are the exhaust manifold heat transfer scaling factor and the discharge coefficients of nozzle-type elements. This is a standard procedure to set-up the engine model, as these types of model are not entirely predictive unless they are tuned.

The turbocharger speed has been set by adjusting the VGT opening by means of a PID controller. The reason for this is that the correlation between the ECM vanes opening demand and the actual vanes flow area is unknown. The turbocharger bearing housing sub-model has been validated against the data showed in **Chapter 3** and the results are shown in **Table 6.4**. The bearings dimensions have been taken from engineering drawings while the axial stiffness has been calculated from the maximum load the thrust bearing can withstand and assuming

linearity. The convective heat transfer correlation has not been calibrated due to the low impact on turbocharger mechanical efficiency.

**Table 6.3** shows the errors of the model results compared to the experimental data. The errors are generally within  $\pm 5\%$ , and this is considered to be a small error. The compressor outlet pressure and temperature are marginally low and high respectively. The low pressure can be caused by imperfections in the map, or by the overestimated air mass flow rate which slightly shifts the operating point on the compressor map. The small error in temperature could be caused either by low scroll heat loss, or by low compressor efficiency.

**Table 6.3 - Numerical results of the complete engine system validation**

	Point 1	Point 2	Point 3	Point 4	Point 5	Point 6	Point 7	Point 8	Point 9
<b>Engine Torque [Nm]</b>	300	580	940	290	590	950	260	560	800
<b>Engine Speed [rev/min]</b>	1701	1701	1701	1800	1800	1800	1890	1890	1890
<b>Compressor Outlet Press. Error</b>	-2.57%	-1.75%	-0.60%	-1.94%	-2.14%	-0.88%	-2.54%	-1.68%	1.72%
<b>Compressor Outlet Temp. Error</b>	0.96%	1.31%	1.21%	1.00%	1.34%	1.49%	1.49%	1.31%	2.57%
<b>Intake Manifold Press. Error</b>	0.78%	1.03%	1.56%	2.27%	1.04%	1.75%	1.81%	1.81%	5.53%
<b>Intake Manifold Temp. Error</b>	1.02%	1.67%	1.80%	1.77%	1.67%	2.41%	1.61%	1.18%	2.25%
<b>Intake Mass Flow Error</b>	1.27%	3.33%	4.75%	1.86%	3.22%	2.33%	2.08%	2.93%	-4.16%
<b>EGR Mass Flow Error</b>	0.69%	3.33%	4.70%	1.86%	3.23%	2.32%	2.08%	2.94%	-4.16%
<b>Exhaust Mass Flow Error</b>	1.28%	3.33%	4.62%	1.90%	3.17%	2.27%	2.10%	2.84%	-3.95%
<b>Exhaust Port Temp. Error (Av.)</b>	3.64%	5.68%	4.49%	6.18%	5.66%	6.23%	5.49%	5.01%	2.94%
<b>Exhaust Manifold Press. Error</b>	0.09%	-3.03%	-2.36%	4.67%	-0.08%	1.95%	3.99%	0.72%	2.42%
<b>Exhaust Manifold Temp. Error</b>	2.10%	1.89%	0.49%	2.60%	0.56%	1.12%	0.94%	-0.23%	-0.71%
<b>Turbine Outlet Temp. Error</b>	3.76%	6.22%	4.63%	5.50%	4.27%	4.80%	3.52%	3.14%	2.31%
<b>EGR Cooler Outlet Press. Error</b>	-0.43%	-3.43%	-2.76%	3.93%	-0.65%	1.18%	3.25%	0.12%	1.90%
<b>EGR Cooler Outlet Temp. Error</b>	5.86%	10.26%	6.09%	9.17%	10.91%	11.19%	9.69%	11.10%	6.64%
<b>BSFC Error</b>	1.69%	1.98%	1.83%	2.46%	1.56%	2.06%	1.32%	1.04%	0.88%

The turbine outlet temperature is slightly high, even when the pressure drop across the turbine and the exhaust manifold temperature are well matched. The reason for this is that the heat loss across the turbine volute is not modelled. This means that the temperature entering the rotor will be marginally higher than on the real engine, leading to more work being extracted for a given pressure ratio.

As the turbocharger speed is matched by adjusting the vanes angle, the only parameter which could show errors in the overall turbocharger efficiency is the exhaust manifold pressure. From **Table 6.3** it can be seen that the turbocharger efficiency is well matched as the exhaust manifold pressure and temperature errors are low. This suggests that the assumptions of no turbine volute heat transfer and no installation effects do not cause excessive error. The only trend which can be seen is that the exhaust manifold pressure tends to be high at low engine loading conditions, but the errors are still acceptable.

**Table 6.4** shows the validation of the bearing losses. There are errors in the load, however, the magnitude of the error is small compared to the turbine torque ( $\approx 0.5\%$  depending on loading condition) and therefore it has a low impact on the overall turbocharger efficiency.

**Table 6.4 – Turbocharger bearing housing validation**

<b>Turbocharger Speed [rev/min]</b>	59028	80037
<b>Axial Force [N]</b>	23.7	51.5
<b>Experiment Bearing Load [Nm]</b>	0.118	0.141
<b>Simulation Bearing Load [Nm]</b>	0.122	0.133
<b>Bearing Load Error</b>	4.08%	-5.64%

The intake manifold pressure tends to be marginally high and this leads to an overestimate of the air mass flow rate. Nevertheless, the errors are not excessively dissimilar to the errors found during the combustion chamber validation, and therefore do not cause excessive error in the combustion process.

The validity of the combustion model and of the injection timing maps provided by *Caterpillar* is confirmed by the low brake specific fuel consumption (BSFC) and exhaust ports average temperature errors. The BSFC is generally higher in the model and this reflects the low IMEP seen during the combustion chamber validation process. Since more fuel is burned, more energy is available when the exhaust valve opens and the exhaust port temperature error tends to be higher than in the previous section.

The EGR mass flow rate error matches the intake mass flow error. The control system has been set-up to match the EGR mass flow rate fraction and the fact that the two error match means that the EGR system always deliver the correct mass flow ratio. The EGR cooler outlet temperatures are high, but this causes a small error in the intake manifold temperature and therefore the error is acceptable.

Overall, the simulation results match the experimental data well, especially considering that this is a low order model partially based on empirical correlations. Engine BSFC error is always within  $\pm 2.5\%$  and in most cases it is below  $\pm 2\%$ , proving that the predicted changes in engine efficiency shown in later sections will be accurate.

### 6.2.3 TRANSIENT TURBOCHARGER BEHAVIOUR VALIDATION

The turbocharger transient response has been validated by comparing the *Dynasty* electrically assisted turbocharger model, with no compressor, against the experimental data presented in **Chapter 5**. This is just a validation and no further tuning of parameters has occurred.

The turbine, bearing housing and motor/generator sub-models implemented in the previous validation have been arranged to replicate the experimental test-rig. The inlet pressure, inlet temperature and outlet pressure of the turbine have been set as time varying boundary conditions and have been obtained from the experimental data. The bearing housing oil flow rate, pressure and temperature have been set to match the test-rig oil flow conditions.

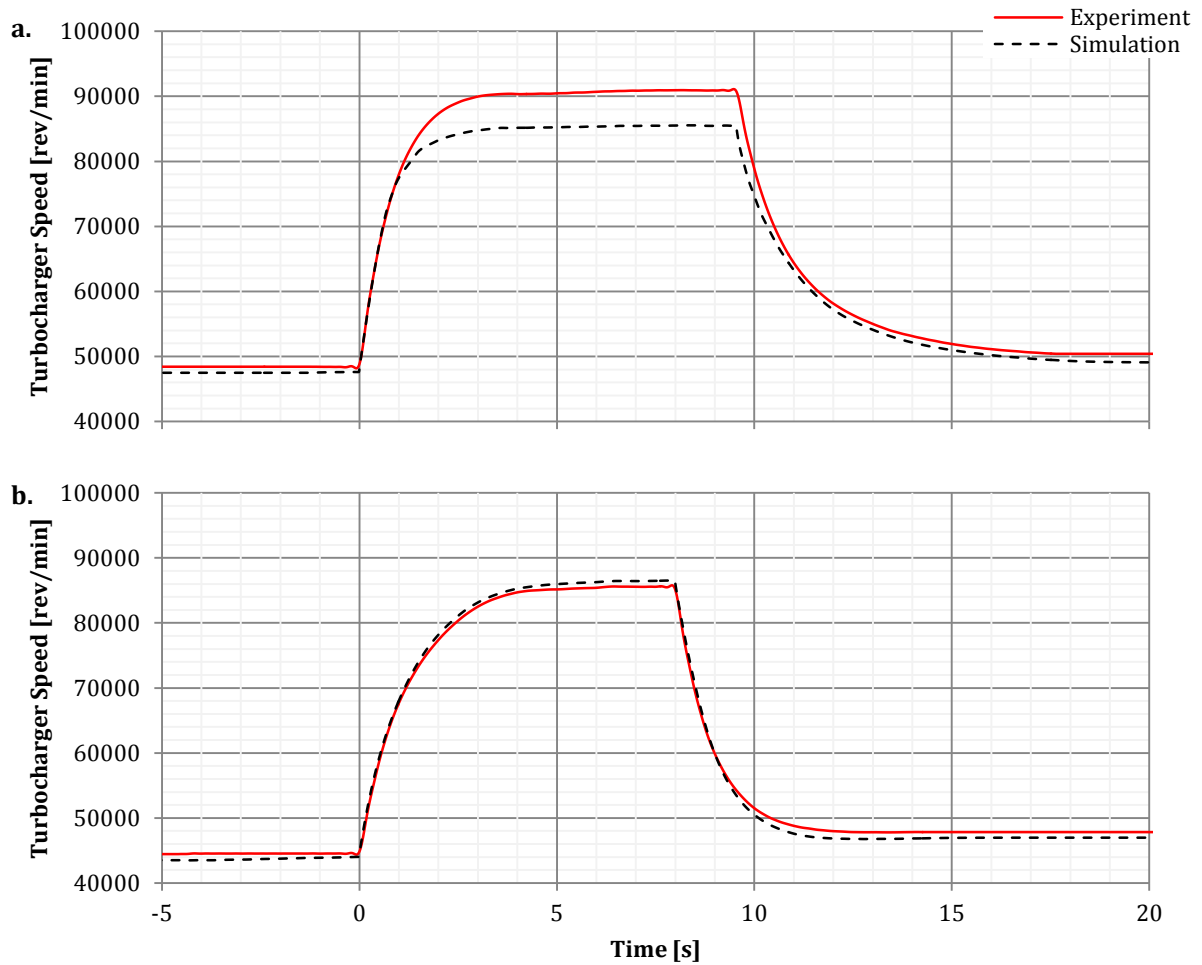


**Figure 6.3 - Validation of the electrically assisted turbocharger in transient conditions. In part a the motor/generator is tuned on in motoring mode and then off. In part b the motor/generator is initially on in generating mode, it is turned off and then on again in generating mode.**

The motor/generator has been actuated in the same way as in the experiment. To obtain the data shown in **Figure 6.3a**, the electrical machine has been turned on in motoring mode at time zero, and then turned off after roughly 9.5 s. In **Figure 6.3b** the electrical machine was initially on in generating mode. It has been turned off at time zero and on again after 8 s.

**Figure 6.3** shows the turbocharger speed traces for the two motor/generator operating cycles. The simulated traces match the experimental traces well both in the steady and transient parts of the cycles. This demonstrates the validity of the model, since correct matching depends on accurate model physics, correct inertia, accurate turbine model and maps, accurate bearing housing model and accurate motor/generator model. More importantly, we can infer that the turbine quasi-steady assumption is valid for this rate of acceleration.

In **Figure 6.3a** the simulated turbocharger maximum speed is approximately 5% low. At these conditions the turbine is acting as a load and the magnitude of this load is estimated from the negative portion of the efficiency map. In this region of the map the efficiency lines gradients are



steep, which means that the turbine load is very sensitive to pressure ratio errors. Other sources of error are bearing housing loss model, turbine map errors and imprecision in the motor/generator torque setting.

The weakness of this approach is that it directly validates only the turbocharger transient response. Nevertheless, this validation shows that *Dynasty* correctly calculates shafts angular accelerations and, since the transient response of this type of engines is governed by the turbocharger and the engine inertia, one can infer that the overall engine transient response predicted by the model will be accurate.

The second weakness is that this experiment occurred in cold flow conditions, and therefore the data cannot be employed to validate the assumption of no turbine thermal inertia. On the other hand, it has been shown in the **Section 6.2.2** that the turbine thermal losses have a small impact on the overall turbocharger efficiency, and therefore this assumption is not expected to cause major differences in transient response.

### 6.3 OPTIMIZATION OF TURBINE VANES OPENING FOR STEADY STATE OPERATION

The scope of this investigation is to study the impact of boost pressure on engine efficiency, focusing on the reduction of pumping losses. The optimization of valve timing, injection timing, and turbocharger flow geometries is outside the scope of this study and its impact will only be discussed.

The objectives of this study are to:

- Understand the mechanisms that relate boost pressure to engine efficiency
- Find optimum boost values for different engine loadings
- Estimate the potential gains in BSFC

#### 6.3.1 BOOST OPTIMIZATION TECHNIQUE DESCRIPTION

In this set of simulations, the engine model is run in steady state conditions and the boost is adjusted by changing the turbine vanes opening. Five different torque demands are simulated and these are 100 Nm, 300 Nm, 500 Nm, 700 Nm and 900 Nm. Since for this application the engine is run at a nominally constant speed of 1800 rev/min, no other speeds are simulated.

The boost is adjusted by decreasing the vanes effective area by 5% steps. Ideally, the initial opening would be 100%. This is not possible for a number of torque demands, as the compressor either runs into choking conditions, or it does not provide enough boost to sustain the required torque. The minimum vane opening is either the opening which results in the maximum turbocharger speed, or 30%, which is the minimum opening tested in **Chapter 4**.

The amount of fuel injected, the number of injections, and the injection timing are controlled by the ECM, while the speed is controlled the speed governor. The torque is changed by changing the load applied by the dynamometer. The EGR mass flow rate has been set at 25% of the intake mass flow rate, and this value is maintained under all torque and boost conditions. This value has been found to be a typical value by researching the literature and studying the experimental data provided by *Caterpillar*

### 6.3.2 $\lambda$ -PARAMETER

To understand how the turbocharger affects the pumping losses, an analytical equation, which describes a simplified system, has been derived. This equation has been obtained by applying the conservation of energy law across the turbocharger and assuming constant pressure turbocharging.

$$\lambda = \frac{T_{turb\ in}}{T_{comp\ out\ is}} \eta_{turbo} = \left( \frac{P_{turb\ in}}{P_{comp\ out}} \right)^{\frac{\gamma-1}{\gamma}} \frac{(P_{comp\ out})^{\frac{\gamma-1}{\gamma}} - (P_{amb})^{\frac{\gamma-1}{\gamma}}}{(P_{turb\ in})^{\frac{\gamma-1}{\gamma}} - (P_{amb})^{\frac{\gamma-1}{\gamma}}} \quad (6.5)$$

The efficiency term represents the total turbocharger efficiency, including the frictional losses. **Equation 6.5** relates the compressor exit pressure and the turbine inlet pressure to a non-dimensional parameter,  $\lambda$ , which is a function of the total turbocharger efficiency, the turbine inlet temperature and the compressor isentropic exit temperature. To better understand how this equation relates to pumping losses, it has been plotted in **Figure 6.4** where the difference between the compressor exit pressure and the turbine inlet pressure has been plotted against the compressor exit pressure.

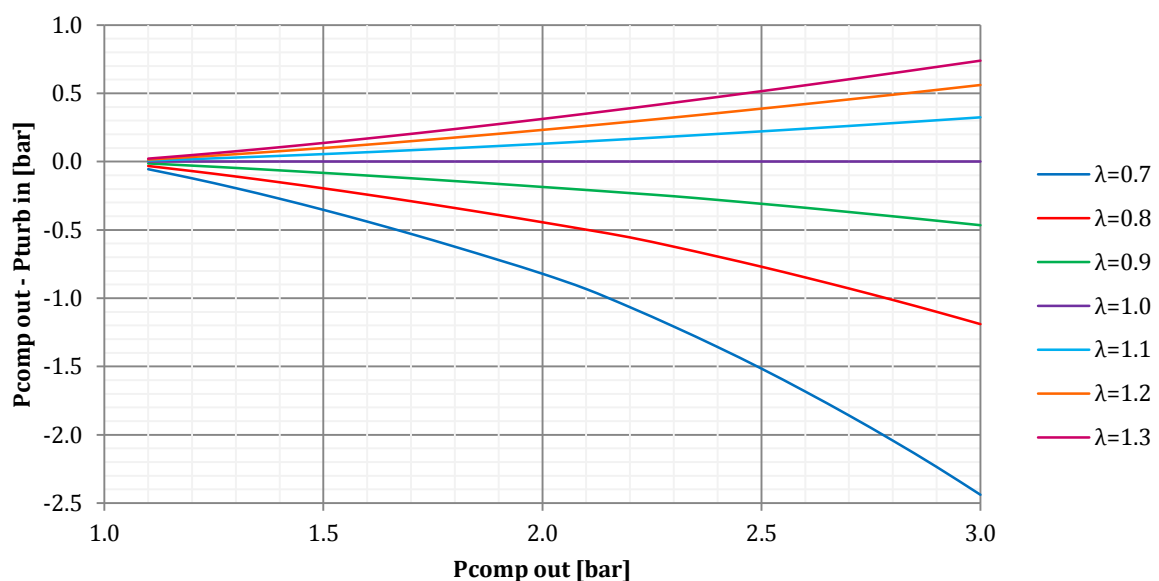


**Figure 6.4** - Plot of the difference between compressor outlet pressure and turbine inlet pressure as a function of compressor outlet pressure for different  $\lambda$ -parameter values. This plot has been obtained from Equation 6.5

If  $\lambda$  is larger than one, increasing the boost pressure causes the compressor exit pressure to increase more than the turbine inlet pressure, which could lead to a reduction in pumping losses. Nevertheless, the  $\lambda$ -parameter is also affected by the boost pressure. If the boost pressure is increased the air to fuel ratio increases leading to lower turbine inlet temperature, while the compressor exit isentropic temperature increases. Consequently, as boost pressure increases, the  $\lambda$ -parameter decreases, which means that an optimum point exists.

### 6.3.3 BOOST OPTIMIZATION RESULTS AND DISCUSSION

The results of this study are shown in **Figure 6.5**. The first of these figures shows how engine BSFC is affected by boost pressure. An optimum boost pressure exists for all the torque demands simulated, apart from the 100 Nm demand. At this torque level the inlet turbine temperature is excessively low and, as a result, the best efficiency is obtained with the lowest boost.

The minimum BSFC ranges from the 318 g/kWh of the 100 Nm torque demand to the 213 g/kWh of the 900 Nm demand. The minimum BSFC decreases as the torque demand increases because the engine frictional load is relatively independent of engine load (Lumley, 1999). As the torque increases, the mechanical efficiency increases, resulting in higher BSFC.

From **Figure 6.5a** and **Figure 6.5b** it can be observed that the minimum BSFC does not occur when the PMEP has the maximum value, but at a higher intake manifold pressure. This is because the boost pressure does not only affect the PMEP, but also the combustion process. Tanin et al. (1999) have demonstrated that, if the difference between the intake and exhaust manifold pressure is maintained constant, a higher boost results in lower BSFC. Nevertheless, if the boost is increased excessively, the pumping losses become dominant and the engine efficiency drops.

Even when the  $\lambda$ -parameter exceeds one, the resulting PMEP is negative. This is partially due to the pressure losses in the ducting, intercooler and manifolds. These losses cause the pressure at the inlet valves to be lower than at the compressor exit, and the pressure at the exhaust valve to be higher than at the turbine inlet, increasing the pumping losses. In addition, there are pressure drops in the inlet filter, exhaust system and after treatment system, causing the compressor inlet and turbine exit pressures to be respectively lower and higher than ambient.

A further reason for the negative pumping work can be understood by observing **Figure 6.6**. This figure shows the cylinder valves flow over crank angle for two different intake manifold pressures and a torque demand of 500 Nm. It can be seen that the higher pressure results in a lower fraction of the exhaust flow occurring in blow-down conditions, that is when the piston

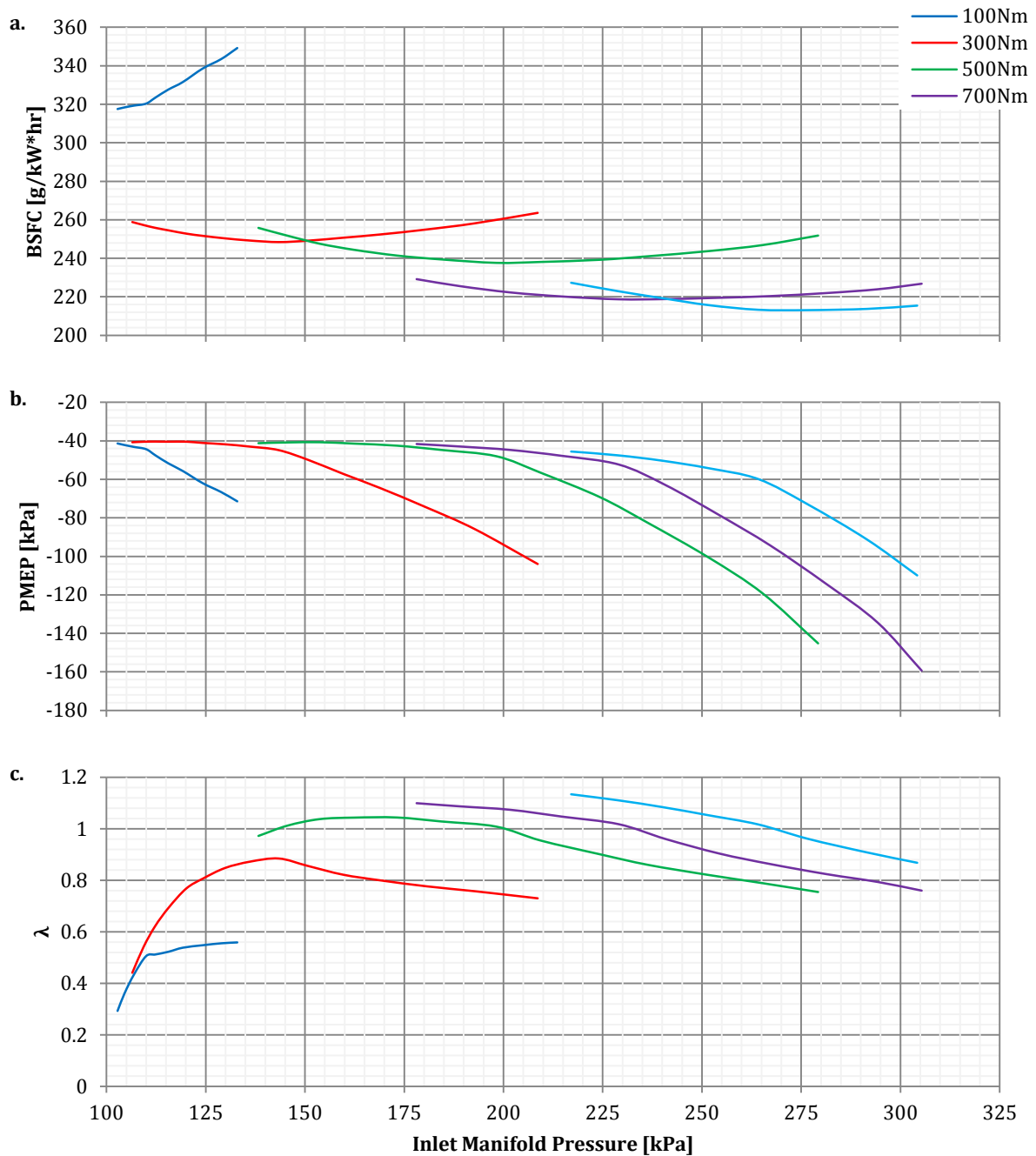


**Figure 6.5 – Engine brake specific fuel consumption, pumping mean effective pressure and  $\lambda$ -parameter as a function of inlet manifold pressure**

velocity is small and the flow is driven by the high in-cylinder pressure generated by the fuel combustion. Because a larger fraction of the exhaust flow occurs when the piston is moving upwards, the piston does more work on the gas resulting in higher pumping losses. This change in fraction could be caused by the fact that there is more mass in the cylinder or that the temperatures are lower, resulting in lower speed of sound.

Despite the flow effects described in the previous paragraphs, which are not captured by this analysis, there is a clear trend between the  $\lambda$ -parameter and the PMEP. As soon as the  $\lambda$ -

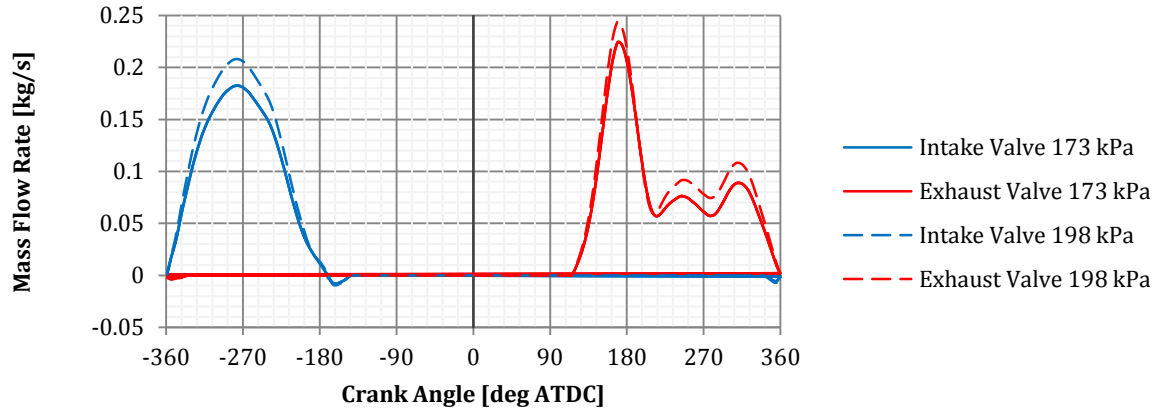


**Figure 6.6 - Intake and exhaust valve mass flow rate as a function of engine crank angle for two different intake manifold pressures**

parameter drops below zero, the pumping losses start increasing rapidly and become dominant over the combustion efficiency. The  $\lambda$ -parameter therefore cannot be used directly to optimize boost pressure for engine efficiency, but it is a good indicator to understand how important the pumping losses are.

The injection timing is the one provided by the ECM and has not been adjusted for boost pressure. This means that the start and duration of the pilot, main and post injections are approximately the same for all boost conditions. If the injection timing parameters were optimized for each boost pressure, we would probably see a shift of minimum BSFC towards lower intake manifold pressures, where the pumping losses are lower. Nevertheless, it is unlikely that the peak efficiency will coincide with the lowest pumping losses, as the combustion process is still affected by boost pressure. Moreover, the injection timing is constrained by emissions and engine structural limits so full optimization might not be achieved.

Engine emissions have not been considered when optimizing boost as the model was not set-up to predict emission levels. Soot emissions are expected to be high since the optimum efficiency boost is lower than typical boost, resulting in less oxygen being available for combustion (Tanin et al., 1999). On the other hand, NO<sub>x</sub> emissions would reduce thanks to the lower combustion temperature of the richer fuel-air mixture. This is beneficial as it could lead to a reduction of the EGR mass flow necessary to meet legislation requirements, which in turn could lead to a further reduction in pumping losses. As the EGR requirements are always met under all boost conditions, the VGT opening has not been compromised to drive EGR gases. On the negative side, high soot emissions could result in higher intake manifold pressures being necessary to meet legislation requirements. This increase of soot emissions is not expected to be excessive, as the fuelling was controlled by the ECM which has a built-in smoke limit calibrated on a real engine.

## 6.4 MOTOR/GENERATOR POWER IMPACT ON ENGINE TRANSIENT RESPONSE

This study focuses on the impact of electric assistance on engine transient response. The scope is to understand the physics behind the engine transient behaviour and how different motor/generator powers affect it.

The objectives of this investigation are to:

- Understand the physics behind turbocharged diesel engine transient response
- Understand how electric assistance reduces turbo-lag
- Assess the improvements in engine transient response with different motor/generator powers
- Find the limitations of electrical machine power dictated by the engine requirements

### 6.4.1 MOTOR/GENERATOR POWER IMPACT INVESTIGATION DESCRIPTION

To achieve the study objectives, six different cases are simulated over two engine load steps. In *Case 1*, the baseline case, no electric assistance is applied. In *Cases 2 to 6*, five different motor/generators, with maximum power of 1 kW, 2.5 kW, 5 kW, 10 kW and 25 kW, are used to assist the transient. The motor/generator power is increased instantaneously to the maximum value as soon as the engine load is increased. This allows to exploit the full potential of the electric assistance as no controller generated lag occurs.

To scale the motor/generator, the moment of inertia is assumed to be proportional to the maximum power. The reason behind this is that the rotor diameter is constrained by the centrifugal stresses at the maximum turbocharger speed. Therefore, it is assumed that the maximum power is increased by increasing the motor/generator length and that the relationship between the two is linear. For the same reason, the rotor drag is also assumed to be proportional to the machine power. In reality the maximum power could be changed by altering motor/generator design parameters such as the number of windings in the coil and the cooling system. However, the redesign of the motor/generator is outside the scope of this study and is not investigated.

Two different load steps are simulated. *Work Cycle A* is a load step from 100 Nm to 399 Nm and *Work Cycle B* is a load step from 534 Nm to 817 Nm. The initial load in *WCA* has been arbitrarily selected as a low load point, while the initial load in *WCB* is the mean load taken from experimental engine operation data provided by *Caterpillar*. For both work cycles, the load step magnitude is 95% of the increase in load which would cause the engine to stall for the baseline case. To ensure that the engine is running in steady state conditions before the load step, the

initial conditions are set to match the steady state values and the simulations are run for 30 seconds before the step in load.

In the steady state part of the simulation the fuel is controlled by the speed governor. As soon as the load step occurs, the speed governor fuel signal is overridden to obtain a burned equivalence ratio of 0.8. This equivalence ratio value is found in the literature as a typical value at which smoke starts to occur. The speed governor is overridden to remove the controller impact on the system transient response, as the scope of this work is to study the physics of engine transient behaviour.

The VGT is set to provide the efficiency optimised boost found in the previous part of the study. The vanes opening is 0.75 for *WCA* and 0.6 for *WCB* and these values are maintained constant throughout the simulations. The EGR demand is set to 25% of the intake mass flow rate as in the previous part of the study, and is regulated by a PI controller.

#### 6.4.2 MOTOR/GENERATOR POWER IMPACT INVESTIGATION RESULTS AND DISCUSSION

The data obtained from this set of simulations is presented in **Figure 6.7** to **Figure 6.15**. The engine torque data is averaged over each firing event (i.e. 1/6 of an engine cycle). The rest of the data has been filtered by means of a low pass filter to remove the pulsations caused by the reciprocating nature of the engine, as these pulsations would have made the results unclear. The filter utilized is a zero-phase-shift, finite-impulse-response (FIR) type. The pass and stop frequencies have been set to 50 Hz and 70 Hz respectively. The attenuation at frequencies above the stop frequency is 60 dB.

**Figure 6.7** and **Figure 6.8** show the time traces of engine speed and torque for both *WCA* and *WCB*. For off-road engines the main quantities that are looked at to quantify the transient response are the speed drop,  $N_{drop}$ , and the recovery time,  $t_{recov}$ . The speed drop is the difference between the nominal engine speed, 1800 rev/min, and the minimum speed reached during the transient. The recovery time is the time taken to recover the nominal speed after the engine load is applied. **Table 6.5** shows the speed drop, recovery time and relative improvement over the baseline for all the cases simulated. **Figure 6.9** is a plot of percentage improvement of speed drop and recovery time against the assistance power. It is clear that electric turbocharger assist is very effective in improving engine transient response, even when the assistance power is low. With a 1 kW Motor/generator, the speed drop is reduced by 49.4% in *WCA* and 21.3% in *WCB* and the recovery time by 58.7% in *WCA* and 56.0% in *WCB*. **Figure 6.9** shows that the majority of the improvements in transient response are obtained with a 5 kW motor, and increasing the power to 25 kW does not produce significant further improvements. The benefits tend to be

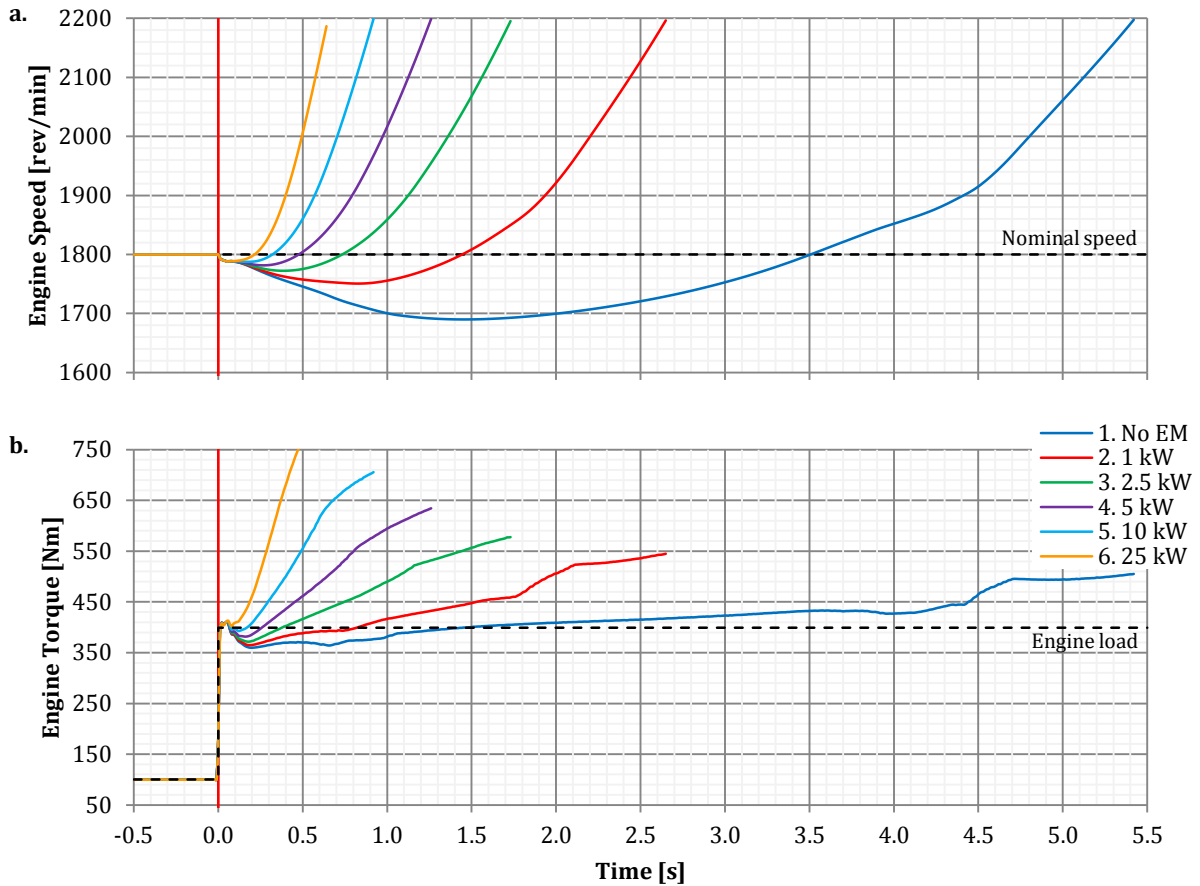


**Figure 6.7 – Engine speed and engine torque time traces for a step change in load from 100 Nm to 399 Nm (WCA)**

higher in *WCA* because the turbine power at the beginning of the transient is lower in this work cycle and therefore the motor/generator power is a larger fraction of the total motoring power.

**Figure 6.7b** and **Figure 6.8b** show that the engine torque rises suddenly soon after the dynamometer load is increased. This occurs due to the sharp increase in equivalence ratio which causes the torque to rise with no need of boost increments. As the equivalence ratio at this stage is fixed to 0.8, to further increase the engine torque so that it exceeds the load, the boost has to increase. When the ETA is not present, the boost increases thanks to the higher exhaust flow temperature and pressure caused by the extra fuel burned, which increase the turbine power. Because the turbine torque and turbocharger loads are not balanced any more, the turbocharger accelerates and continues accelerating until the torques and loads are balanced again. Due to the relatively high turbocharger rotor inertia and the large speed changes required to increase the compressor pressure ratio, the boost increase is slow and this leads to poor engine transient performance.



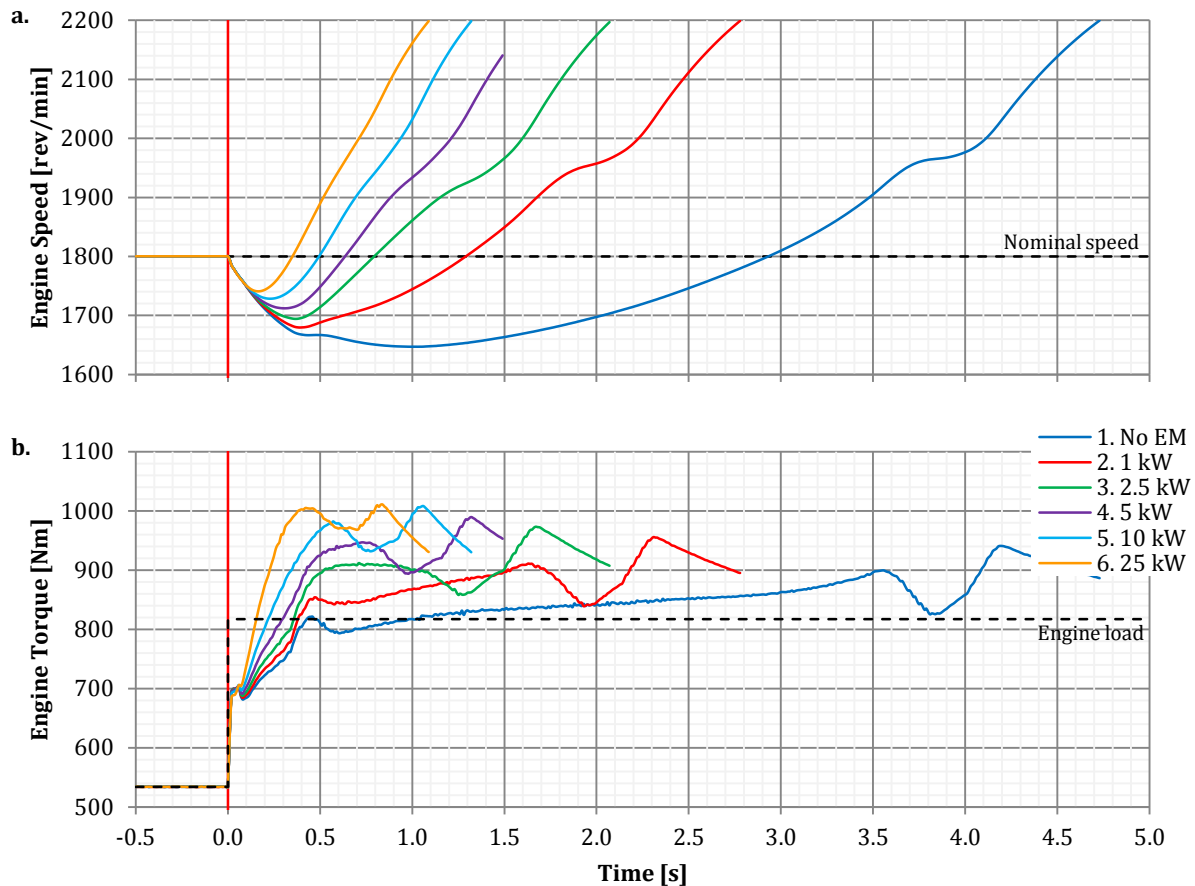


**Figure 6.8 – Engine speed and engine torque time traces for a step change in load from 534 Nm to 817 Nm (WCB)**

From the engine torque traces, it can be seen that the torque peaks at about 0.05 s and then drops. This effect is caused by a reduction of the oxygen content within the cylinders. The sudden increase in fuel injected causes the temperature and pressure within the exhaust manifold to increase rapidly, as shown in **Figure 6.10c** and **Figure 6.11c**. As a result, the amount of exhaust gases trapped within the cylinder and the mass flow rate through the EGR loop increases, reducing the amount of fresh air that enters the cylinders. Moreover, as the equivalence ratio is increased, the exhaust gases have a lower oxygen content. The mass flow through the EGR loop increases because the valve is controlled by a PI controller which cannot adjust the valve instantaneously. Increasing the assistance power reduces the torque drop after the initial peak. This is because even if the fraction of trapped exhaust gases increases, the higher boost limits the reduction in oxygen content.

From **Figure 6.7b** it can be seen that with a 25 kW assistance power, in *WCA* the engine torque never drops below the engine load after the initial peak. Despite this, a speed drop still occurs, and that is caused by the firing delay. The firing delay is caused by the finite amount of time between a firing event and the next. During this time the engine torque cannot be increased

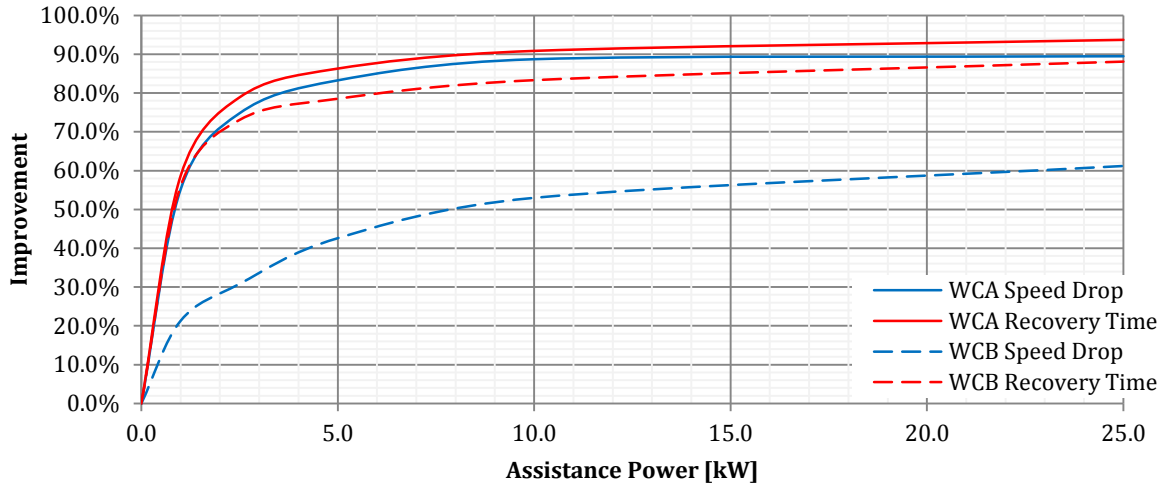


**Figure 6.9 - Percentage improvement of speed drop and recovery time as a function of assistance power**

either because there is no combustion event taking place, or because the ECM cannot change the volume of fuel injected while the injection is occurring. This delay is not boost dependant and therefore it cannot be improved by electric assistance.

**Figure 6.9** shows that the speed drop tends to be improved less compared to the recovery time. This is because the initial boost is the same for all cases and electric assistance does not have a significant impact in the first phase of the transient, where the engine decelerates rapidly. Electric assistance is more effective in the longer time-scales where it is able to build up extra boost, limiting the speed drop and increasing the engine acceleration. The percentage improvement is therefore higher for the recovery time due to the double effect of lower speed drop and higher engine acceleration. This difference is higher in *WCB* than in *WCA* because in *WCA* the initial torque peak magnitude equals the load magnitude, resulting in no engine deceleration in the initial phase of the transient.

**Table 6.5 - Improvements in speed drop and recovery time caused by electric assistance**

	WCA				WCB			
	N <sub>drop</sub> [rev/min]	N <sub>drop</sub> Impr.	t <sub>recov</sub> [s]	t <sub>recov</sub> Impr.	N <sub>drop</sub> [rev/min]	N <sub>drop</sub> Impr.	t <sub>recov</sub> [s]	t <sub>recov</sub> Impr.
<b>1. No EM</b>	110.1	0.0%	3.51	0.0%	153.0	0.0%	2.93	0.0%
<b>2. 1 kW</b>	49.4	55.1%	1.45	58.7%	120.4	21.3%	1.29	56.0%
<b>3. 2.5 kW</b>	27.8	74.8%	0.74	78.9%	105.8	30.8%	0.79	73.0%
<b>4. 5 kW</b>	18.5	83.2%	0.48	86.3%	87.8	42.6%	0.63	78.5%
<b>5. 10 kW</b>	12.5	88.7%	0.32	90.9%	71.9	53.0%	0.49	83.3%
<b>6. 25 kW</b>	11.6	89.4%	0.22	93.7%	59.3	61.2%	0.35	88.1%

It is clear from **Figure 6.10** and **Figure 6.11** that the improvements in engine transient response with electric assistance are due to the higher acceleration of the turbocharger, which in turn causes a higher increase rate of intake manifold pressure. This proves that the the turbocharger inertia is the main cause of poor engine transient response. Adding a low-inertia

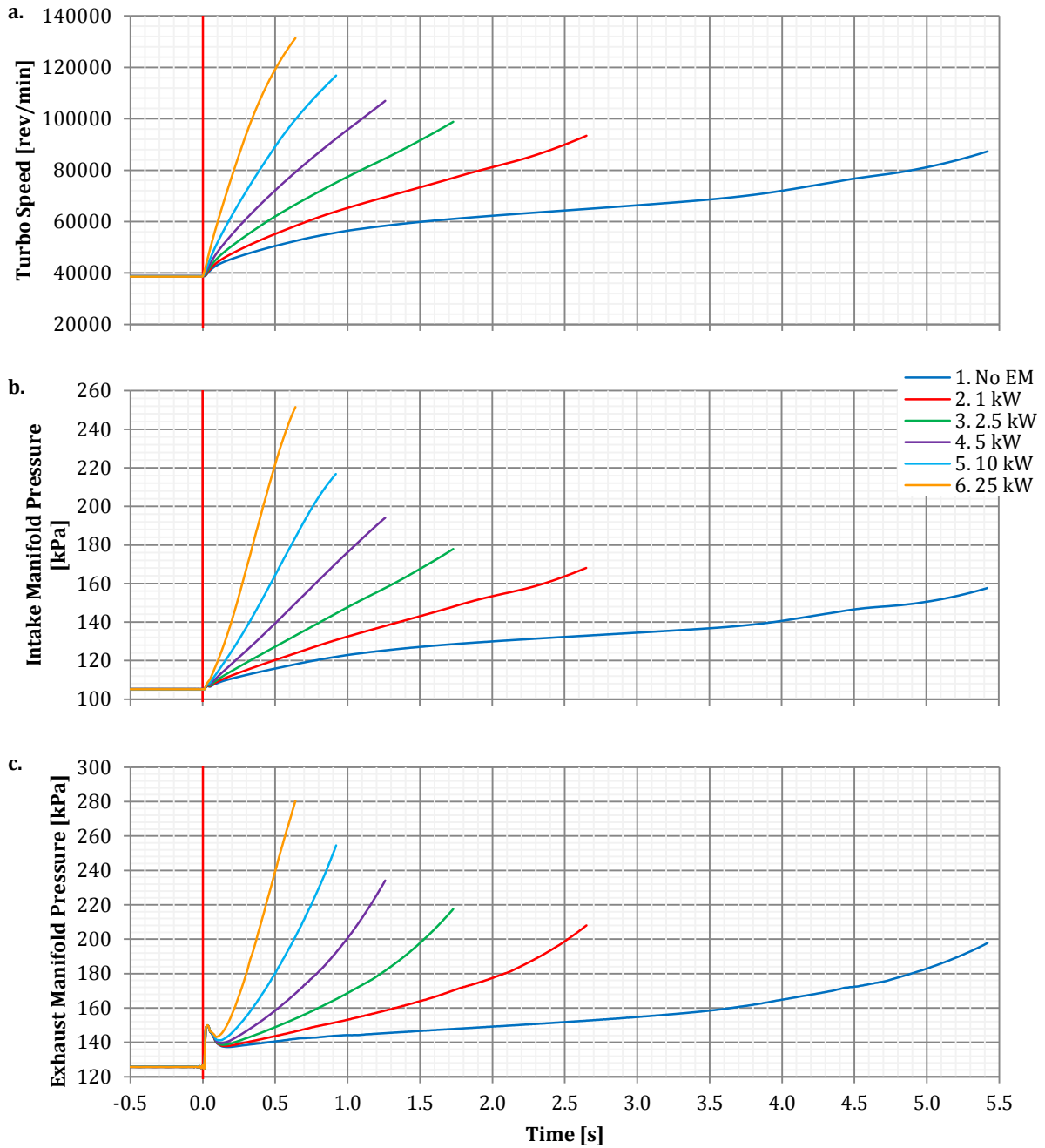
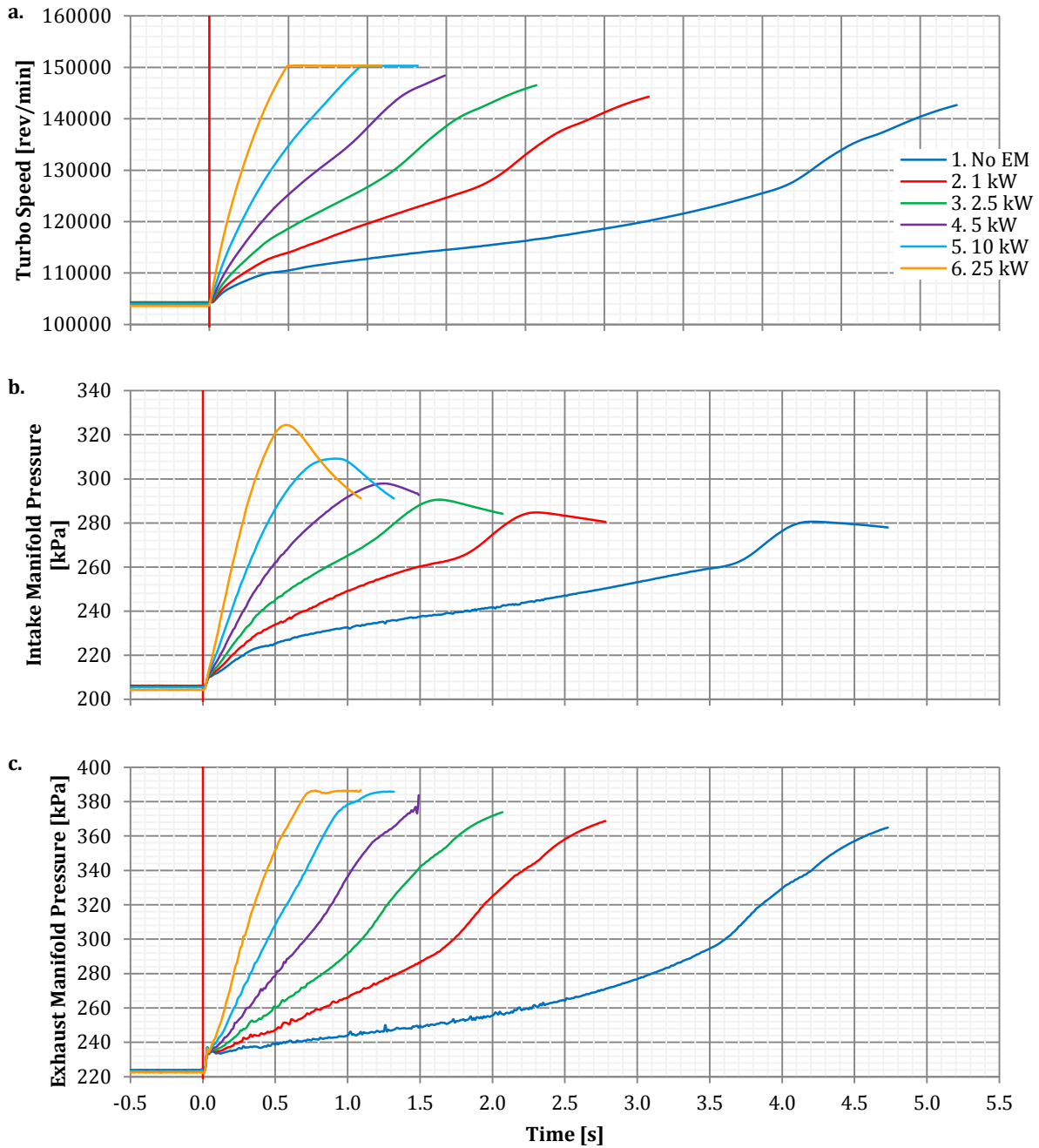


Figure 6.10 – Turbocharger speed, intake manifold pressure and exhaust manifold pressure time traces for a step change in load from 100 Nm to 399 Nm (WCA)

motor/generator to the shaft increases the torque available to accelerate the turbocharger shaft inertia.

$$a = \frac{\tau_{turbo\ bal} + \tau_{EM}}{I_{turbo} + I_{EM}} \quad (6.6)$$

**Equation 6.6**, *Newton's Second Law* applied to a rotating shaft, explains why it is fundamental to utilize a low inertia motor/generator to assist the turbocharger. If the torque to inertia ratio of the motor/generator is equal or lower than torque to inertia ratio of the turbocharger alone,



**Figure 6.11 – Turbocharger speed, intake manifold pressure and exhaust manifold pressure time traces for a step change in load from 534 Nm to 817 Nm (WCB)**

there would be no improvement or worsening of the turbocharger acceleration with any assistance power. Moreover, this equation shows that if the electrical machine size is dominant over the turbocharger size, the acceleration would be dictated by the torque to inertia ratio of the electrical machine and further increments in machine size would not improve transient response. Minimization of the motor/generator inertia has also the advantage of reducing the electrical power consumed during the transients.

The turbocharger inertia is not the only source of turbo-lag. A time delay is also caused by the finite amount of time required to fill the volume between the compressor and the inlet valves, which consists of the compressor scroll, the ducting, the intercooler and the intake manifold. As a result, the pressure lags behind the turbocharger speed. This can be seen from **Figure 6.10** and **Figure 6.11** where the turbocharger speed curve is more convex than the intake manifold pressure curve. Because the volume filling time-scale is much shorter than the turbo acceleration time-scale, this is difficult to see and it is clearer in the cases where the assistance power is higher. This lag poses a further limit on the electrical machine power. If the turbocharger acceleration timescale is already shorter than the intake manifold filling timescale, further increments in motor/generator power would produce very small improvements in engine transient response.

The exhaust manifold pressure traces, shown in **Figure 6.10c** and **Figure 6.11c**, reflect the engine torque pattern and have an initial spike at 0.05 s. The sudden rise in pressure is caused by the extra fuel burned which increases the gas temperatures. The drop is caused by the larger mass flow rate out of the exhaust manifold and the drop in-cylinders oxygen content, which reduces the amount of fuel which can be burned. After this initial spike, the exhaust manifold pressure lags behind the intake manifold pressure when ETA is present. This is because the mass has to be transferred from the intake manifold through the engine and into the exhaust manifold. Due to the reciprocating nature of the engine, the increase in density of the intake manifold is only seen at the exhaust manifold after one engine cycle, when the higher density gas in the cylinder is discharged into the exhaust manifold. As a result, the exhaust manifold pressure lags behind the intake manifold pressure by one engine cycle (2 revolutions). This effect can be seen in **Figure 6.12a** and **Figure 6.13a**, where increasing the assistance power makes the difference between compressor outlet pressure and turbine inlet pressure more positive.

The turbocharger speed is artificially limited to 150,000 rev/min, that is the highest speed at which compressor data is available. When this limit is met, in *WCB*, the engine continues to accelerate, causing the mass flow rate to increase and, due to the compressor characteristics, this results in a drop of pressure ratio (**Figure 6.11b**). The exhaust manifold pressure does not drop since the intake manifold pressure reduction is compensated by the increase in mass flow rate. The intake manifold pressure marginally drops also when the speed limit is not met. This is caused by the combined effect of turbocharger acceleration and EGR mass flow rate reduction which occur towards the end of the simulation. The EGR mass flow rate reduction increases the mass flow through the compressor, which in turn causes a larger pressure drop through the ducting and intercooler. The fact that the compressor is not accelerating at the same rate and

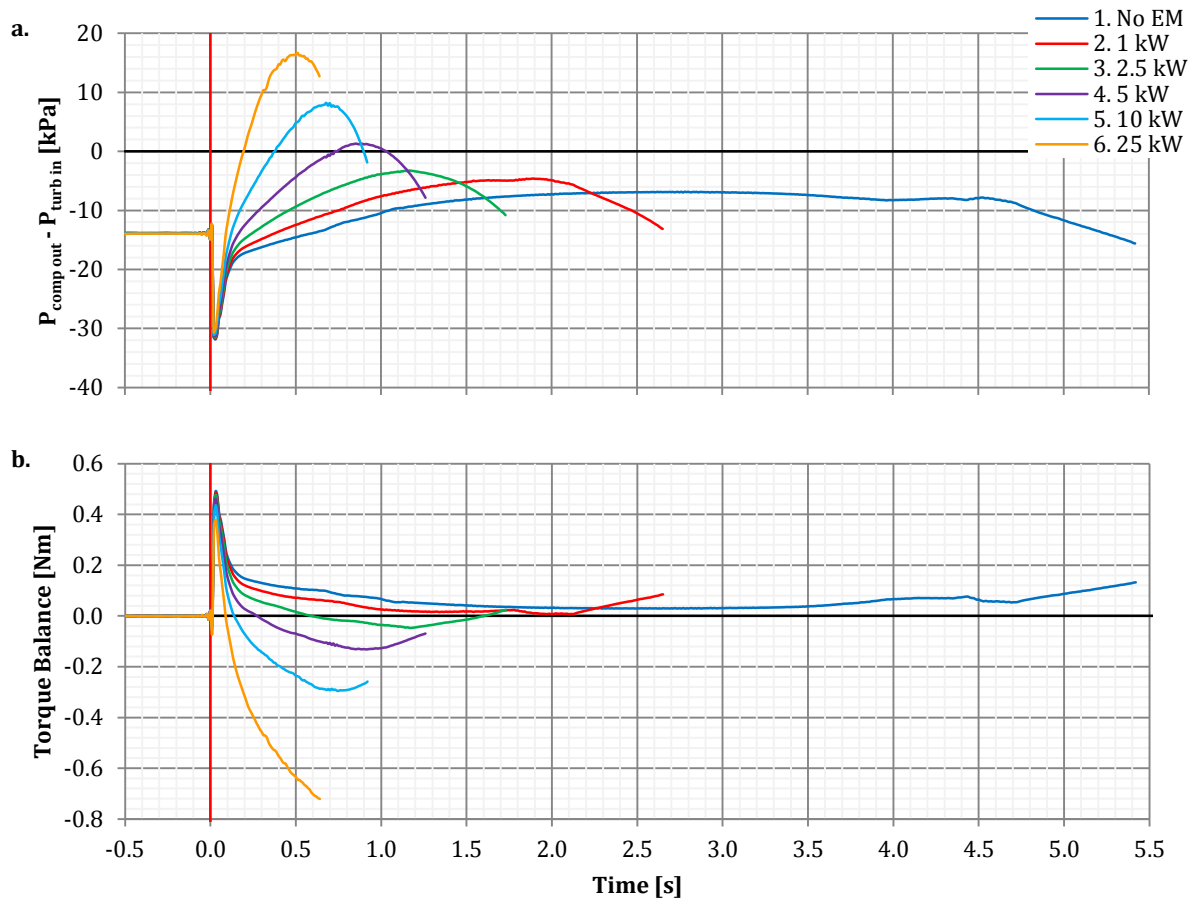


**Figure 6.12 – Compressor outlet pressure minus turbine inlet pressure and turbocharger torque balance time traces for a step change in load from 100 Nm to 399 Nm (WCA). The torque balance is the algebraic sum of the turbine, compressor and frictional moments about the shaft axis (note that motor/generator torque is excluded)**

that the mass flow is increased, causes a shift in operating point towards the choking line with little or no increase in pressure ratio (**Figure 6.15a**).

**Figure 6.12a** and **Figure 6.13a** show the difference between the compressor exit pressure and the turbine inlet pressure. **Figure 6.12b** and **Figure 6.13b** show the turbocharger torque balance, which is the algebraic sum of moments acting on the turbocharger shaft, excluding the motor/generator torque. When the assistance power is increased, the pressure difference rises due to the faster intake manifold pressure increase and the engine mass transfer delay described earlier. Because of this, the turbine torque lags behind the compressor and frictional load, resulting in a negative torque balance. This makes electric assistance less effective since part of the assistance power is used to compress the intake air rather than accelerating the turbocharger.

The compressor operation traces are plotted in **Figure 6.14a** for *WCA* and in **Figure 6.15a** for *WCB*. During the initial part of the transient the compressor operation point is taken away from the surge line when ETA is present. This is because of the intake manifold filling time, which

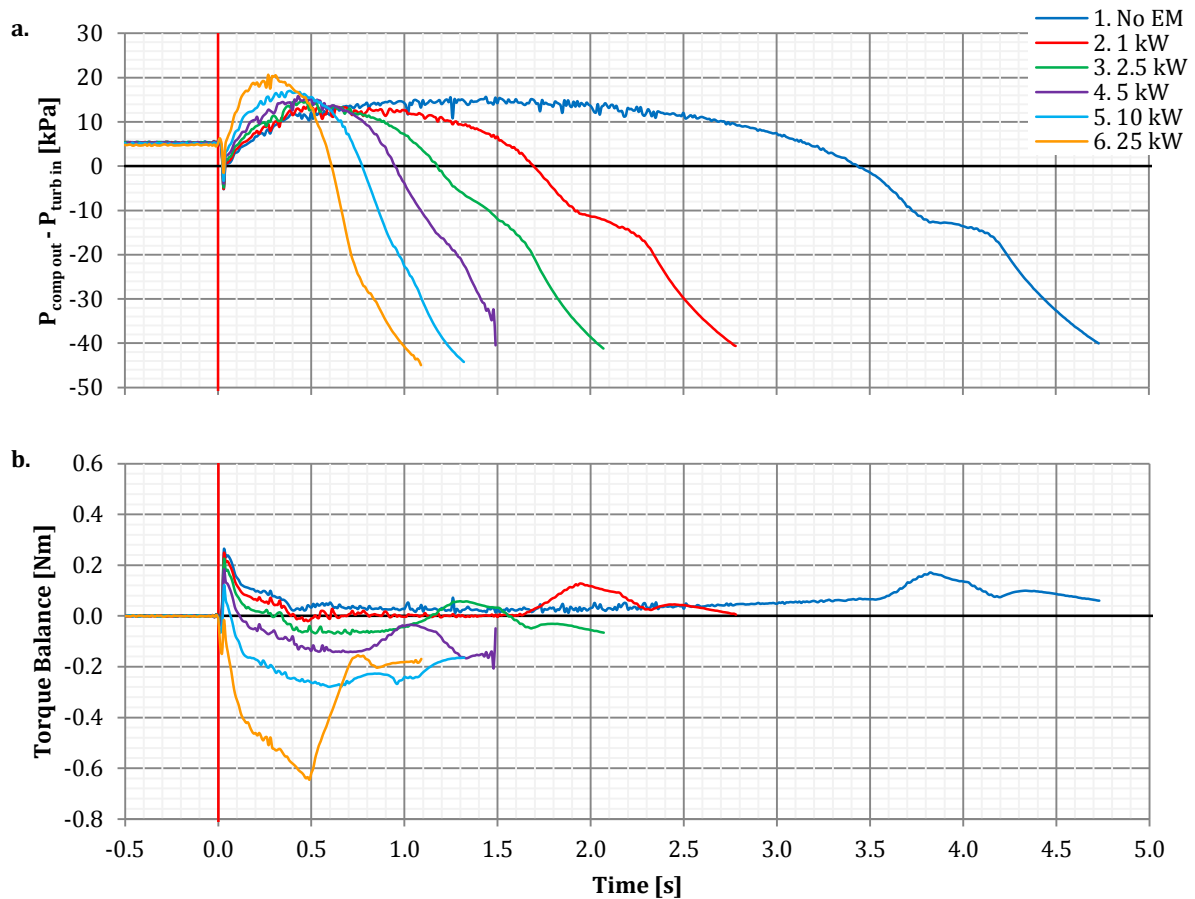


**Figure 6.13 – Compressor outlet pressure minus turbine inlet pressure and turbocharger torque balance time traces for a step change in load from 534 Nm to 817 Nm (WCB). The torque balance is the algebraic sum of the turbine, compressor and frictional moments about the shaft axis (note that motor/generator torque is excluded)**

causes the pressure rise to lag behind the turbocharger speed rise. This results in a shift of the compressor operation point towards the right part of the map, where the mass flow rate is higher. This effect is accentuated by the fact that the exhaust manifold pressure rise lags behind the intake manifold pressure rise. This lag increases the volumetric efficiency of the engine and therefore it also increases the intake manifold filling time. In addition, with ETA the engine speed drop is reduced, resulting in a higher engine mass flow rate and a longer manifold filling time.

In the later part of the transient, the compressor operation traces move to the left of the baseline trace, closer to the surge line, when electric assistance is applied. This is the result of the higher turbocharger speed achieved thanks to the motor/generator. As the turbocharger speed to engine speed ratio is higher with turbocharger assistance, this results in a higher pressure ratio across the compressor. The intake manifold pressure lag still affects the compressor operation, but is not sufficient to compensate for the higher compressor speed build up during the transient

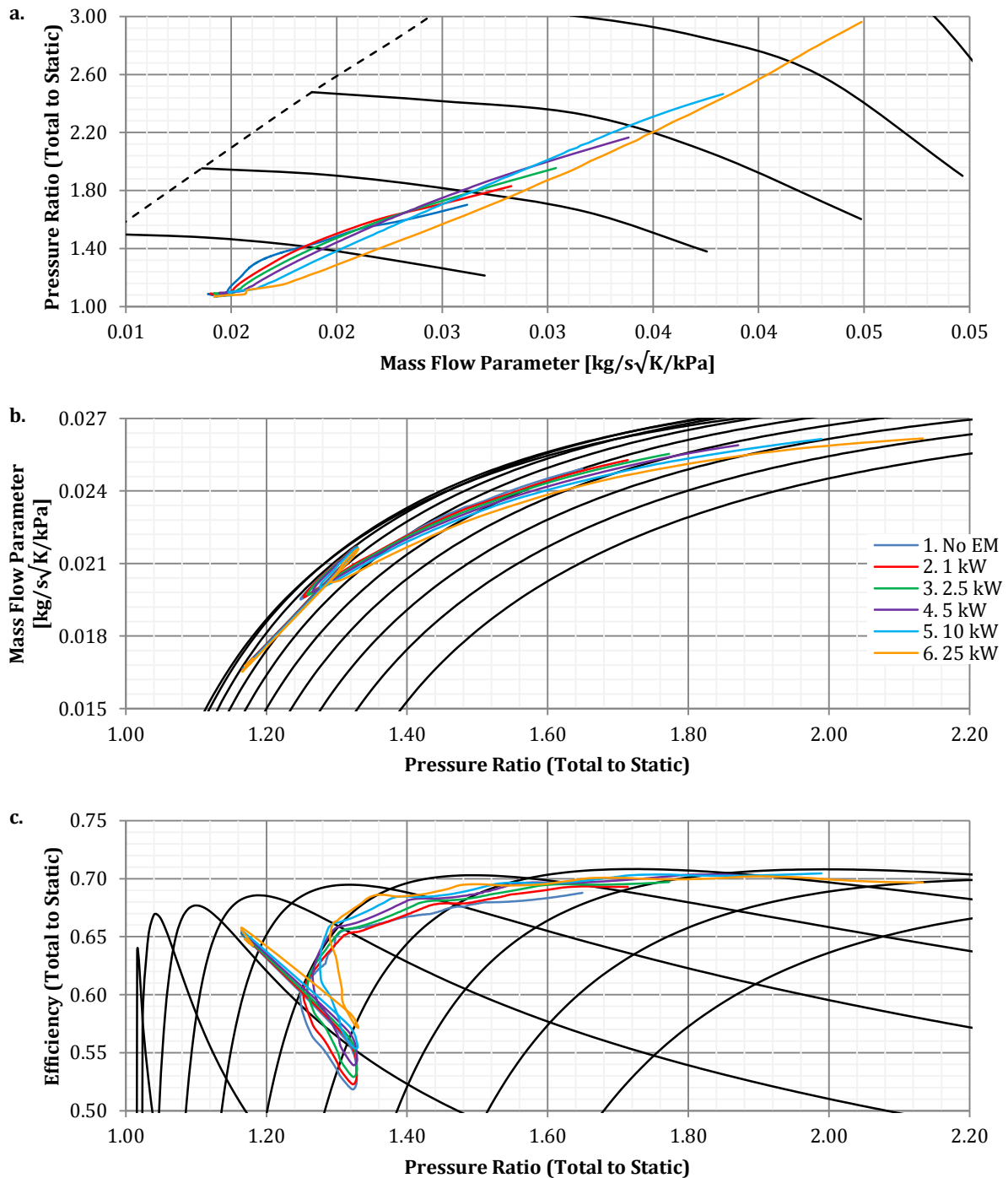


**Figure 6.14 – Compressor and turbine operating traces, plotted on their respective performance maps, for a step change in load from 100 Nm to 399 Nm (WCA). Part a shows the compressor mass flow map, part b shows the turbine mass flow map and part c shows the turbine efficiency map**

The turbine operation traces, shown in **Figure 6.14b**, **Figure 6.14c**, **Figure 6.15b** and **Figure 6.15c**, are less affected by electric assistance than the compressor traces, particularly in *WCB*. This is because the turbine efficiency and mass flow rate are a weaker function of turbocharger speed, especially at the pressure ratios and speeds of *WCB*. As a result, the turbine inlet pressure lag is not sufficient to cause significant deviations from the baseline trace.



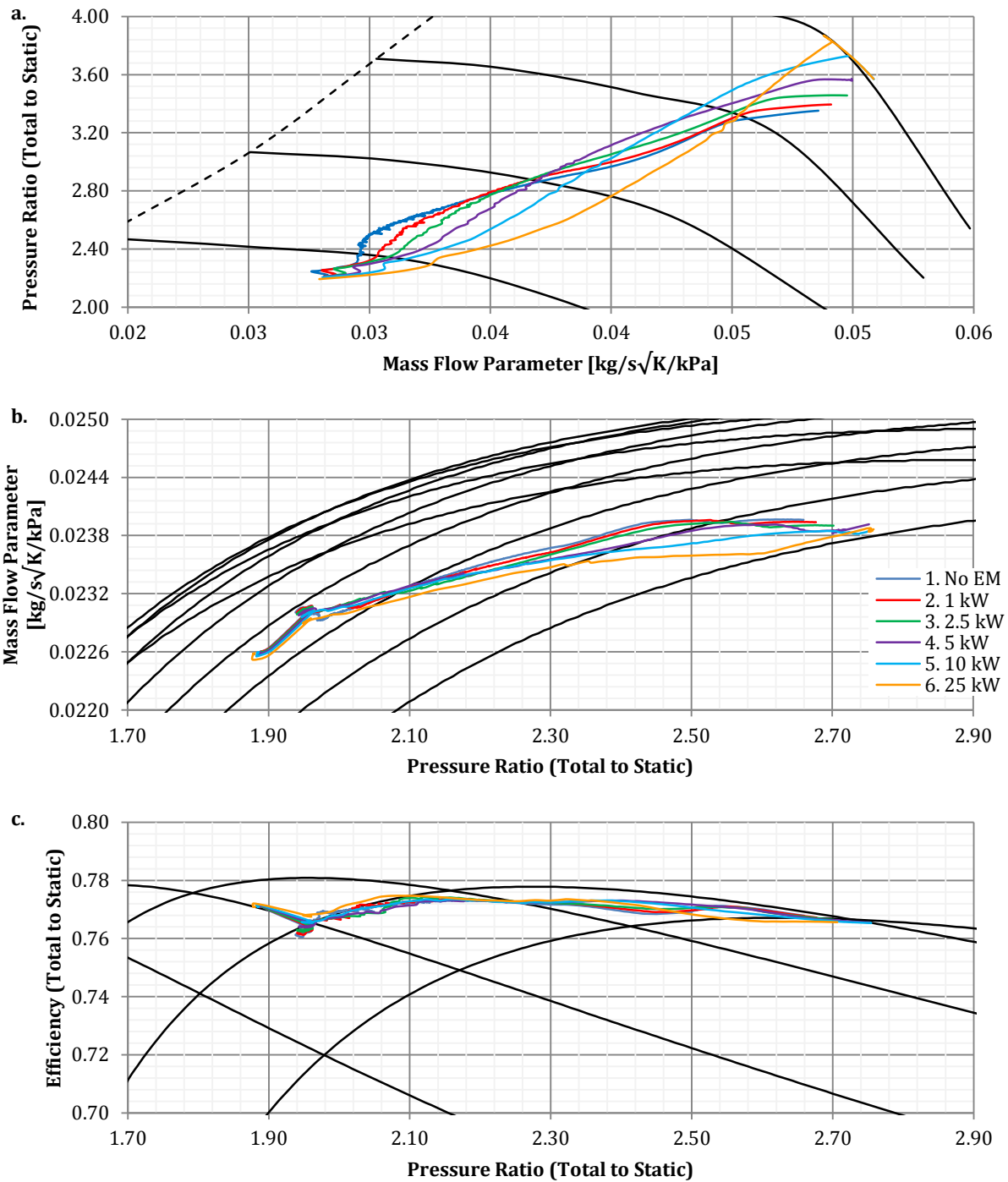


**Figure 6.15 – Compressor and turbine operating traces, plotted on their respective performance maps, for a step change in load from 534 Nm to 817 Nm (WCB). Part a shows the compressor mass flow map, part b shows the turbine mass flow map and part c shows the turbine efficiency map**

The main difference in turbine operation is that the turbine mass flow rate parameter tends to be lower with electric assistance thanks to the higher turbocharger speeds, reflecting the observations made in **Chapter 5**. In *WCA* the turbine follows a more efficient operation path when assisted. This is because at low speeds the efficiency drops rapidly with rising pressure ratio. Since the turbine velocity rises faster with electric assistance, the efficiency drop is reduced. This contradicts the observations made in **Chapter 5**, where the turbine efficiency

drops with electric assistance. The different outcome is explained by the fact that in **Chapter 5** the mass flow rate of gases entering the exhaust manifold (inlet pipe) was maintained constant, while in this study it increases with turbocharger speed. The loop in the turbine operation traces is caused by the spike in turbine inlet pressure that occurs at the beginning of the transient.

As described in **Section 6.1** the compressor and turbine have been modelled in a quasi-steady manner, so one may question the validity of these results. Copeland et al. have derived a non-dimensional number which can be used to assess the level of unsteadiness inside a control volume for oscillating flow (Copeland et al., 2012):

$$\zeta = \frac{2\Delta\rho l}{\rho t c} = \frac{\text{Particle Residence Time Scale}}{\text{Density Change Time Scale}} \quad (6.7)$$

The subscript zero here represents a reference value and  $\Delta\rho$  represents the amplitude of the density waves. If the density change time-scale is much larger than the particle residence time-scale, the flow across the component is considered to be steady. This correlation has been modified so that it can be applied to a transient flow:

$$\zeta = \frac{d\rho}{dt} \frac{Al}{\dot{m}} \quad (6.8)$$

Conceptually the correlation is equivalent to the original. All the flow quantities have been measured at the inlet for the turbine and at the outlet for the compressor. These are good locations as they represent well the flow in the volutes and, since the longest residence time occurs in the volutes, it gives good reference values.

**Table 6.6 - Turbine and Compressor maximum  $\zeta$  number reached during the transients**

	WCA		WCB	
	Compressor	Turbine	Compressor	Turbine
<b>1. No EM</b>	0,0074	0,0917	0,0051	0,0249
<b>2. 1 kW</b>	0,0078	0,0917	0,0055	0,0246
<b>3. 2.5 kW</b>	0,0082	0,0917	0,0062	0,0245
<b>4. 5 kW</b>	0,0088	0,0917	0,0073	0,0242
<b>5. 10 kW</b>	0,0102	0,0918	0,0084	0,0233
<b>6. 25 kW</b>	0,0130	0,0918	0,0103	0,0213

**Table 6.6** shows the maximum  $\zeta$  number reached during the transient, calculated from the filtered results. All the values are significantly smaller than unity, indicating that the engine transient is not causing a large amount of unsteadiness in the turbine and compressor. As a consequence, the filtered compressor and turbine operation traces shown earlier are valid.

Calculating the  $\zeta$  number from the filtered data hides the turbine flow unsteadiness caused by the exhaust flow pulsations and, in reality, the turbine operates under unsteady flow conditions.

This does not invalidate the transient results because the transient unsteady effects occur in the engine and manifolds, which have been modelled in such a way that they capture 1D dynamic flow effects. In addition, the full engine model has been validated in steady state where the turbine model has worked well under unsteady flow and the transient does not significantly increase the unsteadiness of the turbine flow. Finally, the frequency content of the engine transient is significantly lower than the frequency content of the exhaust flow pulsations, so that the two waves are clearly separated by filtering.

Not enough information on production costs has been provided and therefore it is difficult to state which is the best performance/cost compromise. However, **Figure 6.9** shows that motor/generator powers above 10 kW do not cause large further improvements in transient performance. Therefore it is likely that the best compromise sits in the 5 to 10 kW power region, exactly where the motor/generator tested in **Chapter 3** sits. The only drawback of this electrical machine size range is that the power is a small fraction of the engine power, and turbocompounding cannot be fully exploited. This problem is worsened by the fact that the maximum power quoted can be attained only for a short amount of time.

The motor/generator scaling technique is relatively simple. The stator winding configuration could be changed or a gearing system could be implemented to achieve different maximum powers and torque to inertia ratios. Changing the winding configuration to obtain higher powers with no increase in shaft inertia would only marginally affect the results, as the turbocharger shaft inertia was dominant over the motor/generator, and the rotor drag losses are negligible compared to bearing losses. Gearing is unlikely to be implemented in production due to the increase in complexity of the device. This would translate in high cost, complicated maintenance and low reliability, all of which are paramount for the intended engine applications.

## 6.5 ELECTRIC ASSISTANCE AND VARIABLE GEOMETRY TURBINE INTERACTION

One way to improve the transient response of a VGT turbocharged engine is to reduce the turbine vanes opening during the transient. This increases the turbine power and improves the turbocharger acceleration. Having both electric assistance and VGT on the same turbocharger means that there are two degrees of freedom that can be used to improve engine transient performance. It is therefore necessary to study how they interact with each other to understand how they can be controlled.

The objectives of this simulation are to:

- Compare the engine transient performance with the ETA system with that of the VGT system, applying different turbine vanes control strategies
- Investigate the benefits in actuating the turbine vanes of the hybrid system during transients.

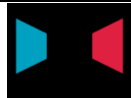




### 6.5.1 ELECTRIC ASSISTANCE AND VGT INTERACTION INVESTIGATION DESCRIPTION

To achieve the objectives of this study, different turbocharging system configurations have been simulated on the two work cycles described in the previous section. The amount of fuel injected and the EGR mass flow rate are controlled in exactly the same way as in the previous study, and a detailed description can be found in **Section 6.4.1**.

The motor/generator implemented to assist the turbocharger is the one described in **Chapter 3**, which has a maximum shaft power of 5.39 kW. In the cases where electric assistance is present, the maximum shaft power is applied instantaneously when the engine load is increased.

The VGT vanes are actuated in two different ways to improve engine transient response. The first method is to set them so that the steady state boost is higher than the best engine efficiency boost. The second actuation method is to close the vanes during the transient. For completeness, the VGT are also opened during the transient to investigate the impact on PMEP. When the VGT is actuated during the transient, all the changes occur instantaneously when the engine load is increased.

**Table 6.7 – Summary of the cases simulated**

Case	Initial boost BSFC optimized	Electrical assistance (ETA)	VGT transient actuation	Sub-cases	
1		Yes	No	No	
2		Yes	No	Yes	a   VGT closed by 25% (0.563 - WCA, 0.450 - WCB)
					b   VGT closed by 50% (0.375 - WCA, 0.300 - WCB)
					c   VGT opened by 25% (0.938 - WCA, 0.750 - WCB)
					d   VGT opened by 50% (1.000 - WCA, 0.900 - WCB)
3		Yes	Yes	No	
4		Yes	Yes	Yes	a   VGT closed by 25% (0.563 - WCA, 0.450 - WCB)
					b   VGT closed by 50% (0.375 - WCA, 0.300 - WCB)
					c   VGT opened by 25% (0.938 - WCA, 0.750 - WCB)
					d   VGT opened by 50% (1.000 - WCA, 0.900 - WCB)
5		No	No	No	a   Initial intake manifold pressure 10% higher
					b   Initial intake manifold pressure 20% higher

Five different main cases have been simulated. In *Case 1*, the baseline case, the initial boost has been optimized for engine efficiency and no VGT or ETA is present. In *Case 2* the turbine vanes have been actuated during the transient and have been either opened or closed by 25% or 50% of the original opening. In *WCA* opening the vanes by 50% was not possible, so they have been set to the maximum opening (1.00). In *Case 3* electric assistance has been applied. In *Case 4* both electric assistance and VGT transient actuation have been applied. In *Case 5* the initial boost has been increased by reducing the VGT opening. Given the large number of combinations available for electric assistance and VGT control, the cases simulated have been summarized in **Table 6.7**.

#### 6.5.2 ELECTRIC ASSISTANCE AND VGT INTERACTION INVESTIGATION RESULTS AND DISCUSSION

**Figure 6.16** to **Figure 6.22** show the results obtained. The data has been filtered exactly in the same manner as in the previous study, apart from the PMEP and engine efficiency traces, which represent the average value over a full engine cycle.

**Table 6.8 – Speed drop and recovery time results**

	WCA				WCB			
	S <sub>drop</sub> [rev/min]	S <sub>drop</sub> Impr.	t <sub>recov</sub> [s]	t <sub>recov</sub> Impr.	S <sub>drop</sub> [rev/min]	S <sub>drop</sub> Impr.	t <sub>recov</sub> [s]	t <sub>recov</sub> Impr.
<b>1. No VGT Actuation</b>	110.1	0.0%	3.51	0.0%	153.0	0.0%	2.93	0.0%
<b>2a. Transient VGT -25%</b>	46.0	-58.2%	1.12	-68.1%	148.7	-2.8%	1.18	-59.7%
<b>2b. Transient VGT -50%</b>	55.5	-49.6%	0.95	-72.9%	157.3	2.8%	0.90	-69.3%
<b>2c. Transient VGT +25%</b>	Engine stall				Engine stall			
<b>2d. Transient VGT +50%</b>	Engine stall				Engine stall			
<b>3. No VGT Actuation ETA</b>	17.7	-83.9%	0.46	-86.9%	86.2	-43.7%	0.62	-78.8%
<b>4a. Transient VGT -25% ETA</b>	19.8	-82.0%	0.43	-87.7%	110.9	-27.5%	0.61	-79.2%
<b>4b. Transient VGT -50% ETA</b>	28.9	-73.7%	0.47	-86.6%	126.9	-17.1%	0.59	-79.9%
<b>4c. Transient VGT +25% ETA</b>	19.6	-82.2%	0.55	-84.3%	90.9	-40.6%	0.83	-71.7%
<b>4d. Transient VGT +50% ETA</b>	21.0	-81.0%	0.61	-82.6%	Engine stall			
<b>5a. Steady In Man P +10%</b>	7.3	-93.4%	0.37	-89.5%	56.9	-62.8%	0.70	-76.1%
<b>5b. Steady In Man P +20%</b>	7.2	-93.5%	0.06	-98.3%	10.8	-92.9%	0.28	-90.4%

The engine speed traces are shown in **Figure 6.16a** for *WCA* and in **Figure 6.17a** for *WCB*, while the recovery time and speed drop are summarized in **Table 6.8**. From the engine speed results it can be seen that:

- The best engine transient response is obtained when the initial boost is 20% higher than the efficiency optimized boost
- Closing the vanes during the transient improves transient response over the baseline
- Opening the vanes when the load is applied causes the engine to stall
- The speed drop with electric assistance is larger than when the initial boost is 10% higher, but the engine acceleration is better

- Turbocharger assistance is more effective in improving engine transient response than closing the VGT vanes when the load is applied
- When ETA is present, closing the vanes increases the speed drop

By inspecting the engine torque curves (**Figure 6.16b** and **Figure 6.17b**), it can be understood why the best transient response is achieved with the highest initial boost (*Case 5b*). With 20% extra intake manifold pressure at the transient start, the engine torque achieved solely by increasing the equivalence ratio has a larger magnitude than the engine load. As a result, the speed drop is not caused by lack of boost, but by the firing delay, which has a much shorter

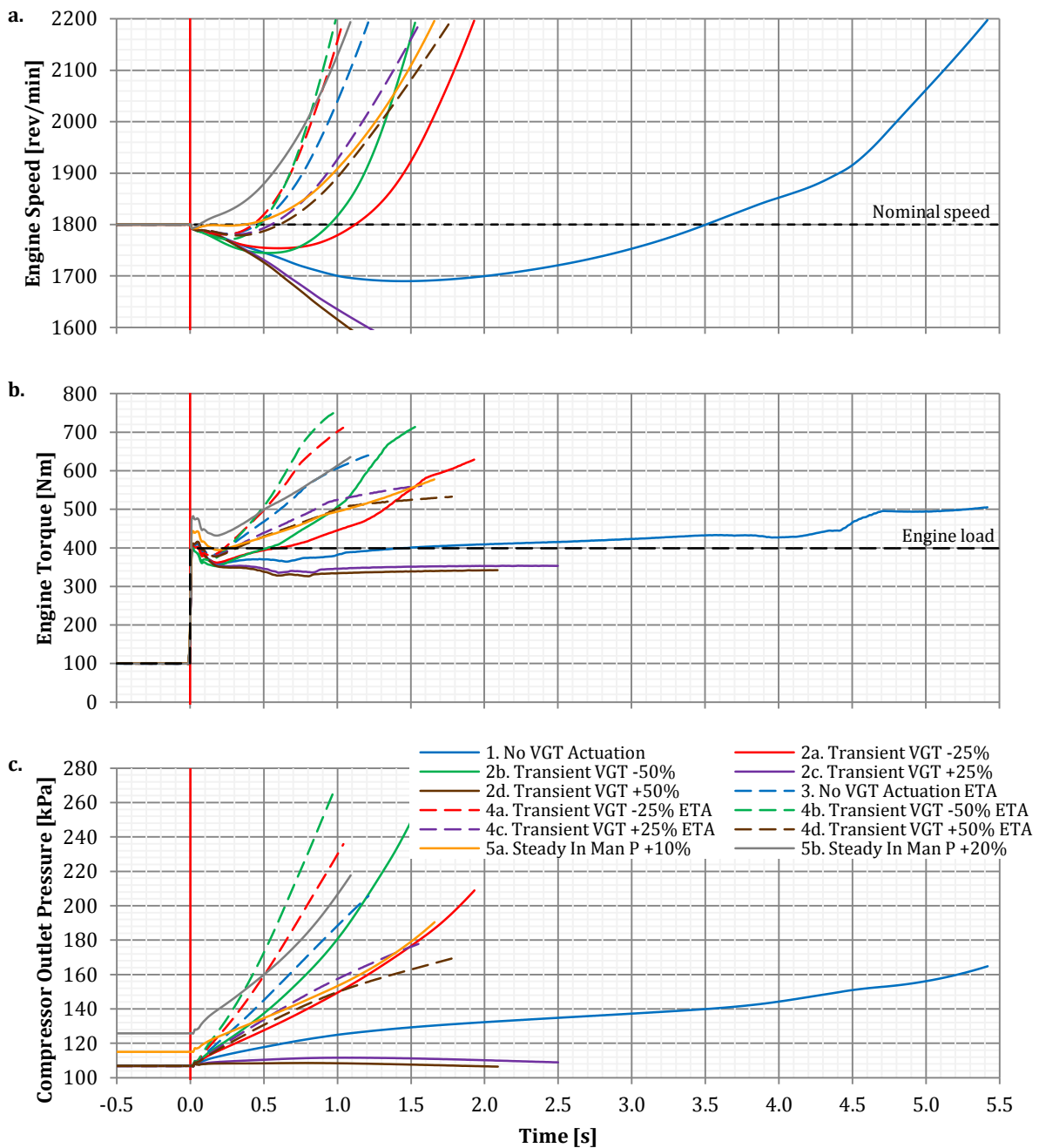


Figure 6.16 - Engine speed, engine torque and compressor outlet pressure time traces for a step change in load from 100 Nm to 399 Nm (WCA)

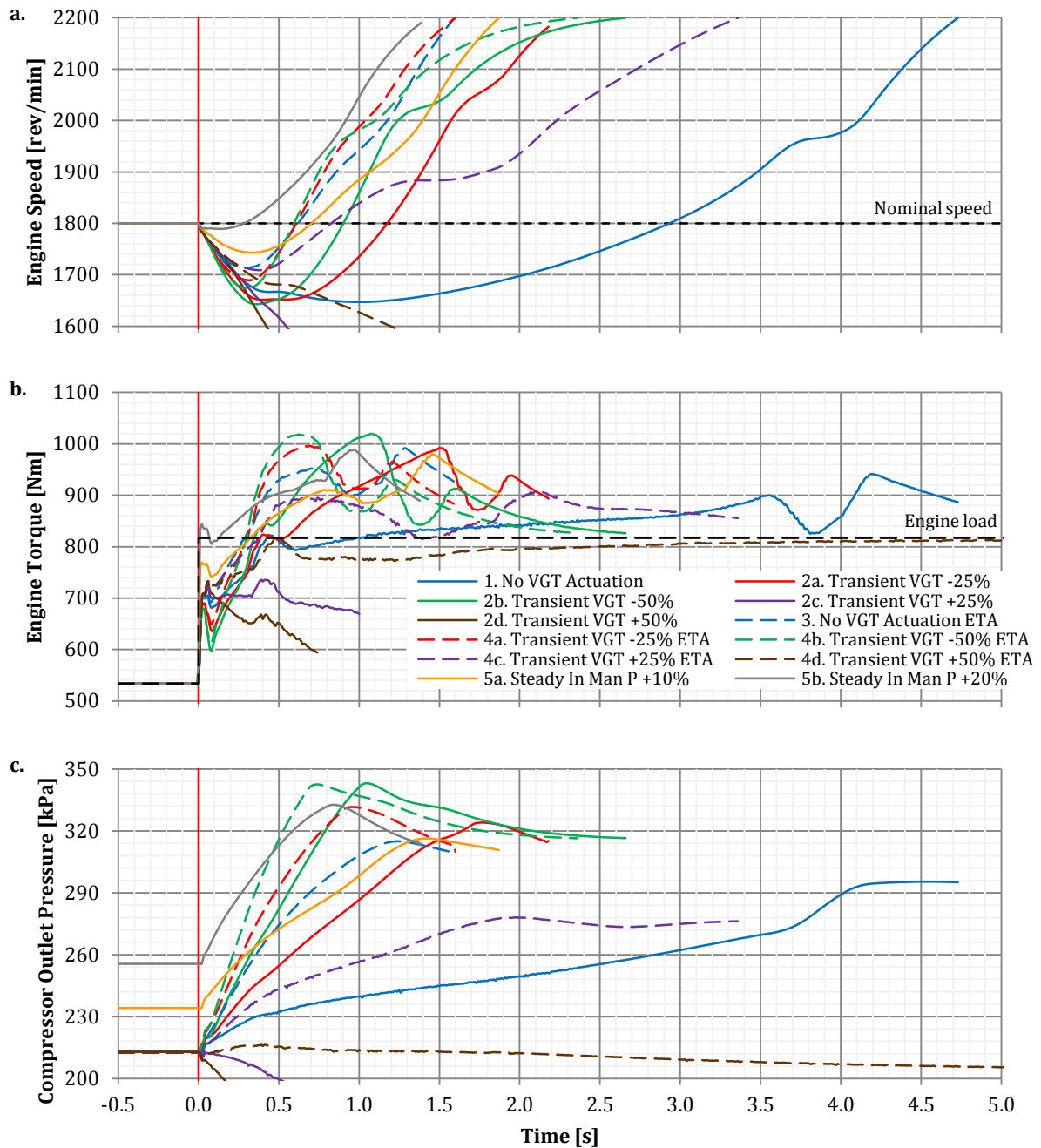
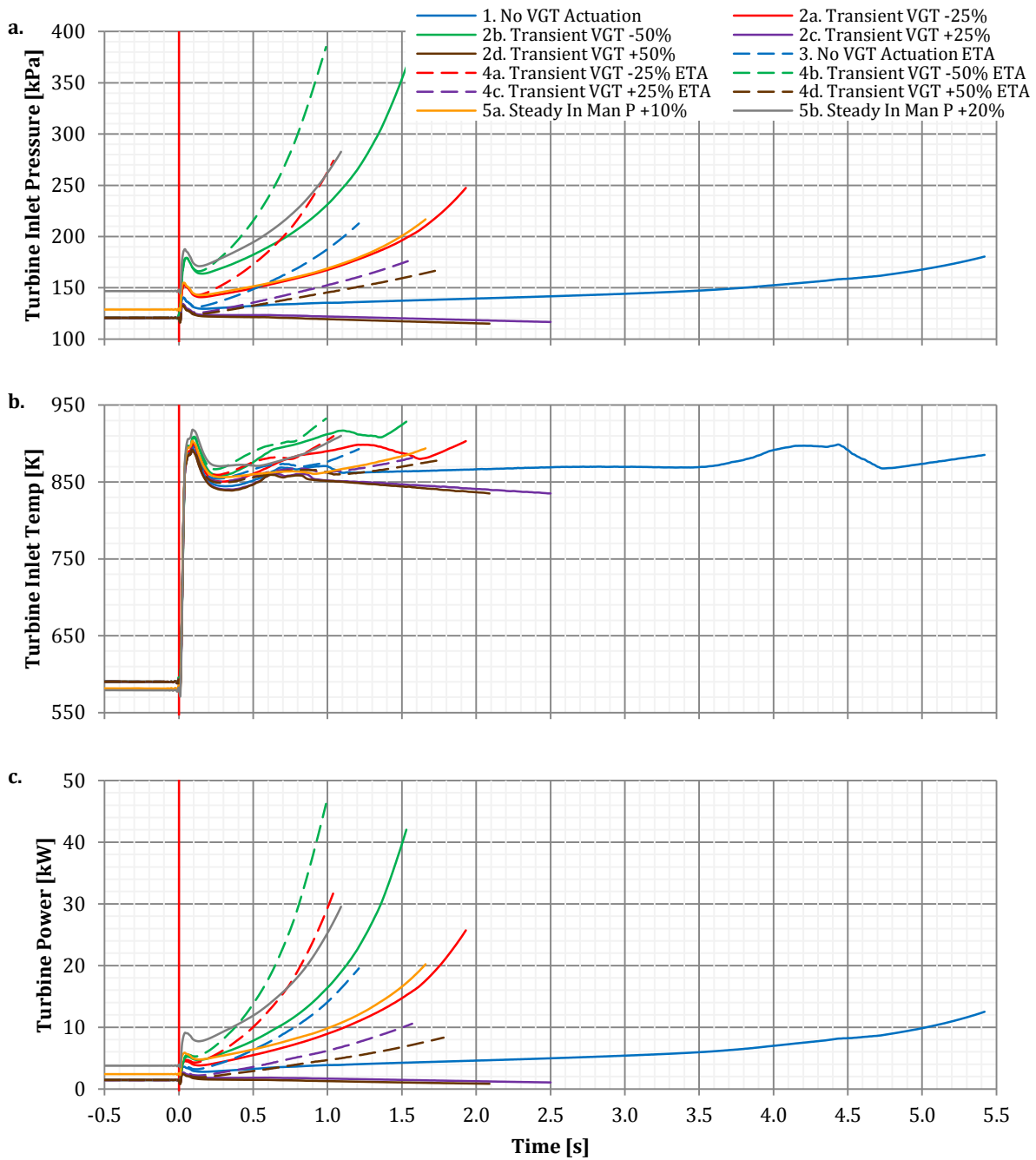


Figure 6.17 – Engine speed, engine torque and compressor outlet pressure time traces for a step change in load from 534 Nm to 817 Nm (WCB)

timescale than the delay caused by the turbocharger inertia.

Closing the vanes when the transient begins (*Cases 2a and 2b*) reduces both the speed drop and recovery time when compared to the baseline. Reducing the VGT opening means that the pressure inside the exhaust manifold builds up faster, resulting in an increase in turbine power (**Figure 6.18c** and **Figure 6.19c**). This causes a higher boost increase rate and the engine torque raises faster (**Figure 6.16** and **Figure 6.17**). The drawback is that the higher exhaust manifold pressure means that the exhaust gases trapped in the cylinder and the external EGR



**Figure 6.18 - Turbine inlet pressure, inlet temperature and power time traces for a step change in load from 100 Nm to 399 Nm (WCA)**

are increased, momentarily reducing the oxygen content in the cylinders. This causes a larger torque drop after the initial peak (**Figure 6.16b** and **Figure 6.17b**, 0 to 0.3 s). In addition, the increase in turbine inlet pressure raises the pumping losses during the transient, impacting negatively on the engine torque.

If the VGT is opened instead of being closed (*Cases 2c and 2d*), the engine stalls. The reason for this is that the turbine power rise (**Figure 6.18c** and **Figure 6.19c**), caused by the increase of fuel injected, is not sufficient to accelerate the turbocharger rapidly enough. The boost does



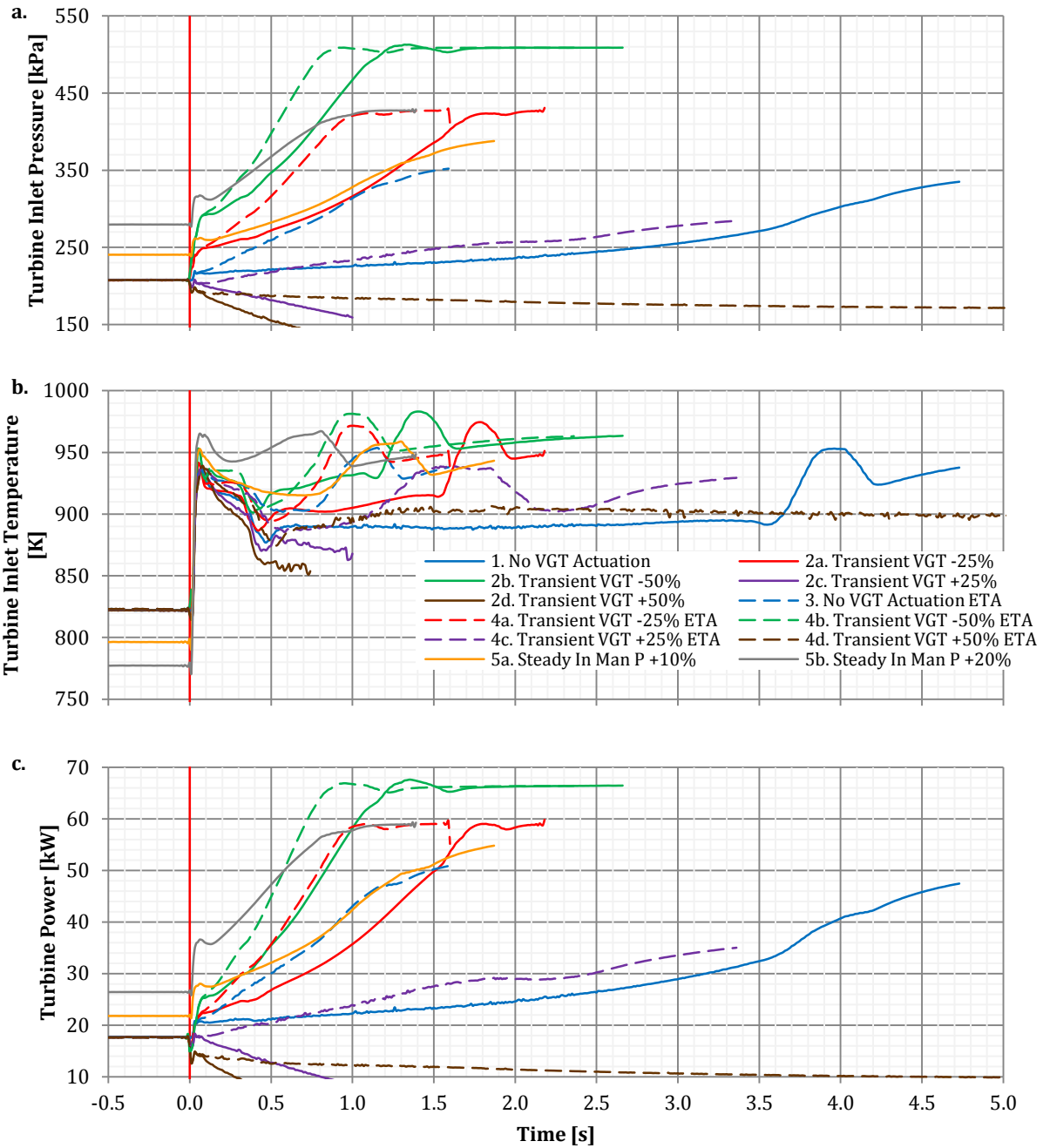


Figure 6.19 - Turbine inlet pressure, inlet temperature and power time traces for a step change in load from 534 Nm to 817 Nm (WCB)

increase but, as the engine speed drops, the turbine power stops rising due to the reduction in mass flow rate. The outcome of this is that the turbocharger decelerates, the boost pressure drops, and the engine stalls.

By comparing turbocharger assistance (*Case 3*) with the case where the initial boost is 10% higher (*Case 5a*), it can be seen that the ETA case has a larger speed drop. This is because the higher boost causes a higher initial torque, while the ETA requires time to increase the boost, and therefore the torque increases gradually. The advantage of turbocharger assist is that the

turbocharger acceleration is higher, and the boost soon rises above the boost of *Case 5a* (**Figure 6.16c** and **Figure 6.17c**). In fact, the recovery time in *WCB* is shorter for the assisted case. This suggests that as the load step is increased, increasing the transient duration for all the cases, electric assistance will perform better and better over boost increments, since more time is available to build up boost. Moreover, the engine speed drop adversely affects the turbine power but not the motor/generator power. As a result, the turbocharger acceleration would be reduced more when the turbocharger is not assisted, further increasing ETA's advantage on larger load steps.

The main reason why engine transient performance is better with electric assistance (*Case 3*) than with transient VGT actuation (*Cases 2a* and *2b*) is that ETA provides more power to accelerate the turbocharger. Closing the turbine vanes by 25% increases the turbine power (**Figure 6.18c** and **Figure 6.19c**) at 0.1 s by 1.03 kW in *WCA* and 1.84 kW in *WCB*, while closing the vanes by 50% improves the turbine power by 1.93 kW in *WCA* and by 4.80 kW in *WCB*. The ETA power at 0.1s is 2.83 kW in *WCA* and 5.37 kW in *WCB*. After 0.25 s, the turbine power difference compared to the baseline is 1.33 kW in *WCA* and 2.86 kW in *WCB* when the vanes are closed by 25%, and the difference is 2.55 kW in *WCA* and 7.10 kW in *WCB* with a 50% VGT opening reduction. The ETA power at 0.25 s is 3.45 in *WCA* and 5.31 in *WCB*. It can be noticed that the *WCB* ETA power is lower than the power increase due to a 50% VGT opening reduction, but the boost increase rate at that time is approximately equal. This is because turbocharger assistance also increases the turbine power thanks to the faster intake manifold pressure build up (compared to baseline). The turbine power difference with the baseline case at this moment in time is 1.09 kW in *WCA* and 3.75 kW in *WCB*. As a result, the highest total power input into the turbocharger is achieved with ETA also at this later stage of the transient.

Turbocharger assistance has some further advantages over transient VGT actuation. First of all, the motor/generator delivers the maximum power with a negligible time lag, while closing the VGT vanes causes the turbine power to increase only after some extra pressure has built up inside the exhaust manifold. The ETA power is independent of exhaust flow conditions and it is not negatively affected by the engine speed, and mass flow rate, drop as the turbine power. The other advantage is that ETA does not directly restrict the exhaust flow, and this improves the engine torque by two different mechanisms. The first mechanism is that the pumping losses (**Figure 6.20a** and **Figure 6.21a**) increase far less with electric assistance and this increases the engine torque. The second mechanism is that the exhaust gases trapped inside the cylinder are much less with ETA, increasing the cylinder oxygen content and allowing more fuel to be burned.

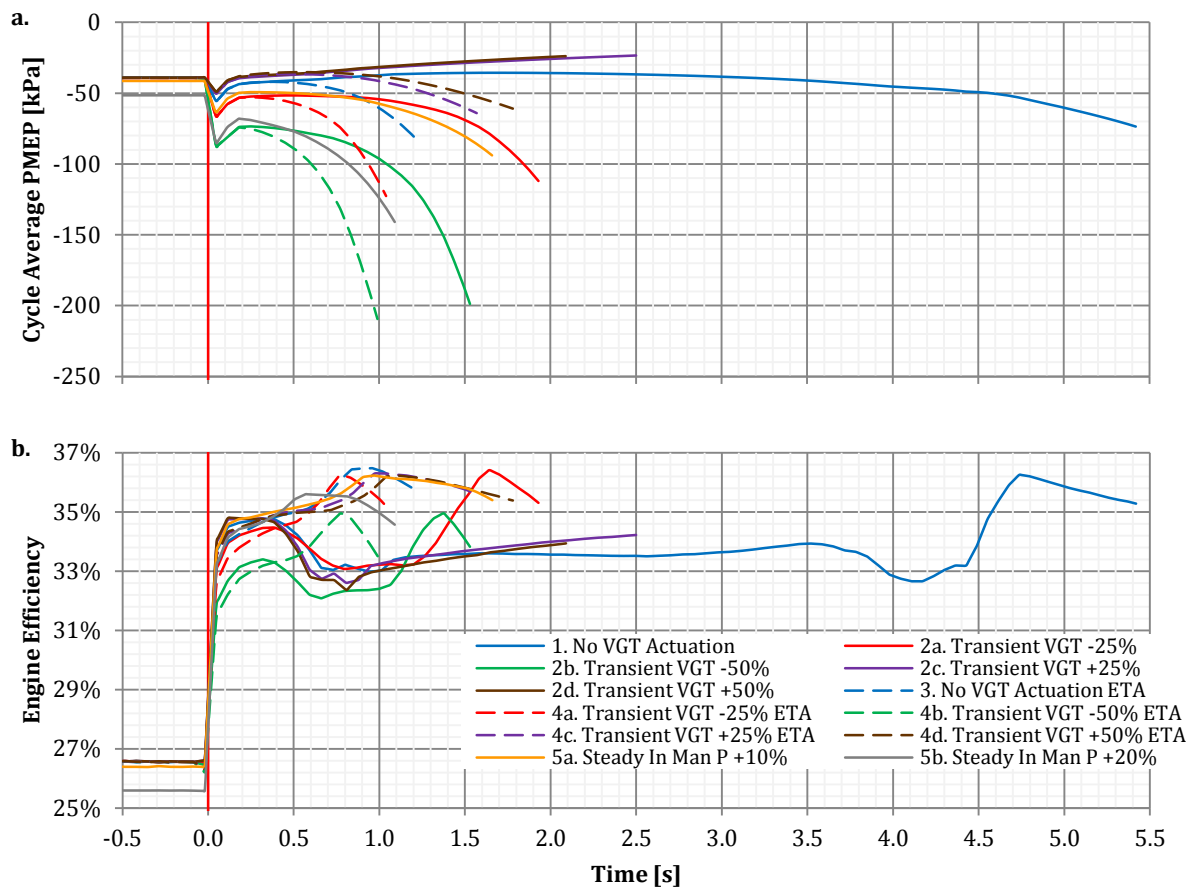


**Figure 6.20 – Engine cycle average pumping mean effective pressure and efficiency time traces for a step change in load from 100 Nm to 399 Nm (WCA). The engine efficiency is calculated from the total energy consumed (i.e. diesel fuel plus electrical energy)**

The mechanisms described in the previous paragraph also explain why the speed drop is higher in *Cases 4a* and *4b*, where both VGT closure and electric assistance are applied simultaneously, than in *Case 3*, where only ETA is applied. The extra exhaust manifold pressure impacts negatively on the engine torque, causing a higher engine deceleration in the initial part of the transient. Nevertheless, the extra turbine power obtained by closing the vanes increases the boost rise rate (**Figure 6.16c** and **Figure 6.17c**), improving the engine torque in the latter part of the transient (after approximately 0.2 s). The final outcome is that the recovery time is approximately the same as when only electric assistance is applied.

As expected, it can be seen from **Figure 6.18** and **Figure 6.19** that increasing the initial intake manifold pressure (*Cases 5a* and *5b*) causes an increment in turbine inlet pressure and a reduction of the turbine inlet temperature. The boost increase also results in a higher peak turbine inlet temperature reached in the initial phase of the transient (around 0.1 s), thanks to the higher exhaust manifold pressure. As a result, the initial step in turbine power results higher and this contributes to the improvement of engine transient performance.

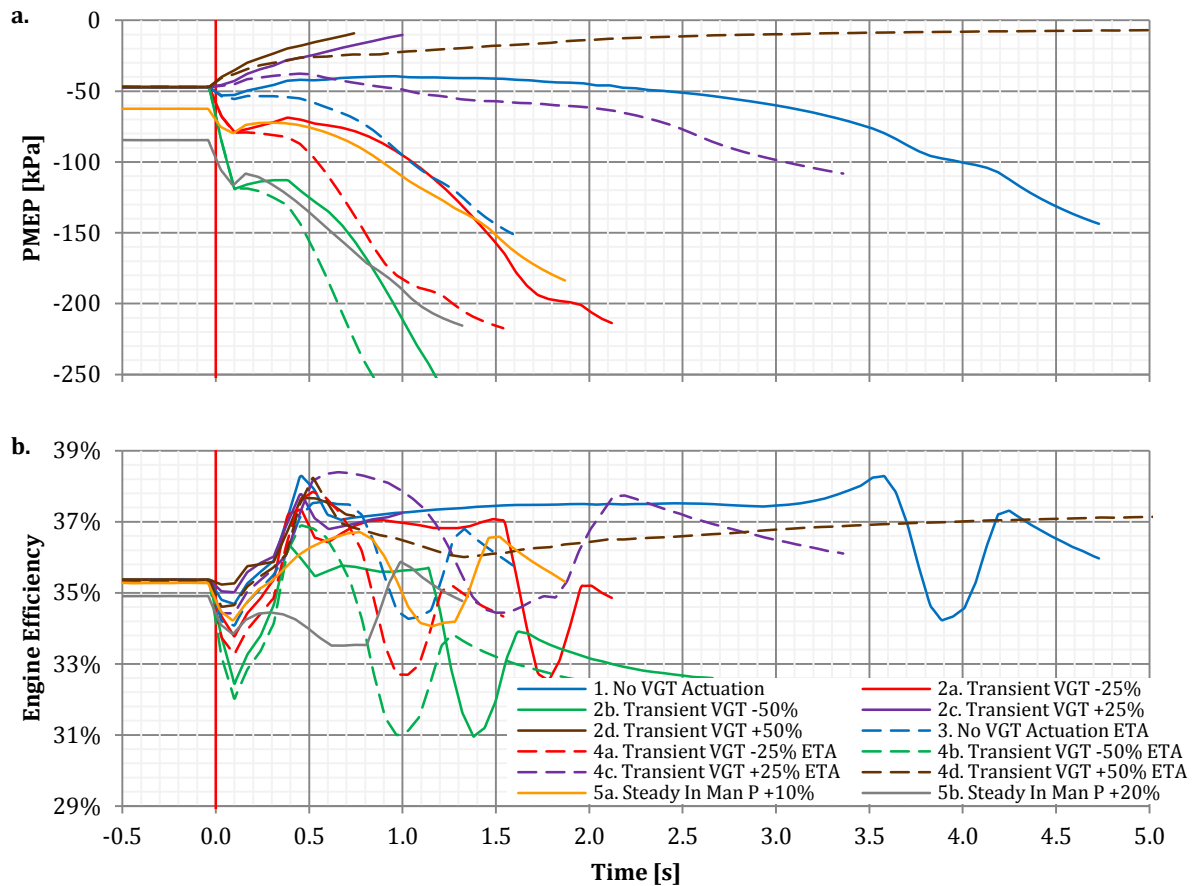


**Figure 6.21 – Engine cycle average pumping mean effective pressure and efficiency time traces for a step change in load from 534 Nm to 817 Nm (WCB). The engine efficiency is calculated from the total energy consumed (i.e. diesel fuel plus electrical energy)**

Closing the turbine vanes when the load is applied (*Cases 2a, 2b, 4a and 4b*) also causes the turbine inlet pressure and temperature at the beginning of the transient to increase. As a result, the initial step in turbine power is increased, but the increase is not sufficient to match the power obtained with the higher initial boosts.

A second effect of the turbine vanes transient closure is that a small and sudden drop in turbine power occurs at the very beginning of the transient in *WCB* (approximately 0.02 s). the drop is of 1.5 kW when the vanes are closed by 25% and of 2.5 kW when the vanes are closed by 50%, but these values are approximative as the timescale at which this effect occurs roughly corresponds to the minimum time period of the filter pass band. This effect is caused by the sudden turbine mass flow rate and efficiency reduction caused by the VGT closure. On a real engine this effect is unlikely to be replicated as the vanes opening could not occur instantaneously due to VGT actuation mechanism inertia and control delays.

The observations made on the turbine inlet pressure traces are also reflected on the PMEP. It can be observed from **Figure 6.20a** and **Figure 6.21a** that the PMEP has a sudden drop when

the transient starts. This is caused by the sudden rise in exhaust manifold pressure which generates an adverse pressure gradient for the flow through the cylinders. Closing the turbine vanes, either before (*Case 5*) or during the transient (*Cases 2a, 2b, 4a and 4b*), causes a larger PMEP drop and a general increase in pumping losses during the transient.

Turbocharger assistance also causes a reduction of PMEP, but this occurs at a later stage of the transient and is of smaller magnitude compared to the reduction caused by VGT closure. This was unexpected as ETA adds power to the turbocharger and, as we have seen in the previous section, it generates a favourable pressure gradient for the flow across the cylinders. The main reason of the PMEP reduction is that the engine speed drop is lower, and this rises the fraction of exhaust gases which are expelled from the cylinder by piston movement. This effect is accentuated by the fact that the turbine flow becomes more restricted as the turbine speed increases.

**Figure 6.20b** and **Figure 6.21b** show the engine efficiency traces during the transient. The engine efficiency is calculated from the total energy consumed, so it includes the electrical power consumed when electric assistance is present. These figures show that the engine efficiency reflects the trends in PMEP. Closing the turbine vanes during the transient causes a reduction of engine efficiency due to the increased pumping losses. Turbocharger assistance reduces the engine efficiency as well, and this is mainly due to the electrical power consumed to accelerate the turbocharger. Nonetheless, this efficiency reduction is minimal thanks to the low power consumed by the motor/generator, when compared to the power consumption of the engine. Moreover, these transient engine efficiency traces are not fully representative of the actual ETA fuel consumption benefits. For example, The motor/generator can slow down the turbocharger when the engine load is reduced, and this cannot be captured by these work cycles. By doing this, it recuperates some of the turbocharger kinetic energy which would otherwise be dissipated by the compressor, as unwanted boost, and by the bearings, as heat. The ETA can also be controlled to achieve electric turbocompounding, but this is outside the scope of this study.

Increasing the initial boost by 10% reduces the steady state engine efficiency by 0.17% (0.62% relative reduction) in *WCA* and by 0.09% (0.25% relative reduction) in *WCB*, while a 20% increase worsens the efficiency by 0.97% (3.67% relative reduction) in *WCA* and 0.46% (1.29% relative reduction) in *WCB*. The engine efficiency reduction with the 10% boost rise is minimal and this boost increase provides significant improvements in transient response. This indicates that electric assistance and minor boost increments can be combined to reduce speed drop

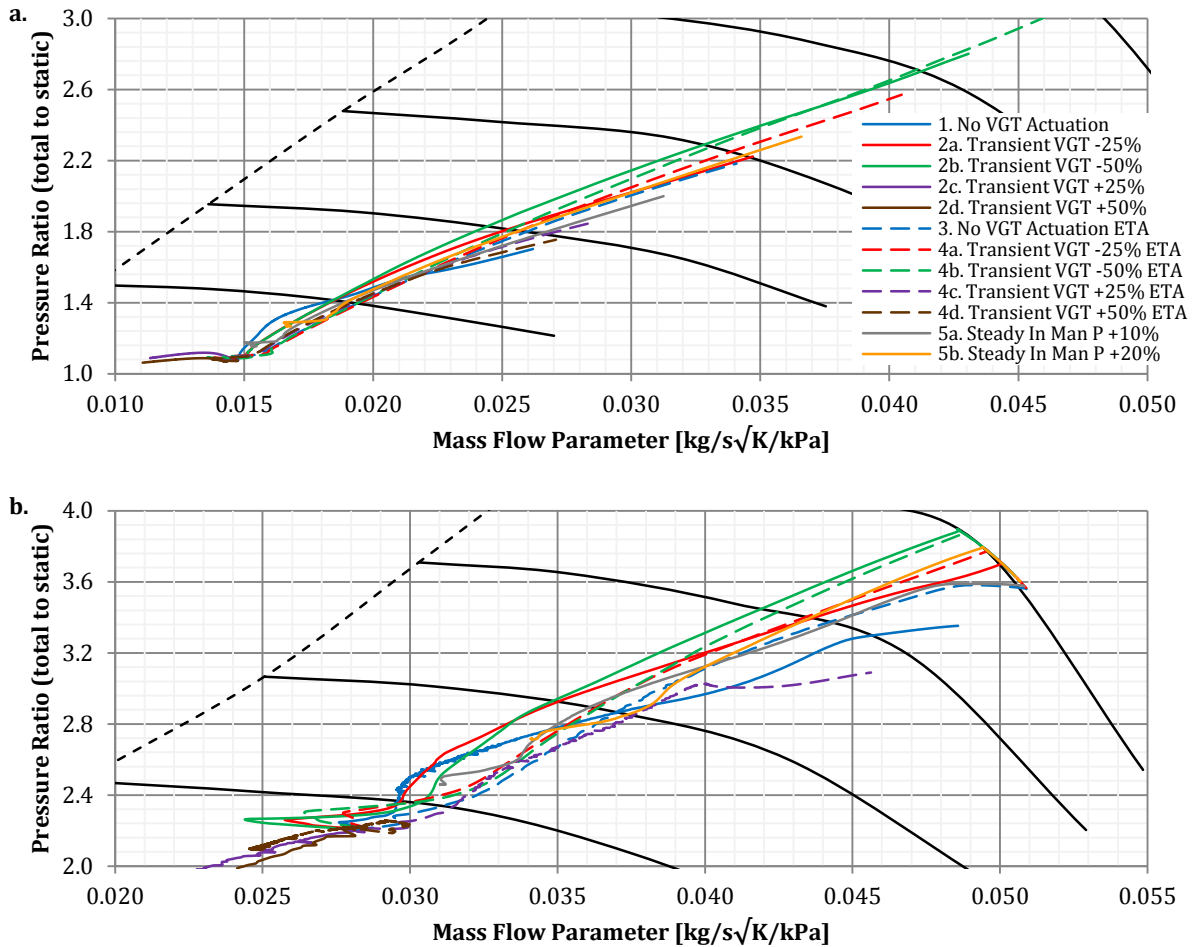


**Figure 6.22 – Compressor operating traces plotted on the device performance map. In part a the work cycle is a step change in load from 100 Nm to 399 Nm (WCA). In part b the work cycle is a step change in load from 534 Nm to 817 Nm (WCB).**

while still having good fuel consumption. Fine tuning is required to achieve the best compromise.

**Figure 6.22** shows the compressor operating traces for both work cycles. The deviations from the baseline trace are smaller than the deviations caused by high power assistance observed in the previous section. Closing the turbine vanes during the transient causes a significant shift towards the surge line in the final part of the simulation. In *WCA* closing the vanes has a similar effect to the ETA, where the trace is shifted away from the surge line due to the filling of the intake manifold. In *WCB* there is a sudden shift of operating conditions towards the surge line when the turbine vanes are closed. This is due to the larger sudden increase of external EGR caused by the non perfect control.

The main outcomes of this study are that the ETA is more effective in improving engine transient response than VGT and that actuating both systems simultaneously is not more effective than actuating only the ETA. For this reason, one may conclude that the VGT system

becomes redundant when the turbocharger is assisted. This is not true, since the vane opening to achieve the most efficient boost changes depending on engine loading conditions. This suggests that a possible strategy to control the two systems would be to utilize the ETA to improve transients while the VGT would be used to improve steady state BSFC. More specifically, the turbocharger speed would be controlled through the motor/generator, while the vanes opening would be actuated to control the turbine power so that it matches the power consumed by the compressor and bearings.

The turbine vanes actuation in this study has not been optimized, and it is likely that VGT actuation could potentially lead to better engine transient response than what has been found here. Nevertheless, due to the large difference in engine transient performance between the VGT and ETA systems, it is improbable that optimization of the VGT control strategy would produce the same level of benefits of the ETA. A detailed optimization of the vanes actuation strategy is required to achieve the full system potential, and this is outside the scope of this project.

## 6.6 CHAPTER SUMMARY

This chapter focused on the impact of electric turbocharger assistance on the dynamics of an off-road heavy-duty diesel engine. A 1D dynamic model of the turbocharged engine has been developed and calibrated/validated against experimental data. This model has been utilized to complete three different studies.

The first study consisted of an optimization of the boost aimed at improving engine efficiency under different engine loading conditions. It has been found that engine boost affects the pumping losses which, in turn, affect the BSFC. An analytical relationship between the intake and exhaust manifold pressures, under constant pressure turbocharging conditions, has been found. This relationship leads to a non-dimensional number,  $\lambda$ , which is a function of turbocharger efficiency, turbine inlet temperature and compressor isentropic outlet temperature. Although this non-dimensional number cannot be utilized to predict pumping losses, it has been found from the simulations results that a strong correlation between the two exists. Boost also influences the combustion process and the indicated engine efficiency is adversely affected by low boost. As a result, the optimum BSFC does not coincide with the minimum pumping losses but occurs at a higher boost.

The second study concerned the turbocharged diesel engine dynamics during two different load step increments. The results show that there are four main sources of transient delay in a turbocharged diesel engine. These delays are:

- *Turbocharger speed delay* – this is the delay caused by the finite amount of time required to accelerate the turbocharger. This is the major source of turbo-lag.
- *Intake manifold filling delay* – this is caused by the finite amount of time required to pressurize the volume between the compressor exit and the engine.
- *Engine mass transfer delay* – The gases are transferred from the intake manifold to the exhaust manifold by the pumping action of the engine. The gases enter the cylinder during the intake stroke, are compressed and combusted, and are expelled during the exhaust stroke. This delay results in a reduction of the power available to accelerate the turbocharger and slows down the engine response.
- *Firing delay* – this delay is not caused by the turbocharger but by the amount of time that passes between the increase in engine load and the next injection event.

The transient behaviour of the standard engine has then been compared to the behaviour of engines equipped with turbocharger electric assistance of different powers. The electric assistance directly reduces the “turbocharger speed delay” by accelerating the turbocharger. Since this delay is an order of magnitude larger than the other delays, the engine speed drop that occurs when the load is applied can be reduced by up to 89%. The best improvements are obtained with a 25 kW motor/generator, but a 5 kW machine can generate improvements of a similar magnitude.

Other than by the packaging and the rotor-dynamics, the motor/generator size is limited by its inertia and the intake manifold filling time. If the electrical machine size is increased so that its inertia becomes dominant over the turbocharger inertia, further increments in size would result in very minor improvements in turbocharger acceleration. If the “turbocharger speed delay” is already significantly shorter than the “intake manifold filling delay”, further increments in assistance power would produce negligible improvements in engine transient response.

In the final study, the effectiveness of electric turbocharger assistance in improving the engine transient response has been compared to that of the variable geometry turbine. It has been found that the best response is obtained by increasing the boost before the transient begins, but it has the drawback of reducing engine steady state efficiency. Nevertheless, electric turbocharger assistance is more effective than actuating the turbine vanes when the load is applied. This is for a number of reasons:

- Electric turbocharger assistance provides more power to accelerate the turbocharger
- The power increase occurs with a negligible time delay, as it does not require the filling of the exhaust manifold



- The extra engine mass flow generated by the electric assistance increases the turbine power
- The turbocharger assistance power does not depend on exhaust flow conditions
- Electric turbocharger assistance does not restrict the exhaust flow

Closing the turbine vanes during the transient when electric assistance is present does not provide benefits in transient response. Nevertheless, the vane opening which generates the optimum boost varies depending on engine loading conditions, making variable geometry necessary to achieve the best fuel consumption. As a result, it has been suggested to control the turbocharger speed during the transient with the motor/generator, and to maintain the speed in steady state by actuating the turbine vanes.

## 6.7 FURTHER WORK

Further work is necessary to demonstrate the electric assistance benefits on a real application. First of all a control system capable to manage the turbocharger assistance during transients needs to be developed, starting from the findings of this study. This would allow the simulation of this system over more realistic engine working cycles, so that the fuel benefits gains demonstrated here can be confirmed.

The work presented in this chapter is based on simulations of an experimentally validated model. To more accurately quantify the engine transient performance and BSFC benefits obtained with electric assistance, parts of this investigation have to be repeated experimentally. This investigation cannot be replicated exactly experimentally as, for example, only one machine size is available and the engine will need a full control system to avoid over-speeds.

This investigation focused on the BSFC reduction by boost optimization. Turbocharger assistance can also improve BSFC through turbocompounding and by allowing more engine down-sizing and down-speeding. According to the literature, these two routes could lead to even higher BSFC improvements than what has been shown here and, as a result, they need to be explored.

## 7. CONCLUSIONS

The work presented is concerned with the impact of electric turbocharger assistance on off-highway diesel engine performance. In this project the electromagnetic and aerodynamic performance of an electrically assisted turbocharger prototype were characterized to investigate the impact of electric assistance on the turbine and compressor flow and to utilize the data collected to study how engine transient performance is affected by the electric turbocharger assistance.

### 7.1 RESEARCH OBJECTIVES

The objectives of this thesis were identified via a survey of the relevant literature and by the sponsoring companies' requirements. The objectives were to:

1. Experimentally characterize the performance of the motor/generator employed to assist the turbocharger, to understand what are the turbocharger losses introduced by electric assistance
2. Study the turbine steady and unsteady aerodynamic performance in regimes with electrical assistance, to understand if the aerodynamic losses are affected by electric assistance
3. Investigate the impact of electric assistance on engine transient response and how it is affected by electrical machine performance
4. Study how the turbocharger assistance system and the turbine variable geometry system can be employed simultaneously to improve engine transient response and pumping losses

### 7.2 RESEARCH ACHIEVEMENTS

The first objective was met in the study presented in **Chapter 3**, where different electrical machine performance maps were generated and the losses occurring within the bearing housing and motor/generator were quantified. The machine was characterized via a novel test-rig which allows the measurement of the electrical machine torque up to the maximum rotational speed. The electrical machine was characterized twice. In the first characterization it was possible to characterize the motor/generator efficiency up to the maximum rotational speed. When the bearing losses were not included, the peak efficiency of the motor/generator was found to be 92% and to occur at a rotational speed of 120,000 rev/min. The peak power was found to be 3.5 kW in motoring mode and 5.4 kW in generating mode. This first iteration revealed that the electrical machine control system was not fully optimized, so better torque and efficiency could be obtained. In the second testing iteration, the accuracy of the torque

measurement system was improved and the electrical machine control parameters were optimized by the controller designer, based on the data from the first testing iteration. However, in this second testing iteration it was possible to characterize the motor/generator up to only 80,000 rev/min due to vibration issues. The efficiency and power output in motoring mode at 80,000 rev/min were significantly improved after the optimization of the control system. The peak efficiency was 92% and the peak power was 4.3 kW in motoring mode and 4.5 kW in generating mode. The test-rig was capable of separating the frictional losses (i.e. bearing plus rotor drag losses) from the electromagnetic losses occurring in the electrical machine. However, it was not possible to separate the bearing frictional losses from the rotor aerodynamic drag loss. This second loss was estimated via computational fluid dynamics techniques and at 140,000 rev/min (maximum device rotational speed) it was found to be only 63 W. This means that, because the motor/generator rotor drag losses are small and because the electromagnetic losses are negligible when the electrical machine is off, the electric assistance has a negligible impact on the turbocharger steady state operation when the motor/generator is not in use.

The second objective, which concerns the impact of electrical assistance on the turbine performance, is covered in **Chapter 4**, for the steady state effects, and in **Chapter 5**, for the unsteady effects. In **Chapter 4** the turbocharger turbine was characterized in steady state at low pressure ratio. These low pressure ratio conditions occur when the turbine is motored by the electric assistance system. The turbine efficiency and mass flow rate characteristics were mapped utilizing the test-rig developed for the electrical machine characterization. Thanks to the motoring capabilities of the electrical machine, it was possible to overcome the frictional losses occurring in the turbocharger and the windage losses occurring in the turbine, so that the turbine was tested down to a pressure ratio of 1.00. It was found that the mass flow rate does not drop to zero at a pressure ratio of one, but at a higher pressure ratio. Below this critical zero-mass-flow pressure ratio, the flow in the turbine was reversed and the turbine operated as a low efficiency compressor. The cause of these effects is the centrifugal head generated by the rotation of the gases in the turbine. The turbine isentropic efficiency has a peak at a velocity ratio of 0.7 and drops to negative values (i.e. turbine does work on the fluid) as the pressure ratio is decreased. The efficiency at the zero-mass-flow pressure ratio is negative infinity because the isentropic work is zero (zero mass flow), while work is done on the fluid by the turbine. This zero-mass-flow pressure ratio and the magnitude of the reverse mass flow were found to vary with turbine rotational speed and nozzles settings.

In **Chapter 5** it was shown that the speed transients generated by the electrical machine have a small impact on the turbine operation and that the electrical machine torque oscillations have a negligible impact on the turbine flow. The first part of **Chapter 5** focused on the unsteady

effects driven by the turbine speed changes. These unsteady effects are caused by the change of turbine swallowing capacity with rotational speed and are generated by the filling and emptying of the exhaust manifold, represented by the test-rig pipe-work, and turbine volute. These unsteady effects are small, but they can negatively impact the capabilities of the electric assistance in improving engine transient response. This is due to a reduction of turbine swallowing capacity and efficiency during turbocharger accelerations. The second part of **Chapter 5** reported on the unsteady effects generated by the motor/generator torque oscillations. A *Fast Fourier Transform* analysis was carried out on the turbine inlet and outlet pressure signals to see if the torque oscillations caused pressure waves. No pressure oscillations were observed at the frequency of the torque fluctuations when the machine operated in generating mode and only minor oscillations were observed when the machine operated in motoring mode. It was argued that these oscillations cannot significantly affect turbine performance as their magnitude is small and they have a similar frequency to the much stronger pressure oscillations caused by the turbine rotor-stator interaction.

The third and fourth objectives of this research were met in **Chapter 6**, where an experimentally validated, dynamic, one-dimensional engine model was used to show that:

- Electric assistance significantly improves the engine transient response.
- For this particular application most of the transient response improvement can be achieved with an assistance power in the 5 to 10 kW range.
- VGT could be actuated to improve fuel consumption, but cannot significantly improve the engine transient response when electric assistance is present.

This chapter was divided in three different studies. The first study described in the chapter consisted of an optimization of boost pressure for engine efficiency. The boost was varied by changing the VGT settings and it was found that it affects the engine efficiency by altering the pumping losses and the combustion process. It was demonstrated that the optimum boost depends on the turbocharger efficiency, the exhaust gases temperature and the pressure ratio across the compressor. The second study concerned the impact of electric assistance on engine transient response and the sizing of the motor/generator. The main reason for improved transient response of the engine was the faster turbocharger acceleration. However, as the motor/generator power was increased the engine transient response improvements become proportionally less significant. This was because with powerful electrical machines, a large fraction of the assistance power was utilized to compress the intake air rather than accelerating the turbocharger. The optimal assistance power required to reduce the turbo-lag for this engine was found to be in the 5 to 10 kW range, and more powerful machines did not reduce the turbo-

lag significantly more. This showed that the motor/generator implemented in the assisted turbocharger prototype developed by the project partners is well matched for this application. In the last part of the chapter, the electric assistance and VGT systems were compared to understand if there are benefits in having both systems on the same turbocharger. Electric assistance was more effective in improving engine transient response than VGT and no transient response benefits were found by having both systems on the same device. However, VGT was not found to be redundant, as it could be utilized to optimize the steady state boost over different engine loading conditions or, if the electric assistance has a dedicated battery, to increase the turbine power output when the electrical machine is recharging this battery.

### 7.3 RECOMMENDATIONS FOR ASSISTED TURBOCHARGER PROTOTYPE IMPROVEMENTS

The electrically assisted turbocharger prototype developed by the project partners is well matched to the engine and the electrical machine power output is within the optimal range (5 to 10 kW) to improve engine transient performance. As a result, only minor fuel consumption benefits are expected to occur by further optimizing the matching and no significant improvements in engine transient response are expected to occur with a more powerful motor/generator. To further optimize the turbocharger match for fuel consumption, the boost could be optimized computationally by assuming a constant efficiency turbocharger, and the real turbocharger could be selected so that the maximum turbocharger efficiency coincides with the optimal boost.

As demonstrated in **Chapter 6**, the VGT system is not redundant, as it could be utilized to optimize the boost over different engine loading conditions. However, the engine efficiency vs. boost curve does not have a sharp peak, and therefore it could be possible to remove the VGT system and still obtain good fuel consumption over a wide range of engine loading conditions. However, VGT might still be required for turbocompounding and further investigation on this topic is required.

This electrical machine is not suitable for turbocompounding due to the low power absorption capacity and due to the fact that it cannot run in a continuous manner. However, there is evidence in the literature that even with a low power motor/generator, but capable of running in continuous mode, mild turbocompounding could be implemented to reduce the engine alternator load. This solution would provide fuel consumption benefits without the need of a fully hybridizing the engine.

An enhancement to the turbocharger would be the implementation of *Active Control Turbocharging* (ACT) to improve the turbine efficiency in unsteady flow. The turbocharger turbine is designed to operate in steady flow, but the exhaust flow strongly pulsates due to the

opening and closing of the engine valves. ACT is a system which changes the nozzles angle during the flow pulsations to maintain a good rotor inlet incidence angle throughout the flow changes. The main concern on the implementation of ACT on an electrically assisted turbocharger was that the two systems can interfere with each other. The results of **Chapter 5** show that the motor/generator would not generate significant unsteady flow effects in the turbine. Some unsteady effects have been observed during turbine speed transients, but the deviations in turbine performance are mainly caused by the filling and emptying of the exhaust manifold and the flow in the nozzles and rotor behaves in a quasi-steady manner. Therefore, the ACT benefits demonstrated by Pesiridis (2007) will not be significantly affected by the electric assistance and the two systems can be implemented on the same device. Packaging is not expected to be an issue as ACT requires the same amount of space of the VGT system already installed on the assisted turbocharger prototype tested in this PhD project.

Variable geometry compressors have the capacity of shifting the surge line so that the compressor operating range is extended (Herbst et al., 2011). This system could be easily implemented on an electrically assisted turbocharger. However, the results of **Chapter 6** show that this system is not needed for this particular application, as the compressor always operate efficiently and surge is not an issue. In addition, it has been shown that electric assistance shifts the compressor operating point away from the surge line when it accelerates the turbocharger, and therefore surge is unlikely to be an issue also in other applications.

#### 7.4 SUGGESTIONS FOR FURTHER WORK

This thesis has mainly focused on the impact of electric assistance on the turbocharger turbine, and the impact on the compressor has only been studied computationally as part of the engine transient performance investigation. This computational study covered the effects of speed transients, but the effects of the motor/generator torque fluctuations on compressor performance have not been considered. The rotor oscillations caused by the torque fluctuations could have a larger impact on the compressor than on a turbine, as the compressor flow has an adverse pressure gradient. The oscillations could promote boundary layer separation, causing stall and surge. It is therefore important to understand if these torque fluctuations can shift the surge line, as this would reduce the compressor operating range.

The fuel consumption benefits have to be demonstrated on real world work cycles. It has not been possible to do this as part of this PhD project as an electric assistance control system was not available at the time of writing this thesis. Simulating the engine performance on a real world work cycle would improve the accuracy of the fuel consumption reduction figures published in this thesis. In addition, such a simulation would provide data on the electric

assistance duty cycle. If an accurate thermal model of the motor/generator and turbocharger is also developed, this simulation would provide useful data for the design of the cooling circuit.

An important area which needs to be investigated further is the energy storage arrangement and managing system. Several options are available to configure this system. For example, the turbocharger motor/generator could have a dedicated battery which is not connected to any other component. Another option is to have a single battery which is shared by all the machine electrical systems. In this latter case, mild turbocompounding could be implemented, as recommended in the previous section. It is necessary to quantify the fuel consumption benefits and costs of the different energy storage systems to maximise the potential of electric assistance.

The testing facility utilized to characterise the turbine could be further developed to allow the testing of different turbines. The motor/generator could be replaced with a more powerful machine so that the turbines can be characterized up to choking conditions. This would allow to test turbines over the full operating range, so that extrapolation would no longer be necessary. In addition, this test-rig could also be utilized to characterize compressors. The test facility could also be redesigned to allow the characterization of turbines in hot conditions. This would allow to study the impact of thermal losses on the turbine or, if the turbine is well insulated, to obtain the aerodynamic performance with a more representative fluid temperature.

There is room for further work to be done on the turbocharger bearing losses characterization. A dedicated test-rig could be built to characterize the bearing load over several rotational speed, load and temperature conditions. The turbocharger rotor mass properties should be maintained identical to the actual turbocharger to replicate the rotor-dynamics effects occurring when the turbocharger is mounted on an engine. In addition, this test-rig should be able to set the axial load on the shaft and provide power to the rotor without impacting the rotor-dynamics.

## REFERENCES

- Abernethy, R.B., Benedict, R.P. and Dowdell, R.B. (1985) 'ASME Measurement Uncertainty', *Journal of Fluids Engineering*, vol. 107, no. 2, pp. 161-164.
- Ahn, J.W. (2011) 'Switched Reluctance Motor', in Lamchich, M.T. (ed.) *Torque Control*, Vienna: InTech.
- Algrain, M.C. (2005) 'Controlling an Electric Turbo Compound System for Exhaust Gas Energy Recovery in a Diesel Engine', IEEE Electro Information Technology, Lincoln (NE). Available: DOI:10.1109/EIT.2005.1627004.
- Amar, M. and Kaczmarek, R. (1995) 'A General Formula for Prediction of Iron Losses Under Nonsinusoidal Voltage Waveform', *IEEE Transactions on Magnetics*, vol. 31, no. 5, pp. 2504-2509.
- Ansys Inc. (2012) *Ansys CFX Help System*, Canonsburg (PA): Ansys Inc.
- Arnold, S., Balis, C., Barthelet, P., Poix, E., Samad, T., Hampson, G. and Shahed, S.M. (2005) *Garrett Electric Boosting Systems (EBS) Program*, Internal Report, Morris Township (NJ): Honeywell Inc.
- Arnold, S., Balis, C., Jeckel, D., Larcher, S., Uhl, P. and Shahed, S.G. (2005) 'Advances in Turbocharging Technology and its Impact on Meeting Proposed California GHG Emission Regulations', SAE World Congress, Detroit (MI). Available: DOI:10.4271/2005-01-1852
- Balis, C., Middlemass, C. and Shahed, S.M. (2003) 'Design & Development of e-Turbo for SUV and Light Truck Applications', OSTI Diesel Engine Emissions Reduction Workshop, Newport (RI). Available: <http://www.osti.gov/scitech/servlets/purl/828952>
- Benajes, J., Luján, J., Bermúdez, V. and Serrano, J.R. (2002) 'Modelling of Turbocharged Diesel Engines in Transient Operation. Part 1: Insight into the Relevant Physical Phenomena', *Proceedings of the Institution of Mechanical Engineers, Part D: Journal of Automobile Engineering*, vol. 216, no. 5, pp. 431-441.
- Bumby, J.R., Crossland, S. and Carter, J. (2006) 'Electrically Assisted Turbochargers: Their Potential for Energy Recovery', IET Hybrid Vehicle Conference, Coventry, 43-52. Available: <http://ieeexplore.ieee.org/>
- Bumby, J.R., Spooner, E.S., Carter, J., Tennant, H., Mego, G.G., Dellora, G., Gstrein, W., Sutter, H. and Wagner, J. (2004) 'Electrical Machines for Use in Electrically Assisted Turbochargers', IET Power Electronics, Machines and Drives, Edinburgh, 344-349. Available: DOI:10.1049/cp:20040310
- Bumby, J.R., Spooner, E. and Jagiela, M. (2006) 'Equivalent Circuit Analysis of Solid-Rotor Induction Machines with Reference to Turbocharger Accelerator Applications', *IET Electric Power Applications*, vol. 153, no. 1, pp. 31-39.
- Bumby, J.R., Spooner, E. and Jagiela, M. (2006) 'Solid Rotor Induction Machines for Use in Electrically-Assisted Turbochargers', IET Power Electronics, Machines and Drives, Dublin, 341-345. Available: <http://ieeexplore.ieee.org/>



- Calverley, S.D. (2001) *Design of a High Speed Switched Reluctance Machine for Automotive Turbo-Generator Applications*, PhD Thesis, Sheffield: University of Sheffield.
- Calverley, S.D., Jewell, G.W. and Saunders, R.J. (2005) 'Prediction and Measurement of Core Losses in a High-Speed Switched-Reluctance Machine', *IEEE Transactions on Magnetics*, vol. 41, no. 11, pp. 4288-4298.
- Caterpillar Inc. (2013) *Dynasty Help System*, Peoria (IL): Caterpillar Inc.
- Cellier, F.E. and Kofman, E. (2006) *Continuous System Simulation*, New York (NY): Springer.
- Copeland, C.D., Newton, P., Martinez-Botas, R.F. and Seiler, M. (2012) 'A Comparison of Timescales Within a Pulsed Flow Turbocharger Turbine', *IMEchE Turbochargers and Turbocharging*, London. Available: DOI:10.1533/9780857096135.8.389
- Dantec Dynamics A/S (2013) *Dantec Dynamics Website*, [Online], Available: <http://www.dantecdynamics.com/> [19 Dec 2013].
- European Committee for Standardization (2004) *EN590:2004. Automotive Fuels - Diesel - Requirements and Test Methods*, Brussels: European Committee for Standardization.
- Ferguson, C.R. and Kirkpatrick, A.T. (2001) *Internal Combustion Engines*, 2<sup>nd</sup> edition, New York (NY): John Wiley & Sons.
- Filipi, Z.S., Wang, Y. and Assanis, D. (2001) 'Effect of Variable Geometry Turbine (VGT) on Diesel Engine and Vehicle System Transient Response', *SAE World Congress*, Detroit (MI). Available: DOI:10.4271/2001-01-1247
- Fox, R.W., McDonald, A.T. and Pritchard, P.J. (2004) *Introduction to Fluid Mechanics*, 6<sup>th</sup> edition, Hoboken (NJ): John Wiley & Sons.
- Fraser, A. (2011) 'How Low Can We Go? Challenges and Opportunities of Engine Downsizing to Reduce CO<sub>2</sub> Emissions', *IMEchE Engine Downsizing Seminar*, London.
- Futral, S.M. and Wasserbauer, C.A. (1965) 'Off Design Performance Prediction with Experimental Verification for a Radial Inflow Turbine', *NASA Technical Papers*, no. TN-D-2621.
- Gerke, F.G. (2001) 'Diesel Engine Waste Heat Recovery Utilizing Electric Turbocompound Technology', *OSTI Diesel Engine Emissions Reduction Workshop*, Portsmouth (VA). Available: <http://www.osti.gov/scitech/servlets/purl/827993>
- Gosling, G.R. (2007) *Second Year Mechanical Engineering Design Notes*, London: Imperial College London.
- Hakeem, I. and Khezzar, L. (1994) *The Turbocharger Aerodynamic Test Facility: Description and Operation*, Internal Report, London: Imperial College London.
- Herbst, F., Stöber-Schmidt, C., Eilts, P., Sextro, T., Kammeyer, J., Natkaniec, C., Seume, J., Porzig, D. and Schwarze, H. (2011) 'The Potential of Variable Compressor Geometry for Highly Boosted Gasoline Engines', *SAE World Congress*, Detroit (MI). Available: DOI: 10.4271/2011-01-0376
- Heywood, J.B. (1988) *Internal Combustion Engine Fundamentals*, New York (NY): McGraw-Hill.

- Hopmann, U. and Algrain, M.C. (2003) 'Diesel Engine Electric Turbo Compound Technology', SAE Future Transportation Technology Conference, Costa Mesa (CA). Available: DOI:10.4271/2003-01-2294
- Howe, M.S. (1984) 'On the Absorption of Sound by Turbulence and Other Hydrodynamic Flows', *IMA Journal of Applied Mathematic*, vol. 32, pp. 187-209.
- Hughes, A. (2006) *Electric Motors and Drives Fundamentals, Types and Applications*, 3<sup>rd</sup> edition, Oxford: Elsevier.
- Ibaraki, S., Yamashita, Y., Sumida, K., Ogita, H. and Jinnai, Y. (2006) 'Development of the 'Hybrid Turbo' an Electrically Assisted Turbocharger', *Mitsubishi Heavy Industries Technical Review*, vol. 43, no. 3.
- International Rectifier Inc. (2010) *IRG7PH35UD Data Sheet*, El Segundo (CA): International Rectifier Inc.
- Japikse, D. and Baines, N. (1994) *Introduction to Turbomachinery*, Oxford: Oxford University Press.
- Katrašnik, T., Medica, V. and Trenc, F. (2005) 'Analysis of the Dynamic Response Improvement of a Turbocharged Diesel Engine Driven Alternating Current Generating Set', *Energy Conversion and Management*, vol. 46, no. 18-19, pp. 2838-2855.
- Katrašnik, T., Rodman, S., Trenc, F., Hribernik, A. and Medica, V. (2003) 'Improvement of the Dynamic Characteristic of an Automotive Engine by a Turbocharger Assisted by an Electric Motor', *Journal of Engineering for Gas Turbines and Power*, vol. 125, no. 2, pp. 590-595.
- Kirkup, L. (1994) *Experimental Methods*, Milton: John Wiley & Sons.
- Kolmanovsky, I., Stefanopoulous, A.G. and Powell, B.K. (1999) 'Improving Turbocharged Diesel Engine Operation With Turbo Power Assist System', *IEEE Control Applications*, Kohala Coast (HI), 454-459. Available: DOI:10.1109/CCA.1999.806678
- Kovach, J.T., Tsakiris, E.A. and Wong, L.T. (1982) 'Engine Friction Reduction for Improved Fuel Economy', *SAE Technical Papers*, no. 820085. Available: DOI:10.4271/820085
- Lee, B., Filipi, Z. and Assanis, D. (2009) 'Simulation-based Assessment of Various Dual-Stage Boosting Systems in Terms of Performance and Fuel Economy Improvements', *SAE International Journal on Engines*, vol. 2, no. 1, pp. 1335-1346.
- Lumley, J.L. (1999) *Engines: an Introduction*, New York (NY): Cambridge University Press.
- Mamat, A.M.I., Padzillah, M.H., Romagnoli, A. and Martinez-botas, R.F. (2011) 'A High Performance Low Pressure Ratio Turbine for Engine Electric Turbocompounding', ASME Turbo Expo, Vancouver. Available: DOI:10.1115/GT2011-45541
- Martinez-Botas, R.F. (1993) *Annular Cascade Aerodynamics and Heat Transfer*, PhD Thesis, Oxford: University of Oxford.
- Materu, P.N. and Krishnan, R. (1992) 'Estimation of Switched Reluctance Motor Losses', *IEEE Transactions on Industry Applications*, vol. 28, no. 3, pp. 668-679.

- McCrometer Inc. (2011) *V-Cone Technical Brief*, Hemet (CA): McCrometer Inc.
- Meitner, P.L. and Glassman, A.J. (1983) 'Computer Code for Off Design Performance Analysis of Radial Inflow Turbines With Rotor Blade Sweep', *NASA Technical Papers*, no. TP-2199.
- Michon, M., Calverley, S.D., Clark, R.E., Howe, D., Chambers, J.D.A., Sykes, P.A., Dickinson, P.G., McClelland, M., Johnstone, G., Quinn, R. and Morris, G. (2007) 'Modelling and Testing of a Turbo-generator System for Exhaust Gas Energy Recovery', *IEEE Vehicle Power and Propulsion*, Arlington (TX), 544–550. Available: DOI:10.1109/VPPC.2007.4544184
- Millo, F., Mallamo, F., Pautasso, E. and Mego, G.G. (2006) 'The Potential of Electric Exhaust Gas Turbocharging for HD Diesel Engines', *SAE World Congress*, Detroit (MI). Available: DOI:10.4271/2006-01-0437
- Mizumachi, N., Yoshiki, D. and Endoh, T.A. (1979) 'A Study on Performance of Radial Turbine Under Unsteady Flow Conditions', *Report of the Institute of Industrial Science*, vol. 28, pp. 122-130.
- Münz, S., Schier, M., Schmalzl, H. and Bertolini, T. (2001) *eBooster Design and Performance of a Innovative Electrically Driven Charging System*, Internal Report, Auburn Hills (MI): BorgWarner Inc.
- Newton, P.J. (2014) *An Experimental and Computational Study of Pulsating Flow within a Double Entry Turbine with Different Nozzle Settings*, PhD Thesis, London: Imperial College London.
- Noguchi, T., Takata, Y., Yamashita, Y. and Ibaraki, S. (2005) '160,000-r/min, 2.7-kW Electric Drive of Supercharger for Automobiles', *IEEE Power Electronics and Drives Systems*, Kuala Lumpur, 1380–1385. Available: DOI:10.1109/PEDS.2005.1619904
- Noguchi, T., Takata, Y., Yamashita, Y., Komatsu, Y. and Ibaraki, S. (2007) '220,000-r/min, 2-kW PM Motor Drive for Turbocharger', *Electrical Engineering in Japan*, vol. 161, no. 3, pp. 31-40.
- Oppenheim, A.V. and Schaffer, R.W. (1989) *Discrete-Time Signal Processing*, Upper Saddle River (NJ): Prentice-Hall.
- Panting, J., Pullen, K.R. and Martinez-Botas, R.F. (2001) 'Turbocharger Motor-Generator for Improvement of Transient Performance in an Internal Combustion Engine', *Proceedings of the Institution of Mechanical Engineers, Part D: Journal of Automobile Engineering*, vol. 215, no. 3, pp. 369-383.
- Pesiridis, A. (2007) *Turbocharger Turbine Unsteady Aerodynamics with Active Control*, PhD Thesis, London: Imperial College London.
- Pesiridis, A., Salim, W.S.I.W. and Martinez-Botas, R.F. (2012) 'Turbocharger Matching Methodology for Improved Exhaust Energy Recovery', *IMEchE Turbochargers and Turbocharging*, London, 203-218. Available: DOI:10.1533/9780857096135.4a.203
- Rakopoulos, C.D. and Giakoumis, E.G. (2009) *Diesel Engine Transient Operation*, London: Springer.

- Rodgers, C. (1978) 'A Diffusion Factor Correlation for Centrifugal Impeller Stalling', *Journal of Engineering for Gas Turbines and Power*, vol. 100, no. 4, pp. 592-601.
- Romagnoli, A. (2010) *Aerodynamic and Thermal Characterization of Turbocharger Turbines: Experimental and Computational Evaluation*, PhD Thesis, London: Imperial College London.
- Ryder, O., Sutter, H. and Jaeger, L. (2006) 'The Design and Testing of an Electrically Assisted Turbocharger for Heavy Duty Diesel Engines', *IMEchE Turbochargers and Turbocharging*, London, 157-166. Available: DOI:10.1016/B978-1-84569-174-5.50015-4
- Soares, F. and Costa Branco, P.J. (2001) 'Simulation of a 6/4 Switched Reluctance Motor Based on Matlab/Simulink Environment', *IEEE Transactions on Aerospace and Electronic Systems*, vol. 37, no. 3, pp. 989-1009.
- Stanitz, D.J. (1952) 'Some Theoretical Aerodynamic Investigations of Impellers in Radial and Mixed Flow Centrifugal Compressors', *Journal of Turbomachinery*, vol. 74, no. 4, pp. 473-497.
- Szymko, S. (2006) *The Development of an Eddy Current Dynamometer for Evaluation of Steady and Pulsating Turbocharger Turbine Performance*, PhD Thesis, London: Imperial College London.
- Tanin, K, Wickman, D., Montgomery, D., Das, S. and Reitz, R.D. (1999) 'The Influence of Boost Pressure on Emissions and Fuel Consumption of a Heavy-Duty Single-Cylinder D.I. Diesel Engine', *SAE International Congress and Exposition, Detroit (MI)*. Available: DOI:10.4271/1999-01-0840
- The MathWorks Inc. (2013) *MATLAB Help System*, Natick (MA): The MathWorks Inc.
- Thompson, I., Spence, S., McCartan, C., Thornhill, D. and Talbot-Weiss, J. (2011) 'Investigations into the Performance of a Turbogenerated Biogas Engine During Speed Transients', *ASME Turbo Expo, Vancouver*. Available: DOI:10.1115/GT2011-45317
- Tiikoja, H., Rämmal, H., Abom, M. and Boden, H. (2011) 'Investigations of Automotive Turbocharger Acoustics', *SAE Engines & Vehicles, Capri*. Available: DOI:10.4271/2011-24-0221
- Ugural, A.C. (2003) *Mechanical Design: An Integrated Approach*, New York (NY): McGraw-Hill.
- Wasserbauer, C.A. and Glassman, A.J. (1975) 'Fortran Program for Predicting Off Design Performance of Radial Inflow Turbines', *NASA Technical Papers*, no. TN-D-8063.
- Watson, N. and Janota, M.S. (1982) *Turbocharging the Internal Combustion Engine*, London: The Macmillan Press.
- Wei, W., Zhuge, W., Zhang, Y. and He, Y. (2010) 'Comparative Study on Electric Turbo-Compounding Systems for Gasoline Engine Exhaust Energy Recovery', *ASME Turbo Expo, Glasgow*, 531-539. Available: DOI:10.1115/GT2010-23204
- Woschni, G. (1967) 'A Universally Applicable Equation for the Instantaneous Heat Transfer Coefficient in the Internal Combustion Engine', *SAE Technical Papers*, no. 670931. Available: DOI:10.4271/670931

# APPENDIX A – TURBINE PERFORMANCE DATA IN REVERSE FLOW CONDITIONS

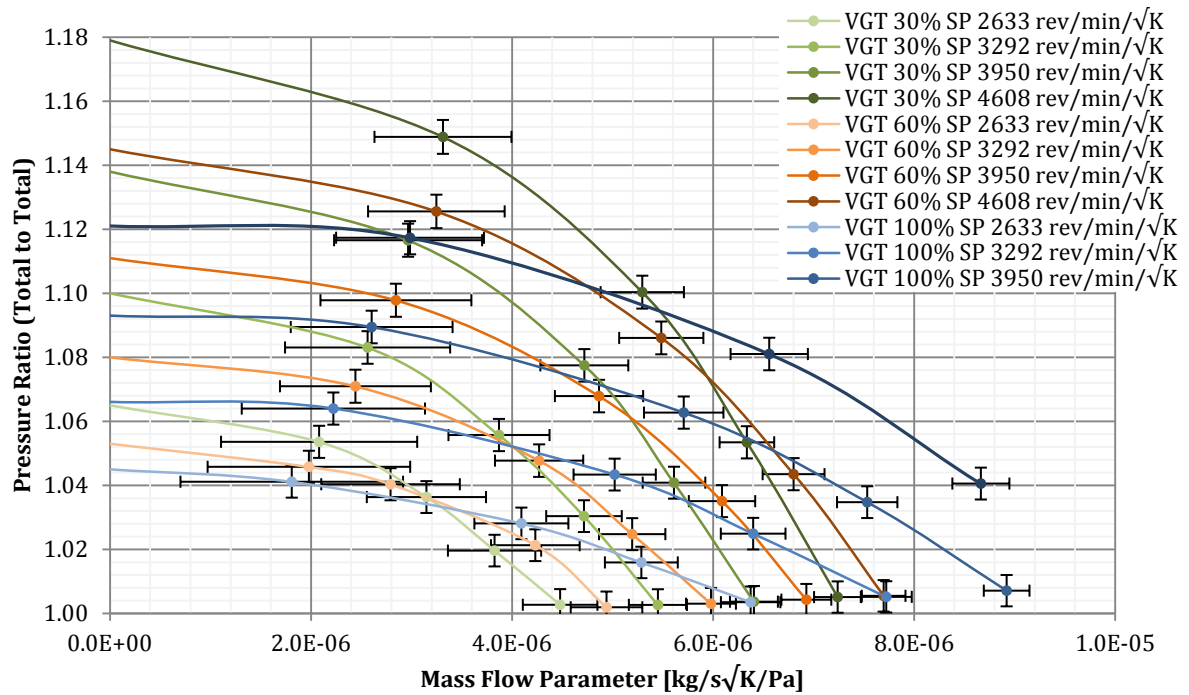


Figure A.1 – Collected turbine mass flow data in reverse flow conditions. Showing the full data set. The total to total pressure ratio definition is given by Equation 4.19, the mass flow parameter definition is given by Equation 4.20 and the speed parameter definition is given by Equation 4.18

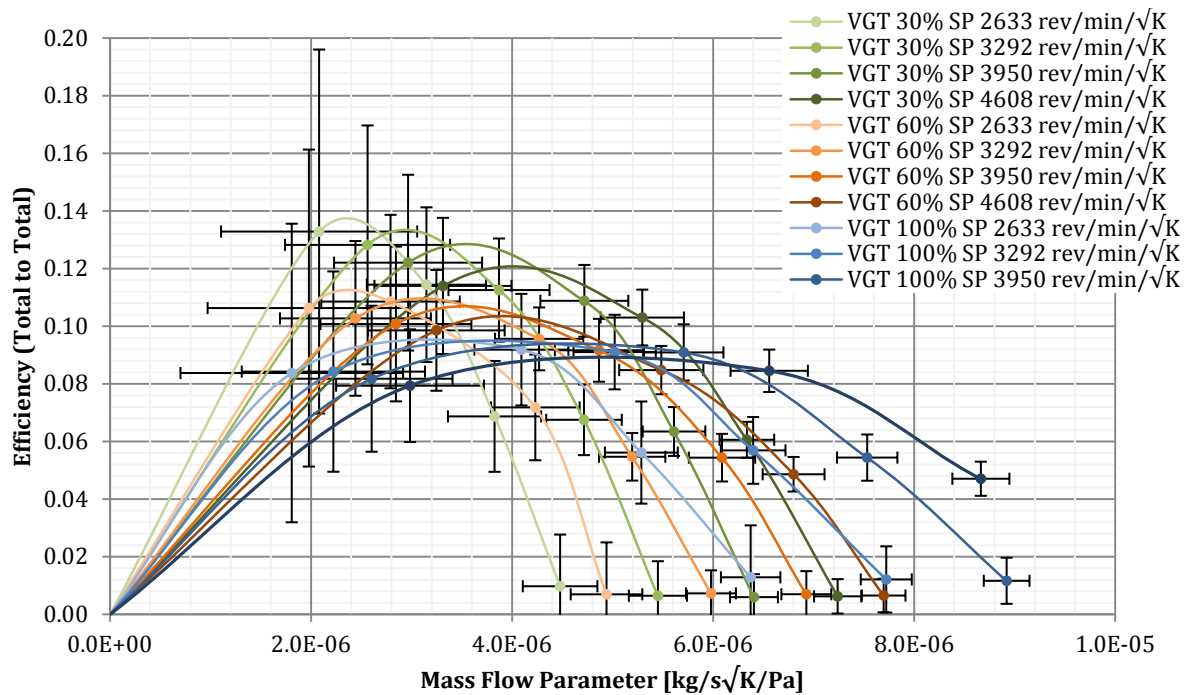


Figure A.2 – Collected total to total efficiency data in reverse flow conditions. Showing the full data set. The total to total efficiency definition is given by Equation 4.21, the mass flow parameter definition is given by Equation 4.20 and the speed parameter definition is given by Equation 4.18

# APPENDIX B – COMPLETE RESULTS SET OF THE STUDY ON THE MOTOR/GENERATOR OSCILLATING TORQUE IMPACT ON TURBINE

SPEED PARAMETER 2633 REV/MIN/ $\sqrt{K}$

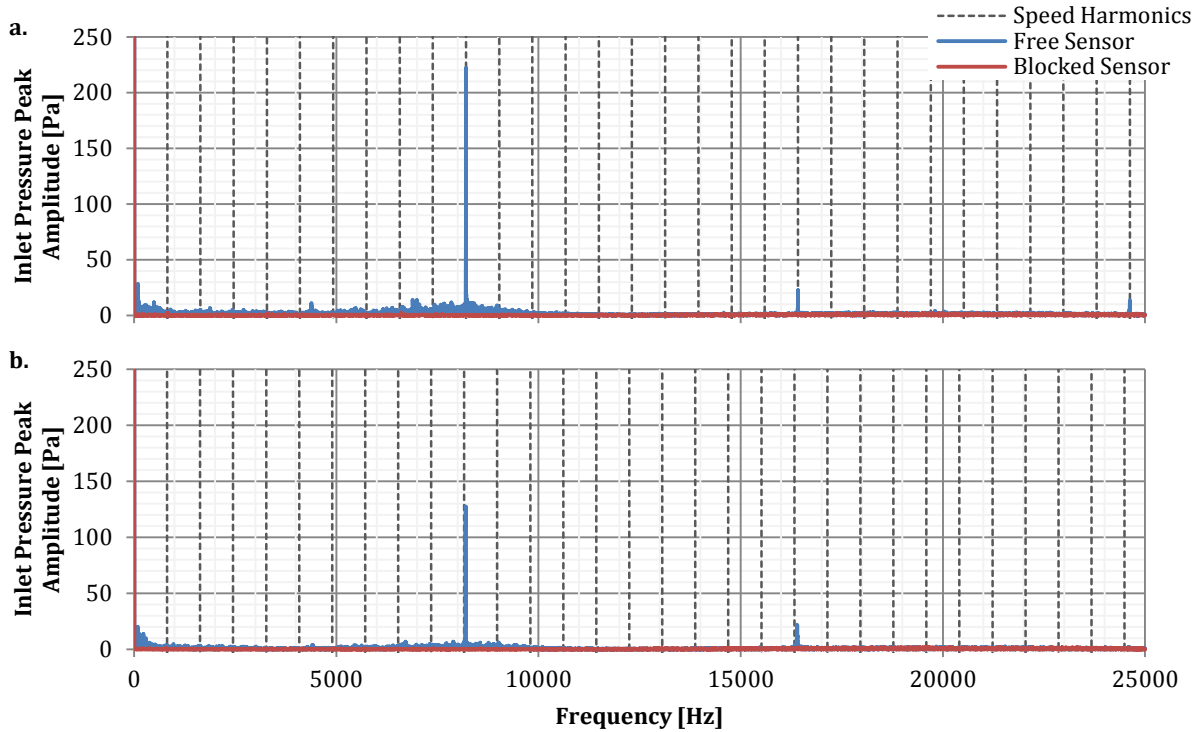


Figure B.1 – Frequency spectrum of the inlet pressure signal. In part a. the electrical machine is operating in generating mode with a 100% torque demand and in part c. the electrical machine is off

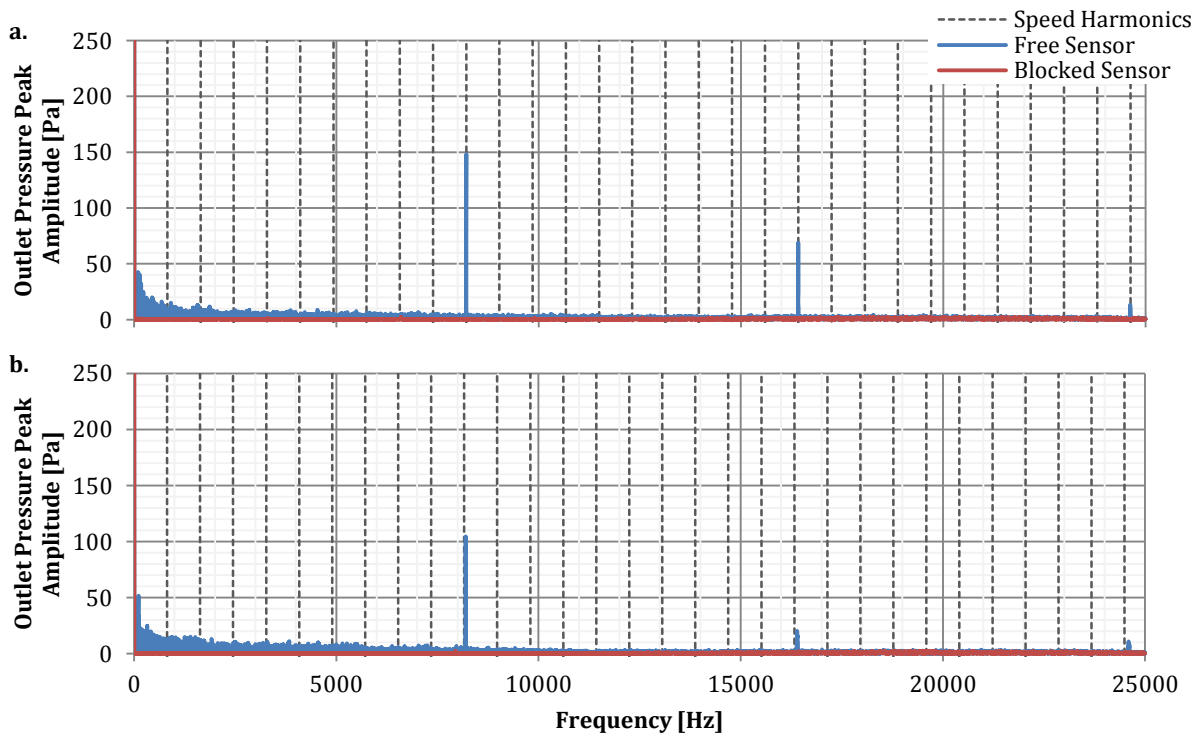


Figure B.2 – Frequency spectrum of the outlet pressure signal. In part a. the electrical machine is operating in generating mode with a 100% torque demand and in part c. the electrical machine is off

SPEED PARAMETER 3292 REV/MIN/ $\sqrt{K}$

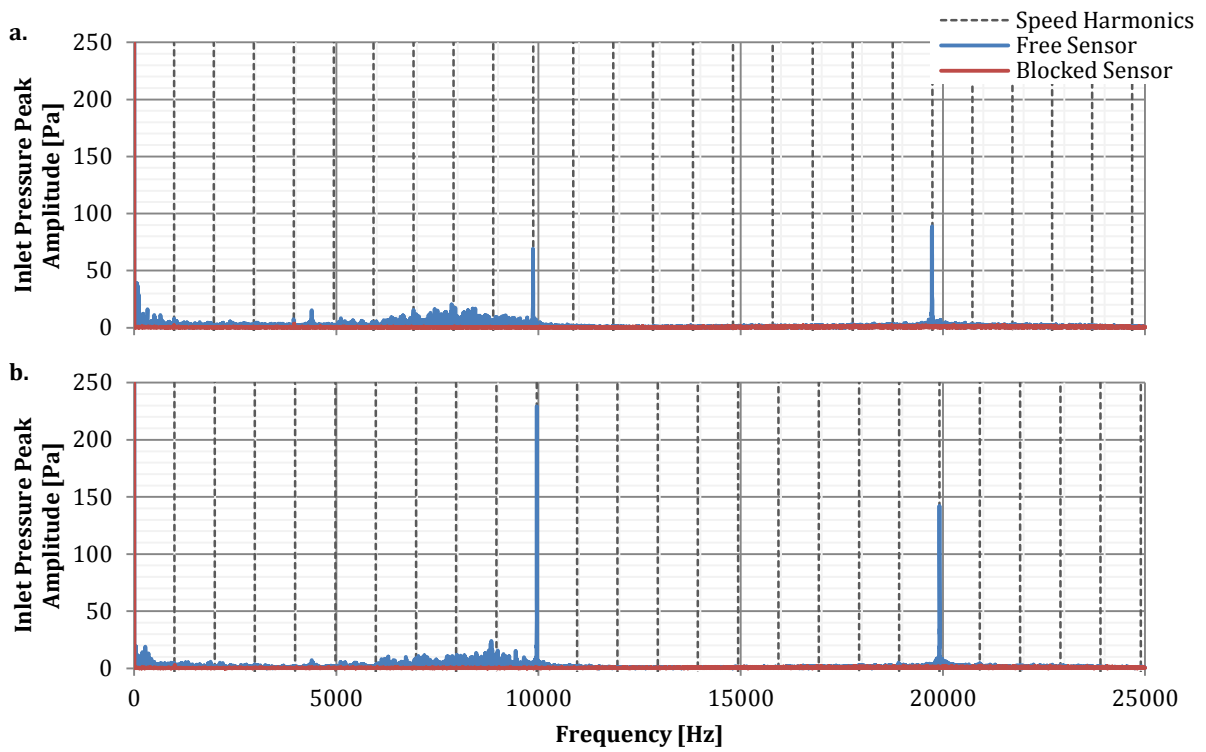


Figure B.3 – Frequency spectrum of the inlet pressure signal. In part a. the electrical machine is operating in generating mode with a 100% torque demand and in part c. the electrical machine is off

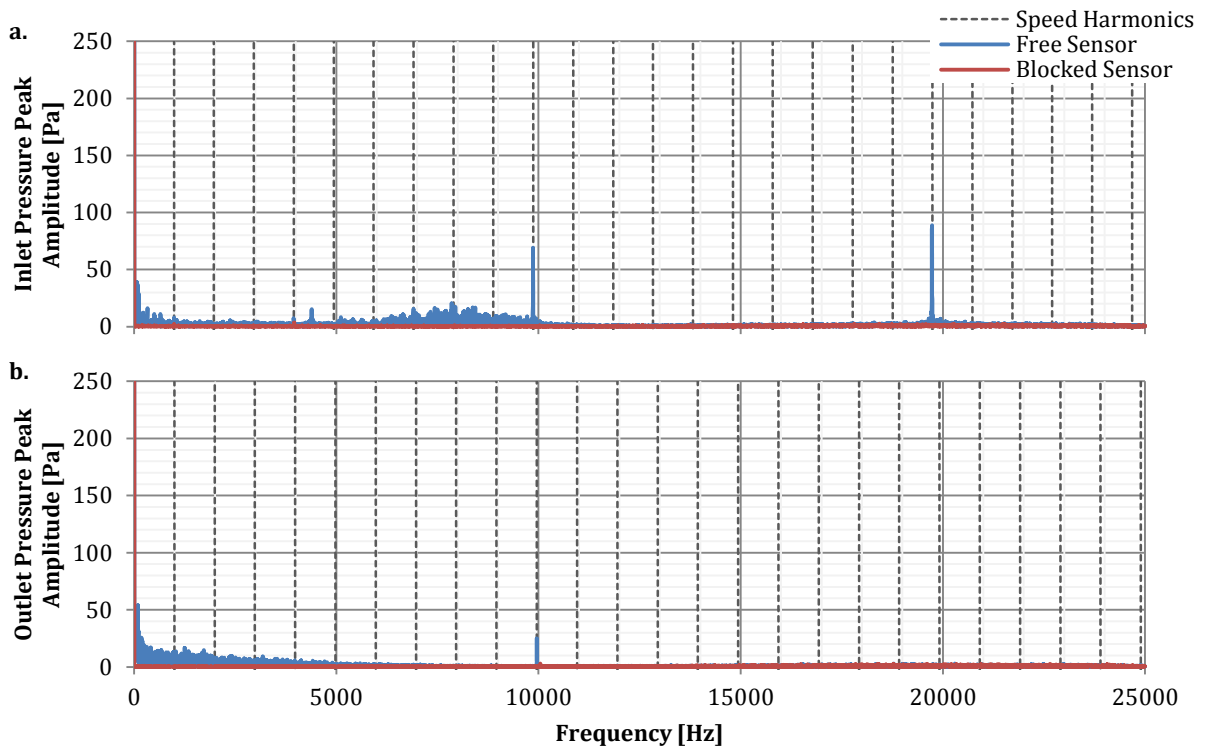


Figure B.4 – Frequency spectrum of the outlet pressure signal. In part a. the electrical machine is operating in generating mode with a 100% torque demand and in part c. the electrical machine is off

SPEED PARAMETER 3950 REV/MIN/ $\sqrt{K}$

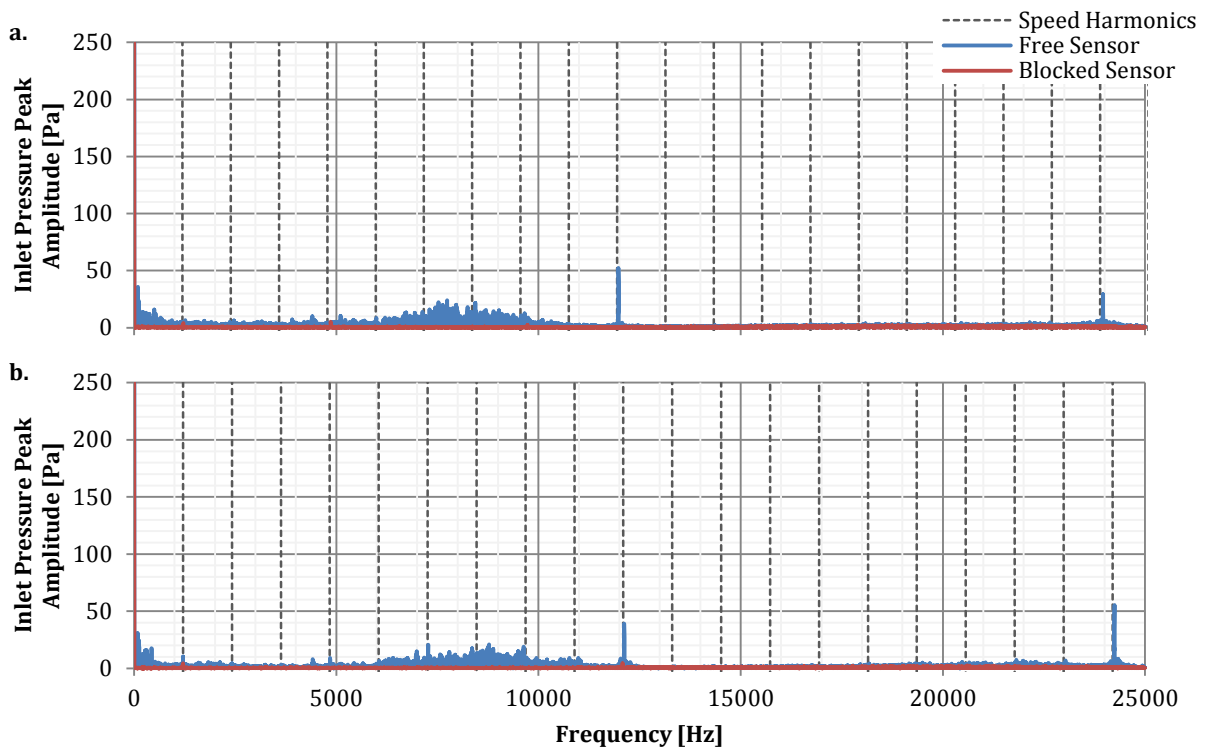


Figure B.5 – Frequency spectrum of the inlet pressure signal. In part a. the electrical machine is operating in generating mode with a 100% torque demand and in part c. the electrical machine is off

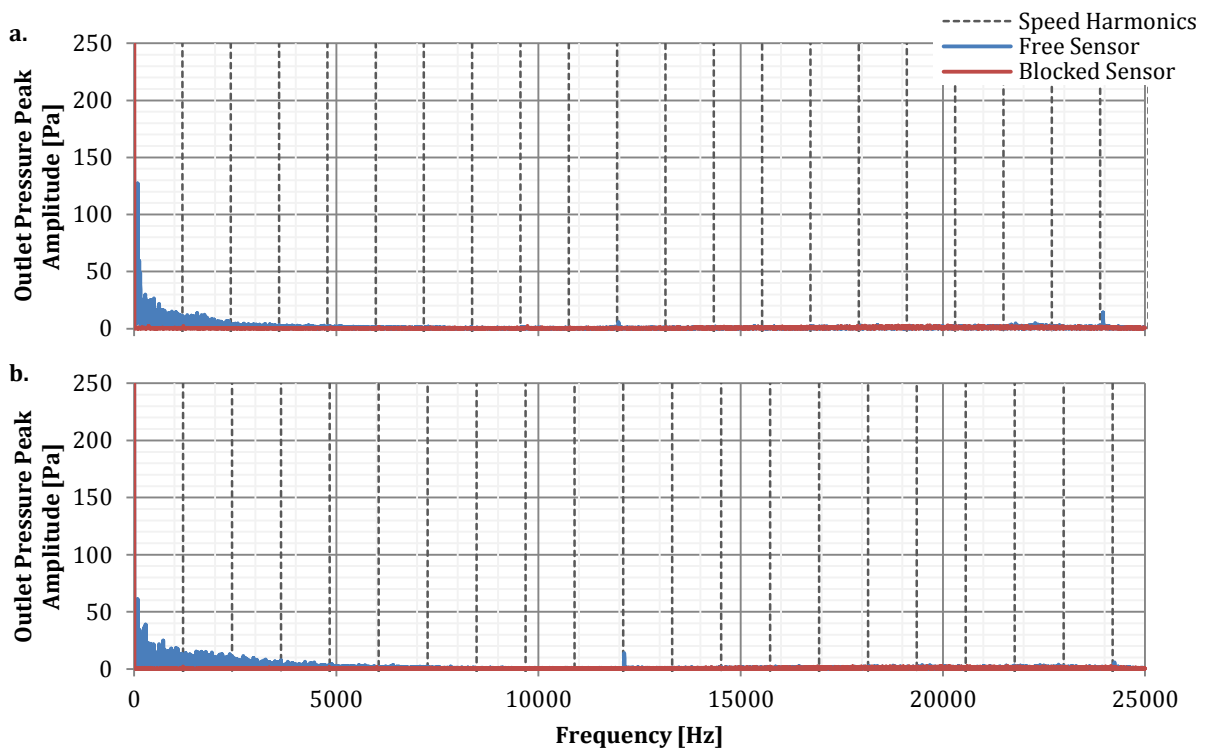


Figure B.6 – Frequency spectrum of the outlet pressure signal. In part a. the electrical machine is operating in generating mode with a 100% torque demand and in part c. the electrical machine is off



# SPEED PARAMETER 4608 REV/MIN/ $\sqrt{K}$

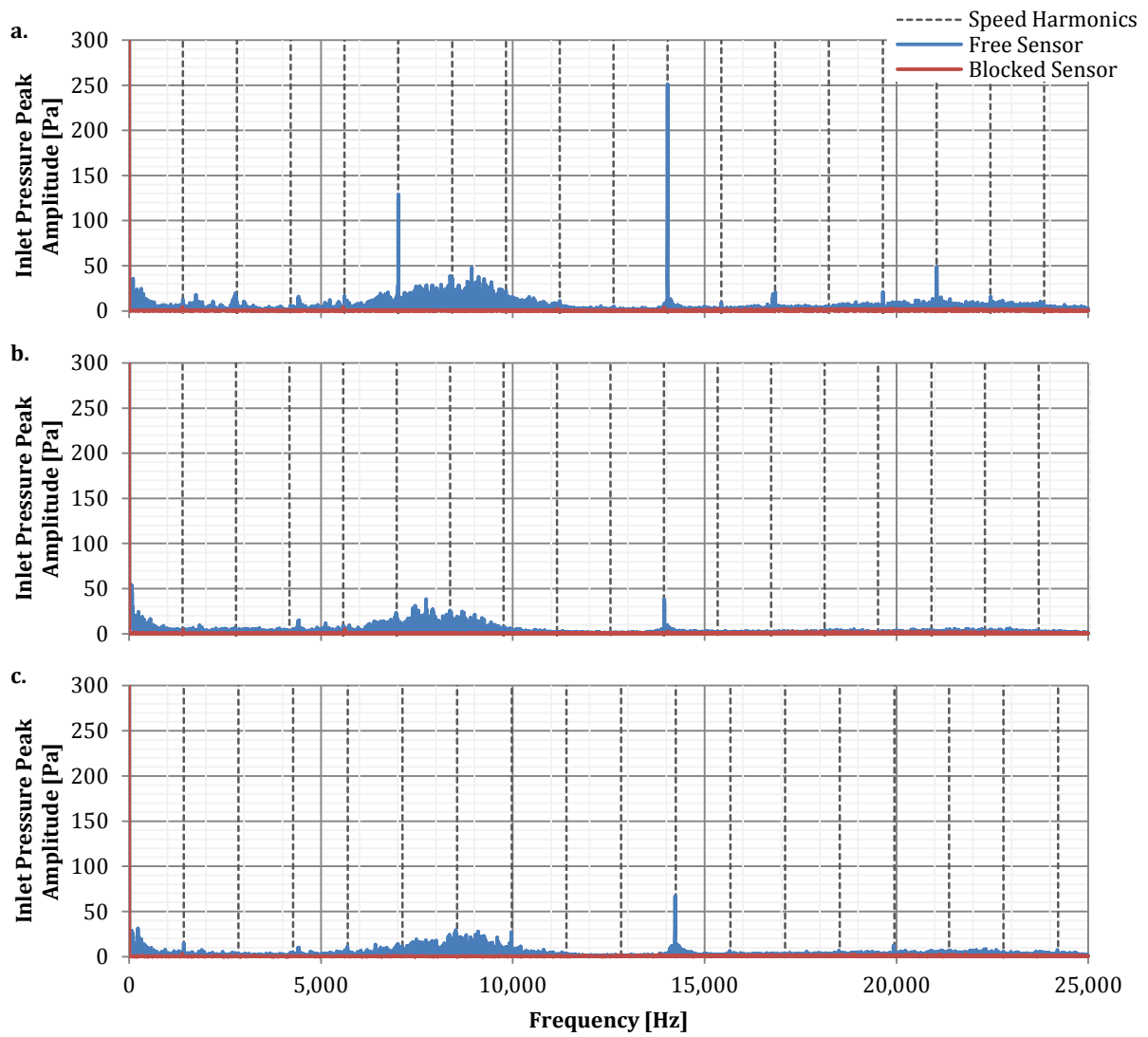
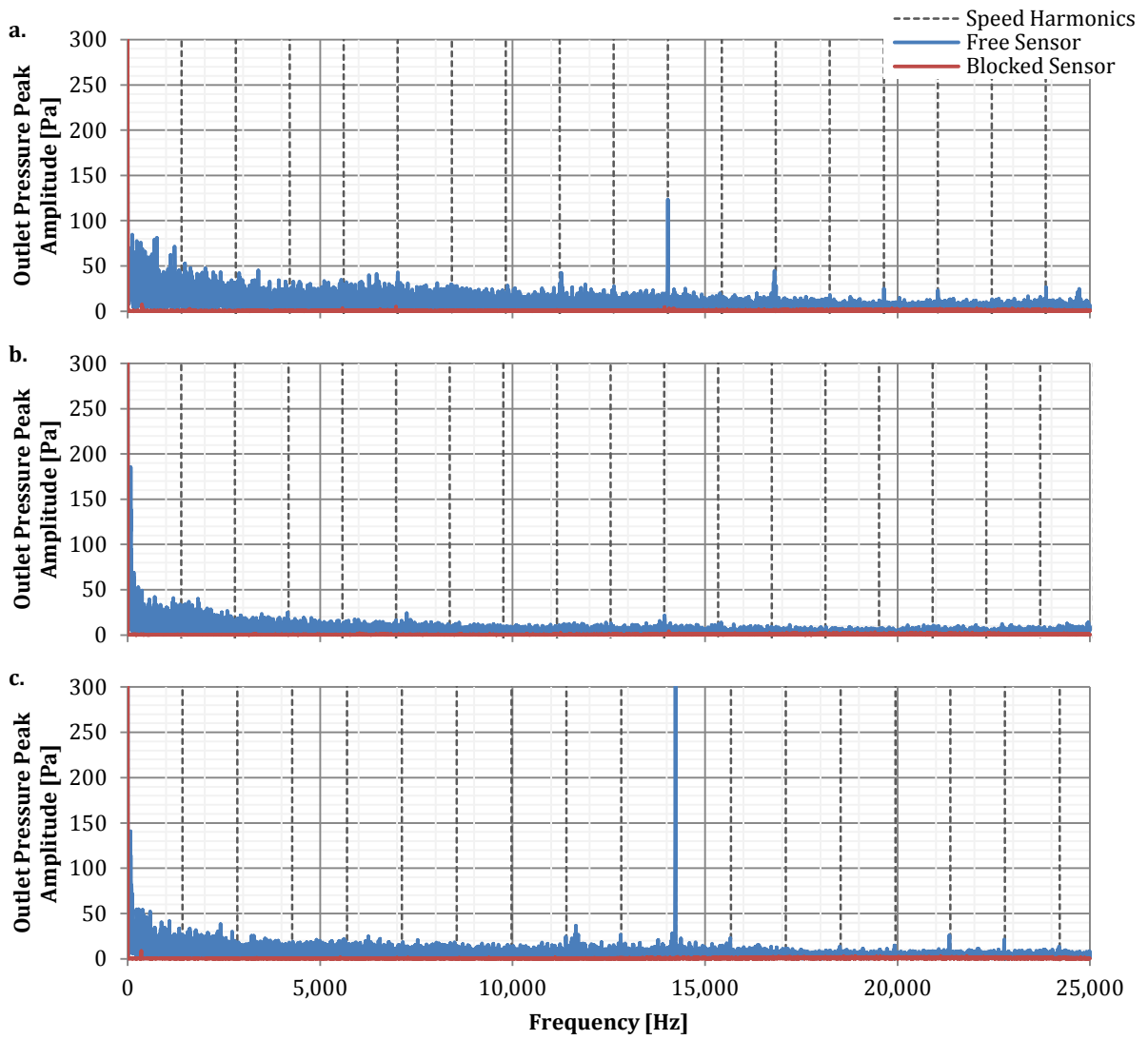


Figure B.7 – Frequency spectrum of the inlet pressure signal. In part a. the electrical machine is operating in motoring mode with a 50% torque demand, in part b the electrical machine is operating in generating mode with a 100% torque demand and in part c. the electrical machine is off



**Figure B.8 – Frequency spectrum of the outlet pressure signal. In part a. the electrical machine is operating in motoring mode with a 50% torque demand, in part b the electrical machine is operating in generating mode with a 100% torque demand and in part c. the electrical machine is off**